UNIVERSITY OF SOUTHAMPTON

A Virtual Boundary Method for Compressible Flow with Application to Aeroacoustics of Compliant Trailing-Edges

by

Stefan Christian Schlanderer

A thesis submitted in partial fulfillment for the
degree of Doctor of Philosophy

in the
Faculty of Engineering and Environment
Aerodynamic and Flight Mechanics Group

March 2017

UNIVERSITY OF SOUTHAMPTON

ABSTRACT

FACULTY OF ENGINEERING AND ENVIRONMENT
Aerodynamic and Flight Mechanics Group

Doctor of Philosophy

by Stefan Christian Schlanderer

This work introduces a novel virtual boundary method for compressible flows with application to aeroacoustics. The method is the compressible extension of the boundary data immersion method (BDIM, Maertens & Weymouth (2015)). The BDIM equations for the compressible Navier-Stokes equations are derived and the accuracy of the method for the hydrodynamic representation of solid bodies is demonstrated with challenging test cases relevant to aeroacoustic applications, including a fully turbulent boundary layer flow and a supersonic instability wave. In addition, it was shown that the compressible BDIM is able to accurately represent noise radiation from moving bodies and flow induced noise generation without any penalty in allowable time step.
The newly introduced framework was employed to investigate the noise radiation from elastic trailing-edges (TE). A study employing elastic TE extensions for airfoils at angle of attack showed a noise amplification when the structural motion is close to resonance. Furthermore significant effects of the elastic TE extension on the characteristics of the laminar separation bubble on the suction side were found, resulting in a global change of the flow around the airfoil. For that reason, in an attempt to avoid changes in circulation complicating the comparison between rigid and elastic TE, a generic setup featuring a flat plate and a vortex generator was developed to investigate different material parameters for the elastic TE. Excess noise was found to be radiated in frequency bands related to the response of the motion of the elastic structure. However, a noise reduction was observed for certain frequency ranges and structural parameters. The noise reduction was associated with an attenuation of the incident pressure fluctuations. When structural damping was taken into account significant noise attenuation compared to the undamped and the rigid cases was found. The noise reduction was attributed to reduced fluctuations of the structural deflections. Finally, the simulation of a fully turbulent flow convecting over an elastic TE showed qualitatively similar behaviour to the two dimensional studies. However, the excess noise from the structural motion was relatively more important than in the two dimensional case and the overall noise reduction was reduced. The motion of the elastic TE is shown to increase the energy in the low wave number spanwise modes.

Contents

Nomenclature

Accronyms

AoA	angle of attack
BDIM	boundary data immersion method
CFD	computational fluid dynamics
DNS	direct numerical simulation
HiPSTAR	**Hi**gh **P**erformance **S**olver for **A**eroacoustic and **T**urbulence **R**esearch
IB	immersed boundary
IIM	immersed interface method
IMBM	immersed boundary method
LES	large eddy simulation
LPCE	linearized perturbed compressible equations
MPI	message passing interface
OASPL	over all sound pressure level
PIV	particle image velocimetry
PSD	power spectral density
RANS	Reynolds-averaged Navier-Stokes equations
SPL	sound pressure level
TE	trailing-edge

Sub- or Superscripts of an arbitrary quantity Φ

$\dot{\Phi}$	temporal derivative of quantity Φ
$\overline{\Phi}$	time averaged quantity Φ
Φ'	fluctuation of a quantity Φ
Φ''	Favre fluctuation of a quantity Φ
Φ^*	quantity with dimensions
Φ^+	quantity Φ in viscous units
Φ^b, Φ_b	indicates a quantity that is defined for a body
Φ^F	indicates a field quantity that is filtered
Φ^f, Φ_f	indicates a quantity that is defined for a compressible fluid
Φ^T	a superscript that denotes a target value on an immersed boundary
Φ_ϵ	indicates a quantity convoluted with a delta kernel or is smoothed
Φ_∞	value at a reference location, e.g. free stream

Φ_L	subscript indicating a quantity from the lower surface of the trailing-edge
Φ_n	the wall normal projection of a vector quantity
Φ_s	indicating a quantity describing a structural property
Φ_U	subscript indicating a quantity from the upper surface of the trailing-edge
Φ_{ref}	reference value
Φ_{rms}	root mean square also denoted standard deviation of quantity Φ
Φ_{ser}	quantities that refer to properties of trailing-edge serrations
Φ_{vib}	a quantity Φ describing the vibration of a cylinder
$\vec{\Phi}$	vector quantity
$\widetilde{\Phi}$	Favre averaged quantity Φ

Symbols

α	empirical constant for integrator of control loop IMBM approach
α	normalization coefficient for a nascent delta kernel K_ϵ
A	amplitude of harmonic body force or motion
A	an area, e.g. of a cross-section
β	empirical constant for proportional control of control loop IMBM approach
$b(\Phi)$	governing equation of a field variable Φ in the solid body domain
χ	abbreviation for $1/[\gamma(\gamma-1)M^2]$
c	speed of sound
C_D	drag coefficient
c_d	damping coefficient
c_f	skin-friction
C_L	lift coefficient
C_p	pressure coefficient
c_p	heat capacity at constant pressure
C_{Df}	skin-friction drag coefficient
C_{Dp}	pressure drag coefficient
C_{Lf}	skin-friction lift coefficient
C_{Lp}	pressure lift coefficient
C_{Su}	Sutherland constant
δ^*	displacement thickness
δ_{ik}	Kronecker delta
d	signed distance from body surface
d_s	length in the span wise direction, i.e. depth
D_{cyl}	Diameter of a cylinder
D_{cyl}	cylinder diameter
dB	decibel
ϵ	half-width of smoothing region

η	second direction in a computational grid, counting with indice j
η	similarity variable in wall normal direction
E	total energy
E_s	Young's modulus
e_{ii}	amplitude of the spanwise spectra of momentum component ii
f	body force acting on a fluid
f	non-dimensional frequency
$f(\Phi)$	governing equation of a field variable Φ in the fluid domain
$f(\tilde{X})$	volume force that drives the velocity of the point $\tilde{X}$ on an immersed body to a desired target value
f_b	frequency of recirculation bubble
F_D	overall drag force
f_D	frequency of drag fluctuations
f_j	natural frequency of a bending beam of mode j
F_L	overall lift force
f_L	frequency of lift fluctuations
f_s	vortex shedding frequency
f_w	weighting of explicit filter
F_{Df}	skin-friction drag force
F_{Dp}	pressure drag force
f_{in}	most dominant input frequency to the trailing-edge noise mechanism
$f_{j,air}$	x-th non-dimensional natural frequency of a structure moving in a vacuum.
$f_{j,vac}$	x-th non-dimensional natural frequency of a structure moving in a vacuum.
F_{Lf}	skin-friction lift force
F_{Lp}	pressure lift force
f_{res}	frequency that is still resolved appropriately on the computational grid
f_{shed}	vortex shedding frequency
Γ	ratio of streamwise and spanwise derivative of pressure
γ	isentropic exponent
Δh	grid spacing
h_e	correlated serration height
h_{ser}	half-height of trailing-edge serrations
h_{TE}	height or thickness of trailing-edge
$\hat{i}$	direction tangential to a body surface
I_s	second moment of inertia of a cross section
$\hat{j}$	direction normal to a body surface
h	inverse of zeroth moment of kernel K_ϵ
K_ϵ	delta kernel

k_1	chord wise wavenumber
k_3	spanwise wavenumber
λ_a	acoustic wave-length
λ_{ser}	wavelength of trailing-edge serrations
$\mathcal{L}$	amplitude variation of characteristics
$\overline{L_2}$	quadratic norm
$\overline{L_\infty}$	infinity norm
L	a length scale
l_z	dimension of the spanwise domain width
$l_{y'}$	spanwise correlation length
μ	dynamic viscosity
μ_0^ϵ	zeroth moment of kernel K_ϵ
μ_1^ϵ	first moment of kernel K_ϵ
μ_m	added mass coefficient
M	Mach number
$\vec{n}$, n_1, n_2, n_3	vector pointing in the wall normal direction, components of the wall normal direction vector
$\vec{\nabla}$	nabla gradient operator
$\hat{n}_c$	joint normal of two intersecting planes
N_x	number of grid points in the x-direction
N_y	number of grid points in the y-direction
N_{tot}	total number of grid points
ν	Poisson ratio
$\mathcal{O}(e)$	order of magnitude of error e
Ω	indicates a domain under consideration
ω	angular frequency
Ω_b	subdomain occupied by a solid body
Ω_f	subdomain occupied by a (compressible) fluid
$\vec{\omega}$, ω_x, ω_y, ω_z	vorticity vector and its three components
Δp_s	pressure loading of structure
Φ	field quantity such as density, velocity or temperature or its governing equation
Φ_m	governing equation of a field quantity that is valid in the whole domain
Π_x	variance of the normalized x-vorticity component
p	pressure
p_i	incident pressure field
p_s	scattered pressure field
p_t	total pressure field
Pr	Prandtl number
φ_j	Mode shape of mode j of a bending beam

q	arbitrary fluid quantity
q_k	heat-flux vector
ρ	density
r, R	radial coordinate in cylindrical coordinates of radial distance from the origin
R_{cyl}	Radius of a cylinder
R_{Su}	ratio between Sutherland constant and freestream temperature
Re	Reynolds number
Re_{δ^*}	Reynolds number based on displacement thickness
$RHS_{u,i}, RHS_T$	right-hand-side of the velocity and temperature equation, respectively
σ	forcing parameter
σ_{ij}	ij component of the Favre stress tensor
σ_{ser}	sharpness the sawtooth of trailing-edge serrations
$\vec{s}$	spatial coordinate in a solid body domain
s	local spatial coordinate of the one-dimensional structural model
St	Strouhal number
τ_{ik}	stress tensor
θ	angle between two intersecting planes or angle in cylindrical coordinate system
T	temperature
t'	Time variable that is used to distinguish between variable that is integrated (t') and the limit of an integral (t)
U, u	velocity
u_τ	friction velocity
V_i	prescribed velocity of solid body
v_s	velocity of the structural motion
v_{vib}	vibration velocity
w_s	deflection of the structure from its neutral position
Δx	grid spacing in x-direction
$\tilde{X}$	vector indicating a point on the surface of an immersed body
$\vec{x}$	vector indicating the location of a point
ξ	first direction in a computational grid, counting with indice i
ξ	transformation operator between coordinate systems $\vec{x}$ and $\vec{s}$
Δy	grid spacing in y-direction
Δz	grid spacing in z-direction

Acknowledgements

The time in which the work presented here was conducted and written was exciting, inspiring, instructive and sometimes frustrating. Many amazing people helped, guided and supported me during that time and I am sorry that I will most likely forget some of them in the following acknowledgements.

First, I would like to thank my first supervisor Professor Richard D. Sandberg for his incredible ability to put the focus on the good things and on how one can still move on even if things did not work out as expected. There were many meetings that cheered me up by orders of magnitude and helped to stay on track and not get tangled up with unimportant things. Second, I want to acknowledge the support and smart comments from my second supervisor Dr. Gabe D. Weymouth. When I got stuck with some validation cases or practical problems of implementing the BDIM he often had a smart idea, derived ad-hoc an important interpolation scheme or remembered having stumbled across something similar. I also would like to thank my examiners Professor Neil Sandham and Dr. Mahdi Azarpeyvand for their efforts and feedback to improve this work.

Thanks to my "senior" PhD colleagues and dear friends Richard Pichler and Patrick Bechlars for sharing their wisdom and experience in the field of coding as well as physics and maths with me. In addition, it was great to be part of some amazing collaborative software projects started by the HiPSTAR team with Sonia Serrano, Javier Otero, Jake Leggett and Florian Hammer. During my time in Soton on the "sun-deck" in the fifth floor of Tizard I enjoyed to company of commander Yusik, my friend Kuti as well as Robert in the office. These guys made me never feel alone and were always good for a laugh.

From my personal environment I deeply acknowledge the patience, understanding and encouraging words of my lady Tina. She believed in me when I did not any more and she tried hard to understand my issues at work getting to some serious expertise in code development and CFD over the years, despite a totally different professional background. I also want to thank my parents and sisters who always supported me and got to love the South of England as much as I did over their visits.

Thanks to all my friends in Soton who made these three years really colourful and enjoyable. It was a great honour to live together with the crew in "Tha Mews", making music with the guys from "The Foil Man Blues" and having a pint or two, a BBQ or a hike with all the other guys.

Chapter 1

Introduction

1.1 Motivation

Increasing air traffic and the growing number of wind turbine installations in the vicinity of populated areas have brought annoyance from aerodynamically generated noise to attention in the past decades. Considerable efforts have been made to investigate noise perception and resulting annoyance from wind turbines (Hubbard & Shepherd, 1991; Pedersen & Persson Waye, 2004; Taylor *et al.*, 2013). The present work is concerned with trailing edge (TE) noise and measures to reduce it. TE noise is generated by the interaction between a sharp TE and pressure fluctuations in the fluid flow. If the boundary layer is turbulent, pressure fluctuations are present over a wide range of frequencies. This causes broadband noise radiation and is a dominant contributor to noise produced in many engineering applications of lifting surfaces such as wings and rotating blades. Acoustic field measurements of wind turbines, for example, showed that the TE is the dominant source of noise (Oerlemans *et al.*, 2007). Where other noise sources can be reduced or avoided by a careful design, TE noise is the only remaining noise source when an airfoil encounters a non-turbulent inflow, even though the level of background disturbances might alter the transition characteristics and therefore also the noise radiation from the TE. However, TE noise is the minimum achievable noise and also denoted as airfoil self-noise (Roger & Moreau, 2004, 2005). Therefore it is necessary to reduce TE noise in order to reduce the noise generated by airframes, wind turbines and fan blades.

1.2 Review of Trailing-Edge Noise Research

In the following section physical mechanisms (section 1.2.1) that cause TE noise are discussed. Section 1.2.2 emphasizes measures that have been reported to reduce TE

noise. Finally, methods that have been applied to investigate TE noise are summarized in section 1.2.3.

1.2.1 Physical Mechanisms

According to Brooks *et al.* (1989) airfoil self-noise can be caused by the following five mechanisms:

1. Turbulent boundary layer trailing-edge noise caused by turbulent fluctuations in the boundary layer convecting over the TE.
2. Laminar boundary layer vortex shedding noise through vortex shedding in the wake. In low Reynolds number flows this mechanism is a dominant quasi-tonal source of noise.
3. Separation and stall noise from an airfoil at high angle of attack caused by vortices shed from boundary layer separation near the TE or low frequency noise caused by large scale separation known as deep stall. In a slightly separated flow the dominant noise radiates from the TE. In contrast to that the noise radiated from an airfoil in deep stall is a result of the interaction between the airfoil's rigid body and the pressure fluctuations generated by the separated flow.
4. TE bluntness noise is caused by vortices shed from the TE. It can be a very important quasi tonal contributor to the overall noise.
5. Noise caused by tip vortex is considered to be relatively weak compared to the other mechanisms.

All of the listed mechanisms except for the tip vortex noise are related to the interaction of pressure disturbances with the solid airfoil TE. In order to estimate the acoustic intensity that is produced by fluctuations in a fluid flow, Lighthill (1952, 1954) developed his theory of "Sound Generated Aerodynamically" in the early fifties. This was at the time when the first passenger aircraft with jet engines were about to enter service and Lighthill wanted to understand and predict jet noise. It was the first general theory that directly estimated the intensity of radiated sound from a fluid flow. The analysis shows that turbulent fluctuations in the freestream are acoustic sources of quadrupole type. They are inefficient acoustic radiators in low speed flows (i.e. with a small Mach number M) as the radiated acoustic intensity scales with $\sim M^8$. Curle (1955) extended this fundamental theory to account for solid boundaries including effects such as reflection and diffraction. In this approach the force that a body exerts on the fluid is represented by a dipole source as an additional term in Lighthill's original equation. Dimensional analysis shows that the presence of a rigid wall increases the radiation efficiency because of the predominant dipole and the acoustic intensity scales with $\sim M^6$. Analytical predictions

of the acoustic intensity radiated by an eddy convecting over a TE show a scaling with $\sim M^5$ and were first investigated by Ffowcs Williams & Hall (1970). Therefore these fluctuations are much stronger sources of noise than freestream or wallbounded fluctuations for low Mach numbers.

Hence the TE geometric singularity, with the characteristics of the flow changing from a wall-bounded to a free-shear flow, enhances sound radiation. The acoustic scattering of incident pressure fluctuations when convecting over the TE can be regarded as a diffraction process. This results in an acoustic field where the amplitude of the radiated noise is higher than that of the incident field (Ffowcs Williams & Hall, 1970; Crighton & Leppington, 1971). The character of the radiated acoustic field depends on that of the incident pressure fluctuations, i.e. whether they are present over a wide range of frequencies or at a single frequency. The presence of the rigid TE converts some of the high-wavenumber near-field energy to sound waves (Crighton & Leppington, 1971). Brooks & Hodgson (1981) suggested as a conclusion from experimental data that the geometric singularity does not lead to a singularity in the velocity field due to the action of viscosity. Furthermore the incident and scattered pressure field overlaying each other result in a vanishing pressure difference at the TE which was also observed in direct numerical simulations (DNS) of Sandberg & Sandham (2008). Hence the scattering phenomena adjusts the pressure in the boundary layer such that the pressure difference is close to zero. This concept also explains the reason for the acoustic field being out of phase on the upper and lower sides of the TE as observed by Brooks & Hodgson (1981) and Sandberg *et al.* (2007).

The influence of moderate thickness and camber of an airfoil on the radiated TE noise can usually be neglected. However, these parameters influence the hydrodynamic field and therefore the fluctuating sources of the acoustic field. The scattering mechanism can be regarded as a global surface effect of the TE, though (Roger & Moreau, 2004). Hence a flat plate can be regarded as the limiting case of an airfoil and has been used as a model of such extensively (Howe, 1978; Moreau *et al.*, 2011). In contrast the finiteness of the chord length can not be neglected when the airfoil extends into the acoustic far field, i.e. is not acoustically compact (Howe, 1999). A non compact airfoil changes the directivity pattern through backscattering from the leading edge. This results in an acoustic field where TE noise at lower frequencies is partially cancelled out by leading edge backscattering (Roger & Moreau, 2005).

1.2.2 Trailing-Edge Noise Reduction

In the previous section the scattering mechanism of TE noise has been outlined. The critical parameters defining the intensity of the scattered noise are the characteristics of

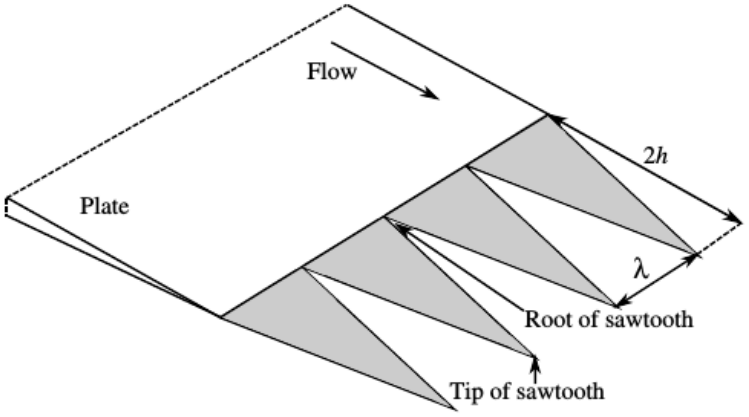

Figure 1.1: Sketch of a flat plate with TE serrations introducing the half height h and wave length λ of the serrations (Moreau & Doolan, 2013*a*). In this work the subscript *ser* is used to distinguish from other heights and wave lengths, clarifying that these quantities describe the serrations, i.e. h_{ser} and λ_{ser}.

the boundary layer (Moreau *et al.*, 2012*b*) and the length of the TE that is wetted by the flow. This is mirrored in the input data that analytical TE noise models, as reviewed in Howe (1978), require. Measures to reduce TE noise by modifying the aforementioned parameters are outlined in the following sections, where 1.2.2.1 covers the concept of low noise airfoil design and 1.2.2.2 modifications of the TE properties.

1.2.2.1 Low Noise Airfoil Design

A turbulent boundary layer developing along the chord of an airfoil can be regarded as an input of the TE radiation mechanism. Therefore a noise reduction can be realized when the evolution of the boundary layer is modified favourably, i.e. the fluctuation levels on the airfoil's aft surface are reduced. This can be achieved by modifying the pressure distribution around the airfoil (Schepers *et al.*, 2007). Lutz *et al.* (2007) and Schepers *et al.* (2007) achieved an overall noise reduction of $1-3$ dB with an improved aerodynamic performance by using an optimized airfoil shape. Lee (2013) used a genetic optimization algorithm and achieved a noise reduction of the overall sound pressure level of 2.6dB with only a slight increase in noise level for high frequencies. Hence low noise airfoil design is an important measure to reduce TE noise and has also proved to reduce noise of full-scale wind turbines (Oerlemans *et al.*, 2009). However, airfoil optimization is often applied to a limited range of operating conditions and thus might lead to unfavourable behaviour in off-design conditions (Ai *et al.*, 2015).

1.2.2.2 Modification of the Trailing-Edge Properties

Howe (1991*a*,*b*) argued that a turbulent eddy only generates significant noise when its wavenumber vector is normal to the TE. He suggested reducing the effective length

along the TE that satisfies this condition, i.e. the length where the wavenumber vector is normal to the TE. This can be achieved by using a serrated instead of a straight TE, as sketched in figure 1.1. In fact analytical analysis of a flat plate with a serrated sawtooth TE (Howe, 1991*b*) predicted that the intensity of radiated noise could be reduced. The magnitude of the predicted reduction depends on the height/amplitude and spanwise spacing/wavelength of the teeth. To achieve a noise reduction the amplitude should be at least of the order of the turbulent boundary layer thickness and the serrations should be inclined at an angle that exceeds about 45° to the direction of the mean flow. Furthermore, noise reductions are only expected for acoustic frequencies f above $fh_{ser}/U \gg 1$, where h_{ser} is the half height of the serrations and U the flow speed. Additionally, a greater noise reduction is predicted for increasing h_{ser}/λ_{ser} with λ_{ser} being the wavelength of the serrations.

Indeed numerous experimental (Dassen *et al.*, 1996; Oerlemans *et al.*, 2009; Gruber *et al.*, 2010*a*,*b*, 2011; Chong *et al.*, 2011; Moreau *et al.*, 2012*a*; León *et al.*, 2016) and numerical (Sandberg & Jones, 2011; Jones & Sandberg, 2012; Arina *et al.*, 2012) studies showed an overall noise reduction in the range of 3-10 dB, depending on the frequency when serrated TE were used. Sandberg & Jones (2011) and Jones & Sandberg (2012) reproduced a similar behaviour of the noise reduction as a function of frequency as the predictions of Howe (1991*b*). However, this is in contrast to the findings of other studies where a noise reduction could be observed for lower frequencies and an increased noise level was found for high frequencies. Gruber *et al.* (2011) speculated from measured velocity spectra and flow visualization that the increased noise level originates from high intensity flow through the trough of the saw teeth. In contrast to previous designs a novel serration geometry with a slitted sawtooth and a random TE distribution of the serrations presented by Gruber & Joseph (2013) and modelled by Azarpeyvand *et al.* (2013) resulted in a low or no increase of noise in the high frequency range. Nevertheless the exact reason for the noise increase at high frequencies remains unclear. In general, predictions based on the model of Howe (1991*b*) overestimated the noise attenuation that was actually found. However, with the new model developed by Lyu *et al.* (2016) the accuracy of the predictions were found to be in better agreement with observations in experiments. In addition the conditions to obtain a noise reduction formulated by Howe (1991*a*,*b*) were upgraded to the two necessary conditions $k_1 h_e \gg 1$ and $k_1 h_{ser} \gg 1$. Here k_1 is the wavenumber in the chordwise direction of a wall pressure gust and h_{ser} is the half-height of the serration. Furthermore, h_e describes the correlated serration height and can be calculated with $2h_e = \sigma_{ser} l_{y'}$, with $l_{y'}$ being the spanwise correlation length and $\sigma_{ser} = 4h_{ser}/\lambda_{ser}$ the sharpness of the sawtooth.

The model of Howe (1991*b*) predicts that noise reduction increases for higher h_{ser}/λ_{ser}. This could be reproduced among 30 serration geometries attached to a NACA6512 airfoil (Gruber *et al.*, 2011). It was found that the effect of serrations was insignificant when

the typical eddy size is larger than the sawtooth length. In contrast to broadband TE noise Moreau *et al.* (2012*a*) and Moreau & Doolan (2013*b*) found that wider serrations yielded higher attenuation of tonal noise in experiments with a flat plate. Gruber *et al.* (2010*a*) extended the theory of Howe (1991*b*) to slitted trailing-edges and concluded that they are less efficient in reducing noise, especially for high frequencies. Experimental data confirmed these findings and showed 2 dB noise reduction in the low frequency range and an increased noise level of 1–2dB in the mid-frequency (300–7000Hz) range.

The aforementioned studies considering airfoils generally used flat plate extensions, also denoted as splitter plates, attached to the actual profile and applied modifications to the TE of the extension. Chong *et al.* (2012, 2013*b*) cut the serrations into the airfoil body without flat plate extensions. This serration type is also termed non-flat plate, non-insertion type or broken serrated TE in the literature. The measured data did not show the typical increased noise level for high frequencies observed when using flat-plate extensions. However a significant contribution of bluntness noise in a narrow frequency band was found. It was speculated that they originate from vortices that are shed from the root of the serrations. Additionally, an overall noise reduction could only be achieved for wide serration geometries which agrees with the results of Moreau & Doolan (2013*b*) for the reduction of tonal noise. The bluntness noise could be reduced by covering the serrations with a mesh screen, although this resulted in a higher noise level at high frequencies (Chong *et al.*, 2013*a*). In a recent study by Vathylakis *et al.* (2015) the gaps between the cut in serrations were filled with different metal foams which eliminated these additional noise sources at minute aerodynamic penalty.

The study of Jones & Sandberg (2012) indicates that the noise reduction by the use of TE serrations is achieved by changing the scattering process itself as the development of the boundary layer upstream of the TE seemed to be hardly affected by the presence of serrations (Gruber *et al.*, 2010*b*; Jones & Sandberg, 2012). Chong & Vathylakis (2015) concluded that the redistribution of momentum and turbulent shear stress in the vicinity of the serrations leads to a reduced efficiency of the scattering process at the TE. High fidelity numerical simulations presented in Jones & Sandberg (2012) showed that the serrations yield a smoother evolution of hydrodynamic quantities over the TE and hence reduce the discontinuity in the change of the boundary condition. In the direct vicinity of the TE, horseshoe vortices are generated in the trough of the serrations (Jones & Sandberg, 2012). These coherent structures increase the spanwise correlation length up to one serration wavelength downstream of the TE. In the wake the spanwise correlation length decreases more rapidly in the serrated case (Jones & Sandberg, 2012). These findings are consistent with experimental data of Moreau *et al.* (2012*a*), who found an increased turbulent length scale in the vicinity of the serrated TE. Further downstream in the wake there are slight differences that become more and

more insignificant with increasing downstream distance. Liu *et al.* (2015, 2016) investigated the properties of the wake of an asymmetric NACAC65(12)-10 with flat plate TE serrations attached. It was found that the velocity profiles vary significantly between the root and the tip location leading to shear stress between those planes. Furthermore a significant reduction of the turbulence levels in the presence of serrations was observed.

Considering the input to the TE mechanism the data presented by Jones & Sandberg (2012) indicate that the wall surface pressure fluctuations upstream of the TE does not feature a change of spanwise correlation levels on the suction or pressure side. Furthermore, the directivity of the acoustic field is not affected by the serrated TE (Moreau *et al.*, 2012*a*). Using their new mathematical model for the prediction of noise originating from serrated TE's Lyu *et al.* (2016) found that the noise reduction can be attributed to destructive interference of the scattered surface pressure.

Apart from a reduction of turbulent boundary layer noise, TE bluntness noise can be reduced by serrations. In this case the modified TE suppresses vortex shedding from the TE (Moreau *et al.*, 2012*a*). In contrast to turbulent boundary layer noise, this is most efficient for wider serration geometries (Moreau & Doolan, 2013*a*). Additionally airfoil instability noise was found to be reduced by applying a non-insertion type serrated TE (Chong *et al.*, 2010, 2011). This kind of noise is generated by laminar boundary layer instabilities that are amplified by a separation bubble close to the TE. The serrations were found to reduce the bubble length and even suppress its generation for higher angles of attack and reduce the efficiency of the scattering process. Thus the mechanism of the noise reduction for laminar airfoil instability noise is partly different from the reduction mechanism of turbulent boundary layer TE noise mentioned above.

Previous studies commonly concluded that the use of flat plate extensions with and without serrations generally does not decrease the aerodynamic performance of airfoils. Static pressure measurements of Gruber *et al.* (2010*a*) showed a negligible effect of serrations on the lift generated. Furthermore, Oerlemans *et al.* (2009) investigated experimentally the effect of adding TE serrations, as well as optimizing airfoil geometry, to full size wind-turbine blades. It was found that for realistic airfoil geometries overall self-noise reductions of $2-3$dB are possible without adversely affecting aerodynamic performance. en reported in Chong *et al.* (2012, 2013*a*); Chong & Joseph (2013). However, recent experimental investigations by Liu *et al.* (2015, 2016) show that, in particular for asymmetric airfoils (NACA65(12)-10), sawtooth trailing-edge serrations decrease the lift coefficient up to 15% for angles of attack in the range of $-5°$ to $10°$ in comparison to the baseline case. Furthermore, the use of non-insertion type serrations may well have effects on the aerodynamic performance, albeit no quantitative data has been reported

in Chong *et al.* (2012, 2013*a*); Chong & Joseph (2013).

Attaching brushes to the TE can be regarded as a limiting case of TE serrations with a short wave length and an infinitely sharp tip. The effect of brushes as a TE modification has been investigated experimentally using flat plates (Herr & Dobrzynski, 2005) and airfoils (Herr, 2007). Similarly to Moreau *et al.* (2012*a*) the broadband noise as well as bluntness induced noise could be reduced compared to the straight TE for low and moderate frequencies. Additionally an increased noise level for high frequencies could be observed. The scaling with the flow velocity was not altered by the addition of the brushes and followed the fifth power law. Hence, Herr & Dobrzynski (2005) suggested that the noise reduction is predominantly achieved by modifying the local flow field around the TE. The reduction of bluntness noise supports this hypothesis. Experimental data of Finez *et al.* (2010) revealed that adding brushes severely reduce the spanwise coherence of typical eddy structures downstream of the TE. Besides the geometric differences a major distinction to serrated TE is the enhanced compliance of the flexible brushes. Herr (2007) showed that brushes with a higher elasticity yielded a better noise reduction.

In general, the effect of elasticity on TE noise has only been considered in the literature with relatively crude assumptions or slightly different emphasis. Crighton & Leppington (1970) carried out an analytical study that considered acoustic scattering characteristics of a compliant half plane. The half plane was considered to react to fluid loading locally only, thus neglecting elastic resistivity. It was shown that compliance can change the scaling of the acoustic pressure to $\sim M^6$ for a relatively flexible plate and heavy fluid loading. Cannell (1975, 1976) and Howe (1992) analysed the acoustic scattering of surface waves at the TE of a fluid loaded plate. Howe (1993) considered structural and acoustic noise of an elastic TE where the intensity of the sound generated was predicted to depend on the fluid loading and the ratio of the incident and coincidence frequencies. Bae *et al.* (2008) numerically investigated the effect of elasticity on TE bluntness and wake induced noise. A recent analytical study relevant to this work was carried out by Jaworski & Peake (2012, 2013). This work considers the interaction of a turbulent eddy with a poroelastic edge of a semi-infinite plate. The results show that a poroelastic edge yields the weakest noise amplification compared to an elastic and a rigid edge. However, when heavy fluid loading is considered the additional advantage of porosity compared to the elastic case vanish. The elastic case shows a strong dependency on the frequency range that is considered. For the low frequency range it shows a seventh power velocity dependency, which changes for higher frequencies, resulting in the same amplification as the rigid case. Both of the aforementioned studies on a poroelastic TE did not consider the effect of additional noise that is created by the motion of the TE. However, in a recent study by Cavalieri *et al.* (2016) the effect of structural resonance

and bending waves were considered together with a finite length of the poroelastic plate. Manela (2011) also accounted for the motion induced sound and found that the noise contribution from the moving TE is amplified by the shed TE vortices and results in an increased noise level at the natural frequencies. Furthermore the flat plate was assumed to be acoustically compact, which is in constrast to Jaworski & Peake (2013). Similarly to Jaworski & Peake (2013), Manela (2011) also predicts a reduction of the TE noise component. Manela & Huang (2013) considered a different configuration featuring a thin airfoil with a flap that is coupled to the wing by a torsional spring. The analysis shows that the elastic flap can lead to a noise attenuation or amplification depending on the natural frequencies of the system. Noise amplification occurs when the natural frequencies of the torsional spring are close to the frequency range of the vortex airfoil interaction. The same frequency dependent behaviour has also been shown for an elastic sheet actuated at its leading edge (Manela, 2012) and an elastic pitching airfoil (Manela, 2013). Very recently an experimental proof of concept by Das *et al.* (2015) investigated the effect of an elastic trailing-edge attached to a flat plate at 0° angle of attack. For the high frequency range the elastic TE case showed a noise reduction of up to 4dB. Overall the elastic TE yielded a broadband attenuation of TE noise of 2dB. However, Das *et al.* (2015) did not report any measurements of the hydrodynamic near-field or the structural deflections when employing elastic TE's making it difficult to conclude on physical mechanisms.

It can be concluded that elasticity plays an important role for the scattering of noise at a TE and the resulting acoustic field. It might well lead to a noise reduction when incorporated in the design process of TE extensions carefully, but potentially also amplify the produced noise level for some frequency ranges or specific sets of parameters.

In addition to the shape and elastic properties, brushes feature another important difference to TE serrations: a comb or a brush is permeable for the fluid. Thereby the geometric discontinuity is smeared out along the brushes via transpiration through the brushes. Herr & Dobrzynski (2005) suggested that viscous damping in the cavities between the brushes plays an important role for noise reduction. The use of porous TE has been investigated in the past in various studies. Jaworski & Peake (2012, 2013) showed that the scattered noise scales with a sixth-power Mach number dependence for a rigid porous TE when low frequencies are considered. Weidenfeld & Manela (2016) developed a computational model of a permeable airfoil based on thin-airfoil theory and compact body calculations and represented the surface porosity by employing Darcy's law. A noise reduction of up to 3dB for the porous airfoil was found alongside a time-delay of the pressure signal. Geyer *et al.* (2010) measured TE noise of airfoils that were made of different porous materials and found a reduction of up to 10 dB and more compared to the non-porous airfoil for low and medium frequencies. For high frequencies an increase

of the noise level occurred, possibly due to surface roughness noise. The use of porous materials led to an increase in drag and a decrease in lift, though. Hence in contrast to TE serrations porous materials do have effects on the aerodynamic performance. A numerical study by Bae & Moon (2011) considered a porous TE attached to a flat plate and observed a significant noise reduction over a wide range of frequencies. The reduction was attributed to the reduced correlation length of the wall pressure fluctuations in the spanwise and streamwise directions. Additionally, the porous TE reduced the length of the separated flow region upstream of the TE at angle of attack. Ali *et al.* (2016) concluded from their measurements and the ratio of the amplitudes of the dominant structures in the streamwise and spanwise direction that the turbulent structures are elongated in the spanwise direction. This also led to a reduction of the energy content of the velocity fluctuations in the near wake. Hence it can be summarized that porous TE can reduce noise radiation significantly. Nevertheless, it must be noticed that effects on the aerodynamic performance are possibly not negligible.

The above outlined measures to reduce TE noise are purely passive methods to influence the hydrodynamic field around the TE and/or modify the scattering mechanism itself. It is also possible reduce TE noise using active measures. Methods that were considered in the past include TE blowing (Winkler *et al.*, 2012*a*), multi-species gas injection (Koh *et al.*, 2013), synthetic jet (Mankbadi *et al.*, 2015) and plasma actuators Inasawa *et al.* (2013). Furthermore TE ailerons (Straub *et al.*, 2001), microtabs (Johnson *et al.*, 2009) as well as morphing structures (Ai *et al.*, 2015) have shown to reduce noise emission and aerodynamic performance. However, active TE noise reduction methods are not delved into in this work.

1.2.3 Methods to Analyse Trailing-Edge Noise

The following section focusses on different approaches to predict TE noise and understand the scattering mechanism. Section 1.2.3.1 outlines analytical, 1.2.3.2 experimental and 1.2.3.3 numerical methods.

1.2.3.1 Analytical Methods

Analytical approaches can give principal dependencies of the scattering characteristics on certain parameters. A vast number of analytical models of TE noise has been developed and differ predominantly in the required input data. Howe (1978, 1999) reviewed those models and suggested distinguishing them using the following three categories:

- Theories that are based on the acoustic analogy by Lighthill (1952), where the quadrupole and dipole sources are determined from the turbulent velocity field.

Such approaches have been developed by Ffowcs Williams & Hall (1970); Crighton & Leppington (1970); Crighton (1972); Howe (1976) among others. As Lighthill (1952) derived them analytically from the Navier-Stokes equations, exact predictions that contain the contributions of all sources can be obtained, when the turbulent velocity field is known.

- Theories that are based on special problems approximated by the linearized hydroacoustic equations such as Chase (1972); Crighton & Leppington (1974); Amiet (1976). In these theories the radiated noise is deduced from pressure fluctuations on both TE surfaces which can be derived from the velocity fluctuations of the hydrodynamic field.
- Ad hoc models with postulated source distributions, as presented by Tam & Yu (1975); Tam & Reddy (1977); Hayden *et al.* (1976), where the strengths and multipole types are determined empirically.

For all of the aforementioned methods, difficulties arise from the provision of accurate input data when calculating the radiated TE noise. In purely analytical approaches the hydrodynamic statistics of the boundary layer need to be modelled with numerous simplifying assumptions. These might not always be justified and usually have a limited validity, as found in Schepers *et al.* (2007). A number of semi empirical turbulent boundary layer models have been developed in the literature, such as one by Moreau *et al.* (2011) and Lee & Cheong (2013), among others. In general, measuring or modelling the statistics of the wall pressure fluctuations under the influence of pressure gradients accurately is a very active field of research (Garcia-Sagrado & Hynes, 2012; Bertagnolio *et al.*, 2014; Martínez-Lera *et al.*, 2014; Kamruzzaman *et al.*, 2015; Stalnov *et al.*, 2016).

When using measured input data further challenges arise: to the author's knowledge there have been no successful attempts to obtain the strength of quadrupole and dipole sources as input data for the first category of model from measurements. For the second class of models the wall pressure statistics must not contain any contributions of the scattered acoustic field. However, Roger & Moreau (2004) showed that the nature of the wall pressure fluctuations is dominated by the aerodynamic pressure, which has a much higher level than the corresponding acoustic fluctuations. Martínez-Lera *et al.* (2014) concluded from an analytical study that the pressure from an incompressible flow description can yield accurate results when dipole noise sources are dominant.

A slightly different approach than the aforementioned methods is symbolic regression. It can be employed to find fundamental dependencies and scaling laws when experimental or numerical data is available. As such it has been applied to datasets from noise measurements of airfoils (Sarradj & Geyer, 2013, 2014).

Physical insights into sound generation can be gained by interpreting terms in the exact equations as in theories based on Lighthill's analogy. By comparing results from DNS or measurements with results obtained from analytical TE noise theories it is possible to identify physical mechanisms that are neglected in the theories and cause the deviations. However, by simplifying the equations in order to be able to spot relations or even calculate quantitative values, additional assumptions are necessary. In acoustic theories it is argued that the fraction of energy transported in acoustic waves is very small compared to the total energy of the fluid motion. Hence back reactions of acoustic waves on the fluid flow are usually neglected. Furthermore, analysis based on acoustic theories usually does not include effects of viscosity. These are small in cases of high Reynolds numbers. For low or moderate Reynolds numbers though, viscosity still affects the behaviour of the flow and the scattering process, as was concluded by Sandberg *et al.* (2007) when comparing results obtained from the theory of Amiet (1976) to DNS data. Especially TE noise models of the second class can not account for additional noise sources, such as reattaching laminar separation bubbles or quadrupole sources in the wake. This can be justified for well behaved flows and vanishingly small Mach numbers. However, laminar separation bubbles and transition to turbulence have been shown to be a significant source of noise (Sandberg *et al.*, 2008, 2009). For subsonic flows with moderate Mach numbers the studies of Tam & Ju (2006); Sandberg *et al.* (2007); Sandberg & Sandham (2008) and Wolf *et al.* (2012*b*, 2013) showed that quadrupole sources in the unsteady wake can not be neglected.

It can be summarized that predictions from analytical models for TE noise can be used to estimate fundamental dependencies. Using such estimations can lead to the design of new experiments or simulations (Howe, 1991*b*; Jaworski & Peake, 2012). Furthermore the contribution of different physical sources to the sound field can be evaluated when analytical results are coupled to experimental or numerical methods Wolf *et al.* (2012*b*,*a*).

1.2.3.2 Experimental Methods

In addition to gain insights into physical mechanisms from measured data of TE noise and the hydrodynamic field, experimental methods are important to validate analytical and numerical models. In an experimental setup it is challenging to separate the TE noise from other noise sources, such as the nozzle lips of the tunnel, the shear layer of an open jet and the collector downstream (Brooks & Hodgson, 1981). Two approaches to accomplish such a separation have been reported in the literature: the use of directional microphones (Herr & Dobrzynski, 2005; Hutcheson & Brooks, 2004) or arrays of microphones (Brooks & Hodgson, 1981; Oerlemans *et al.*, 2009; Chong *et al.*, 2010; Gruber *et al.*, 2010*a*). With directional microphones the TE can be directly targeted. Corrections due to refraction at the shear layer of the open jet usually have to be applied.

When arrays of microphones are used the TE noise components must be extracted by correlating the output of different microphones. This allows the generation of two dimensional sound maps which are useful to evaluate the distribution of noise sources in a plane as shown, among others, by Oerlemans *et al.* (2007, 2009) and Moreau *et al.* (2014).

Measurements of the velocity of the hydrodynamic field in the vicinity of the TE or the wake have been reported using hot wire anemometers (Finez *et al.*, 2010; Moreau *et al.*, 2012*a*,*b*; Moreau & Doolan, 2013*b*; Xu *et al.*, 2013). The intrusive character of this measurement technique is a drawback. The use of the non-intrusive particle image velocimetry (PIV) method to measure the hydrodynamic field in the context of TE noise has only been reported by Schroeder *et al.* (2004). Recently PIV was also used to analyse the hydrodynamic source region of the sound and relate it to the noise observed in the far-field (Pröbsting *et al.*, 2015; Pröbsting & Yarusevych, 2015; León *et al.*, 2016). Breakey *et al.* (2013) and Pröbsting *et al.* (2014) aimed at identifying noise sources by means of time resolved PIV through cross correlating the acoustic pressure in the far field with transverse velocity fluctuations in the near field. Oguma *et al.* (2014) used a different approach and considered the time derivative of the velocity field to calculate the strength of the acoustic sources. To that end they took two snapshots within a very short time interval.

Placing pressure sensors to measure surface pressure spectra is only possible slightly upstream of the TE due to the space constraints at a sharp TE. It has been reported by Brooks & Hodgson (1981); Herr & Dobrzynski (2005); Moreau *et al.* (2011); Moreau & Roger (2009) and was applied to cross-correlate measured noise spectra in the far field and assess analytical predictions using the surface pressure statistics as input.

1.2.3.3 Numerical Methods

With the recent growth in computing power numerical simulations have become a widespread tool in research and industrial applications. Computational fluid dynamics (CFD) can be categorized into Reynolds Averaged Numerical Simulations (RANS), Large Eddy Simulations (LES) and Direct Numerical Simulations (DNS). Conceptionally they differ in the proportion of turbulence that is modelled. In RANS the complete influence of turbulence is modelled whereas in LES only the effect of the small-scales in a turbulent flow is modelled. In DNS all scales of a turbulent flow are calculated directly without any modelling involved. Because of the multiple scales of turbulent flows, DNS is the computationally most expensive approach with the need to also resolve the smallest scales in space and time. On the other hand information about all flow variables at every instant of time and position are available. The computation of sound generated aerodynamically is an additional challenge aside from resolving the relevant scales of turbulent

motion. The energy of the acoustic field is significantly smaller than the energy of the hydrodynamic field. Therefore schemes with very low numerical dissipation need to be applied to resolve acoustic waves. In RANS or LES simulations the influence of the unresolved turbulence is commonly modelled by introducing artificial dissipation making these approaches unsuitable for the direct computation of noise. Furthermore nonreflecting boundary conditions (Poinsot & Lele, 1992; Sandberg & Sandham, 2006) are required in high fidelity numerical simulations to ensure that acoustic waves can leave the computational domain without spurious reflections. In addition computations of sound generated aerodynamically are computationally expensive for two reasons. First, the extent of the acoustic field is significantly larger than that of the hydrodynamic field. This requires a relatively large computational domain that includes the acoustic far field. Second, the timestep constraints for stability reasons are considerably higher in compressible simulations compared to incompressible, as the speed of sound introduces an additional time scale that needs to be resolved.

To overcome the mentioned difficulties hybrid approaches have been used for the simulation of TE noise. In such methods the hydrodynamic near field is computed using CFD and the results are then used as input data for an acoustic solver. That enables the use of computationally cheaper and technically more feasible CFD simulation concepts such as RANS, LES or incompressible DNS. For the computation of the acoustic field, solvers based on models discussed in section 1.2.3.1 (Oberai *et al.*, 2002; Winkler *et al.*, 2010; Wolf *et al.*, 2012*c*) and linearised perturbed compressible equations (LPCE) (Bae & Moon, 2008, 2011) have been reported in the literature, among others. Through the decoupling of the acoustic and hydrodynamic field, back reaction of acoustic waves on the fluid flow are neglected. As a result of that, the effect of acoustic feedback loops as reported in Arbey & Bataille (1983); Nash *et al.* (1999); Desquesnes *et al.* (2007); Sandberg *et al.* (2009); de Pando (2012); Ikeda *et al.* (2015) and Schumacher *et al.* (2014*a*,*b*) featuring laminar flows and moderate Reynolds number flows around airfoils can not be captured with such approaches. Additional challenges of using hybrid methods are the storage of intermediate data and the sensitivity to the position of integration surfaces (Singer *et al.*, 2000). In LES, uncertainties arise from subgrid-stress models for the small-scale structures and the correct representation of laminar-turbulent transition. Furthermore the acoustic sources need to be estimated from the turbulent fluctuating statistics when using RANS (see Cozza *et al.* (2012) for further reference), which increases the proportion of modelling.

The appropriate numerical method strongly depends on the intended application. To make TE noise predictions of a given configuration where the flow is well behaved, i.e. is fully turbulent without flow separation, hybrid approaches with LES yield acceptable results at moderate computational costs (Oberai *et al.*, 2002; Wolf *et al.*, 2012*c*; Wolf

& Lele, 2012; Winkler *et al.*, 2012*b*). Enabled by the moderate computational costs, coupling LES with a shape optimization procedure for low noise airfoil design is feasible (Marsden *et al.*, 2007). Compressible DNS is the most feasible numerical method for investigations that aim to explore the scattering process of pressure fluctuations at a TE (Sandberg & Jones, 2011; Jones & Sandberg, 2012; Ikeda *et al.*, 2012). The reason for that is the greatest physical validity as no modelling of either the acoustic field or small scale turbulence is employed. Furthermore, the hydrodynamic and acoustic field are fully coupled and calculated at the same time.

1.3 Scope of this Work

This section summarizes open research questions concerning TE noise and measures for its reduction that will be within the scope of this work. In section 1.2 the current understanding of turbulent boundary layer TE noise has been outlined. Furthermore, measures to reduce TE noise have been discussed in 1.2.2. The results presented by Jaworski & Peake (2013), Manela (2011) and Manela & Huang (2013) indicate that elasticity affects the amplification of pressure fluctuations which is also supported by experimental results of Herr (2007) and Das *et al.* (2015). To the author's knowledge the influence of various degrees of compliance on the hydrodynamic near-field and the scattering process at the TE have not yet been investigated systematically, other than with analytical methods. The aim of the present work is thus to examine the effect that elasticity has on TE noise. Insights into the relevant mechanisms can guide and improve the design of noise attenuating TE modifications.

Compressible DNS is a numerical method that is suitable for the investigation of noise from elastic TE's, as all quantities of the hydrodynamic and acoustic field are available at every location and instant of time. DNS of TE noise fully coupled to a structural solver have not been reported in the literature yet. The in-house compressible DNS code "HiPSTAR – **Hi**gh **P**erformance **S**olver for **T**urbulence and **A**eroacoustic **R**esearch" was used in this work and is briefly introduced in chapter 2 alongside a newly implemented structural solver. However, for the simulation of noise radiation from an elastic TE a numerical method that can accurately represent the noise radiation of moving bodies in high-fidelity simulations is needed. Such a method has not been presented in literature yet and therefore a method originally proposed for incompressible flow was extended to compressible flow in this work. A literature review on methods to represent moving bodies as well as the newly developed and implemented method are presented in chapter 3. This is followed by the rigorous validation of the novel method with cases relevant to aeroacoustic applications in chapter 4. The newly implemented fluid structure interaction framework is then employed to consider noise radiation from elastic flat-plate extensions attached to an airfoil at angle of attack in chapter 5. Furthermore a generic

flat plate setup with a vortex generator was used to investigate the influence of different material parameters for the structure including structural damping is investigated in chapter 6. Finally a fully turbulent flow convecting over an elastic TE was considered in chapter 7. The work is concluded with a summary of the findings and an outlook to future work in chapter 8.

Chapter 2

Governing Equations and Numerical Methods

This chapter introduces the governing equations for the fluid-structure interaction problem. Furthermore, the numerical methods that were used to solve them are presented. From numerical point of view, fluid structure interaction problems can be broadly classified into monolithic and partitioned approaches. In monolithic approaches, the fluid structure dynamics are solved simultaneously by a unified numerical algorithm as a single system of equations. The interaction between the fluid and the structural dynamics is implicitly incorporated into the solution algorithm. For partitioned approaches the two sets of governing equations are solved by independent algorithms with their own discretization. The coupling is then then achieved by explicit interface conditions (Hou *et al.*, 2012). For the fluid structure interaction framework that was developed in this work a partitioned approach was chosen due to the greater flexibility to incorporate different structural models. Therefore the following introduction to the governing equations and numerical methods is split into a description of the fluid solver in section 2.1 and the structural solver in section 2.2. In general the focus of this chapter is to discuss the methods that were newly implemented.

2.1 Fluid Simulations

The description of the fluid solver is divided into the introduction of the set of governing equations in section 2.1.1 and the documentation of the general framework to solve them in section 2.1.2. The non-reflective boundary conditions are briefly discussed in section 2.1.3. Section 2.1.4 presents an analysis of the in and output to the TE noise mechanism which will be used for data processing in the chapters considering TE noise from elastic TE's.

2.1.1 Governing Equations of Fluid

The flow under consideration is governed by the full compressible Navier–Stokes equations. The physical quantities of interest are the density ρ, the components of the velocity vector u, the static pressure p and the temperature T. The fluid is assumed to be an ideal gas with constant specific heat coefficients. All quantities are made dimensionless using the flow-quantities ρ^*_∞, u^*_∞, T^*_∞ and $c^*_{p\infty}$. The ∞ subscript refers to the value of the quantity in the freestream or an other reference location. Furthermore, L^*_{ref} is a characteristic length scale of the considered domain. The star * superscript indicates a dimensional quantity. When the Navier–Stokes equations are non-dimensionalized with the aforementioned quantities non-dimensional groups can be formed as

$$Re = \frac{\rho^*_\infty u^*_\infty L^*_{\text{ref}}}{\mu^*_\infty}, \quad M = \frac{u^*_\infty}{c^*_\infty}, \quad \text{and,} \quad Pr = \frac{\mu^*_\infty c^*_{p\infty}}{\kappa^*_\infty}\,, \tag{2.1}$$

the dimensionless Reynolds (Re), Mach (M) and Prandtl (Pr) number. The dynamic viscosity μ^*_∞ is a property of the fluid and is a function of temperature $\mu^*_\infty = f(T^*_\infty)$. The reference speed of sound is defined by $c^*_\infty = \sqrt{\gamma\, p^*_\infty/\rho^*_\infty}$ with the isentropic exponent $\gamma = 1.4$. For simplicity, all equations in this section are presented in tensor notation. With these definitions the non-dimensional continuity, momentum and the energy equations are:

$$\frac{\partial \rho}{\partial t} + \frac{\partial}{\partial x_k}\left(\rho u_k\right) = 0\,, \tag{2.2a}$$

$$\frac{\partial}{\partial t}\left(\rho u_i\right) + \frac{\partial}{\partial x_k}(\rho u_i u_k) = -\frac{\partial p}{\partial x_k}\delta_{ik} + \frac{\partial}{\partial x_k}\tau_{ik}\,, \tag{2.2b}$$

$$\frac{\partial}{\partial t}\left(\rho E\right) + \frac{\partial}{\partial x_k}\left(\rho u_k E\right) = \frac{\partial}{\partial x_k}\left[u_i\tau_{ik} - u_k p - q_k\right]\,, \tag{2.2c}$$

where the total energy is defined as $E = T/\left[\gamma(\gamma-1)M^2\right] + 1/2 u_i u_i$. The stress tensor is computed as

$$\tau_{ik} = \frac{\mu}{Re}\left(\frac{\partial u_i}{\partial x_k} + \frac{\partial u_k}{\partial x_i} - \frac{2}{3}\frac{\partial u_k}{\partial x_k}\delta_{ik}\right) \tag{2.3}$$

and the heat-flux vector as

$$q_k = \frac{-\mu}{(\gamma-1)M^2 PrRe}\frac{\partial T}{\partial x_k}\,. \tag{2.4}$$

The Prandtl number is assumed to be constant with a value of $Pr = 0.72$. The temperature dependency of the molecular viscosity μ is expressed using Sutherland's law resulting in

$$\mu = T^{\frac{3}{2}} \frac{1 + R_{\mathrm{Su}}}{T + R_{\mathrm{su}}}\,, \tag{2.5}$$

where the ratio R_{Su} of the Sutherland constant C_{Su} over freestream temperature T^*_∞ is set to $R_{\mathrm{Su}} = 0.36867$ (White, 1991). The system of equations is closed with the non-dimensional equation of state $p = (\rho T)/(\gamma M^2)$ to obtain the pressure.

When time averaged statistics are considered a flow quantity q can be decomposed with the Reynolds decomposition as

$$q = \overline{q} + q'\,, \tag{2.6}$$

where $\overline{q}$ is the mean and q' the fluctuation. As a measure for the strength of fluctuations the variance of flow quantity q will be denoted by $\overline{q'^2}$ in this work. When the decomposition $q = \overline{q} + q'$ is substituted into the compressible Navier–Stokes equations additional cross-correlations between the velocity u_i as well as the total energy E and the density ρ arise which are not present in the incompressible equations. Therefore the Favré average is introduced for the aforementioned quantities u_i and E as

$$\widetilde{q} = \frac{\overline{\rho\, q}}{\overline{\rho}}\,. \tag{2.7}$$

Based on this averaging procedure the quantity q can then be decomposed with

$$q = \widetilde{q} + q''\,, \tag{2.8}$$

where the tilde denotes the Favré mean and the double prime the Favré fluctuations. When this decomposition is substituted into the momentum equation (2.2b) and averaged over time aside the Favré mean additional correlations of the velocity fluctuations arise. They are commonly summarized as the Reynolds stress tensor as (Wilcox, 1998)

$$\tau_{ij} = -\overline{\rho u_i'' u_j''}\,. \tag{2.9}$$

2.1.2 Fluid Solver

As mentioned in section 1.2.3.3, DNS of aeroacoustics is the computationally most expensive numerical method. This is due to the need to resolve the small scale flow features in space and time as well as the acoustic field which commonly has greater length and time scales (Sandberg, 2015). To make these simulations feasible numerical methods with high accuracy, that can be implemented in parallel computing architectures efficiently, are needed. To that end, a four–point 4^{th}-order accurate standard-difference scheme is employed in HiPSTAR to calculate spatial derivatives. As it is an explicit

method, parallelization is achieved by domain decomposition with halo-cell exchange. This means that two neighbouring processors exchange information at grid points adjacent to their common boundary. The exchange is such that, using the information of the grid points from the neighbouring processor, the interior finite difference scheme can be used. The exchange of the content of the halo-cells is done employing the MPI-library. At the boundaries of the computational domain one-sided Carpenter boundary stencils (Carpenter *et al.*, 1999) with six points are employed. Beside a good parallelization as well as suitable and accurate numerical methods, the computational resources of each core need to be used efficiently. Each core is equipped with a cache which is a memory unit it can access very fast. In addition there is the RAM with a much higher volume but also significantly slower connection to the core. In order to reduce the usage of the slow RAM, it is preferable to minimize memory usage of a CFD-code and maximize the cache usage. To that end, HiPSTAR employs an ultra low-storage five-step 4^{th}-order accurate Runge–Kutta scheme (Kennedy *et al.*, 2000) for the integration in time. This integration scheme only needs two registers, i.e. two copies of the whole flow field, and therefore reduces the memory consumption. Curvilinear geometries in the $x-y$-plane can be considered by pre-multiplying the metric terms when taking derivatives as described by Sandberg (2009). While the spatial discretization of $x-y$-plane employs finite differences with an efficient domain decomposition method, the spanwise direction is discretized with a spectral method (Sandberg, 2015). Consequently, the collocation points in the spanwise direction are equispaced and only periodic boundary conditions can be used. The spanwise direction is parallelized with a shared-memory parallelism using the OpenMP API (Sandberg, 2015). The stability of the code is enhanced by a skew-symmetric splitting of the nonlinear terms (Kennedy & Gruber, 2008). Furthermore a sixth-order accurate high-wavenumber cut-off explicit filter (Bogey *et al.*, 2009) using an 11-point stencil with a weighting of $f_w = 0.2$ is employed after every full Runge–Kutta cycle.

2.1.3 Characteristic Boundary Conditions

Non-physical numerical reflections at the domain boundaries are avoided by using characteristic boundary conditions. At the inflow they are applied in an integral formulation as described by Jones (2008). For the outflow a zonal characteristic boundary condition (Sandberg & Sandham, 2006) is used to avoid spurious pressure-oscillations from the outflow boundary which is subject to the passage of nonlinear disturbances, i.e. vortical structures.

In subsonic flows the pressure and density level at the outflow boundary is determined by the flow conditions upstream and downstream of that point. A perfect non-reflecting outflow boundary condition does not provide information about the downstream conditions as it does not allow any information to enter the domain. Hence such a boundary

can lead to a drifting pressure and density level over time and was in fact observed in preliminary simulations. In the present studies, the influence of flow conditions downstream of the outflow boundary are modelled with an approach to estimate the incoming wave amplitudes, as presented in Poinsot & Lele (1992). This method was extended to the zonal characteristic boundary condition in this work by setting the amplitude variation $\mathcal{L}$ of the incoming wave to

$$\mathcal{L} = \sigma\,(1 - M^2)(p - p_\infty)\frac{c}{L_{\text{ref}}}\,, \tag{2.10}$$

where σ is a forcing parameter that was set to $\sigma = 0.2$, c the speed of sound at the outflow and L_{ref} a reference length of the domain. With this approach is was possible to achieve a constant average pressure and density level over time.

2.1.4 Analysis of the Input and Output of TE Noise Mechanism

The input to the trailing-edge noise mechanism are the fluctuations of the incident pressure difference between the upper and lower surface of the plate $\Delta p_i'$. These incident pressure fluctuations are one contribution to the total pressure difference $\Delta p_t'$. The other contribution to this total pressure difference is the scattered field $\Delta p_s'$. The fluctuations of the total pressure difference $\Delta p_t'$ can be expressed with

$$\Delta p_t' = \Delta p_i' + \Delta p_s'\,. \tag{2.11}$$

From the compressible DNS or experiments only the total pressure difference is available and in general a distinction between scattered and incident pressure field is not possible. However, when the experiment is designed such that there are no pressure disturbances from vortex shedding or a turbulent boundary layer on one side, the only pressure fluctuations in the flow on that side will be the ones scattered from the TE. For the following analysis it is assumed that this is the case for the lower side of the TE which then leads to

$$p_{t,L}' = p_{s,L}'\,, \tag{2.12}$$

where the lower surface is denoted by the subscript L. Using the fact that the scattered pressure fluctuations are the same in magnitude but opposite in phase on both surfaces leads to

$$p_{s,U}' = -p_{s,L}' = -p_{t,L}'\,. \tag{2.13}$$

Here the subscript U refers to the upper surface. Note that this equation also contains the contribution from pressure fluctuations that might be imposed on the fluid by the structural motion of the elastic TE. Hence, a comparison of the scattered field between rigid and elastic TE might be biased by this additional contribution. Furthermore, equation 2.13 assumes that the effect of curvature in the deflected state when considering an elastic TE does not change the scattered field. Due to the relatively small deflections

of the elastic fraction this assumption can be justified. Adding the total pressure on the lower and upper side of the plate leads to

$$\begin{aligned} p'_{t,U} + p'_{t,L} &= p'_{i,U} + p'_{s,U} + p'_{s,L} \\ &= p'_{i,U} + p'_{s,U} - p'_{s,U} \\ &= p'_{i,U} \,. \end{aligned} \tag{2.14}$$

A similar analysis was conducted by Sandberg & Sandham (2008) for a turbulent flow on the upper surface and has shown to be meaningful in the context of TE noise theories. As mentioned in Sandberg & Sandham (2008), this analysis assumes that the unsteady flow on the upper surface does not influence the scattered pressure field substantially.

In this work several TE noise studies will be conducted with two dimensional simulations to develop and validate a novel numerical framework. As in three dimensions, the fundamental physical mechanism is the scattering of an incident pressure field at the TE. It can be regarded analogous to a two dimensional wave in a three dimensional flow, resulting in pressure disturbances that convect over the TE at the same time, i.e. are perfectly correlated in the spanwise direction. In contrast, the incident pressure disturbances of a three dimensional turbulent flow convecting over the TE have a phase difference. This can result in cancellation and amplification leading to a dependence of the TE noise on the spanwise correlation length (Amiet, 1976). For more details about the modified equations of Amiet (1976) for two dimensional flows, the reader is referred to Sandberg (2007) and Sandberg *et al.* (2009).

2.2 Structural Solver

This section describes the structural solver. First the governing equation that is solved is introduced in section 2.2.1 and in section 2.2.2 the numerical method to solve it is outlined.

2.2.1 Governing Equations of the Structure

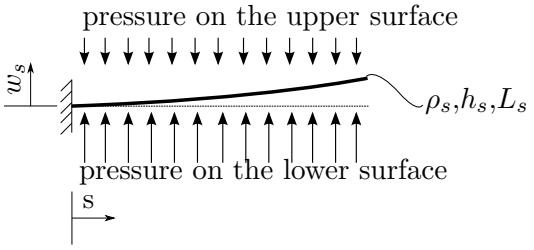

Figure 2.1: Illustration of the one dimensional structural model. The deflections are uniform in spanwise direction.

In this work the interaction of a fluid flow with a thin beam that is clamped on one side is considered. It is assumed that the cross section is constant and the material properties are uniform. In figure 2.1 the topology of the structure and its load is shown. The structural model is one dimensional and is defined by the local coordinate s which defines the position along the axis of the beam. The deflection w_s is perpendicular to the neutral position of the beam. It is assumed that the impact of the fluid on the solid structure is given by the pressure difference between upper and lower side of the plate only. Therefore, a very high extensional rigidity is assumed and the influence of the wall shear stress on the structure is neglected. In this case, the equation of motion for the structure can be modelled by the Euler-Bernoulli beam equation with (Thomsen, 2004)

$$\rho_s A_s \frac{\partial^2 w_s}{\partial t^2} = \Delta p_s - E_s I_s \frac{\partial^4 w_s}{\partial s^4} \,, \tag{2.15}$$

where ρ_s denotes the structural density and A_s is the cross section of the beam. In the calculation of A_s the height of the cross section is denoted by h_s and the depth by d_s. The resulting line load from the pressure difference is represented by Δp_s. Finally, the term $E_s I_s$ is the bending rigidity with Young's modulus E_s and the second moment of inertia of the cross section $I_s = h_s^3\, d_s/(12 - 12\nu^2)$ with the depth d_s and the Poisson ratio ν, which will always be assumed to be $\nu = 0.3$, which is representative of many common materials. In this study, the bending rigidity $E_s I_s$ is assumed to be sufficiently high to result in small deflections only. To assess the deflections relative to the length of the beam they are typically normalized by the length, i.e. w_s/L_s. Dimensionless quantities are obtained by nondimensionalizing with the reference fluid density which results in

$$\rho_s = \rho_s^* \times \frac{1}{\rho_{\infty,f}^*} \,. \tag{2.16}$$

Using a combination of the reference density and velocity the Young's modulus can be nondimensionalized with

$$E_s = E_s^* \times \frac{1}{\rho_\infty^* U_\infty^{*2}} \,. \tag{2.17}$$

All length scales are assumed to be consistent with the non-dimensional length scales of the fluid simulation.

This model does not account for rotational inertia of the cross section and shearing deformation. Those two effects are gaining importance when higher modes of frequencies or large deflections are considered. Deflections are considered small for $\frac{\partial w_s}{\partial s} < 1$ (Fertis, 2006). When integrated over the length of the beam this yields $w_s/L_s \ll 1$. Furthermore, rotational inertia and shearing deformation can not be neglected when the ratio of length to height of the beam is small (Timoshenko *et al.*, 1974).

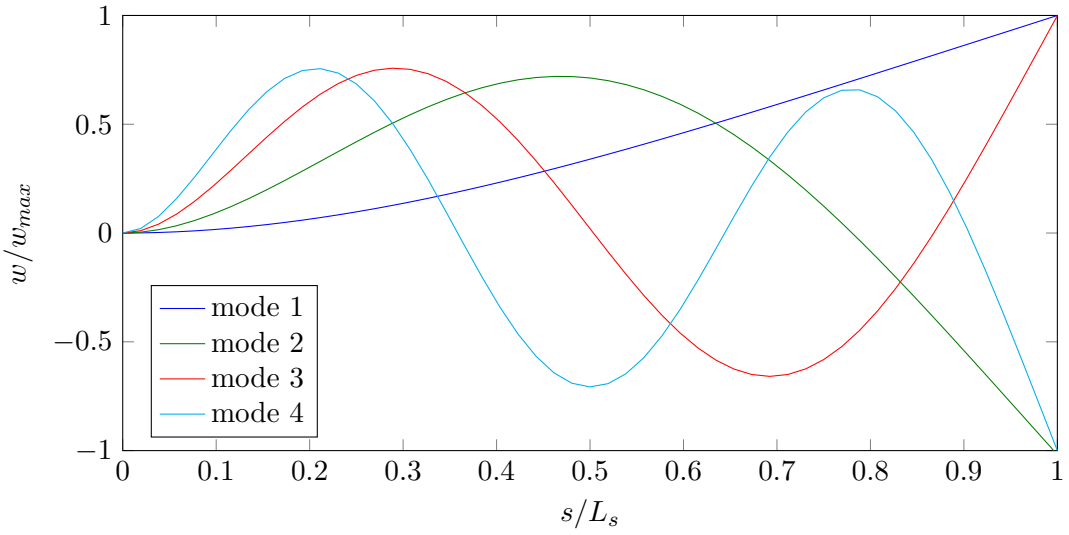

Figure 2.2: Shape of the first four bending modes, normalized by maximum deflection.

The natural frequencies are the vibration frequencies of a bending beam without external forcing and damping, i.e. free vibrations. The analytical natural frequencies for a beam that is clamped on one side and free on the other can be calculated as (Thomsen, 2004)

$$f_j = \frac{\lambda_j^2}{2\pi L^2}\sqrt{\frac{EI}{\rho_s A}} \text{ with } \lambda_1 = 1.875 \text{ and } \lambda_j = (2j-1)\pi/2 \text{ for } j = 2, 3, 4 \text{ etc.} \tag{2.18}$$

The natural frequencies are the resonant frequency where the response of the beam to an external forcing with a bounded amplitude is vibration with an unbounded amplitude. For an external forcing at any other frequency, the beam is expected to vibrate at a combination of the external forcing frequency and the natural frequencies (Thomsen, 2004). Each natural frequency can be associated with a mode shape φ which can be calculated with (Thomsen, 2004)

$$\begin{aligned}\varphi_j(s) = &\cosh(\lambda_j s/L_s) - \cos(\lambda_j s/L_s) \\ &- \frac{\cosh(\lambda_j) + \cos(\lambda_j)}{\sinh(\lambda_j) + \sin(\lambda_j)} \left(\sinh(\lambda_j s/L_s) - \sin(\lambda_j s/L_s)\right) ,\end{aligned} \tag{2.19}$$

where λ_j is defined in equation 2.18. Figure 2.2 visualizes the mode shape of the first four bending modes for a clamped beam with a free end. It can be seen that the number of nodes, i.e. points where the deflection is zero, is increasing with each mode.

When the elastic motion of a structure immersed in a fluid is considered the structural behaviour can be influenced by the effect of added mass. For the structure the surrounding fluid increases its effective mass when the inertia of the fluid can not be neglected relative to the inertia of the structure itself. As a result the resonant frequencies are lowered (Sader *et al.*, 2015). The added mass coefficient μ_m can be used to estimate the

influence of effects of added mass and is calculated with (Kornecki *et al.*, 1976)

$$\mu_m = \frac{\rho_f L_s}{\rho_s h_s} \,. \tag{2.20}$$

It is a measure of the inertial behaviour of the fluid relative to the inertia of the solid. The effect of the added mass on the natural frequencies in air $f_{j,air}$ can be approximated with

$$f_{j,air} = f_{j,vac}\sqrt{\frac{1}{1+\mu_m}} \,, \tag{2.21}$$

where $f_{j,vac}$ are the natural frequencies of the structure in a vacuum (Sader *et al.*, 2015).

2.2.2 Numerical Method for the Structural Solver

The structural solver first calculates the right hand side of equation (2.15) using the pressure load from the fluid simulation and the spatial derivative of the deflection. The solution is then advanced in time by integration. This integration is performed with the fourth-order accurate ultra low storage Runge-Kutta scheme that is also used for time advancement in the fluid simulation. To that end, equation 2.15 is reformulated as a system of two first order differential equations. With the introduction of the structural velocity v_s this yields

$$\frac{\partial w_s}{\partial t} = v_s \tag{2.22a}$$

$$\frac{\partial v_s}{\partial t} = \frac{1}{\rho_s A_s}\left(\Delta p_s - E_s I_s \frac{\partial^4 w_s}{\partial s^4}\right) \,. \tag{2.22b}$$

The spatial discretization to calculate the $\partial^4 w_s/\partial s^4$ term is achieved with the fourth-order accurate compact finite difference scheme proposed by Kim & Sandberg (2012). The fourth derivative of the deflection is calculated recursively. In order to suppress spurious oscillations from the structure boundaries a high wave number optimised filtering scheme described in Kim (2010) is employed after each Runge-Kutta stage and after taking the derivative. This combination of compact difference scheme and filter employed recursively was found to introduce fewer instabilities at the boundaries than standard difference schemes or when taking the fourth derivative in one step.
The coupling to the fluid solver is achieved at the beginning of each time step by gathering the pressure values on the upper and lower surface of the plate from the fluid solver. The pressure is then unchanged for the rest of the Runge-Kutta loop. The position and velocity of the structure is updated once at the end of each timestep. Since the timestep is small in order to capture the relevant time scales of the fluid motion the influence of the discrepancy in time should be negligible. Indeed, no differences could be found between simulations where the structural deflection and velocity and the pressure were updated after every Runge Kutta stage and simulations with the aforementioned “weak” coupling.

The implementation of the structural solver allows future users to easily add terms to the right hand side of equation 2.15 to account for additional effects such as strain and rotation.

Chapter 3

Representation of Moving Bodies in High Fidelity Simulations

This chapter is concerned with the representation of moving bodies in high fidelity simulations. Section 3.1 gives an overview of available methods in the literature. The concept of a particular promising method for incompressible flows, the boundary data immersion method (BDIM), is introduced in section 3.2 and an extension for compressible flows is proposed in section 3.3. Finally, the implementation of the newly extended framework is presented in section 3.4.

3.1 Literature Review

Accurate computation of fluid flows in the vicinity of complex geometries or moving bodies is a severe challenge. One approach for such flow simulations uses body-fitted curvilinear computational grids. For this approach, grids must be designed such that geometric boundaries coincide with the grid and domain boundaries. Boundary conditions can then be realized by prescribing desired values of flow quantities on the boundaries. In this approach the main challenge is the generation of adequate grids and the treatment of geometric discontinuities. Furthermore, keeping track of neighbouring grid points in unstructured grids or merging multiple simple grid blocks are additional challenges that need to be taken care of. When considering moving boundaries the grid needs to be recomputed at each timestep during a simulation, making grid-fitted boundary methods computationally prohibitively expensive for high-fidelity numerical simulations. In addition, the quality of the grid can be affected adversely when high deflections from the original location, as for example in a flapping flag problem, are considered.

As an alternative to body-fitted simulations, immersed boundary methods (IMBM) have become a popular tool to impose boundary conditions upon boundaries that do not coincide with the computational grid. Besides the ability to simulate moving bodies this class of boundary methods enables the simulation of complex geometries on relatively simple meshes, thus reducing the effort of grid generation. Alongside the enormous growth of computational power in recent years, IMBMs have enabled the consideration of multi-physics phenomena such as fluid-structure interaction problems. Furthermore, flow control and optimization problems incorporating moving control surfaces or morphing bodies can be studied with recent advances of IMBMs. However, IMBMs often have a low order of accuracy or add significant computational overhead when used for moving bodies, where the IMBM needs to be reinitialized for each timestep.

The majority of the IMBM are inspired by the physics of a fluid flow in the vicinity of solid bodies. As there is no flow through the body a flow exerts a force in the normal direction to the surface caused by pressure. In case of no-slip walls in viscous fluid flows there is a tangential force acting on the body caused by the shear stress. In turn, the body exerts normal and tangential forces to the fluid with opposite sign. These two forces can be considered as the influence on the flow field that a solid body immersed into a fluid has. Therefore, a wall boundary condition can be realized by exerting an appropriate set of forces to the fluid in order to mimic the influence of the solid body on the flow field (Goldstein *et al.*, 1993). This can be shown by reconsidering the momentum equation in a slightly more general form than presented in equation 2.2b with

$$\frac{\partial}{\partial t}\left(\rho u_i\right) + \frac{\partial}{\partial x_k}(\rho u_i u_k) = -\frac{\partial p}{\partial x_k}\delta_{ik} + \frac{\partial}{\partial x_k}\tau_{ik} + f\,, \tag{3.1}$$

where f is a volume force. The classification by Mittal & Iaccarino (2005) distinguishes IMBMs according to the way the volume force f is treated. The two major classes are continuous and discrete forcing approaches. In continuous methods the volume force is based on a continuous formulation of the governing equations i.e. before they are discretized. The advantage of this class of methods is that they are independent of the discretization. In contrast to that discrete forcing approaches manipulate the discrete operators directly and therefore depend on the numerical scheme that is employed. They can be further subdivided into methods that calculate the volume force explicitly or use it to derive a boundary reconstruction where the boundary conditions are prescribed directly. In the latter case, the forcing terms themselves are usually not calculated explicitly. However, in general the use of the nomenclature introduced by Mittal & Iaccarino (2005) is not used consistently in the literature. Figure 3.1 presents a classification of IMBMs based on how the interface is represented and the role of the aforementioned volume force f. The basic ideas and concepts of the most common IMBM used for finite differences listed in figure 3.1 are introduced briefly in the following passage.

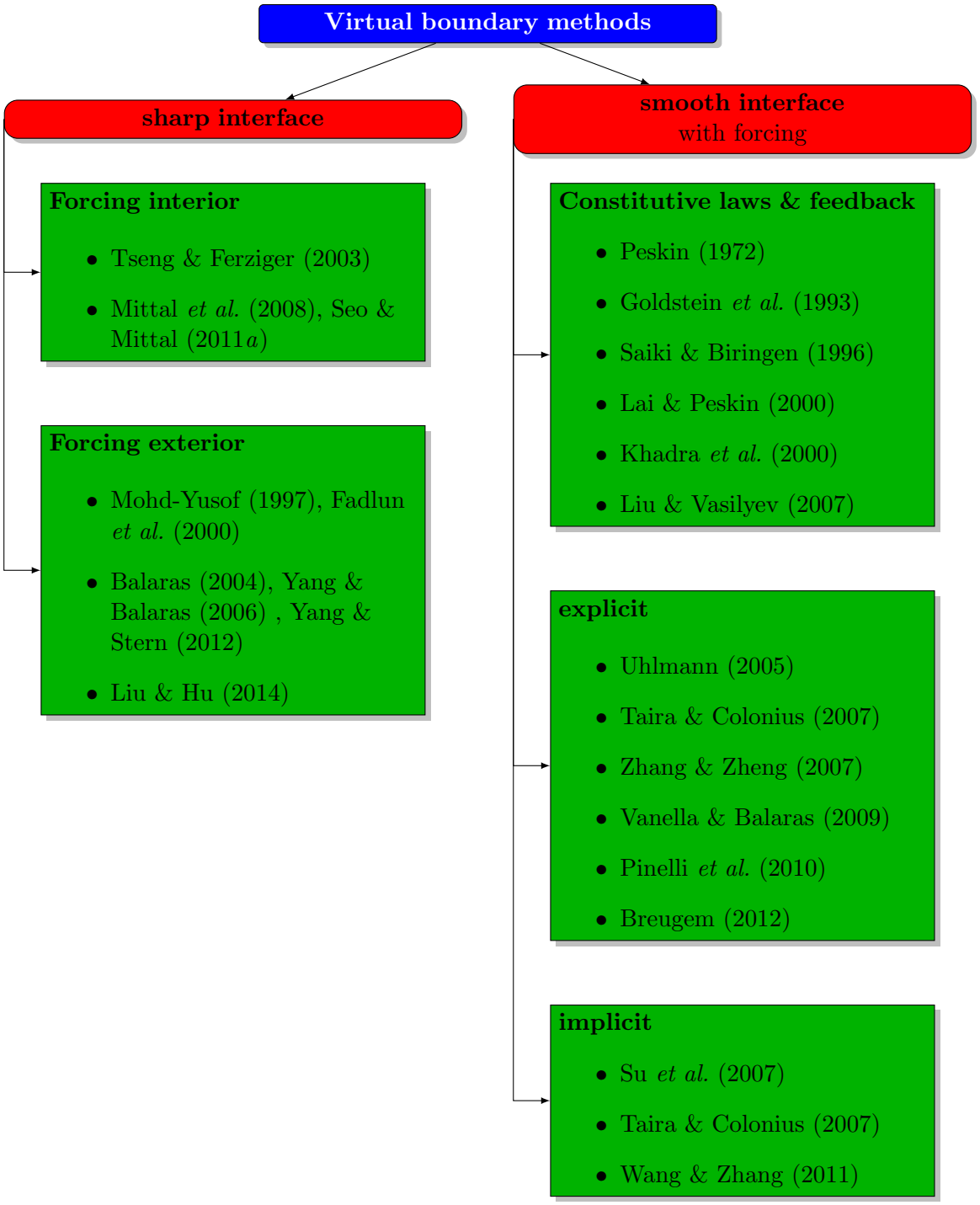

Figure 3.1: Classification of virtual boundary methods based on the resulting interface representation and how the volume force f in equation 3.1 is determined.

In direct discrete forcing approaches the values of grid points in the vicinity of the solid boundary are modified with computational stencils such that the target velocity on the wall is imposed directly and result in a sharp interface representation. As a result, the volume force does not need to be calculated explicitly. The direct discrete forcing approaches can be subdivided in two classes of methods which are predominantly distinguished by the location of the grid point that is used to reconstruct the solid boundary. In ghost-cell approaches the points just inside of the solid body are used for a reconstruction of the boundary (Tseng & Ferziger, 2003). Another method is to manipulate the grid points just outside the solid body which are then denoted forcing points which was first developed by Mohd-Yusof (1997) in a spectral framework and extended to finite differences by Fadlun *et al.* (2000). The forcing scheme used for the boundary reconstruction was generalized by Balaras (2004) for complex bodies. On the one hand, such approaches result in a sharp and accurate interface representation at the boundary with no additional stability constraints and high accuracy. On the other hand, it is usually necessary to prescribe a pressure boundary condition on the surface in the incompressible case (Mittal & Iaccarino, 2005). Computational costs increase severely when considering problems featuring moving boundaries as the modified stencils need to be recomputed for each timestep. Additionally spurious pressure oscillations have been reported which are caused by sudden changes of the classification of grid points from forcing/ghost point to solid or fluid point or vice versa. This is also denoted the freshly cleared cell problem (Udaykumar *et al.*, 2001). In order to reduce these oscillations several additional treatments have been proposed by Yang & Balaras (2006), Mittal *et al.* (2008), Seo & Mittal (2011*a*), Yang & Stern (2012), Luo *et al.* (2012) and Liu & Hu (2014) which further increase the complexity and computational cost of the methods.

In contrast to sharp interface methods explicit momentum forcing techniques evaluate the volume force that drives the velocity on the interface location to the target value and then spread it to adjacent grid points which leads to a smooth representation of the boundary. In these methods the boundary conditions are prescribed indirectly. In order to find an appropriate set of volume forces there are two different strategies:
In continuous forcing approaches the terms that force the velocity on a boundary to the target value is added to the Navier–Stokes equations before discretization. As a result this class of methods does not depend and use any information of the discretization at all. However, the volume forces can not be calculated analytically. In the original IMBM for elastic bodies by Peskin (1972) the force on the fluid was determined by a constitutive law, i.e. the Hooke's law. However, the extension to rigid bodies modelled as a very stiff elastic body leads to stability constraints due to the stiff system of equations. A widely used continuous IMBM approach proposed by Goldstein *et al.* (1993) for a spectral framework uses a feedback-loop to estimate the forces to drive the flow field to the given target velocity on the boundary. The equation to determine the volume force on the

immersed surface $f(\tilde{X})$ is

$$f(\tilde{X}) = \alpha \int_0^t (U(\tilde{X}, t') - U^T(\tilde{X}))\mathrm{d}t' + \beta(U(\tilde{X}) - U^T(\tilde{X}))\,, \tag{3.2}$$

where $U(\tilde{X}, t)$ is the velocity field interpolated on the immersed boundary (IB) point. The target velocity on the body surface is referred to as $U^T(\tilde{X})$. The controller consists of proportional and integrating actions where the respective gains α and β are empirical constants. The integral part of the controller in equation 3.2 integrates the deviation between actual and target value on the immersed surface over time and thus takes the history into account. In contrast, the proportional controller only considers the deviation of the instantaneous values. The same forcing approach was employed by Saiki & Biringen (1996) in a finite difference framework.

Special cases of this approach using only one of the controller actions have been used among others by Lai & Peskin (2000) (proportional controller) and by Khadra *et al.* (2000) (integrating controller). Even though Brinkman penalization methods are derived from porous media equations, with porosity and permeability approaching zero they effectively result in a control loop approach using a proportional control action only. Liu & Vasilyev (2007) developed a penalization method for compressible flows resulting in direct modifications of all conservative equations including continuity. Nevertheless, all of the mentioned control loop approaches result in a stiff set of equations and usually yield additional time step restrictions (Mittal & Iaccarino, 2005). However, Margnat & Morinière (2009) showed that these restrictions can be circumvented by an appropriate choice of the control parameters for steady flows without a loss of accuracy. In unsteady flow cases a balance between time step restrictions and level of oscillations around the target velocity values which are introduced by the control loop needs to be found. Indeed for preliminary simulations carried out in the scope of this work the timestep using a control loop approach had to be reduced to two third of the timestep used in simulations with body-fitted boundary conditions. This was necessary due to high gains in α and β to obtain reasonable results.

In the indirect discrete forcing methods, the volume forces are calculated from the discretized Navier–Stokes equations. In contrast to the continuous forcing methods, the calculation of the forcing terms use knowledge of the discretization method, i.e. the temporal discretization. In projection methods for incompressible flows a prediction of the velocity field to calculate the required forcing term is usually used. In contrast to continuous forcing approaches no empirical constants need to be specified and the boundary conditions are imposed exactly at the immersed boundary point location. Furthermore, there are no time step restrictions as the velocity field is predicted with the same discretization in time that is used for time marching (Zhang & Zheng, 2007). This concept

can be subdivided into categories of how the forcing term is evaluated. In the first category that was employed in by Uhlmann (2005), Zhang & Zheng (2007), Yang *et al.* (2009), Vanella & Balaras (2009), Pinelli *et al.* (2010) and Breugem (2012) the forcing term is calculated explicitly from the surrounding grid points. Uhlmann (2005) and Yang *et al.* (2009) showed that the smooth representation of the boundary significantly reduced the pressure oscillations in problems involving moving boundaries. Furthermore, Breugem (2012) increased the numerical accuracy of the method by Uhlmann (2005) for particle laden flows to second order by introducing an inward retraction of the represented surface.

In the second category, the forcing term at the boundary location is calculated implicitly by solving a linear system of equations. This strategy was employed among others by Su *et al.* (2007), Taira & Colonius (2007) and Wang & Zhang (2011). It is worthwhile pointing out that Taira & Colonius (2007) include the implicit force through a modified Poisson equation in their method and therefore satisfies the continuity equation and no-slip condition exactly.

All of the aforementioned explicit momentum forcing techniques require, and strongly depend on, interpolation and force spreading schemes. The interpolation schemes are needed to obtain the values of flow field quantities on the boundary grid point (often denoted as a Lagrangian marker) from the Eulerian grid where they are computed. Furthermore, a procedure to distribute the calculated forcing terms to the adjacent grid points needs to be applied which leads to a smeared out representation of the interface. On the one hand, this results in a loss of accuracy which makes most of these schemes first-order accurate. On the other hand, smoothing has been found to reduce numerical oscillations for moving boundaries (Yang *et al.*, 2009) circumventing the need of field extension methods as proposed by Yang & Balaras (2006) and Yang & Stern (2012), among others. Uhlmann (2005) used a regularized delta function as to transfer information from the Eularian to the Lagrangian grid which was optimised to simulate spherical particles immersed in a fluid. Pinelli *et al.* (2010) extended the method to arbitrary immersed boundary shapes on Cartesian non-uniform and curvilinear grids by introducing interpolation and spreading operators based on the so-called Reproducing Kernel Particle Method (RKPM). Toja-Silva *et al.* (2014) suggested a radial basis function to carry out the interpolation and spreading procedure in one step. Vanella & Balaras (2009) calculated the volume force on the Lagrangian marker in the same way as Uhlmann (2005) but employed a transfer function between Eularian and boundary grid for the interpolation and force spreading based on a moving-least-square approximation and claim to recover sharp-like behaviour as in the aforementioned direct discrete forcing approaches. In general, the derivation of the force spreading schemes is mostly rather ad-hoc without physical motivation and the force spreading schemes are not necessarily

independent of the boundary grid discretization, i.e. the distribution of the Lagrangian markers. To address the latter issue when two delta functions associated with a Lagrangian marker overlap Breugem (2012) employed a multidirect forcing scheme that iteratively determines the forces on the Eularian grid such that the target velocity is enforced on the Lagrangian markers collectively.

Approaches that incorporate the coupling between the boundary and the Eulerian grid in jump conditions in the vicinity of the immersed boundary are usually referred to as immersed interface methods (IIM). The jump conditions result in direct corrections of the numerical schemes (Harris, 2013). In a recent work by Uddin *et al.* (2014) the solution from the interface is extrapolated smoothly from the interface into the solid domain, similarly to the concept of ghost-cell methods. However, the overhead for the initialization and computation of the extrapolated flow field, employing an independent solver for an elliptic partial differential equation, seems to make this approach prohibitively expensive for the simulation of moving bodies. Due to the complex jump conditions and the dependency on the numerical schemes the immersed interface class of methods is not considered in depth here, for more details on IIM refer to Xu & Wang (2006).

Many engineering applications are characterized by flows with high Reynolds numbers. However, a key problem with all aforementioned methods that are feasible to represent moving boundaries, i.e. momentum forcing approaches, is the accurate prediction of high Reynolds number flows. The reason for this weakness is a lack of accuracy of the representation of the velocity gradient at the wall. Considering a flat plate as a solid body domain at rest adjacent to a fluid domain with a flow, the velocity field along the wall normal direction is continuous. This is ensured by the no-slip condition that is usually applied by setting the velocity of the fluid on the wall equal to the wall velocity which is the purpose of all IMBM methods. In contrast to the velocity field its gradient has a discontinuity in that direction at the interface between both domains caused by the "kink" in the velocity profile. As the wall velocity gradient increases with Reynolds number this discontinuity grows as well (Maertens & Weymouth, 2015). Therefore the error made by momentum forcing approaches increases with an increase in Reynolds number. Furthermore force interpolation and spreading schemes as used by Uhlmann (2005) in a momentum forcing approach assumes a smooth field otherwise they become first order accurate or need additional treatment (Peskin, 2003). The higher error and lowered order of accuracy has to be compensated by a finer grid resolution. This typically goes along with a decrease in timestep when using explicit time integration schemes making such a strategy computationally prohibitively expensive.

A method denoted "Boundary Data Immersion Method (BDIM)" that has recently been proposed for incompressible simulations by Weymouth & Yue (2011) and Maertens &

Weymouth (2015) overcomes many of the aforementioned weaknesses. The concept of this approach is to map the governing equations of the solid body and fluid domain at the interface. This results in a set of meta equations that is valid in both domains and ensures a smooth transition. For incompressible fluids the resulting formulation is similar to discrete momentum forcing approaches. However, an important extension is the inclusion of an additional term in the pressure equation. While the velocity field is not necessarily divergence free the additional term enforces continuity in the pressure equation. This was shown to reduce non-physical pressure oscillations often observed in momentum forcing methods (Griffith & Peskin, 2005; Muldoon & Acharya, 2008). Maertens & Weymouth (2015) increased the order of accuracy of the mapping between both domains to second order by taking the normal derivative to the surface into account. According to the classification of Mittal & Iaccarino (2005) this method is a continuous forcing approach as its derivation is based on the continuous equations only and not on the discretized problem. Hence, the BDIM does not depend on the discretization scheme and the underlying grid. With regard to the classification introduced in figure 3.1 the BDIM leads to a smooth representation of the fluid-solid interface but no forces are calculated. In general the reasoning and justification of the method is derived in an analytical way and less ad-hoc than discrete momentum forcing approaches.

The majority of aforementioned IMBMs and their extensions considered incompressible fluid flow. For aeroacoustics and compressible fluid flow there are only few methods published, among them are two for inviscid flow Chaudhuri *et al.* (2011); Tran & Plourde (2014). In the class of noise propagation problems with prescribed noise sources Casalino *et al.* (2004) and Arina (2008) as well as Cand *et al.* (2004) and Liu & Wu (2008) presented IMBMs in the frequency and time domain, respectively. Hybrid approaches for aeroacoustic research obtain a noise source field from a flow simulation which is then used as input for acoustic analogies to calculate the acoustic far-field. For this class of computational aeroacoustics Seo & Mittal (2011*b*) developed a sharp interface IMBM for the linearized perturbed compressible equations (LPCE). They validated the method with flow induced noise from stationary objects and acoustic scattering problems. Another hybrid approach was employed by Margnat (2015) who coupled an incompressible flow solver using Goldstein's feedback forcing (Goldstein *et al.*, 1993) approach with Curle's analogy.
To the authors knowledge all IMBM in the literature for viscous compressible flows were intended and validated to represent stationary bodies (De Palma *et al.*, 2006; de Tullio *et al.*, 2007; Ghias *et al.*, 2007; Liu & Vasilyev, 2007; Sandberg & Jones, 2011; Hu *et al.*, 2013). Among these studies that consider aeroacoustics Sandberg & Jones (2011) used a ghost cell approach to represent stationary flat plate extensions of airfoils to investigate trailing-edge noise with direct numerical simulations (DNS). Due to the complexity of the boundary reconstruction and the additional treatment for freshly cleared grid points this method would increase computational cost critically for moving boundary

problems, rendering it unsuitable for high-fidelity simulations. In the class of continuous forcing methods Liu & Vasilyev (2007) developed a Brinkmann penalization method with a unique density treatment modelling the solid as a high impedance medium for aeroacoustic simulations, however without presenting results for flow induced noise. The feedback forcing character of this approach leads to timestep restrictions when using explicit time marching which increases computational cost prohibitively.

Thus, when using a compressible flow solver to directly compute the hydrodynamic and aeroacoustic field simultaneously a method is required that can include the effects of moving bodies and the associated noise generation. Such a method would also enable the consideration of vibro-acoustic problems. Because of the many favourable advantages the aforementioned BDIM was extended for the use in compressible flows and as a framework implemented into the in-house code HiPSTAR. The general concept of the BDIM is introduced in section 3.2 and the extension to compressible flows is derived in section 3.3.

3.2 The Concept of the Boundary Data Immersion Method

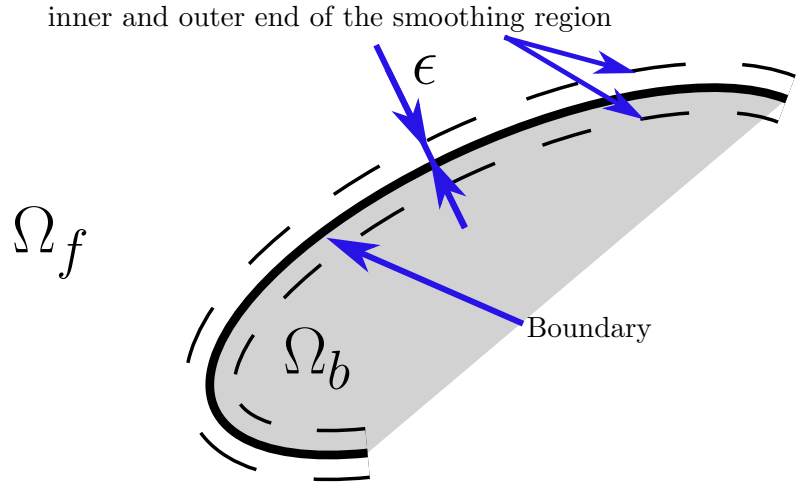

Figure 3.2: Subdomains under consideration for the derivation of the BDIM equations.

For the derivation of the BDIM meta equation a domain that incorporates a solid body subdomain Ω_b and a compressible fluid subdomain Ω_f are considered, as sketched in figure 3.2. The general formulation for a meta equation Φ_m of an arbitrary field variable Φ is given by

$$\Phi_M(\vec{x},t) = \begin{cases} b(\Phi,\vec{x},t) & \text{, for } \vec{x} \in \Omega_b \\ f(\Phi,\vec{x},t) & \text{, for } \vec{x} \in \Omega_f \end{cases}, \tag{3.3}$$

where b and f are the governing equations for the quantity Φ as a function of space $\vec{x}$ and time t in the solid body and fluid domain, respectively. To couple both subdomains

Domain Type	Volume	Area	Line	Point
Dimensions	3	2	1	0
α	$\epsilon^3\left(\frac{2\pi}{3}-\frac{4}{\pi}\right)$	$\epsilon^2\left(\frac{\pi}{2}-\frac{2}{\pi}\right)$	ϵ	1

Table 3.1: Normalization coefficient α for the nascent delta kernel defined in equation 3.4 as defined by Weymouth (2008).

smoothly, a nascent delta kernel K_ϵ of radius ϵ defined as

$$K_\epsilon(\vec{x},\tilde{X}) \equiv \begin{cases} \frac{1}{2\alpha}\left[1+\cos\left(\pi\frac{|\vec{x}-\tilde{X}|}{\epsilon}\right)\right] & \text{, for } \frac{|\vec{x}-\tilde{X}|}{\epsilon}<1 \\ 0 & \text{, else} \end{cases}, \tag{3.4}$$

is employed (Weymouth, 2008). The normalization coefficient α is listed in table 3.1 and ensures that the zeroth moment of the kernel for any point within the subdomain but outside of the smoothing region is one. Thus, both subdomains can be coupled by a convolution of the governing equation and the kernel which results in

$$b_\epsilon(\Phi,\vec{x},t) = \int_{\Omega_b} b(\Phi,\vec{x}_b,t)K_\epsilon(\vec{x},\vec{x}_b)\mathrm{d}\vec{x}_b\,, \tag{3.5}$$

and

$$f_\epsilon(\Phi,\vec{x},t) = \int_{\Omega_f} f(\Phi,\vec{x}_f,t)K_\epsilon(\vec{x},\vec{x}_f)\mathrm{d}\vec{x}_f\,, \tag{3.6}$$

respectively. With this step the domain of each individual governing equation is extended to the whole domain which is the union of both subdomains $\Omega = \Omega_b \cup \Omega_f$. Hence, the governing meta equation of the field variable Φ is simply

$$\Phi_{M,\epsilon} = b_\epsilon + f_\epsilon \text{ for } \vec{x}\in\Omega\,, \tag{3.7}$$

where the subscript ϵ indicates that smoothing is employed at the interface between both domains that are combined with the meta equation.

The role of the convolution is to "switch off" the governing equations in the complementary subdomain where they are not valid (i.e. fluid equations in solid domain and vice versa). Furthermore it allows a smooth transition between both subdomains over a smoothing region with a half-width of ϵ, where both governing equations contribute to the solution. Thus, the smoothing extends the range of the governing equation of each domain by ϵ. This approach results in continuous profiles for the tangential velocity and its wall normal derivative. When ϵ approaches zero a sharp interface can be reproduced. Considering the velocity field, a sharp transition would lead to a kink in the profile resulting in a discontinuity in its derivative. Furthermore, the governing equation is strictly only valid in the respective subdomain in this case. However, for a sharp interface the numerical operators would need to be modified, e.g. with one

sided finite difference stencils, as they are only valid to be applied to continuous fields. Thus, the width of the smoothing region is a trade-off between the numerical accuracy, which requires a large smoothing region, and the modelling error introduced by having a smooth interface.

Maertens & Weymouth (2015) use a Taylor series expansion of the convolution integral of equation 3.5 and 3.6 which results in

$$\begin{aligned} b_\epsilon(\Phi,\vec{x},t) =& \int_{\Omega_b} b(\Phi,\vec{x}_b,t)K_\epsilon(\vec{x},\vec{x}_b)\mathrm{d}\vec{x}_b \\ =& \int_{\Omega_b} \left(b(\Phi,\vec{x},t) + \vec{\nabla}b(\Phi,\vec{x},t)\cdot(\vec{x}_b-\vec{x})\right) K_\epsilon(\vec{x},\vec{x}_b)\mathrm{d}\vec{x}_b + \mathcal{O}(\epsilon^2) \\ =& b(\Phi,\vec{x},t)\int_{\Omega_b} K_\epsilon(\vec{x},\vec{x}_b)\mathrm{d}\vec{x}_b \\ &+\vec{\nabla}b(\Phi,\vec{x},t)\cdot\int_{\Omega_b}(\vec{x}_b-\vec{x})K_\epsilon(\vec{x},\vec{x}_b)\mathrm{d}\vec{x}_b + \mathcal{O}(\epsilon^2)\,, \end{aligned} \tag{3.8}$$

and can be performed analogously for the fluid equation $f(\Phi,\vec{x},t)$. For a simplification of the convolution integrals two requirements are necessary:

1. smoothing only occurs near the boundary/interface
2. smoothing occurs in the normal but not in the tangential direction of the boundary.

The Taylor series expansion in equation 3.8 neglects higher order terms as they would incorporate terms that are non-local and therefore violate requirement one. Using the aforementioned requirements the tangential component of the gradient of the governing equation $b(\Phi,\vec{x},t)$ is neglected, assuming a locally flat boundary. For cases where this is not justified a special treatment is presented in section 3.4.1. Furthermore the kernel K_ϵ is simplified and becomes only dependant on the distance to the boundary. With that, Maertens & Weymouth (2015) simplified equation 3.5 resulting in

$$b_\epsilon(\Phi,\vec{x},t) \approx b(\Phi,\vec{x},t)\,\mu_0^{\epsilon,b} + \frac{\partial b}{\partial n}(\Phi,\vec{x},t)\,\mu_1^{\epsilon,b}\,, \tag{3.9}$$

and

$$f_\epsilon(\Phi,\vec{x},t) \approx f(\Phi,\vec{x},t)\,\mu_0^{\epsilon,f} + \frac{\partial f}{\partial n}(\Phi,\vec{x},t)\,\mu_1^{\epsilon,f}\,, \tag{3.10}$$

with μ_0^ϵ being the zeroth and μ_1^ϵ first moments of the kernel K_ϵ over their respective subdomains.

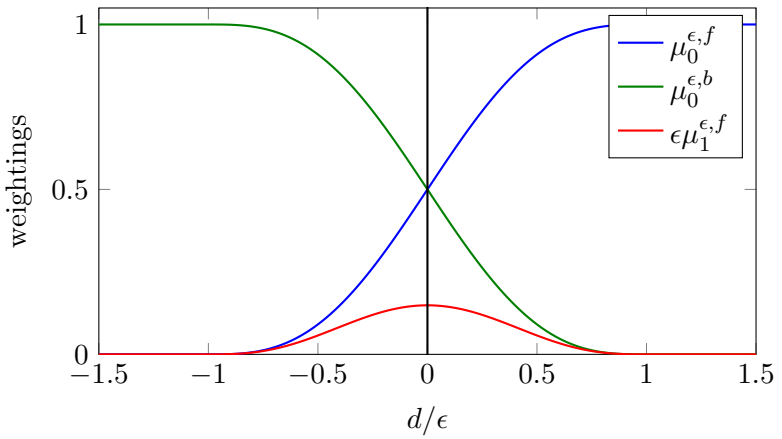

Figure 3.3: Zeroth and first moment of the kernel for the fluid and solid body domain in the vicinity of the wall surface.

With the simplified kernel K_ϵ normalized for domain type line, the zeroth moment of K_ϵ for the fluid domain is

$$\mu_0^\epsilon(d) \equiv \mu_0^{\epsilon,f}(d) = \begin{cases} \frac{1}{2}\left[1 + \frac{d}{\epsilon} + \frac{1}{\pi}\sin(\frac{d}{\epsilon}\pi)\right] & \text{, for } |d| < \epsilon \\ 0 & \text{, for } d \leq -\epsilon \\ 1 & \text{, for } d \geq \epsilon \end{cases}, \tag{3.11}$$

and the first moment is

$$\mu_1^\epsilon(d) \equiv \mu_1^{\epsilon,f}(d) = \begin{cases} \epsilon\left[\frac{1}{4}\left(1 - \frac{d}{\epsilon}^2\right) - \frac{1}{2\pi}\left(\frac{d}{\epsilon}\sin(\frac{d}{\epsilon}\pi) + \frac{1}{\pi}\left(1 + \cos(\frac{d}{\epsilon}\pi)\right)\right)\right] & \text{, for } |d| < \epsilon \\ 0 & \text{, for } |d| \geq \epsilon \end{cases}. \tag{3.12}$$

Both are visualized in figure 3.3 for the two subdomains. In these expressions for the zeroth and first kernel moment, d is the signed distance from the surface where values with $d < 0$ refer to the inside and $d > 0$ to the outside of the solid body. For the solid body domain the symmetry of the kernel functions can be used resulting in $\mu_0^\epsilon(d) \equiv \mu_0^{\epsilon,f}(d) = \mu_0^{\epsilon,b}(-d) = 1 - \mu_0^{\epsilon,b}(d)$ and $\mu_1^\epsilon(d) \equiv \mu_1^{\epsilon,f}(d) = \mu_1^{\epsilon,b}(-d) = -\mu_1^{\epsilon,b}(d)$, respectively (Maertens & Weymouth, 2015). Using equation 3.7 with 3.9 and 3.10 together with the kernel moments from equation 3.11 and 3.12 the resulting meta equation can be assembled and results in

$$\begin{aligned} \Phi_\epsilon = {} & f(\Phi, \vec{x}, t)\,\mu_0^\epsilon + b(\Phi, \vec{x}, t)\,(1 - \mu_0^\epsilon) \\ & + \mu_1^\epsilon \frac{\partial}{\partial n}\left(f(\Phi, \vec{x}, t) - b(\Phi, \vec{x}, t)\right). \end{aligned} \tag{3.13}$$

This meta equation will be used in the following section to derive the BDIM equations for compressible flows. The zeroth and first kernel moments, i.e. μ_0^ϵ and μ_1^ϵ, can be interpreted as interpolation functions between both subdomains with their respective

sets of governing equation. The derivative term increases the accuracy of this interpolation function as it reduces the error of the Taylor expansion from $\mathcal{O}(\epsilon)$ to $\mathcal{O}(\epsilon^2)$. In Maertens & Weymouth (2015) the derivative correction term determined the order of accuracy of the method when ϵ and the grid were refined. In this work results will be denoted "first order" when the derivative correction in equation 3.13 is not included, hence $\mu_1^\epsilon = 0$. The framework will be called second order when the derivative term is included. This nomenclature at this point is only based on the error from the Taylor expansion and the naming employed by Maertens & Weymouth (2015). The actual accuracy and convergence properties will be evaluated in section 4.

In the vicinity of sharp edges of a body surface, e.g. a rectangular trailing-edge, the kernel moments need to be interpolated between two line segments in order to properly account for the contribution of both surfaces. To that end the interpolation approach detailed in 3.4.1 was employed.

3.3 The Boundary Data Immersion Method for the Compressible Navier-Stokes Equations

In order to use the BDIM meta equation in a compressible flow solver, the conservative equations in 2.2 need to be mapped to the governing equation of the solid body. Since the governing equations of the fluid were already introduced in equation 2.2, the equations for the solid domain are introduced first.
The conservation of mass for a solid results in the same expression as for a compressible fluid, namely

$$\frac{\partial \rho}{\partial t} + \frac{\partial}{\partial x_k}\left(\rho u_k\right) = 0\,. \tag{3.14}$$

Furthermore the solid body has a prescribed velocity $V_i(\vec{s}, t)$ which can be provided a priori with an analytical equation or a time dependent solution from a structural solver or a flow control framework. It can vary in space given by $\vec{s}$, which is a location vector in the internal coordinate system of the body, and time. In addition the temperature $T_s(\vec{s}, t)$ within the solid body domain is prescribed as a constant or by another input function. Hence the governing equation for the velocity component i, $b(u_i, \vec{x}, t)$, and temperature $b(T, \vec{x}, t)$ of the solid body are

$$b(u_i, \vec{x}, t) = \xi\, V_i(\vec{s}, t)\,, \tag{3.15}$$

and

$$b(T, \vec{x}, t) = \xi\, T_s(\vec{s}, t)\,, \tag{3.16}$$

where ξ is the transformation operator from the internal coordinate system of the structure to the one of the fluid. Note that the dependence of all quantities on the location

is neglected in the notation throughout the following paragraphs in order to enhance readability. Nevertheless all quantities can vary in space. Since the conservation of mass is the same physical principle and has the same expression in both subdomains no mapping of the governing equations is needed. Before the velocity equation 3.15 of the solid can be mapped to the momentum equation 2.2b of the fluid both equations need to be reformulated in order to describe the same physical quantities. The left-hand side of equation 2.2b can be expanded as

$$\begin{aligned}\frac{\partial}{\partial t}(\rho u_i) + \frac{\partial}{\partial x_k}(\rho u_i u_k) &= u_i\frac{\partial \rho}{\partial t} + \rho\frac{\partial u_i}{\partial t} + \rho u_k\frac{\partial u_i}{\partial x_k} + u_i\frac{\partial \rho u_k}{\partial x_k} \\ &= \rho\left[\frac{\partial u_i}{\partial t} + u_k\frac{\partial u_i}{\partial x_k}\right],\end{aligned} \tag{3.17}$$

since the sum of the first and the last term of right-hand-side of the expanded equation are the continuity equation multiplied by u_i and therefore are zero. After some rearrangement with the right-hand-side from equation 2.2b the change of the fluid velocity in time is

$$\frac{\partial u_i}{\partial t} = -u_k\frac{\partial u_i}{\partial x_k} + \frac{1}{\rho}\left[-\frac{\partial p}{\partial x_k}\delta_{ij} + \frac{\partial}{\partial x_k}\tau_{ij}\right] = RHS_{u,i}\,. \tag{3.18}$$

$RHS_{u,i}$ will be used as an abbreviation for the right-hand-side of the velocity equation in the following derivation. The expression for the velocity field can then be obtained by integrating this equation over a time step Δt resulting in

$$f_v(u_i, t_0 + \Delta t) = u_{i,f}(t_0 + \Delta t) = u_{i,f}(t_0) + \int_{t_0}^{t_0+\Delta t} RHS_{u,i}\,dt\,. \tag{3.19}$$

With an Euler forward integration or a generalized Runge-Kutta substep in time this equation can be discretized with

$$f_v(u_i, t_0 + \Delta t) = u_{i,f}(t_0 + \Delta t) = u_{i,f}(t_0) + RHS_{u,i}\,\Delta t\,. \tag{3.20}$$

Since the governing equations for the velocity in both subdomains are now defined with equation 3.15 and 3.20 they can be replaced in 3.13 which leads to

$$\begin{aligned}u_{i,\epsilon}(t_0 + \Delta t) = {} & \left[u_{i,f}(t_0) + RHS_{u,i}\Delta t\right]\mu_0^\epsilon \;+\; b(u_i, t)\,(1 - \mu_0^\epsilon) \\ & +\; \mu_1^\epsilon\frac{\partial}{\partial n}\left[u_{i,f}(t_0) + RHS_{u,i} - b(u_i, t)\right]\,.\end{aligned} \tag{3.21}$$

In contrast to incompressible fluid solvers where the pressure equation is commonly solved separately from the rest of the right-hand-side of equation 3.18 all of these terms are treated the same way in the compressible in-house code “HiPSTAR” that is used in this work. Therefore the mapped velocity field of the fluid can be summarized with its integral formulation which results in

$$u_{i,\epsilon}(t) = u_{i,f}(t)\mu_0^\epsilon \;+\; b(u_i, t)\,(1 - \mu_0^\epsilon) \;+\; \mu_1^\epsilon\frac{\partial}{\partial n}\left[u_{i,f}(t) - b(u_i, t)\right]\,. \tag{3.22}$$

In the same manner as carried out for the velocity equation the left-hand-side of the total energy equation 2.2c can be expanded

$$\frac{\partial}{\partial t}(\rho E) + \frac{\partial}{\partial x_k}(\rho u_k E) = E\frac{\partial \rho}{\partial t} + \rho\frac{\partial E}{\partial t} + \rho u_k \frac{\partial E}{\partial x_k} + E\frac{\partial \rho u_k}{\partial x_k}\,. \tag{3.23}$$

The sum of the first and the last term of the right-hand-side of the expanded equation are the continuity equation multiplied by the total energy E and hence add up to zero. By substituting the definition of the total energy $E = T/\left[\gamma(\gamma-1)M^2\right] + 1/2 u_i u_i$ and the abbreviation $1/\left[\gamma(\gamma-1)M^2\right] = \chi$ this yields

$$\begin{aligned}
\rho\frac{\partial E}{\partial t} + \frac{\partial}{\partial x_k}(\rho u_k E) &= \rho\left[\chi\frac{\partial T}{\partial t} + \frac{1}{2}\frac{\partial u_i u_i}{\partial t}\right] + \rho u_k\left[\chi\frac{\partial T}{\partial x_k} + \frac{1}{2}\frac{\partial u_i u_i}{\partial x_k}\right] \\
&= \rho\left[\chi\frac{\partial T}{\partial t} + u_i\frac{\partial u_i}{\partial t}\right] + \rho u_k\left[\chi\frac{\partial T}{\partial x_k} + u_i\frac{\partial u_i}{\partial x_k}\right] \\
&= \rho\left[\chi\frac{\partial T}{\partial t} + u_k\chi\frac{\partial T}{\partial x_k}\right] + \rho u_i\left[\frac{\partial u_i}{\partial t} + u_k\frac{\partial u_i}{\partial x_k}\right]\,.
\end{aligned} \tag{3.24}$$

The two terms in the final brackets of the last line are the left-hand-side of the expanded momentum equation 3.17 multiplied by u_i. They represent the change of kinetic energy of the fluid after applying the chain rule. Using that fact together with the right-hand-side of equation 2.2c the change of temperature in time can be expressed by

$$\begin{aligned}
\frac{\partial T}{\partial t} &= -u_k\frac{\partial T}{\partial x_k} + \frac{1}{\rho\chi}\frac{\partial}{\partial x_k}\left[u_i\tau_{ik} - u_k p - q_k + u_i p\delta_{ik} - u_i\tau_{ik}\right] \\
&= -u_k\frac{\partial T}{\partial x_k} + \frac{1}{\rho\chi}\frac{\partial}{\partial x_k}\left[-u_k p - q_k + u_i p\delta_{ik}\right] = RHS_T\,.
\end{aligned} \tag{3.25}$$

Analogous to the time integration of the velocity the temperature at time $t = t_o + \Delta t$ is

$$f_T(T, t_0 + \Delta t) = T_f(t_0 + \Delta t) = T_f(t_0) + RHS_T\,\Delta t\,, \tag{3.26}$$

and can be substituted into the general meta equation together with the governing equation for the solid's temperature 3.16

$$\begin{aligned}
T_\epsilon(t_0 + \Delta t) = &\left[T_f(t_0) + RHS_T\Delta t\right]\mu_0^\epsilon + b(T,t)\,(1-\mu_0^\epsilon) \\
&+ \mu_1^\epsilon\frac{\partial}{\partial n}\left[T_f(t_0) + RHS_T\Delta t - b(T,t)\right]\,.
\end{aligned} \tag{3.27}$$

With the same reasoning as for the velocities the BDIM equation for temperature can be simplified with its integral formulation

$$T_\epsilon(t_0 + \Delta t) = T_f(t)\mu_0^\epsilon + b(T,t)\,(1-\mu_0^\epsilon) + \mu_1^\epsilon\frac{\partial}{\partial n}\left[T_f(t) - b(T,t)\right]\,. \tag{3.28}$$

As the resulting BDIM equations can all be expressed with the integral formulation, the boundary data immersion can be applied after the integration and no adaptation of the solving algorithm for the right-hand-side is needed. Furthermore this is consistent with

the application of body-fitted boundary conditions which are performed at the same stage of the simulation.

A comparison between the derived meta equations 3.22 and 3.28 and discrete momentum forcing reveals that the first order BDIM is very similar to discrete momentum forcing. When the μ_0^ϵ and $1 - \mu_0^\epsilon$ terms are regarded as the interpolation and force spreading operators, then the only difference between both approaches is the physical reasoning for using them and how these operators work. The analytical and general reasoning however is a strength of the BDIM approach offering robust and smooth coupling where other approaches depend on the surface discretization and force interpolation and spreading procedures. In addition, the second order extension of the approach offers higher order interpolation between both subdomains and reduces bias of the velocity gradient discontinuity.

3.3.1 The Continuity Mapping for the Boundary Data Immersion Method

In the incompressible meta equations derived in Weymouth & Yue (2011) and Maertens & Weymouth (2015) there is an additional weighting for the pressure term as a boundary condition for the pressure equation. This is a result of the special algorithmic treatment of the pressure by the Poisson equation in incompressible flow simulations, which is in principle not required in the present compressible framework. However, it was found that for bluff bodies where the body surface alignment with the underlying grid is arbitrary, instabilities on single grid points could grow just inside the boundary smoothing region. These instabilities would eventually lead to diverging simulations. The analysis of the contributing terms of the continuity equation

$$\frac{\partial \rho}{\partial t} = -\frac{\partial}{\partial x_k}\left(\rho u_k\right) = -\left(\rho \frac{\partial u_k}{\partial x_k} + u_k \frac{\partial \rho}{\partial x_k}\right) , \tag{3.29}$$

at these grid points showed that the instabilities were caused by the bias in the derivative terms of the velocity, i.e. the first term, which contains the incompressible contribution. In particular the derivative in the wall tangential direction leads on average to a non-zero right-hand-side of the continuity equation. In order to ensure robust simulations without prescribing something non-physical it is suggested to map the right-hand-side of equation 3.29 to

$$\frac{\partial \rho}{\partial t} = -\left(\rho \frac{\partial u_n}{\partial n}\right) . \tag{3.30}$$

Here the subscript and direction n mean the wall normal direction. This is exactly the simplified right-hand-side of the continuity equation at the wall for a stationary body. In this case the second term in brackets of equation 3.29 is zero and the only non-zero component of the first term is the derivative of the wall normal velocity component in the wall normal direction. Strictly speaking equation 3.30 is not the governing equation

of the solid interior but an interface condition. Replacing equation 3.29 and 3.30 in the general meta equation 3.13 results in

$$\frac{\partial \rho_\epsilon}{\partial t} = -\frac{\partial \left(\rho u_k\right)}{\partial x_k}\mu_0^\epsilon - \left(\rho \frac{\partial u_n}{\partial n}\right)\left(1-\mu_0^\epsilon\right) - \mu_1^\epsilon \frac{\partial}{\partial n}\left(\frac{\partial \left(\rho u_k\right)}{\partial x_k} - \left(\rho \frac{\partial u_n}{\partial n}\right)\right), \tag{3.31}$$

as meta equation for the right-hand-side of the continuity equation. In the current implementation, the wall normal derivative of a fluid quantity Φ is calculated by a wall normal projection of the gradient, i.e.

$$\frac{\partial \Phi}{\partial n} = \nabla \Phi \cdot \vec{n}\,. \tag{3.32}$$

In case Φ is a vector quantity, i.e. $\vec{\Phi}$, and the wall normal derivative of the wall normal vector direction is needed a second projection is required. When it is expanded it results in

$$\begin{aligned}
\frac{\partial \Phi_n}{\partial n} &= \frac{\partial \Phi_n}{\partial x_1}n_1 + \frac{\partial \Phi_n}{\partial x_2}n_2 + \frac{\partial \Phi_n}{\partial x_3}n_3 \\
&= \left(\frac{\partial \Phi_1}{\partial x_1}n_1 + \frac{\partial \Phi_2}{\partial x_1}n_2 + \frac{\partial \Phi_3}{\partial x_1}n_3\right)n_1 \\
&+ \left(\frac{\partial \Phi_1}{\partial x_2}n_1 + \frac{\partial \Phi_2}{\partial x_2}n_2 + \frac{\partial \Phi_3}{\partial x_2}n_3\right)n_2 \\
&+ \left(\frac{\partial \Phi_1}{\partial x_3}n_1 + \frac{\partial \Phi_2}{\partial x_3}n_2 + \frac{\partial \Phi_3}{\partial x_3}n_3\right)n_3\,.
\end{aligned} \tag{3.33}$$

3.4 Implementation of the Boundary Data Immersion Method

This section gives some details of the actual implementation of the BDIM into the in-house DNS code. Section 3.4.1 describes how the interpolation functions μ_0 and μ_1 are calculated at the intersection of two planes. The concept of the algorithm that was used to evaluate the signed distance function is introduced in section 3.4.2. Furthermore a special algorithmic treatment for the simulation of bluff bodies is introduced in section 3.4.3 and was found to be crucial for stable simulations.

3.4.1 Intersections of two Planes

In the vicinity of sharp corners, i.e. the intersection of two line segments or planes, there might be grid points within a distance lower than the smoothing region halfwidth ϵ to both planes, which is the case in the situation sketched in figure 3.4. In that case the assumption of a smooth interface does not hold and special treatment is needed. The analytical treatment suggested by Maertens & Weymouth (2015) was found to lead to interpolation functions μ_0 and μ_1 that were not smooth when rectangular intersections

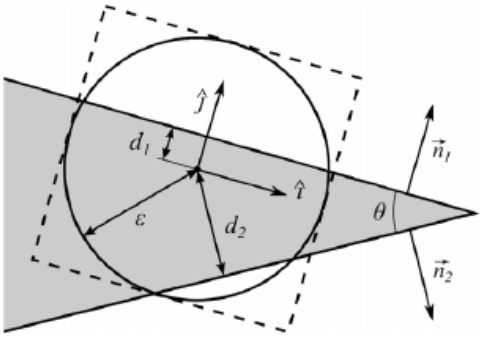

Figure 3.4: Schematic of a point in the vicinity of two intersecting line segments (figure from Maertens & Weymouth (2015)).

were considered.

Therefore the approach that was used for the validation and production cases of this work are based on a heuristic approach suggested in private communication by Dr. Gabriel Weymouth. The following derivation of the joint moments for the compound plane is reproduced from the published paper Schlanderer *et al.* (2017) and is based on original work by Dr. Gabriel Weymouth.

First we use equation 3.11 to determine the moment at point $\vec{x}$ of each of the component planes a and b, and call them $\mu_{0,a}$, $\mu_{0,b}$. We name these planes such that $\mu_{0,a} \leq \mu_{0,b}$, i.e. $\vec{x}$ is further into the fluid relative to a. In the case that x is not near the intersection, the moment of the shape c defined as the intersection of a and b is simply the moment of a,

$$\mu_{0,c} = \mu_{0,a} \,, \tag{3.34}$$

However, when $\vec{x}$ is in the smoothing region of both a and b, such that $0 < \mu_{0,a} \leq \mu_{0,b} < 1$, then both planes contribute to the compound moment. An approximate value for the compound moment in this case is

$$\mu_{0,c} = \mu_{0,a} \mu_{0,b}^{\log_2 \frac{\pi}{\theta}} \,, \tag{3.35}$$

subject to the bound

$$\mu_{0,c} \geq \max(0, \mu_{0,a} + \mu_{0,b} - 1) \,. \tag{3.36}$$

We see that the angle θ between a and b determines how heavily $\mu_{0,b}$ influences the compound moment. For $\theta = \pi$, the compound shape is flat and there is no change to equation 3.34. For $\theta < \pi$, the shape is a sharp corner, and the moment decreases sharply as you approach the intersection of the two planes. The bound ensures that the compound moment is still accurate for very small angles when the kernel regions of the two planes do not overlap.

Once this moment is established, it implicitly defines the effective distance d_c and normal $\hat{n}_c$ of the compound shape. If $\mu_{0,c}$ is given by equation 3.34 then $d_c = d_a$ and $\hat{n}_c = \hat{n}_a$. Otherwise, the distance d_c is found by inverting equation 3.11. Note that the bounds on $\mu_{0,c}$ ensure we only need the first line of equation 3.11. Let us call h the inverse of equation 3.11 , i.e.

$$d(\vec{x}) = h(\mu_0(\vec{x}))\,.$$

Then $d_c = h(\mu_{0,c})$ is used in equation 3.12 to find the effective first moment $\mu_{1,c}$ without issue.

The normal $\hat{n}$ is defined as

$$\hat{n}(\vec{x}) = \vec{\nabla} d(\vec{x}) = h'(\mu_0)\vec{\nabla}\mu_0(\vec{x})\,, \tag{3.37}$$

where

$$h' = \frac{\partial h}{\partial \mu_0}\,,$$

and we note that h' only scales the magnitude not the direction of the normal. First, let's assume that the lower bound equation 3.36 is active, then the normal is proportional to

$$\hat{n}_c \propto \vec{\nabla}\mu_{0,a} + \vec{\nabla}\mu_{0,b} = \frac{\hat{n}_a}{h'(\mu_{0,a})} + \frac{\hat{n}_b}{h'(\mu_{0,b})}\,,$$

where equation 3.37 is used to substitute the normal for each component. We see the effective normal is a weighted sum of the component normals.

Next, using equation 3.35, applying the chain rule, and substituting the normals for each component as before gives

$$\hat{n}_c \propto \frac{1}{\mu_{0,a}}\frac{\hat{n}_a}{h'(\mu_{0,a})} + \frac{\log_2(\frac{\pi}{\theta})}{\mu_{0,b}}\frac{\hat{n}_b}{h'(\mu_{0,b})}\,,$$

where again we see that the angle θ determines the relative influence of plane b.

3.4.2 Evaluation of the Signed Distance Function

In order to use the BDIM during a simulation and apply the meta equation 3.13 to the temperature and velocity field the functions μ_0^ϵ and μ_1^ϵ need to be evaluated at the grid point locations of the fluid grid. Since μ_0^ϵ and μ_1^ϵ only depend on the signed distance from the body surface it is this function that every implementation of the BDIM will hinge on in terms of functionality and computational cost. For bodies with the shape of a circle with radius R_{cyl} the calculation of the signed distance D for a given grid point location $(x_{\text{point}}, y_{\text{point}})$ is straightforward with

$$D = \sqrt{(x_{\text{point}} - x_{\text{origin}})^2 + (y_{\text{point}} - y_{\text{origin}})^2} - R_{cyl}\,, \tag{3.38}$$

where the origin of the circle is at $(x_{\text{origin}}, y_{\text{origin}})$. In addition to the simple calculation of the signed distance, the circle can also be defined comparatively concisely by specifying its radius and origin. However, for more general shapes such as a deflected bending beam or membrane a more general representation is needed. This can be achieved by employing polygons, based on a chain of piecewise straight line segments which can form an arbitrary shape. This description has the limitation that it can only represent two dimensional shapes without any further additions. However, it can be extended to three dimensions and for the current purpose the representation of two dimensional bodies is sufficient.

With the previous explanations and future applications for elastic trailing-edges in mind the following requirements for the algorithm to evaluate the signed distance function can be formulated:

- the signed distance function shall be evaluated for arbitrarily shaped bodies that are defined by a polygonal shape with an arbitrary number of line segments
- the algorithm has to work robustly on curvilinear grids where the grid spacing is not uniform
- should be extensible for three dimensional geometries
- the algorithm has to be fast enough such that it is feasible to calculate the signed distance every timestep, therefore:
- the algorithm should only evaluate the distance function within a certain distance D outside of the body (mostly this will be $D = +\epsilon$)

The last requirement can be explained with the fact that the fluid equations are solved in the entire domain and the velocity and temperature field only need to be altered for all grid points $d < +\epsilon$. It is therefore desirable that the algorithm produces a list of fluid points that are within $d < +\epsilon$ and that the calculation of the meta equation 3.13 is limited to these points. Furthermore, additional computational cost can be saved when the signed distance function is only evaluated for the subset $d < +\epsilon$ and not all grid points.

The last two requirements mentioned above exclude brute forcing approaches in which the perspective of a fluid grid point is: “How far am I away from the surface?” and “Which is the line segment I am closest to?”. With this perspective the distance of a grid point to every line segment is calculated and the minimum is taken. The procedure is then repeated for all grid points in the fluid grid.

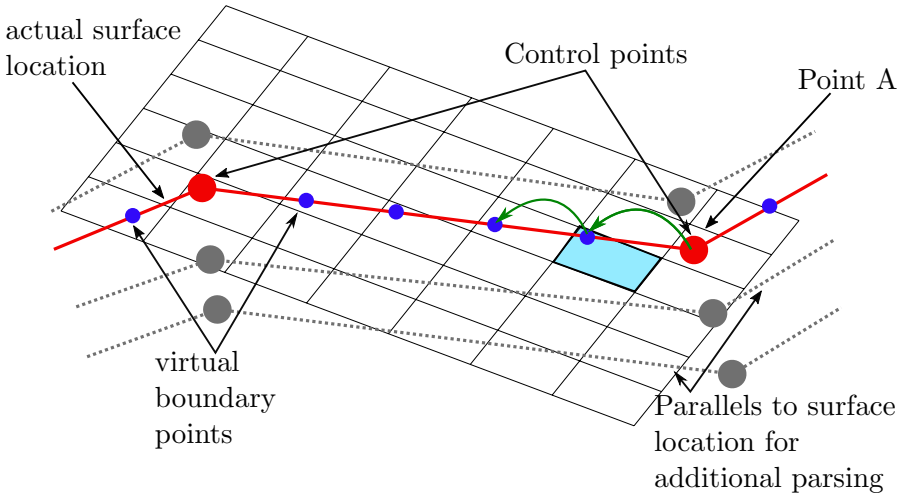

Figure 3.5: Sketch of the concept of the parsing algorithm to evaluate the signed distance function.

The general idea of the currently-implemented algorithm is to change the perspective to the individual line segment of the polygon that asks from its perspective: "Which grid points of the fluid grid are close to me such that I am their closest line segment?" and "How large is the normal distance to them?". Figure 3.5 shows a sketch of the concept of the currently implemented algorithm to evaluate the signed distance function. The surface of the solid is indicated with the red line and is defined by control points defining the beginning and end of the individual line segments of the polygon. For each line segment one end point is located in the underlying grid first. Let us assume it is control point A in the sketch. Once the four grid points that enclose this point are found the distance to each line of the adjacent line segments can be calculated with the interpolation introduced in section 3.4.1.

Then a new "virtual" boundary point, indicated by the blue dot, is calculated by moving in the direction of the line segment for a distance in the order of the local grid size. The surrounding grid cell, indicated by the blue shaded area, of this virtual boundary point is then located on the underlying grid. For each of the four surrounding grid points the signed normal distance to the surface can be calculated by a projection of the displacement vector between grid and virtual boundary point on the wall normal direction. Once this is carried out for all four grid points forming the surrounding grid cell the next virtual boundary point is calculated. This procedure is repeated until the end of the line segment is reached and interpolation between two line segments as detailed in section 3.4.1 is employed. In order to find all relevant points on the fluid grid for which $d < +\epsilon$ the parsing is repeated with a wall normal offset of $+\epsilon$, $-\epsilon$, -2ϵ, etc.. The maximum offset towards the interior of the solid depends on the thickness of the body which determines how many times the parsing has to be repeated to find all interior

points.

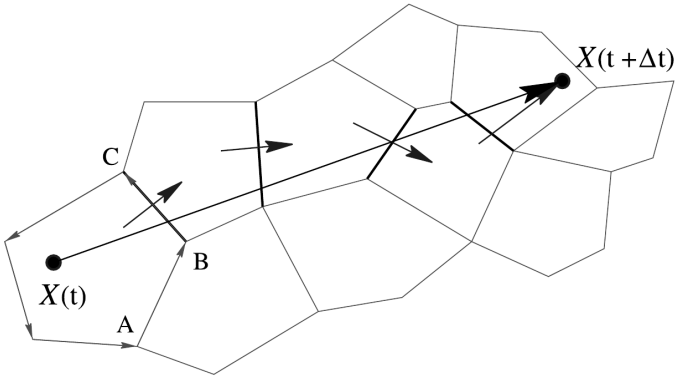

Figure 3.6: Sketch of the working principle of the locating algorithm (figure from Chordá *et al.* (2002)).

The performance of the introduced algorithm hinges on an efficient method to locate the four surrounding grid points of a given location on curvilinear grids. To that end the directed searching algorithm proposed by Chordá *et al.* (2002) was implemented. The principle of this method is sketched in figure 3.6 and is based on the computationally inexpensive test of whether a point is on the left of an interface. If this test is successful for all interfaces forming a grid cell, the desired point is located. When the desired point is not within the current grid cell, the test is repeated for the next cell neighbouring the interface, where the point to the left test failed, until the point is located.

With this directed searching approach the next virtual point of the parsing algorithm sketched in figure 3.5 can be located within one or two iterations if the search starts at the location of the current virtual point leading to a highly efficient algorithm to evaluate the signed distance function.

3.4.3 Special Algorithmic Treatment for Bluff Bodies

For our finite-difference implementation of the BDIM framework, we found that for slender objects such as thin plates it is important to ensure that the thickness of the solid body is at least such that it is represented by a factor of 1.5 to 2 times the number of points of the numerical stencil. If the solid object is represented by fewer grid points the results are strongly biased by direct coupling of the two surfaces through the numerical stencil.
It is quite common to employ high order wave-number optimised filters along with high order finite differences. The purpose of these filters is to damp instabilities with wave numbers that are higher than what could be resolved by the grid, without affecting the physical solution. Typically these filters have much larger stencils than the underlying

finite difference scheme. In the current code, we employ a sixth-order accurate high-wavenumber cut-off filter proposed in (Bogey *et al.*, 2009) with a stencil of 11 points. We found that this large stencil sometimes leads to a bias inside the solid, in particular when the surface of the body is not aligned with grid lines. This would eventually lead to diverging simulations. In order to reduce this bias we applied the first order BDIM meta equation to the filtered field of quantity Φ which results in

$$\Phi_\epsilon = \Phi_F \mu_0^{\epsilon,F} + \Phi_U (1 - \mu_0^{\epsilon,F}) \,, \tag{3.39}$$

where all super and subscripts F indicate the filtering operation, hence Φ_F is the filtered field of Φ. Furthermore, the unfiltered field is Φ_U and the resulting field with a smooth transition between filtered and unfiltered field is Φ_ϵ. With this algorithmic treatment of the filtering the bias can be eliminated by essentially switching the filter off inside the solid. We found it essential to evaluate $\mu_0^{\epsilon,F}$ (used to switch the filter on and off) with an offset towards the inside of the solid of ϵ, resulting in the following argument for equation 3.11

$$\mu_0^{\epsilon,F} = \mu_0^{\epsilon} \left(\frac{d + \epsilon}{2\epsilon} \right) \,, \tag{3.40}$$

to avoid instabilities in the density field on the grid points just next to the boundary of the smoothing region at the interior of the solid. As equation 3.39 is only applied to the filtering operation and not prescribing any boundary conditions itself, the effects on the physical representation of the body can be neglected. The role of the filtering in general and in particular the bluff body filter treatment is to enhance the numerical stability by damping out non-physical oscillations with minimal influence on the physical result.

Chapter 4

Validation of Used Methods

This chapter assesses the accuracy of the extended and newly implemented BDIM in section 4.1 and the implementation of the structural solver in section 4.2.

4.1 Validation of the Boundary Data Immersion Method

This section presents the results of validation cases that are highly relevant to aeroacoustic simulations. To the best of the author's knowledge most of the cases considered here have not been used to validate IMBMs in the past. When flow-induced noise due to fluid-solid interaction is considered, a very accurate representation of the near-wall flow is crucial. This is attributed to the fact that fluctuations in the boundary layer are the "input" of the noise scattering mechanism. Hence it needs to be assessed whether the BDIM framework is capable of accurately reproducing the physical behaviour close to the solid wall at an arbitrary and grid-independent location.

To assess the representation of the fluid flow and the data-capturing approach, a cylinder in a uniform flow is considered first (section 4.1.1). As a rigorous test case for the near-wall behaviour the simulation of viscous instability growth in a flat plate boundary layer, also denoted Tollmien-Schlichting-Waves (TS-waves), was chosen as suggested by von Terzi *et al.* (2001) in section 4.1.2. Besides the accurate representation of incompressible flow features, the correct modelling of the thermodynamic fluctuations in a boundary layer are essential in high-fidelity simulations, since the noise is calculated directly from the compressible Navier–Stokes equations. In order to evaluate and validate these features of the BDIM framework the growth of oblique waves in a flat plate boundary layer at $M = 3$ is considered in section 4.1.3. This is a three dimensional flow case and therefore also validates the implementation for applications with three dimensional flows. Furthermore, the capability of the BDIM to simulate a wall bounded

flow with a wide range of length and time scales is evaluated by considering a turbulent boundary layer in section 4.1.4. Since the goal of this work is to simulate noise from elastic trailing-edges the BDIM needs to be capable of accurately simulating acoustic noise radiation from moving bodies. To that end,the noise radiation from the cross-section of an oscillating cylinder is considered in section 4.1.5.

4.1.1 Flow Around a Stationary Cylinder

The canonical flow around a static cylinder at Reynolds number $Re_{D_{cyl}} = 100$ is considered first as a validation case which offers a large amount of reference data in the literature. Furthermore, it is used to validate the data capturing approach to obtain flow field information on the immersed body surface.

4.1.1.1 Setup

The Mach number was set to $M = 0.1$, thus compressibility effects are expected to be negligible. The flow is simulated in a domain where the cylinder is placed at the origin and the domain boundaries are $-27D_{cyl} < x < 30D_{cyl}$ and $-30D_{cyl} < y < 30D_{cyl}$. The cylinder is immersed in a fluid flow with a streamwise velocity of unity which is prescribed at the inflow. The upper and lower boundaries are modelled as non-reflective characteristic freestream boundary conditions. At the outflow boundary the zonal characteristic boundary condition proposed in Sandberg & Sandham (2006) is employed. The grid is spaced uniformly in the x and y directions within a region of $-2R_{cyl} < x < 2R_{cyl}$ and $-2R_{cyl} < y < 2R_{cyl}$. The uniform grid spacing was $\Delta x = D_{cyl}/120$, thus resulting in 180 points within the equidistant discretization. The grid was then stretched towards the boundaries over 95 grid points with polynomial functions. The smoothing region half-width is set to $\epsilon = 2\Delta x = 2\Delta y$. Furthermore, the mapping of the continuity equation, as introduced in equation 3.31, had to be employed.

4.1.1.2 Results – Accuracy and Datacapturing on Immersed Surface

The forces acting on the cylinder are calculated from the pressure and skin-friction values on the surface of the cylinder. To that end, the cylinder surface was discretized by 360 points equally distributed over the circumference. Since the values within the smoothing region are not physical, the surface quantities were evaluated with a distance of ϵ from the actual surface. The accuracy of the pressure force is expected to not be affected by that. However, the skin-friction will be underestimated with this method. This is not a specific problem related to the BDIM but occurs in other IMBM approaches as well (Pourquie, 2009). The relevant flow quantities, i.e pressure and wall normal velocity gradient are interpolated from the four surrounding fluid grid points onto the surface

grid using bilinear interpolation as described in Saiki & Biringen (1996).

The final values for the forces acting on the cylinder are obtained by a panel integration over all surface points. The quantities that are used to assess the accuracy of the BDIM are introduced in the following paragraph. The Strouhal number St can be considered as non-dimensional frequency and is calculated with

$$St = \frac{f_{shed} D_{cyl}}{U_\infty}\,, \tag{4.1}$$

where f_{shed} is the vortex shedding frequency, D_{cyl} the cylinder diameter and U_∞ the freestream velocity. The drag coefficient C_D is the non-dimensional drag force the flow exerts on the cylinder and is calculated with

$$C_D = \frac{F_D}{\frac{1}{2}\rho U_\infty^2 A}\,, \tag{4.2}$$

where F_D is the drag force, ρ the fluid density and A the projected area of the cylinder in the direction of flow per unit spanwise extent. When only the contribution of the pressure drag is considered and the drag force is only calculated by the pressure drag force F_{Dp}, the drag coefficient is denoted C_{Dp}. On the other hand, C_{Df} is the drag coefficient calculated with the drag force resulting from skin-friction F_{Df}. The lift coefficient C_L can be defined analogously with

$$C_L = \frac{F_L}{\frac{1}{2}\rho U_\infty^2 A}\,, \tag{4.3}$$

where F_L is the overall lift force exerted on the cylinder. The lift coefficient calculated from the pressure force F_{Lp} is denoted C_{Lp}. Similarly to the drag, C_{Lf} is the lift coefficient calculated using the skin-friction lift force F_{Lf}.

The results for the Strouhal number, the lift fluctuations as well as the drag are presented in table 4.1. They are presented alongside data available in the literature from experiments (Norberg, 1994; Tritton, 1959), body-fitted simulations (Park *et al.*, 1998; Henderson, 1995; Zhang *et al.*, 1995) and other IMBMs (Choi *et al.*, 2007; Chiu *et al.*, 2010; Russell & Wang, 2003; Maertens & Weymouth, 2015). Given the scatter among the reported results the data obtained from simulations with the BDIM agree reasonably well with the values from literature.

[1]Park *et al.* (1998)
[2]Henderson (1995)
[3]Zhang *et al.* (1995)
[4]Choi *et al.* (2007)
[5]Chiu *et al.* (2010)
[6]Russell & Wang (2003)
[7]Maertens & Weymouth (2015)1st order
[8]Maertens & Weymouth (2015) 2nd order

Source	St	C_D	C_L	C_{Dp}	C_{Df}	C_{Lp}	C_{Lf}
Experiment	0.164	1.25	-	-	-	-	-
[1]	0.165	1.33 ± 0.009	± 0.3321	0.99 ± 0.0082	± 0.0010	± 0.295	± 0.042
[2]		1.33		1.00	0.32	-	-
[3]	0.172	1.42	± 0.3536	-	-	-	-
[4]	0.164	1.34 ± 0.011	± 0.315	-	-	-	-
[5]	0.167	1.35 ± 0.012	± 0.315	-	-	-	-
[6]	0.165	1.34 ± 0.007	± 0.276	-	-	-	-
[7]	0.167	1.31 ± 0.009	± 0.321	1.01 ± 0.0085	0.30 ± 0.0008	± 0.292	± 0.035
[8]	0.167	1.31 ± 0.009	± 0.313	1.00 ± 0.0081	0.30 ± 0.0007	± 0.285	± 0.034
1st order	0.165	1.35 ± 0.011	± 0.348	1.03 ± 0.0104	0.32 ± 0.0010	± 0.314	± 0.040
2nd order	0.165	1.32 ± 0.011	± 0.333	1.02 ± 0.0010	0.30 ± 0.0008	± 0.304	± 0.036

Table 4.1: Summary of the results from the cylinder case employing the first and second order BDIM to represent the cylinder shape for the baseline resolution of $\Delta x = D_{cyl}/120$. The results are compared to experimental data (St from Norberg (1994) with estimated uncertainty of 0.8%, C_D from Tritton (1959) with estimated measurement error of 6%), body-fitted simulations (source 1: Park *et al.* (1998), source 2: Henderson (1995), source 3: Zhang *et al.* (1995)) and other IMBMs (source 4: Choi *et al.* (2007), source 5: Chiu *et al.* (2010),source 6: Russell & Wang (2003), source 7: Maertens & Weymouth (2015)). The references to the source can also be found in the footnote of the page.

4.1.1.3 Formal Order of Convergence

In order to evaluate the formal order of convergence for the numerical setup the simulation of the flow around the cylinder was repeated on six grids that were coarser than the one of the baseline simulation from the previous section. The resolution levels are defined in multiples n of the baseline resolution with $nD_{cyl}/120 = [3, 4, 6, 8, 10]$. The computational cost for the study was reduced by setting the Mach number to $M = 0.3$ which allowed an increase of the time step of the simulation. Since there is no analytical solution for this flow problem the data from the highly resolved case presented in the previous section with a grid spacing of $\Delta x = \Delta y = D_{cyl}/120$ was used as a reference.

Commonly, the L_2 norm is considered as a measure for the global error made by the boundary scheme. The L_∞, on the other hand, highlights the local error close to the boundary. Figure 4.1 presents the results for the convergence study in the L_2 (4.1a and 4.1b) as well as in the L_∞ (4.1c and 4.1d) norm for the velocity and pressure fields over the different grid resolutions. In general, it can be found that the results with the first order framework always yield an error that is higher than that obtained with the second order correction. For the L_2 and L_∞ norms the difference in error of the velocity field from the first order approach is a factor of $2.6 - 8.6$ higher than that of the second order BDIM. For the pressure field the differences are a bit lower but still significant with a factor of $2.0 - 3.0$. Each plot of figure 4.1 also shows first and second order slopes. Comparing these to the convergence data one can find that the first order

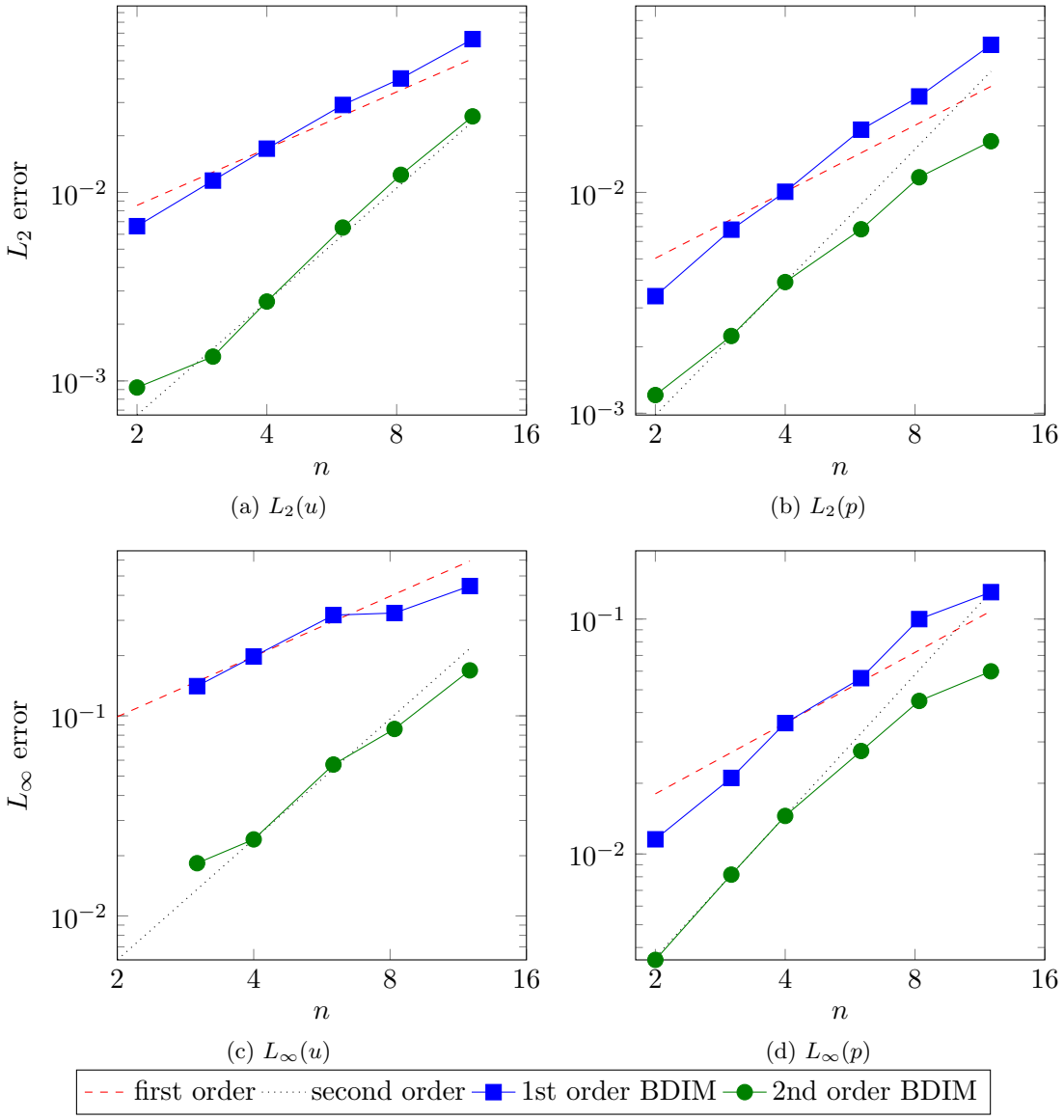

Figure 4.1: L_2 and L_∞ convergence of the velocity and pressure field for the flow around a stationary cylinder. A first and second order slope are shown as reference.

approach yields a convergence rate that is slightly higher than first order for the velocity field (4.1a and 4.1c) in both the L_2 and L_∞ norm. In contrast to that the second order framework shows second order convergence approximately in the L_2 and L_∞ norm. For the pressure field the convergence rates of both approaches are approximately the same with second order for the higher resolution levels and slightly lower for the coarsest two.

4.1.2 Tollmien-Schlichting Validation Case

Tollmien-Schlichting waves (TS-waves) are two dimensional viscous laminar boundary layer instability waves with small (linear) disturbance amplitudes. In experiments they

resolution	Δx	N_x	Δy_{wall}	N_y	N_{tot}
1	3.01×10^{-2}	151	1.00×10^{-3}	43	6493
2	2.30×10^{-2}	151	7.50×10^{-4}	58	11716
3	1.50×10^{-2}	301	5.00×10^{-4}	87	26187
4	1.14×10^{-2}	404	3.75×10^{-4}	116	46864
5	5.68×10^{-3}	808	1.88×10^{-4}	261	210888

Table 4.2: Grid spacing and number of grid points in each direction and the total number of points for each resolution level.

are commonly initiated with either wall blowing and suction or a vibrating ribbon. Downstream of the excitation the disturbance amplitudes initially decay before they amplify in the unstable region of the boundary layer. In particular in low disturbance environments TS-waves can be an early stage of transition to turbulence (Fasel & Konzelmann, 1990). von Terzi *et al.* (2001) suggested using this case as a rigorous validation case for IMBMs due to the importance of an accurate representation of the near wall velocity gradients to simulate the instability growth rates correctly. The description of the case is divided into two parts: 4.1.2.1 introduces the numerical setup and 4.1.2.2, 4.1.2.4 and 4.1.2.3 present the results from the simulations.

4.1.2.1 Setup

In order to obtain a reference using the same code, simulations with body-fitted boundary conditions were conducted first. For this case a rectangular domain was specified with $0.258 < x < 8.2$ and $0 < y < 0.15$ using a Cartesian grid with uniform grid spacing for $0.258 < x < 3.34$ and employing stretching for the zonal characteristic outflow boundary condition. Nine different grid resolution levels have been considered spanning a factor of 16. The grid spacing in the streamwise direction and at the wall including the number of points in each direction and the total number of grid points are reported in table 4.2. In the wall normal direction the grid was stretched for $y > 0.0$ towards the freestream boundary. The stretching and the grid point distribution was specified as a fifth order polynomial function with non-zero coefficients for the odd exponentials. The function was mapping the index to a physical coordinate, i.e.

$$f: \ \text{index}_j \rightarrow \text{location}_y \, . \tag{4.4}$$

A Blasius boundary layer profile with $\delta^* = 5.6 \times 10^{-3}$ and $Re_{\delta^*} = 280.67$ was prescribed at the inflow using the integrated characteristic boundary condition suggested in Jones (2008). The Mach number was set to $M = 0.25$. At the freestream boundary a non-reflective characteristic boundary condition was employed. The boundary layer instabilities were initiated by hydrodynamic disturbances which were introduced into

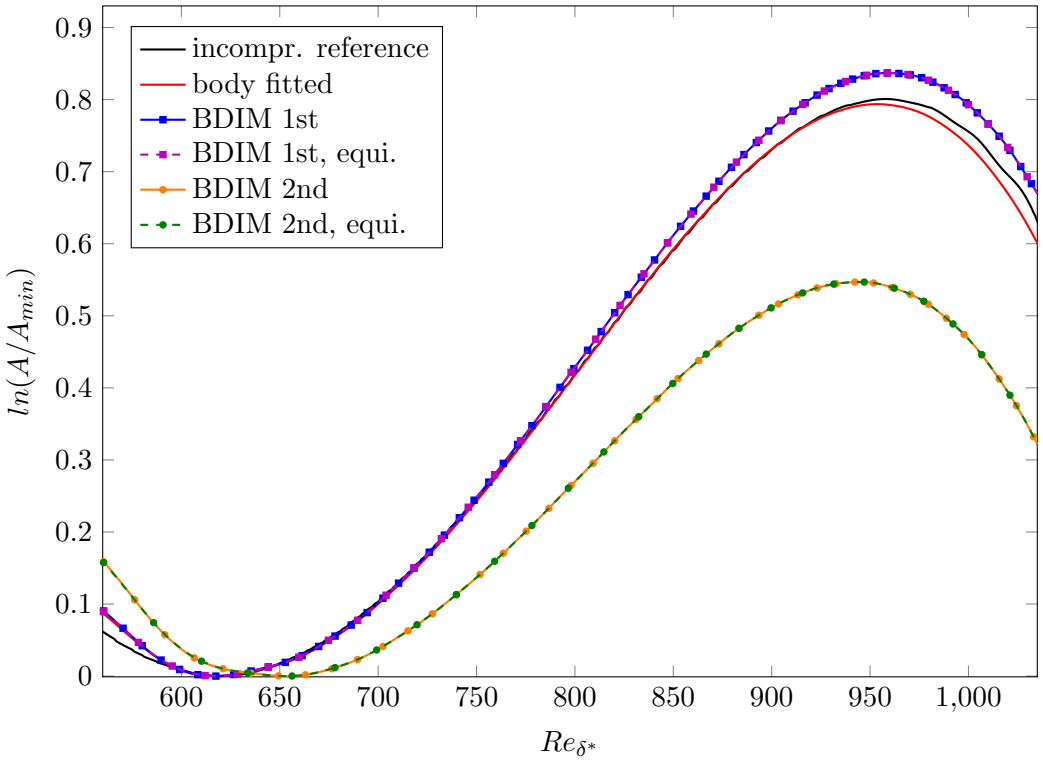

(a)

Figure 4.2: Maximum disturbance amplitude of the streamwise velocity component over the streamwise location comparing the results from simulations with body-fitted and immersed boundary conditions to the incompressible reference (Fasel & Konzelmann, 1990). The results of the BDIM framework calculated on an equidistant (equi.) grid in the wall normal direction are presented with dashed lines.

the boundary layer by periodic volume forcing through adding a source term to the momentum equation at $(x, y) = (0.4, 0.01)$. The forcing frequency was $f = 2.22$ with an amplitude of $A = 1 \times 10^{-1}$ for the volume force.

In order to run cases where the BDIM represents the wall, the grid in the wall normal direction was mirrored below the wall position. As the fifth order polynomial function specifying the grid distribution is a symmetric function, the grid metrics are continuous for an arbitrary number of derivatives. The space below the wall position was initialized with zero velocity and uniform density. The wall was placed on the first grid point in the wall-normal direction of the original grid. The timesteps in the BDIM and body-fitted simulations are the same, since the BDIM does not impose any additional timestep restrictions.

4.1.2.2 Results – Instability Growth Rates and Eigenfunctions

After the initial transient until the instability waves are statistically stationary data from two forcing periods was captured. For postprocessing the Fourier transform of a timeseries of the captured data was calculated. From the amplitudes of the streamwise velocity component u the maximum amplitude across the boundary layer was determined at each streamwise location and then normalized by the lowest amplitude of all streamwise positions. These disturbance growth rates are presented in figure 4.2 for resolution level 5 comparing the incompressible reference (Fasel & Konzelmann, 1990) with results employing body-fitted boundary condition with the code used in this work and the first and second order BDIM. It can be appreciated that the growth rate with the body-fitted boundary conditions is in excellent agreement with the incompressible reference. Minor deviations can only be identified downstream of the maximum amplitude. The first order BDIM yields good agreement in the initial stage of the disturbance growth. However, the peak amplitudes are slightly overestimated. The deviation is comparable to the differences of the ghost-cell method presented by Sandberg & Jones (2011) and used to represent TE serrations in direct noise computations in Jones & Sandberg (2012). The results from the second order BDIM are in poor agreement with all other cases and the amplitudes are significantly under predicted. Furthermore, the onset of the instability growth is shifted downstream. This is surprising as the second order correction indeed leads to an improvement in convergence and the results for the flow around a cylinder presented in section 4.1.1. To ensure that the poor performance is not due to grid stretching in the near-wall region, the simulations were repeated with an equidistant grid in the wall normal direction covering the whole domain. The results are also presented in figure 4.2 and show no appreciable difference to the stretched grid.

Figure 4.3 presents the disturbance amplitude of the streamwise velocity component as a function of the distance from the wall. The comparison between the BDIM and the body-fitted cases in figure 4.3a reveals that the amplitudes are under-predicted when using the BDIM as wall boundary condition. This is also true for the first order BDIM that overestimated the growth rates of the TS-waves in figure 4.2. However, the qualitative difference can be explained by the normalization with the minimum amplitude of all streamwise locations employed to calculate the data in figure 4.2, thus the over-prediction is relative to the minimum amplitude. The second order BDIM shows even lower amplitudes and as seen from figure 4.2 the amplitudes are not only absolutely under-predicted but also relative to the minimum amplitude. In figure 4.3b the same data is replotted but normalized with the maximum amplitude throughout the boundary layer profile. The qualitative and quantitative agreement of both the BDIM cases with the references is excellent for the inner and outer peak.

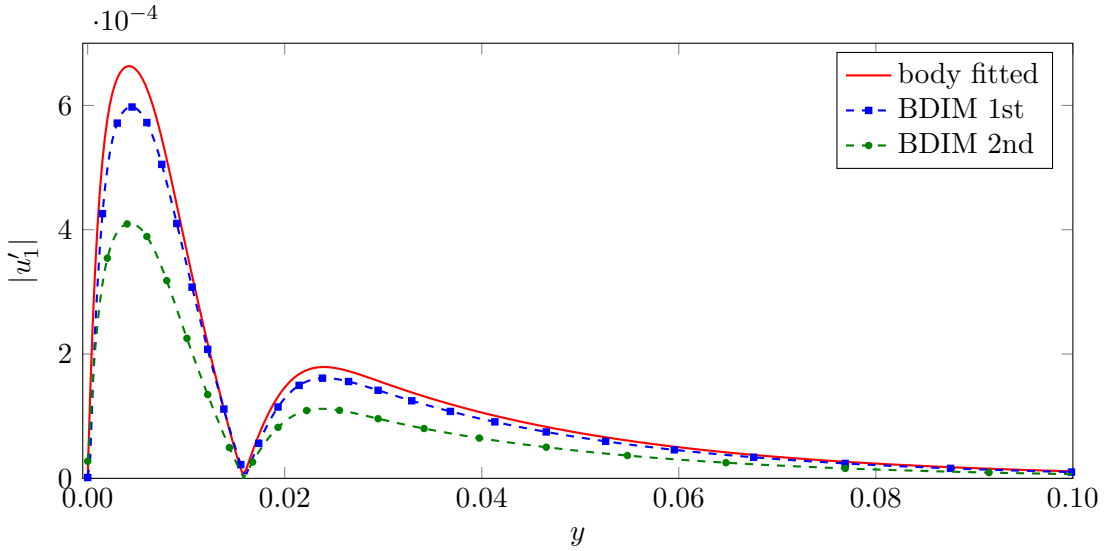

(a) unscaled disturbance amplitude

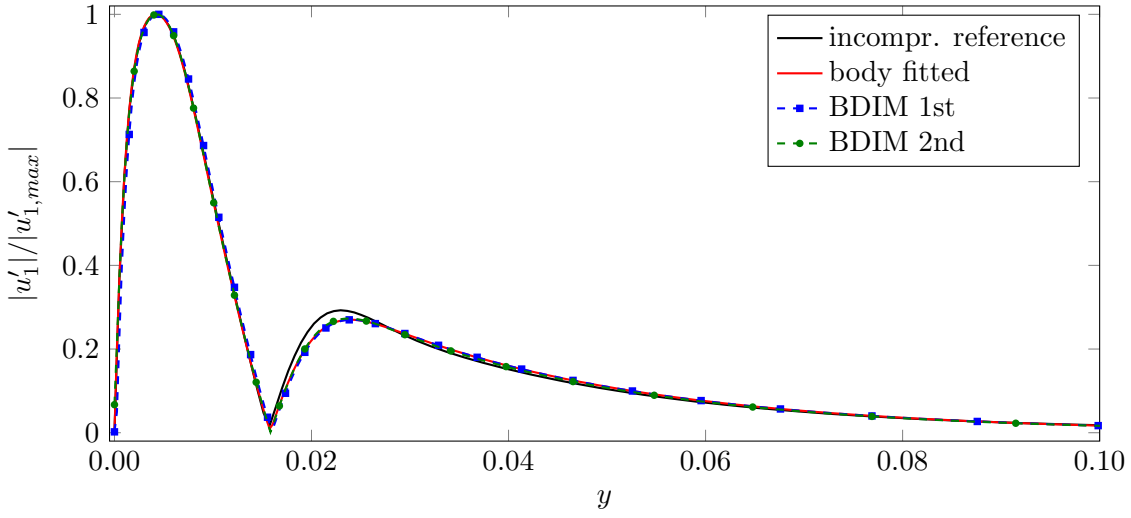

(b) disturbance amplitude normalized with maximum of the profile at this location

Figure 4.3: Disturbance amplitude of the streamwise velocity component as a function of the wall distance at the streamwise position $Re_{\delta^*} = 800$ comparing the results from simulations with body-fitted and immersed boundary conditions.

4.1.2.3 Results – Comparison of the Averaged Statistical Profiles

TS-waves are linear boundary layer instabilities which means it is assumed that the growth of disturbances only depends on the mean flow and but that there is no influence of the disturbances on the mean flow. Therefore, an examination of the mean flow should be able to explain differences observed in the instability growth rates and the poor performance of the second order BDIM. The near-wall velocity profiles are presented as a function of the wall normal coordinate normalized by the smoothing region half-width ϵ in figure 4.4. Furthermore the gradients in the wall normal direction are presented in the same plot as the growth of the instabilities depends on the exact representation of

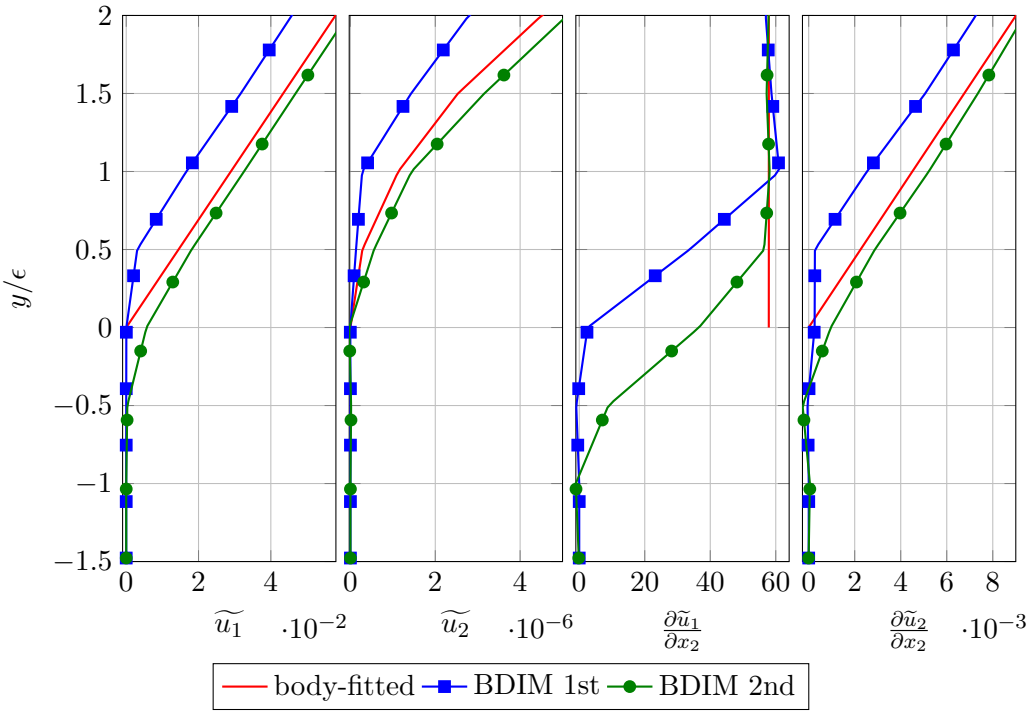

Figure 4.4: Profiles of the Favre averaged streamwise and wall normal velocity components $\widetilde{u_1}$ and $\widetilde{u_2}$, respectively, and their derivative in wall normal direction in the vicinity of the solid-fluid interface.

these quantities (von Terzi *et al.*, 2001). For the streamwise velocity profile it can be observed that the second order BDIM takes better advantage of the whole smoothing region $-1 < \epsilon < 1$ compared to the first order BDIM, which utilizes half of the region at best. As a result the first order BDIM leads to a shift of the velocity profile in the wall normal direction. Potentially an inward retraction of the actual surface location as suggested by Breugem (2012) could partly correct these deviations. In contrast to that, the second order BDIM leads to a reasonably good agreement with the body-fitted reference. The same general trends can be observed for the wall normal velocity component $\widetilde{u_2}$, albeit the transition in the smoothing region is less apparent due to the vanishing slope at at the wall. The derivative of the wall normal velocity $\frac{\partial \widetilde{u_2}}{\partial x_2}$ shows qualitatively the same trend as the streamwise velocity component. In contrast to the other quantities considered here, the profile of the streamwise velocity derivative $\frac{\partial \widetilde{u_1}}{\partial x_2}$ is not continuous at the wall. This can be clearly seen in the profile from the body-fitted simulation. The BDIM has to represent this discontinuity in a continuous way. For the first order BDIM it can be found that the transition takes place only in the second part of the smoothing region and leads to an overshoot outside the smoothing region. The second order BDIM shows a smooth representation of the discontinuity entirely within the smoothing region. It can be summarized that the additional derivative information allows the BDIM to take better advantage of the whole smoothing region and thereby represent the velocity profiles and even the discontinuity of the derivative more accurately.

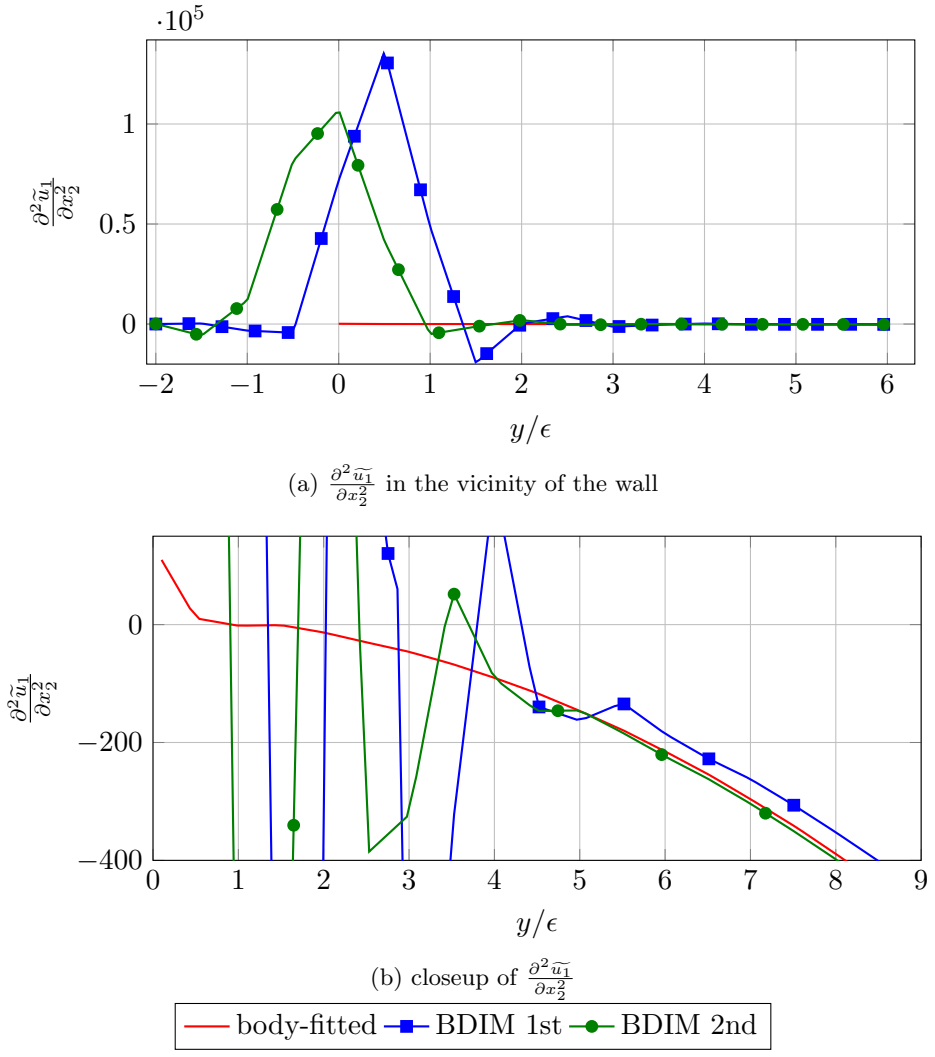

(a) $\frac{\partial^2 \widetilde{u_1}}{\partial x_2^2}$ in the vicinity of the wall

(b) closeup of $\frac{\partial^2 \widetilde{u_1}}{\partial x_2^2}$

Figure 4.5: Profiles of the second derivative in wall normal dirction of the Favre averaged streamwise velocity component $\frac{\partial^2 \widetilde{u_1}}{\partial x_2^2}$ comparing the results from the body-fitted simulation with the BDIM

The second derivative of the streamwise velocity component $\frac{\partial^2 \widetilde{u_1}}{\partial x_2^2}$ is considered in figure 4.5. The overview in the subfigure 4.5a shows that the BDIM leads to a very pronounced peak of $\frac{\partial^2 \widetilde{u_1}}{\partial x_2^2}$ at the location of the wall. This is not surprising as the discontinuity of the first derivative leads to a second derivative that is mathematically not defined with a value of infinity. The BDIM has to represent this discontinuity in a continuous way and therefore high values in $\frac{\partial^2 \widetilde{u_1}}{\partial x_2^2}$ are expected. For the first order BDIM framework the peak is offset towards the freestream by approximately 0.5ϵ, where ϵ is the smoothing region halfwidth, which is consistent with the shift towards the freestream of the profiles presented in figure 4.4. Moreover large overshoots to positive and negative values can be found. When the second order BDIM is employed the dominant peak is in perfect alignment with the surface of the wall and is reduced in comparison to the first order framework. Furthermore, the overshoots are smaller and more confined to the direct vicinity of the smoothing region. To allow a better comparison to the data from

the body-fitted case figure 4.5b shows a close-up of the near wall region. The body-fitted data features an inflection point one grid cell away from the wall where the analytical solution for the Blasius boundary layer would require that the inflection point is at the wall (Criminale *et al.*, 2003). Considering the first order BDIM, the overshoots reach approximately to a wall distance of 5ϵ. At greater wall distances the profile is offset towards the freestream as found for the profiles in figure 4.4 as well. The results are improved with the second order framework where the overshoots are reduced in amplitude and only reach to $y = 4\epsilon$. Further away from the wall the agreement is excellent.

Considering the significantly smoother and more accurate representation of the velocity profile and its first and second derivative at the wall when the second order BDIM is employed, the higher error in the growth rates in comparison to the first order framework is surprising. The cause of these deviations is not clear at this moment. It can only be speculated that the growth of the TS-waves depends on the precise value of the velocity gradient at the wall and the location of the inflection point. Both of them can inherently not be matched with an analytical solution within the smoothing region. With the help of linear stability theory it could be investigated if the differences in the mean velocity profiles are the cause for the difference in the instability growth rates or if their cause are dynamic effects, i.e. not related to the mean flow. However, the tools required for such an investigation are beyond the scope of this work.

4.1.2.4 Results – Formal Order of Convergence

To evaluate if the agreement of the second order BDIM with the references improves with higher resolution four refined cases were run. Together with a further four cases using coarser grids the formal order of convergence of the first and second order framework can be analysed. Figure 4.6 presents the deviation of the disturbance amplitude obtained from the BDIM to the body-fitted results using the highest resolution level in the L_2 and L_∞ norm in figure 4.6a and figure 4.6b, respectively, over the wall normal grid spacing. For reference, the first and second order slopes are plotted in addition. It is apparent that for the two lowest resolution levels the error is very high and indeed the analysis of the growth rates showed no "TS-wave like" behaviour. It should be mentioned, though, that the same was true using the body-fitted boundary conditions at these two resolution levels. Therefore, the simulations were not attempted with the second order BDIM framework. Apart from these two data points the agreement between first order slope and the data from the first order BDIM is very good. Thus, for the simulation of TS-waves the first order BDIM leads to a first order convergence in both norms considered here. The order of convergence is increased to second order when employing the derivative correction in the BDIM, i.e. the second order BDIM. However, the error level of these cases is significantly higher and they are comparable

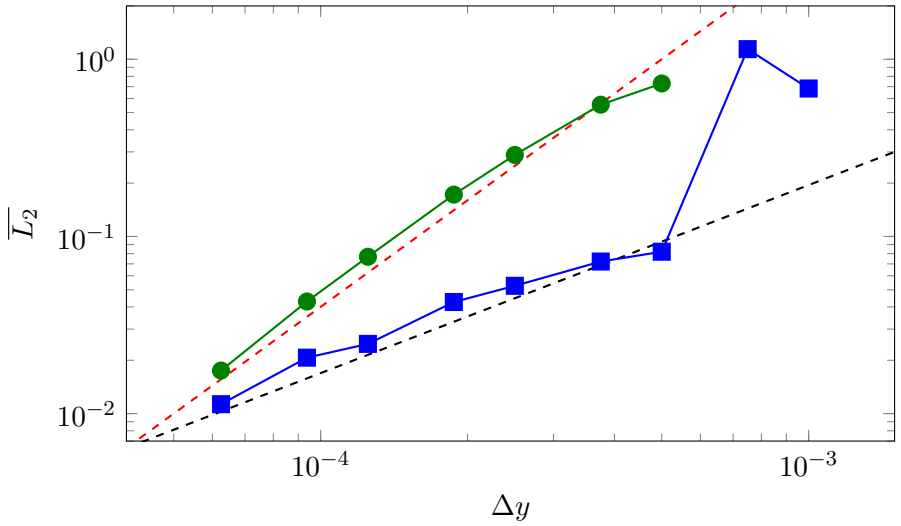

(a) Error in the L_2 norm of growth rate

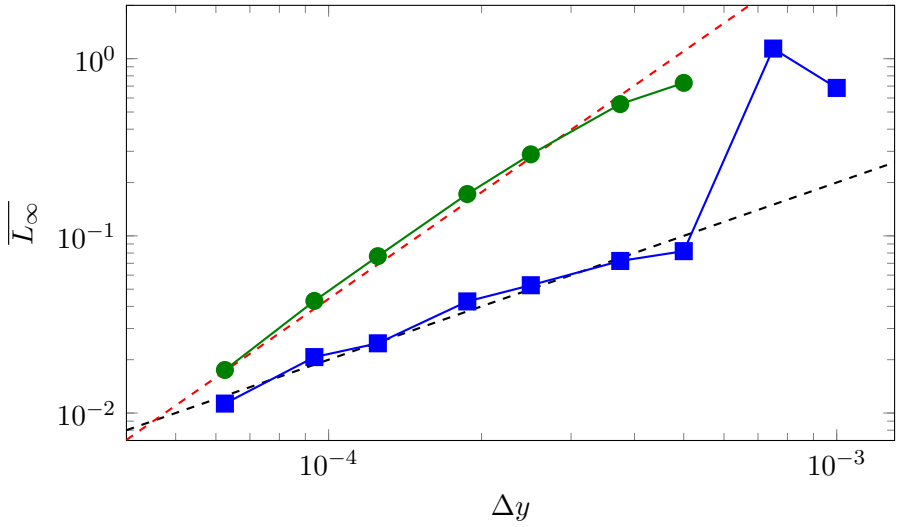

(b) Error in the L_∞ norm of growth rate

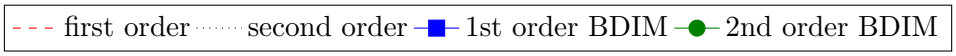

Figure 4.6: Formal order of convergence of the growth rates of Tollmien-Schlichting waves in the infinity norm for $650 < Re_\delta < 1025$

only for the highest resolution level. Thus, it can be concluded that the poor agreement with the references found in the previous section 4.1.2.2 can not be attributed to lack of resolution as the convergence of the second order BDIM is indeed second order.

4.1.3 Supersonic Oblique Wave Validation Case

In supersonic boundary layers three dimensional instabilities, also denoted oblique waves, become more important and are dominant at $M = 3$ (Mayer *et al.*, 2011). The accurate simulation of these instabilities does not hinge on the velocity gradient at the wall

location itself. However, an accurate representation of the near-wall thermodynamics is crucial in the supersonic flow case. Therefore the growth of viscous instabilities in a supersonic flat plate boundary layer at $M = 3$ is considered as a rigorous test case to assess the correct modelling of the thermodynamic fluctuations close to the wall. In high-fidelity direct noise computations this is an important aspect since the noise is calculated directly from the compressible Navier–Stokes equations.

Oblique waves are three dimensional instabilities that can lead to breakdown into turbulence in supersonic boundary layers. They are considered particularly relevant in low disturbance environments since they need very low disturbance thresholds to be initiated. The oblique breakdown features a linear, an early and a late non-linear regime (Mayer *et al.*, 2011). For the validation of the BDIM the focus is on simulating the linear regime. The description of the case is divided into two parts: 4.1.3.1 introduces the numerical setup, 4.1.3.2 assesses the accuracy of the BDIM and 4.1.3.3 presents the results from a convergence study.

4.1.3.1 Numerical Setup

The flow under consideration is a supersonic flat plate boundary layer at $M = 3.0$ and $Re = 1,578,102$. In order to trigger the instabilities the flow was disturbed close to the wall by adding a harmonic forcing term to the right hand side of the wall normal component of the momentum equation 2.2b in the second spanwise Fourier mode. The amplitude of the volume force was $A = 1.0 \times 10^{-3}$ and the frequency was $f = 12.558136$. The forcing was spread over a circular area in the $x-y-$plane, thus mimicking the effect of a vibrating ribbon. At the inflow boundary the integral formulation of the characteristic boundary condition (Jones, 2008) was used to prescribe a Blasius boundary layer profile with a Reynolds number, based on displacement thickness, of $Re_{\delta^*} = 273$. At the freestream and outflow boundaries non-reflective characteristic boundary conditions were applied.

For the body-fitted baseline reference case a rectangular Cartesian grid with $1.59172 \times 10^{-3} < x < 0.45598$ and $0.0 < y < 4.70223 \times 10^{-2}$ was employed. In the streamwise direction the 281 grid points were distributed equidistantly with $\Delta x = 1.623 \times 10^{-3}$ over the whole domain. In the wall normal direction the grid spacing stretched from $\Delta y = 3.51 \times 10^{-5}$ at the wall to $\Delta y = 1.644 \times 10^{-3}$ at the freestream boundary. The spanwise direction was discretized with a spectral method using two Fourier modes for a spanwise extent of $\Delta z = 0.0299817$.
In the validation case where the BDIM represents the wall boundary condition, 20 grid points were mirrored in the wall normal direction. As detailed in paragraph 4.1.2.1 and equation 4.4 for the TS-wave case, the grid point distribution was specified with a

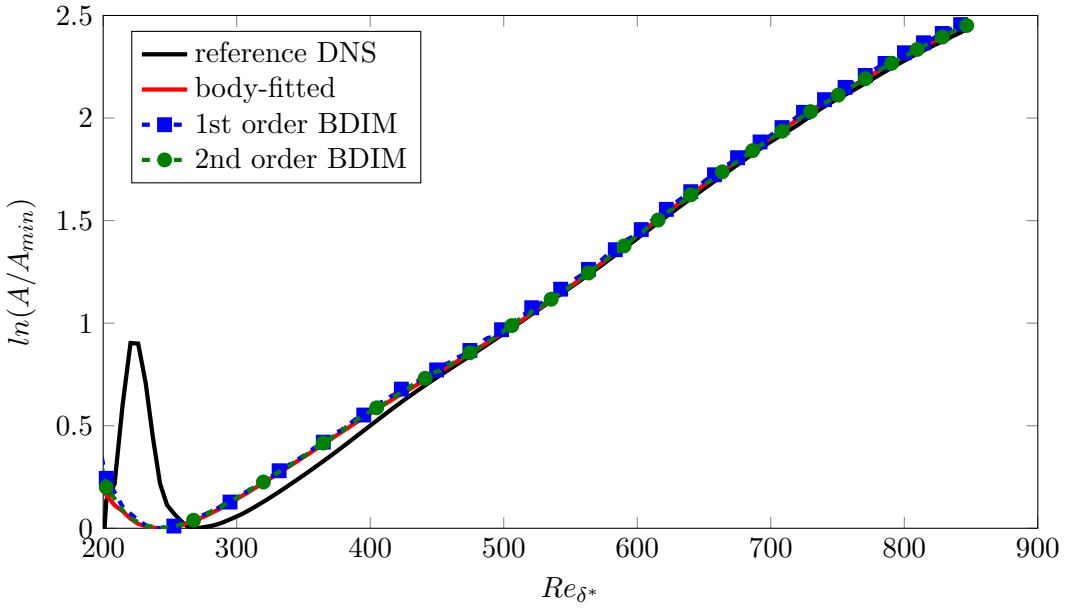

Figure 4.7: Amplitude of streamwise velocity disturbance as a function of the streamwise position comparing data from Husmeier *et al.* (2005) with simulations using the BDIM and body-fitted boundary conditions.

symmetric polynomial function. This ensures that the grid metrics of the mirrored grid are continuous at the wall location. The void below the original position of the wall was initialized with zero velocity and uniform density and temperature. The smoothing region half-width ϵ in units of wall-normal grid spacing in the simulations was $\epsilon = 2.0\Delta y$.

4.1.3.2 Results - Accuracy

After the initial transient, instantaneous snapshots of the flow field were gathered for two forcing cycles. From the temporal Fourier transform of the streamwise velocity component the maximum amplitude across the boundary layer was determined as a function of x and then normalized by the lowest amplitude of all streamwise positions during post-processing. Figure 4.7 compares the results obtained with the BDIM to represent the wall with data using body-fitted boundary conditions with the same code and a reference DNS (Husmeier *et al.*, 2005). It can be noted that there are slight differences between the reference Husmeier *et al.* (2005) and the body-fitted case in the region of the onset of the instability growth. These can be explained by the fact that the forcing was introduced differently in both cases. Overall it can be appreciated that both the first and second order BDIM reproduce the growth rates very accurately, but the second order BDIM is slightly closer to the reference.

In addition to the instability growth rate, the fluctuation amplitudes of the streamwise velocity u, the density ρ and the temperature T are evaluated in figure 4.8 as a function of the normalized wall distance η at $Re_{\delta*} = 700$. The amplitudes are normalized by

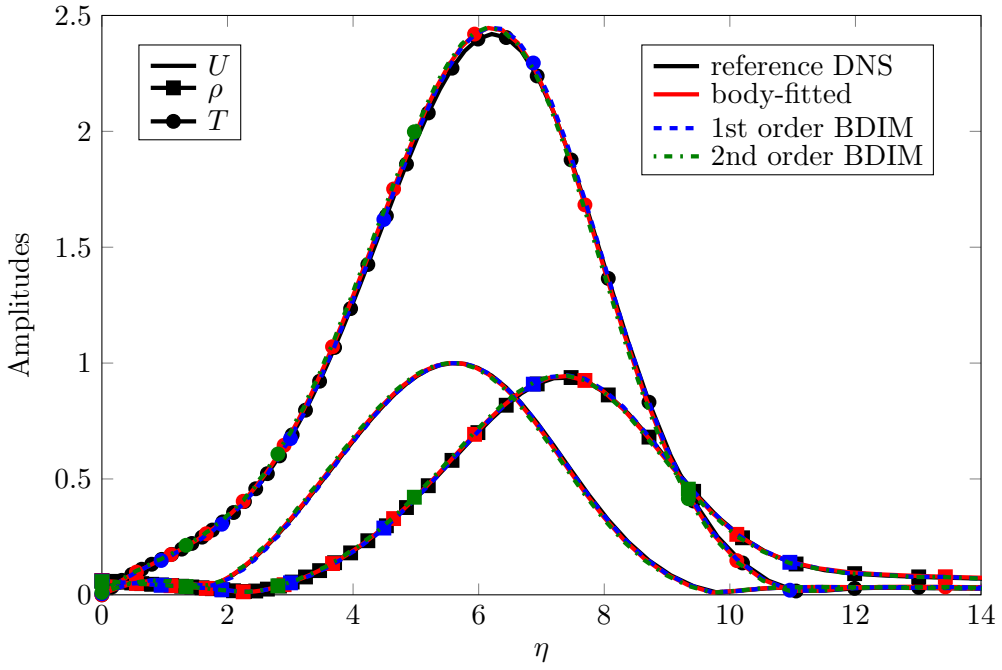

Figure 4.8: Amplitude distribution of perturbations of streamwise velocity U, density ρ and temperature T in the wall-normal direction at $Re_{\delta^*} = 700$ from the simulations using the BDIM in comparison to simulations with body-fitted boundary conditions and to the results from Husmeier et al. Husmeier *et al.* (2005). The wall normal distance y is represented with the similarity variable $\eta = y\sqrt{U/(\nu x)}$, where U is the streamwise velocity component, ν the viscosity and x the streamwise position. All amplitudes are normalized by the maximum of the velocity amplitude.

the maximum velocity amplitude. The velocity amplitude profile proves that the very good agreement between the BDIM and the references is not limited to the maximum amplitude of the velocity fluctuations as presented before. It also matches the shape of the profile along the wall normal direction perfectly. Furthermore, the fluctuations of the thermodynamic quantities density ρ and temperature T are computed very accurately. In addition, the normalization that was chosen shows that density fluctuations are almost as high as the velocity fluctuations and the temperature fluctuations are a factor of roughly 2.4 higher that the velocity fluctuations, thus underlining the importance of a good representation of the near wall thermodynamic quantities. Computing these quantities accurately even for low energies is crucial for direct noise computations.

Overall, the results show that the BDIM is capable of accurately representing highly sensitive instability growth adjacent to a wall in a three dimensional compressible flow.

4.1.3.3 Results - Convergence

A study with 4 additional resolution levels all together spanning a factor of 16 change in resolution was carried out in order to establish convergence of the instability growth

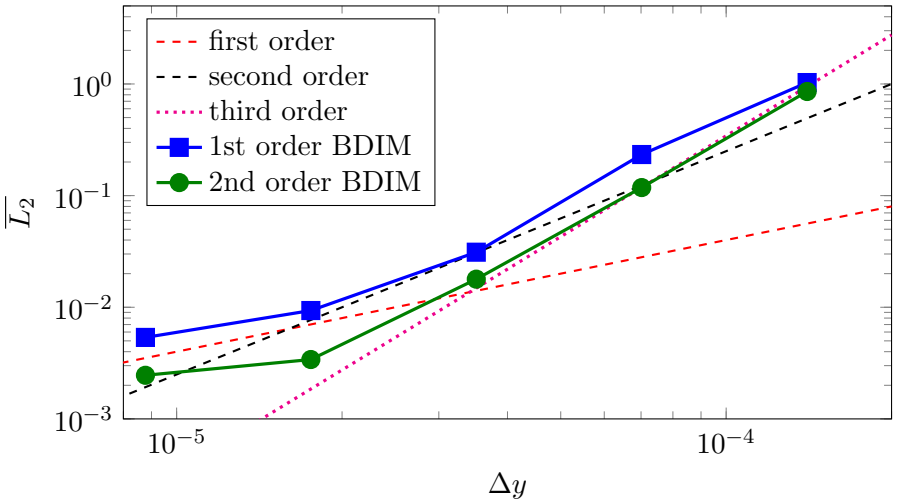

Figure 4.9: L_2 convergence of the instability growth rates comparing the first and second order BDIM. A first, second and third order slope are plotted as reference.

rate for this supersonic case. The results are compared employing the L_2 norm of the disturbance amplitude in the streamwise extent $300 < Re_{\delta^*} < 800$ relative to the body-fitted reference in Figure 4.9. The first order BDIM yields a convergence rate that varies between an order of 1.5 and 3 and tails off at the highest resolution. The second order BDIM shows a constant convergence rate that is estimated to be $2.5 - 3$. It also shows the tail-off at the highest resolution. Overall the error level is lower than in the first order case. From the visual inspection of the instantaneous flow field, the tail-off is most likely due to a shock downstream of the inflow.

4.1.4 Turbulent Boundary Layer

In many engineering applications featuring fluid flow with moving or stationary solid objects the flow is turbulent. In particular, aeroacoustic noise generation from the interaction of fluid flow with solid objects, such as turbulent interaction or trailing-edge noise, is very sensitive to an accurate representation of the physics in the near wall region. The fully turbulent flow over a flat plate is used to assess the accuracy of the BDIM in representing the near wall physics in the presence of a large range of temporal and spatial scales in combination with a relatively high velocity gradient discontinuity at the wall.

4.1.4.1 Numerical Setup

The domain for the turbulent boundary layer incorporated the streamwise range of $1073 < Re_\theta < 1595$ where Re_θ is the Reynolds number based on momentum thickness. The wall normal grid spacing was constant along the streamwise direction. When scaled with the local viscous units the maximum spacing was $\Delta y^+ = 0.97$. In the wall normal

direction the grid was stretched towards the freestream boundary over 90 grid points to $\Delta y^+ = 106$ at a distance of $20.6\delta^*$, where δ^* is the displacement thickness at the outflow. The grid spacing in the streamwise direction was uniform with maximum value of $\Delta x^+ = 18.0$ when scaled with the local viscous units. The spanwise domain width was $l_z = 5\delta^*$, which has been found sufficient in previous unpublished studies validating the code. A spectral method with 32 modes was used to discretize the domain width which yields a spanwise grid spacing of $\Delta z^+ = 8.13$, which is comparable to the resolution used in (Schlatter *et al.*, 2009). At the inflow time-dependant synthetic turbulent fluctuations were superimposed to a time-averaged mean turbulent velocity profile. To that end, random fluctuations were filtered using the digital filter method proposed by Klein *et al.* (2003) and extended to compressible flows by Touber & Sandham (2009). This method has been shown to result in good predictions of second order moments such as velocity fluctuations and integral turbulent length scales downstream of a development region with roughly 20δ length. The freestream and outflow boundary condition were both prescribed using characteristic boundary conditions. At the outflow the zonal approach was employed Sandberg & Sandham (2006).
When the BDIM was employed to impose the wall boundary condition 20 grid points were mirrored below the actual surface of the wall and initialized with zero velocity, uniform density and the wall temperature. As in the previous two sections considering boundary layer flows, the grid metrics are continuous at the wall location due to a symmetric polynomial function that defines the grid point distribution.

4.1.4.2 Results – Effect of Second Order Correction

One of the main challenges for immersed boundary methods that do not modify the discretization at the boundary by reconstructing the boundary is posed through the discontinuity of the velocity gradient $\frac{\partial u_1}{\partial x_2}$ at the wall. Figure 4.10 presents the streamwise velocity profile and its wall normal gradient in direct vicinity of the wall for the body-fitted and the two BDIM simulations. The kink and discontinuity in the velocity profile and its derivative, respectively, are immediately apparent in the body-fitted simulation. The overall trends are similar to the profiles considered in figure 4.4. However, due to the higher Reynolds number in this case the discontinuity in the wall normal derivative is higher. The results obtained with the first order BDIM show that the velocity profile is offset towards the free stream at all wall normal locations. Furthermore, the smoothing region of halfwidth $\epsilon = 2\Delta y$ is hardly used to transition from the governing equations of the solid body to the fluid. In contrast, the second order BDIM features a much smoother transition between the two sets of governing equations and also takes advantage of a larger fraction of the smoothing region. In that case the deviation in the velocity profile from the body-fitted reference is very small at the boundary of the smoothing region and can be neglected at greater wall distances.

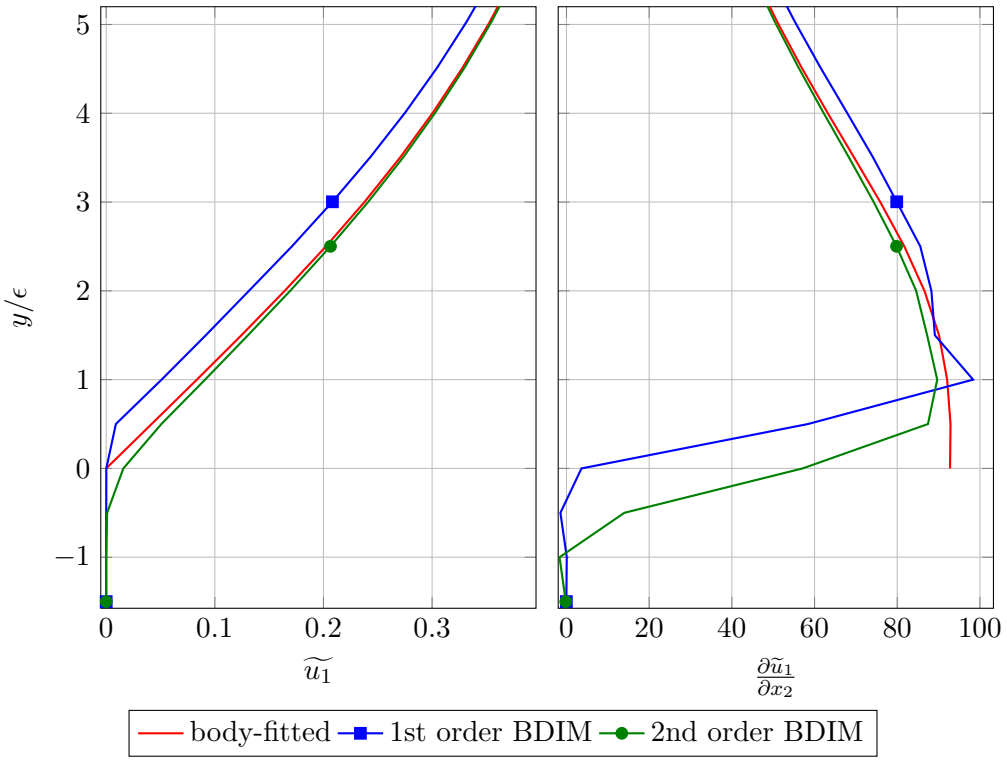

Figure 4.10: Streamwise velocity profile and its gradient in wall normal direction over the wall normal distances normalized by the smoothing region halfwidth ϵ in direct vicinity of the wall for the turbulent boundary layer flow at $Re_\theta \approx 1410$.

Considering the wall normal derivative of the streamwise velocity component $\partial u_1/\partial x_2$ profile it can be found that the first order BDIM introduces overshoots towards the solid body and the fluid. The maximum overshoot is at the fluid boundary of the smoothing region and significant deviations from the reference as well as an offset towards the freestream can be observed. When the second order correction is employed there is only a single overshoot towards the solid and the discontinuity is bridged in a considerably smoother fashion. The difference to the reference at the fluid boundary is fairly small and vanishes towards the freestream.

4.1.4.3 Results – Comparison to Literature and Viscous Scaling

Turbulent quantities are commonly normalized by viscous scales derived from the friction velocity $u_\tau = \sqrt{\nu \frac{\partial \widetilde{u_1}}{\partial x_2}}$ for which the wall gradient $\frac{\partial \widetilde{u_1}}{\partial x_2}$ is needed. From the discussion of figure 4.10 it is apparent that the value at the wall location will not yield any meaningful results when the BDIM is employed, which is a common difficulty for IMBMs. However, the value of $\frac{\partial \widetilde{u_1}}{\partial x_2}$ at the fluid boundary $y = \epsilon$ can be used as reasonable approximation for the value at the wall itself as for a zero pressure gradient boundary layer $\partial^2 \widetilde{u_1}/\partial y^2 = 0$ (Pope, 2000). Figure 4.11 compares the streamwise velocity profile scaled in viscous units from simulations obtained with our code and the incompressible reference data from Schlatter & Örlü (2012). It can be observed that the body fitted

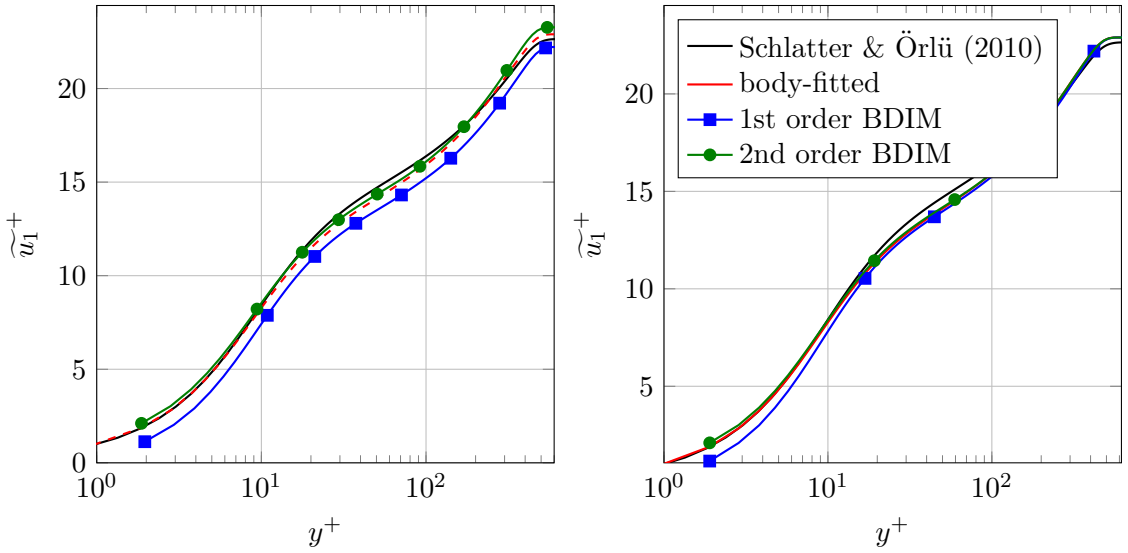

(a) normalization of the velocity profiles of the BDIM simulations calculated with $\frac{\partial \widetilde{u_1}}{\partial x_2}$ at $y = \epsilon$

(b) velocity profiles of the BDIM simulations normalized with $\frac{\partial \widetilde{u_1}}{\partial x_2}$ from body-fitted simulations

Figure 4.11: Turbulent boundary layer velocity profile scaled with viscous units comparing the BDIM to the body-fitted boundary conditions and the reference data from Schlatter & Örlü (2010).

simulation shows slight deviations from the reference in the wake region. This can be attributed to the short domain and inflow length of the current case and the relatively low Reynolds number of $Re_\theta = 1410$. However, for the purpose of a comparison of the effect of different wall boundary conditions, i.e. body-fitted and immersed boundary the agreement is reasonable. The comparison of the first order BDIM with the data from the body-fitted case confirms the initial observation of an offset in Figure 4.10. The effect of this offset leads to considerable deviations from the reference far into the outer region due to the wrong scaling derived from $\frac{\partial \widetilde{u_1}}{\partial x_2}$. However, when the data is scaled with the velocity gradient from the body-fitted simulations, as shown in figure 4.11b, the velocity profile matches the reference for $y^+ > 20$ but shows the same offset for $y^+ < 20$. In contrast to that, the second order BDIM shows very good agreement throughout the entire profile with some minor overestimates. As for the first order framework, the agreement of the case employing the second order correction with the reference improves further when the profile is scaled by viscous units calculated from the body-fitted simulation.

Figure 4.12 presents Favre averaged velocity fluctuation profiles scaled in viscous units. The comparison of the body-fitted Schlatter & Örlü (2012) data again shows some minor differences in particular for the streamwise component σ_{11}. This is due to the reasons noted earlier and for the sake of assessing the BDIM approach the agreement is seen as sufficiently good. The offset in the data obtained with the first order BDIM is prominent in all components and besides the offset all amplitudes are underestimated. The second order framework improves the offset considerably, as already seen for the velocity profile.

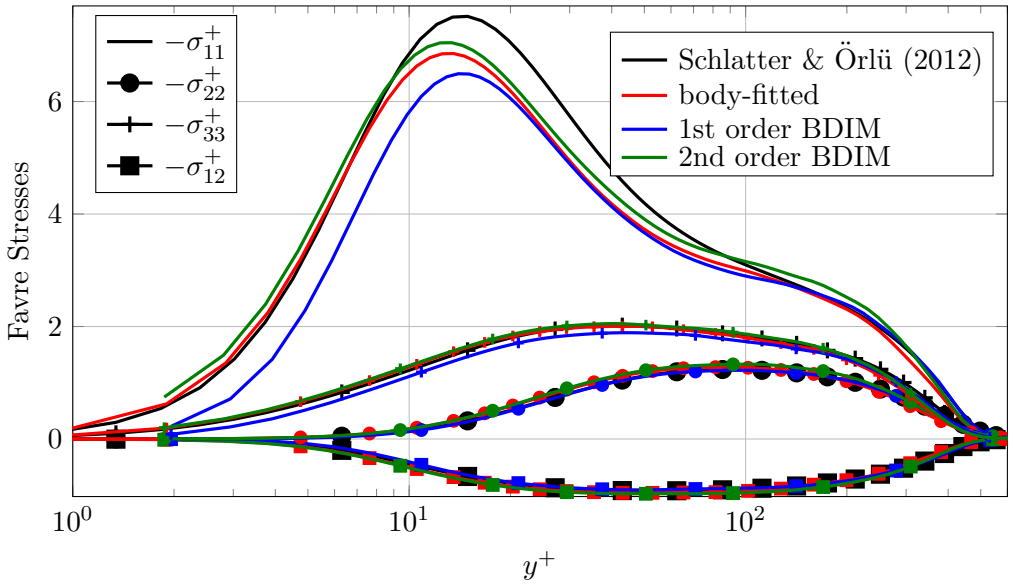

(a) normalization of the velocity profiles from the BDIM simulations calculated with $\frac{\partial \widetilde{u_1}}{\partial x_2}$ at $y = \epsilon$

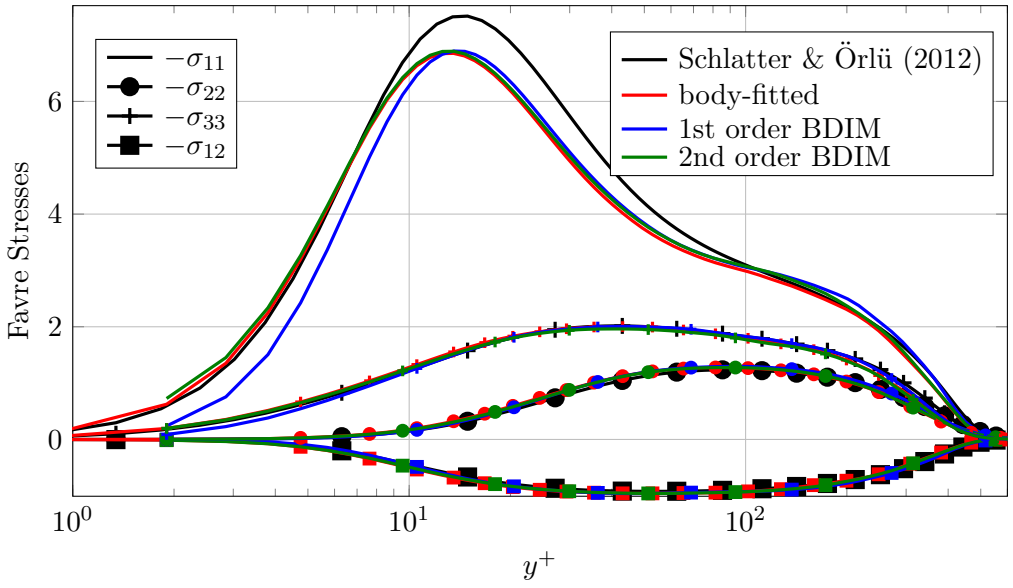

(b) profiles from the BDIM simulations normalized with $\frac{\partial \widetilde{u_1}}{\partial x_2}$ from body-fitted simulations

Figure 4.12: Turbulent boundary layer velocity fluctuations profiles scaled with viscous units comparing the BDIM to the body-fitted boundary conditions and reference data from literature (Schlatter & Örlü, 2012)

The shape of the profile as well as the amplitude is captured well for all components except the streamwise velocity fluctuations σ_{11}, where the amplitude is slightly overestimated. However, when the data obtained from both BDIM simulations is scaled with viscous units of the body-fitted case, as presented in figure 4.12b, the deviation in the peak amplitude of the σ_{11} component vanishes and overall good agreement is obtained with the reference data. For this scaling the amplitude of σ_{11} also matches the reference closely. However, between the wall and peak production the amplitude of the first order

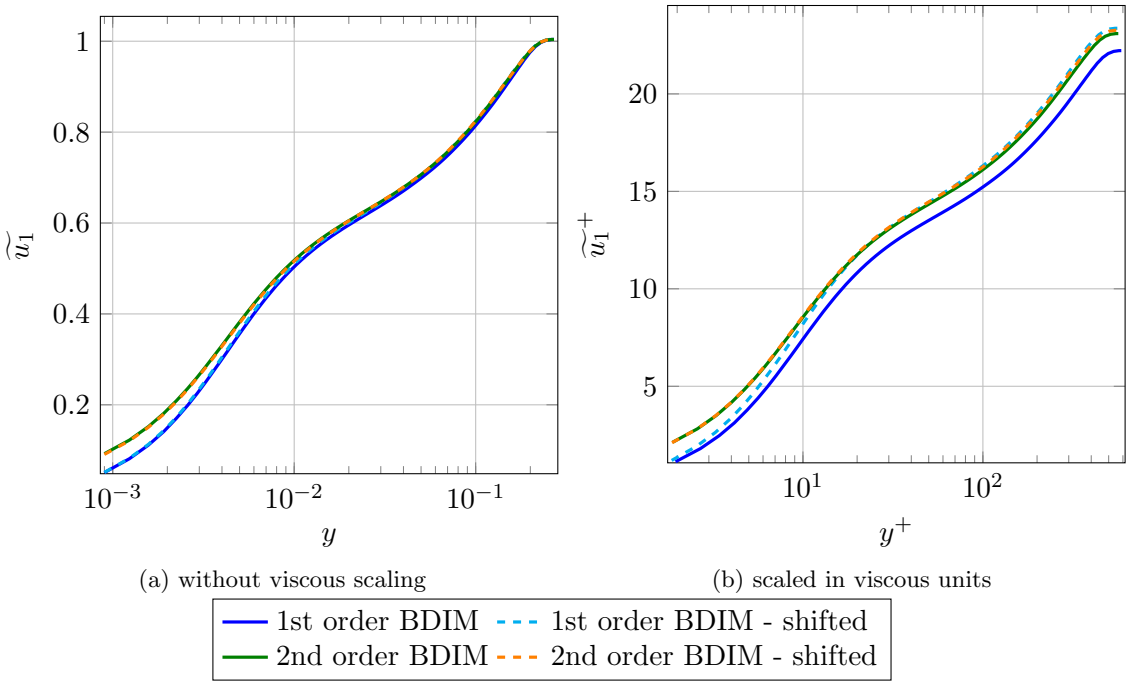

(a) without viscous scaling (b) scaled in viscous units

Figure 4.13: Comparison of the streamwise velocity profile without scaling (a) and in viscous units (b) of the two BDIM approaches with and without offset in the wall normal direction

BDIM framework is still underestimated.

In conclusion, this data shows that the velocity gradient at the wall can be modelled with the value at $y = \epsilon$ when using the BDIM to calculate the viscous scaling. When the first order framework is employed the friction velocity u_τ is underestimated which leads to an offset of all profiles towards the freestream. Overall, the second order framework leads to excellent agreement with the reference data.

4.1.4.4 Results – Modelling the Location of the Body Surface

In the previous paragraphs the surface of the wall when employing the BDIM was coinciding with the underlying mesh in order to assess the accuracy of the framework when representing a wall adjacent to a turbulent flow. However, the purpose of the BDIM is to represent bodies immersed in fluid flow that do not necessarily coincide with the underlying grid. Therefore two additional simulations have been run where the surface of the plate has an offset in the wall normal direction and is located between the first two grid points of the original grid, i.e. $y^+ \approx 0.5$ instead of $y^+ = 0$.

In the following comparison of the cases with and without an offset of the wall location the y and y^+ coordinate were always corrected accordingly. Figure 4.13a compares profiles of the streamwise velocity component without viscous scaling. It is apparent that the profiles of the shifted and non-shifted cases are barely distinguishable. Despite the fact that the offset to the original surface location is small, deviations could be identified when the wall normal coordinate was not corrected according to the offset. This indicates that the mean velocity profile can be represented very accurately even when the surface does not coincide with the underlying grid with an accuracy that is of the order of half a grid point.

In figure 4.13b the same profiles are compared in viscous units. The data from the first order BDIM framework reveals differences between the cases with the two different surface locations from a wall distance of $y^+ \approx 3$ which is becoming more and more pronounced towards the freestream. In contrast to that, the profiles obtained with the second order BDIM are still in perfect agreement. That means that the offset increases the uncertainty in the prediction of the velocity gradient at the wall when using the first order BDIM. Indeed the estimated u_τ (calculated from data at $y = \epsilon$) changes from $u_\tau = 0.045$ without offset to $u_\tau = 0.043$ whereas it does not change in the first two significant digits when employing the second order BDIM with $u_\tau = 0.43$.

The velocity fluctuations for the same cases are presented in figure 4.14. For the unscaled fluctuations shown in figure 4.14a the most prominent differences between the two surface positions can be found at the peak of the streamwise component σ_{11} and are more prominent in the first order framework. When the data is scaled with viscous units as shown in figure 4.14b all differences vanish for the second order BDIM, showing perfect agreement in shape and amplitude of the velocity fluctuations. At the same time the differences increase for the first order case as was already observed for the averaged velocity profile.

Overall the BDIM is capable of modelling the exact surface location very accurately as shown with the mean and fluctuations of the velocity profiles. When the first order framework is employed the velocity gradient at the wall is predicted less accurately and the streamwise velocity fluctuations are overestimated. In contrast, the second order framework shows perfect agreement for both surface locations. Most likely the difference between the first and second order results can be attributed to the fact that the first order framework hardly uses the full extent of the smoothing region, as mentioned in the discussion of figure 4.10.

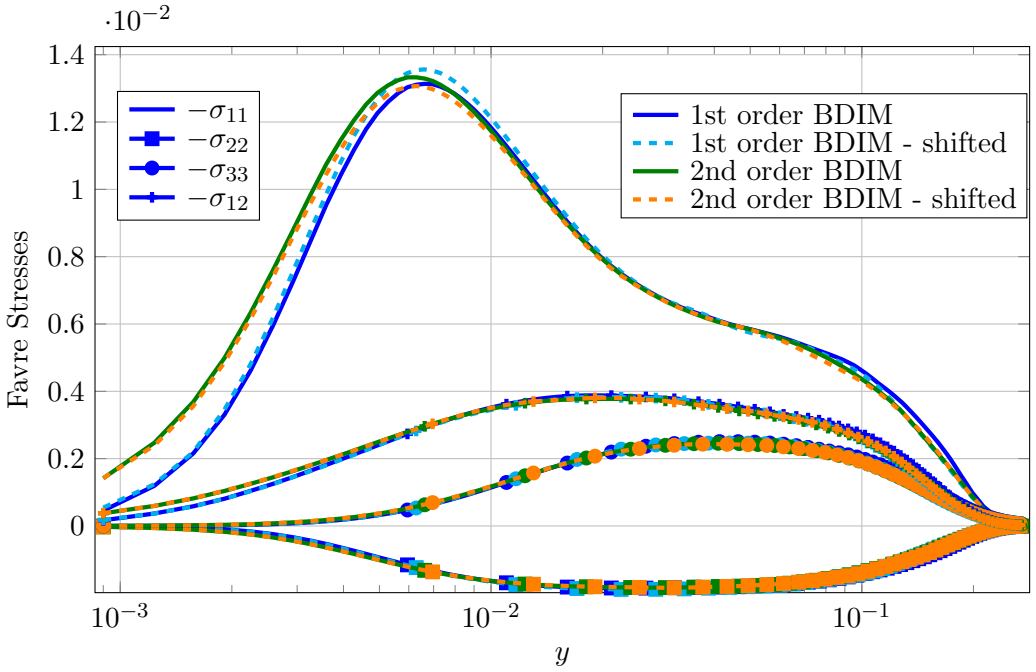

(a) favre averaged velocity fluctuations without scaling

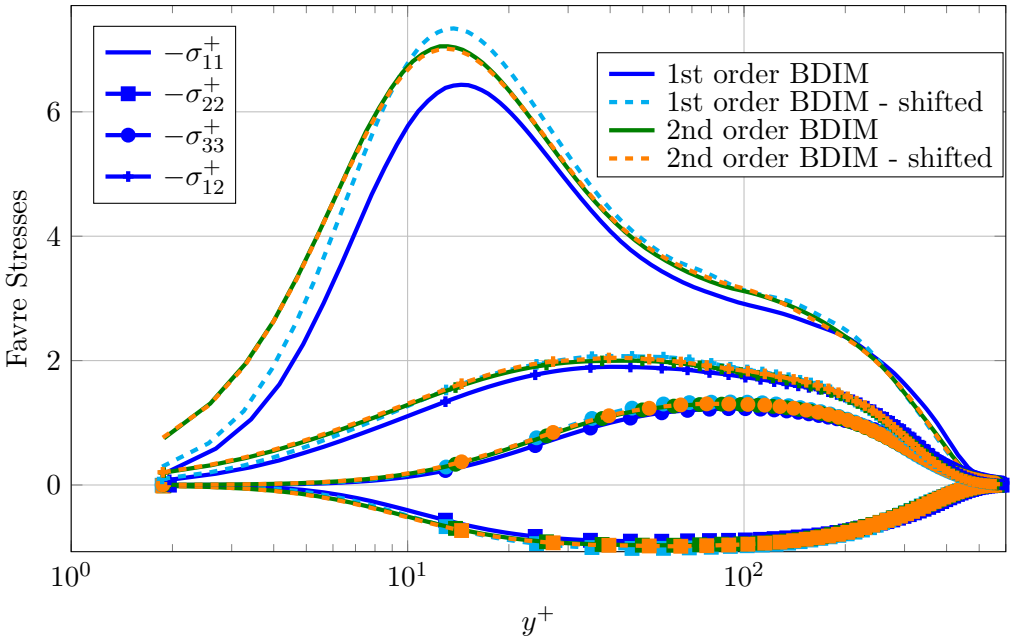

(b) favre averaged velocity fluctuations in viscous scaling

Figure 4.14: Favre averaged velocity fluctuation profiles scaled comparing results with and with out offset in wall normal direction when using the BDIM.

Thus, it can be concluded that the BDIM can be used to accurately represent a wall when wall bounded turbulence is considered. It was shown that the second order correction improved the results considerably. This can be attributed to the much better representation of the discontinuity present in the velocity gradient at the wall. In addition, the exact location of the plate surface can be represented very accurately leading to a “sharp like” modelling of the surface.

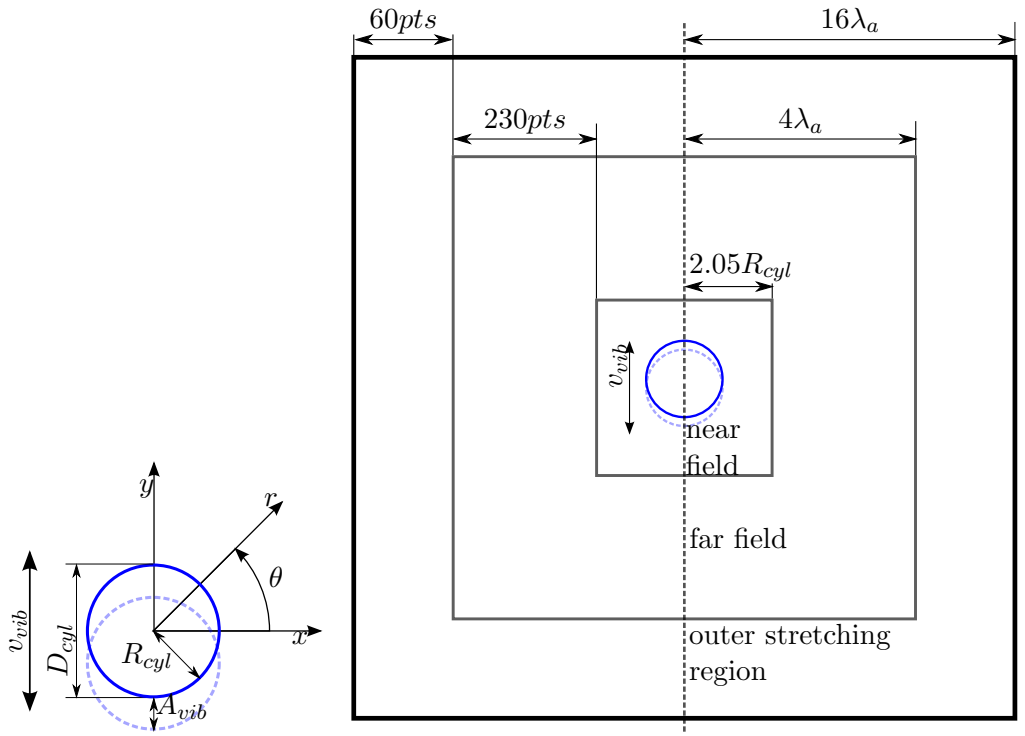

(a) Nomenclature for the physical problem under consideration

(b) Topology of the grid including the different resolution levels.

Figure 4.15: Introduction of the nomenclature for the physical problem and the grid.

4.1.5 Noise Radiation of a Vibrating Cylinder

A great advantage of compressible direct numerical simulations is that the generation of flow noise can be investigated without any further modelling as the relevant physical mechanisms are incorporated in the governing equations, i.e. the hydrodynamic and acoustic field are solved simultaneously. The use of the BDIM in such simulations enables the consideration of noise generation by flow interaction with moving objects such as the simulation of TE noise from an airfoil or a flat plate featuring an elastic TE. Therefore, this section focusses on the BDIM's capability to represent the acoustic noise generation of a moving body. The noise radiation from a transversely oscillating cylinder in a medium at rest, i.e. a freestream velocity of $U_\infty = 0$, is a test case that evaluates this capability and offers an analytical solution to compare to. Furthermore, the acoustic field is not superimposed with a hydrodynamic field. The description of the case is divided into two parts: 4.1.5.1 introduces the numerical setup and 4.1.5.2 presents the results from the simulations.

4.1.5.1 Numerical Setup

The cylinder is considered to have an infinite extension in the spanwise direction, hence the problem can be analysed by considering the two dimensional cross-section. Figure 4.15a shows a sketch of the vibrating cross-section with the coordinate system and the nomenclature. Assuming a harmonic vibration of the cylinder the displacement w_{vib} from the original position can be expressed by

$$w_{vib} = \frac{A_{vib}}{j}\, e^{j\omega_{vib}t}\,, \tag{4.5}$$

which is assumed to be a purely translational motion in the $y-$direction. The vibration amplitude A_{vib} was set to 0.05 and the cylinder's diameter $D_{cyl} = 2R_{cyl}$ was set to unity. This results in a vibration amplitude of 5% of the diameter. The non-dimensional vibration frequency was $f_{vib} = \omega_{vib}/2/\pi = 0.03$. Taking the temporal derivative $\dot{w}_{vib}$ of equation 4.5 leads to the velocity of the cylinder v_{vib}

$$\dot{w}_{vib} = v_{vib} = A_{vib}\,\omega_{vib}\, e^{j\omega_{vib}t}\,, \tag{4.6}$$

which results in a maximum velocity of $\max(|v_{vib}|) = 9.42 \times 10^{-3}$ with the parameters mentioned above. The Mach number M was assumed to be unity. As the freestream velocity U_∞ is zero, the Mach number can be interpreted as the non-dimensional speed of sound. The choice of the value for the Mach number M and frequency f_{vib} determines the acoustic wave length λ_a and therefore also the compactness ratio D_{cyl}/λ_a of the noise source. Since a compact vibrating cylinder is a weak source of noise, the vibration frequency f_{vib} had to be chosen such that the noise level in the far field was above machine accuracy. The resulting acoustic wave length is $33.\overline{33}$ which results in a compactness ratio of $D_{cyl}/\lambda_a = 0.03$.

The cylinder's cross section was discretized with a Cartesian grid that is symmetric with respect to the $x-$ and $y-$ axis. In figure 4.15b, the topology of the computational domain and the grid is presented as a schematic. For a compact cylinder, i.e. $\lambda_a\ D_{cyl} \ll 1$ the main challenge is to incorporate and resolve both the acoustic near and far field in the computational domain. In the near field close to the cylinder all the length scales in the sketch are normalized by the cylinder's diameter D_{cyl} since this is what governs the resolution. As indicated in figure 4.15b, the area around the cylinder is surrounded by $1.05\,R_{cyl}$ of the same grid spacing, before the grid is stretched with a cosine function to the outer grid spacing. Furthermore, this is the region where the resolution will be altered.

The relevant length scale in the far field is the acoustic wave length λ_a, thus all dimensions in the far field are normalised by it. One acoustic wave-length was resolved by 20

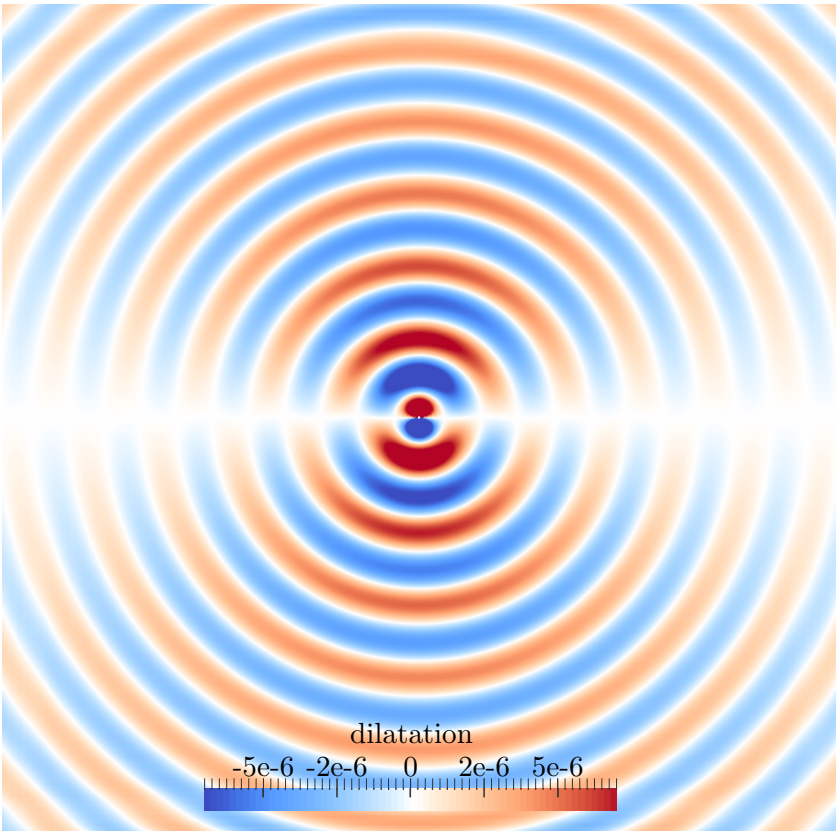

Figure 4.16: Instantaneous dilatation contours at an arbitrary instant of time from simulation W33R1 with $\lambda_a = 33.\overline{33}$ and a smoothing region for the BDIM of $\epsilon/\Delta x = 1.3$.

grid points. This is a comparatively high resolution, however it was employed to avoid excessive ratios of the grid spacing between the near and far field. Since the oscillating cylinder is the only noise source and its strength is rather low, even minor reflections from the domain boundaries were found to contaminate the acoustic field. In order to damp the outgoing acoustic waves the numerical boundary conditions were supported by grid stretching towards the boundaries resulting in a resolution of two grid points per acoustic wave length at the boundaries.

All the dimensions and grid number counts shown in figure 4.15b refer to the "inner" boundary before the transition region to the new resolution level occurs. At all four boundaries non-reflective characteristic boundary conditions were employed. The domain was initialized uniformly with density and temperature and zero velocities.

4.1.5.2 Results – Accuracy

Figure 4.16 shows a snapshot of the dilatation levels to give an initial overview of the acoustic field. The dipole character of the sound radiation from the oscillating cylinder can be clearly identified by the high dilatation levels aligned with the cylinder motion

in the $y-$ direction. Along the axis perpendicular to that direction the radiated noise vanishes. The contour levels show distinct wave fronts resulting in a very clean acoustic field with no evidence of any numerical reflections from the domain boundaries.

After the initial qualitative assessment of instantaneous simulation results a more rigorous statistical evaluation will follow. To that end, the time averaged data from the simulation will be compared to the analytical solution of the radiation problem. With the assumption of an inviscid medium and linear acoustics, i.e. small amplitudes, the analytical solution for this radiation problem is (Blackstock, 2000)

$$p^{'} = Re\left\{\left|-j\rho_{\infty}v_{vib}cos(\theta)\frac{H_1^{(2)}(kr)}{M\,H_1^{(2)'}(kR_{cyl})}e^{j\omega_{vib}t}\right|\right\}, \tag{4.7}$$

where $H_1^{(2)}$ is a Hankel function of the second kind and first-order accurate and $H_1^{(2)'}$ its derivative. Furthermore, ρ_{∞} is the mean density of the medium at rest (Blackstock, 2000). The near field can be approximated by (Blackstock, 2000)

$$p_{rms} = \frac{1}{\sqrt{2}}\left|-j2\pi f_{vib}\rho_{\infty}v_{vib}R_{cyl}^2M^2\frac{1}{r}\right| \quad , \tag{4.8}$$

and the far field approximation is (Blackstock, 2000)

$$p_{rms} = \frac{1}{\sqrt{2}}\left|2\pi^2 f_{vib}^{1.5}\rho_{\infty}R_{cyl}^2v_{vib}M^{1.5}\frac{1}{\sqrt{r}}\right| \quad . \tag{4.9}$$

For an initial assessment of the performance of the BDIM in this application a resolution of $\Delta x = D_{cyl}/160$. Figure 4.17 compares the sound pressure level as a function of the radial distance of the two simulations with the analytical solution. The data was extracted along the radial direction aligned with the cylinder's motion. Thus, the figure shows the decay of the acoustic pressure fluctuations as a function of the distance from the cylinder's center in the main radiation direction. The range is chosen such that the acoustic near and far field are both included. In addition to the analytical solution the near and far fields approximations are presented showing the two principal dependencies of the pressure fluctuations $p_{rms} \sim 1/r$ and $p_{rms} \sim 1/\sqrt{r}$ for small and large values of r (Morse, 1948). It can be appreciated that the data obtained from the numerical simulation qualitatively match the analytical references closely in all regions. Quantitatively the simulations employing the BDIM agree reasonably well with the reference but overestimate the sound pressure level by 0.53dB for the first order BDIM and 0.29dB for the second order BDIM at this resolution level of $\Delta x = \Delta y = D_{cyl}/160$.

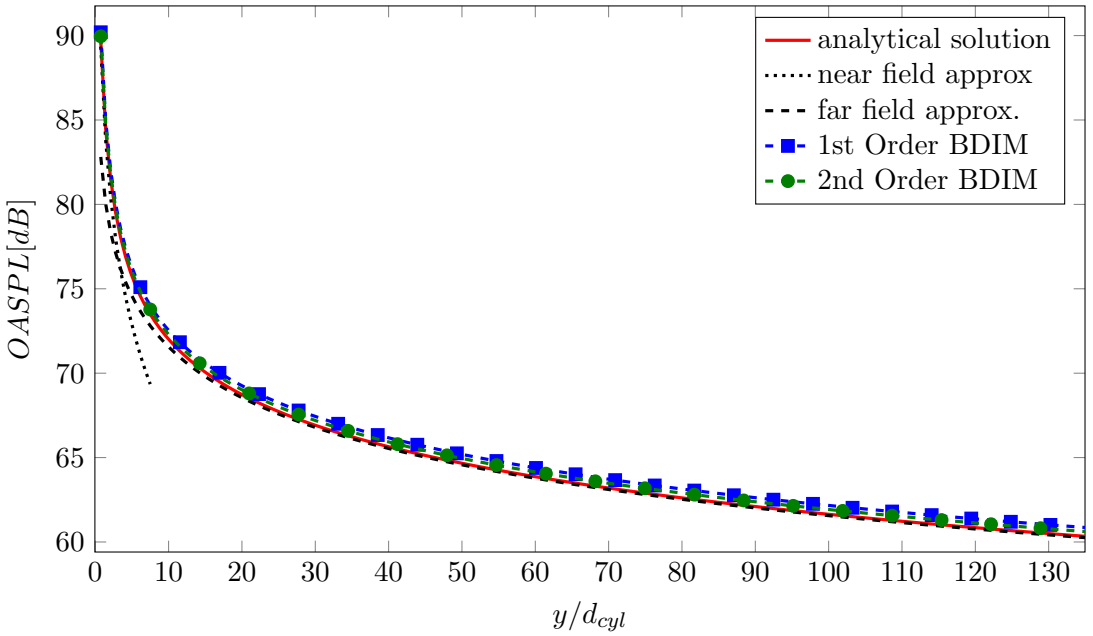

Figure 4.17: Comparison of the overall sound pressure level SPL over distance y/D_{cyl} in the direction of the body motion between analytical solution and data from a simulation using the BDIM. The range covers $1.2R_{cyl} < y < 4\lambda_a$ which includes the near and far field and the approximations of the analytical solution for the respective range.

After the statistical evaluation of the results in the radial direction the overall sound pressure level of this resolution level is compared to the reference in the circumferential direction at a given distance from the origin. Figure 4.18 shows the directivity plot comparing the three data sets at a distance of $r = 2\lambda_a$. The dipole type directivity pattern that was also found in the instantaneous snapshot in figure 4.16 can be clearly identified. It can be appreciated that the shape of the directivity pattern simulated by the BDIM is in excellent agreement with the analytical reference. As in the radial direction the amplitudes of the two simulations employing the BDIM agree reasonably well with the reference but slightly overestimate the noise level.

4.1.5.3 Results – Convergence

Table 4.3 compares the averaged deviation from the analytical reference along the main radiation direction for the first and second order BDIM for different resolution levels. The deviation from the analytical solution is a factor of 1.39 to 1.92 higher when the first order BDIM is employed compared to the second order. The formal order of convergence of the data presented in table 4.3 is visualized in Figure 4.19. It is obvious that the first and second order BDIM converge with the same rate of approximately one. The major difference between the two is the level of the deviation, as discussed before. The fact that both cases yield the same rate of convergence is not surprising. As shown with the results from the turbulent boundary layer in Figure 4.10, the main effect of the second

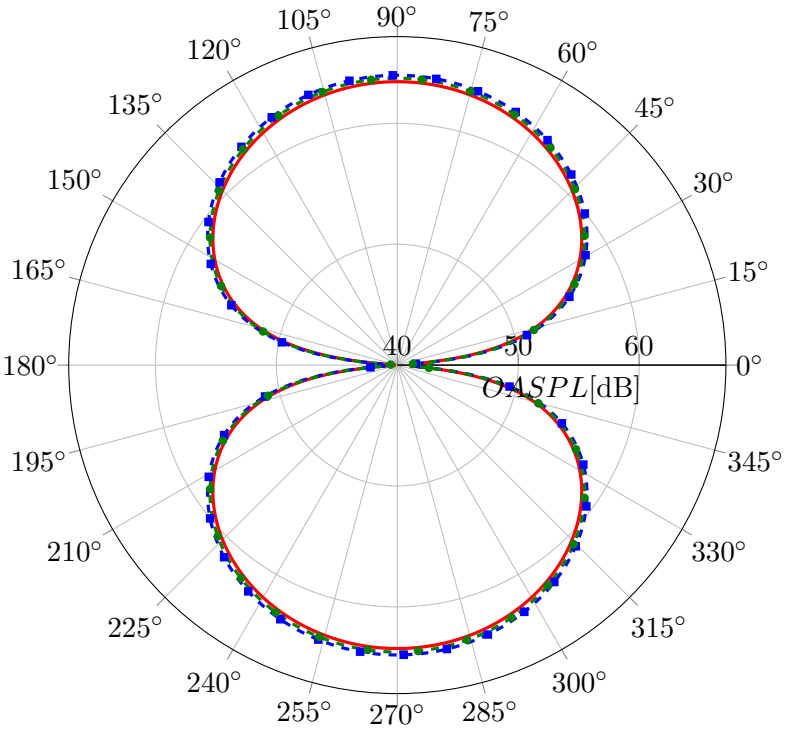

Figure 4.18: Directivity plot for overall sound pressure level at $r = 2.1\lambda_a$ comparing the analytical solution with the simulation results using the BDIM.

N_{pts}/D_{cyl}	$A_{vib}/\Delta x$	1st Ord BDIM $\Delta OASPL$[dB]	2nd Ord BDIM $\Delta OASPL$[dB]
20	1	2.91	1.64
40	2	1.64	0.88
80	4	0.92	0.48
160	8	0.53	0.29
320	16	0.34	0.21
640	32	0.25	0.18

Table 4.3: Summary of deviation from the analytical reference for different resolution levels using the first and second order BDIM .

order correction is the improved representation of the discontinuity in the wall velocity gradient in the wall bounded shear flow. In the current case considering an oscillating cylinder in a medium at rest shear is only non-zero in for angles not aligned with the main radiation direction and the values are very small.

For the highest resolution a tail off can be observed for both cases. This is not the case when the data is referenced to the highest resolution case and instead of the analytical reference. This indicates that the tail off is not due to boundary conditions but that the simulation converges to a different solution as is also suggested by the constant offset found in the previous discussion. The most likely reason for that is the assumption of

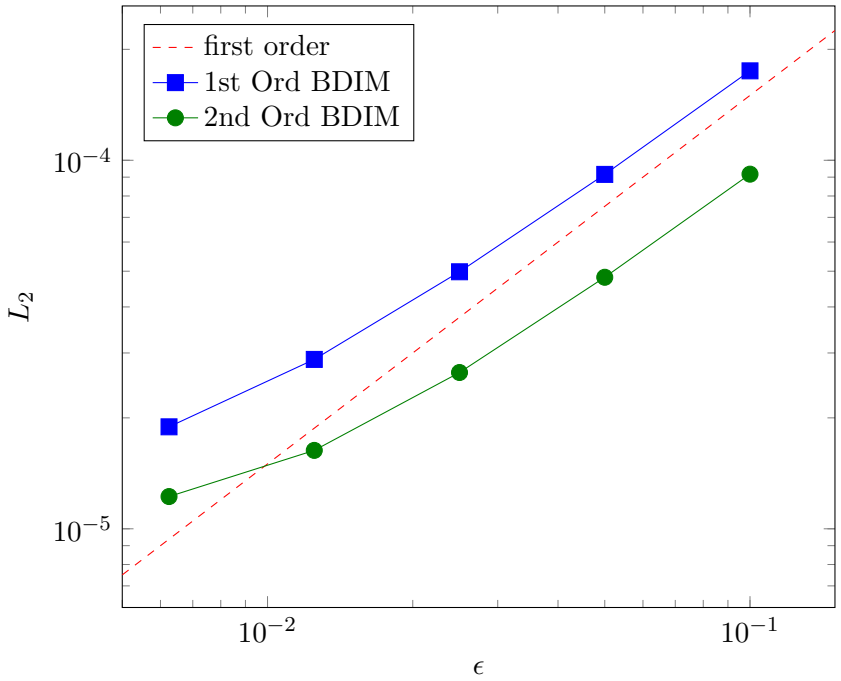

Figure 4.19: Convergence of the pressure fluctuations relative to the analytical reference over the kernel half-width ϵ for the first and the second order BDIM.

an inviscid fluid in the derivation of the analytical solution. However, the simulations do have a finite viscosity. An additional test simulation showed that when the viscosity is increased by two orders of magnitude the deviation between the analytical solution and the simulated result decreases to $\Delta OASPL = 0.47$dB on the $N_{pts}/D_{cyl} = 80$ grid using the second order framework. When viscosity was reduced by two orders of magnitude this deviation grew to $\Delta OASPL = 1.72$dB on the same grid and with the same method. It is speculated that the action of viscosity adds an additional component of fluid acceleration tangential to the translation direction.

In summary, the overall agreement with the analytical reference is excellent considering the very low energies that are involved in this acoustic test case. This validation case demonstrates that the BDIM is an appropriate method to perform high-fidelity simulations featuring noise radiation from moving bodies.

4.1.6 Summary of the Findings

This chapter assessed the accuracy and convergence of the BDIM framework with very challenging test cases of high relevance for high-fidelity and direct noise simulations. It was shown that the second order correction not only increases the convergence rate when the grid is refined but also improves the results. In particular, the discontinuity of the streamwise velocity gradient $\frac{\partial \widetilde{u_1}}{\partial x_2}$ in the wall normal direction is represented significantly

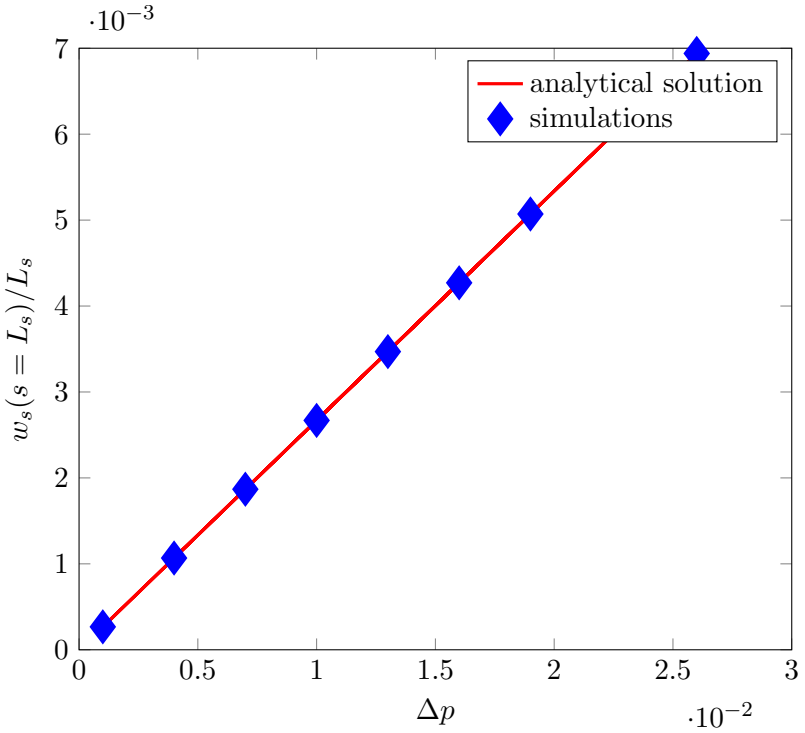

Figure 4.20: Comparison between simulated steady state deflection at the free end $w_s(s = L_s)$ normalized by the length of the structure L_s of the length and the analytical solution for different pressure loadings Δp. The structural parameters were $E_s I_s = 6.5 \times 10^{-3}$ and $\rho_s = 400$.

more accurately and smoother with the second order framework. Despite the smoothing region that is employed to represent the solid body immersed in fluid a "sharp-like" representation of the actual wall position was found for a wall normal offset of half a grid point. Furthermore it was demonstrated that the BDIM is a capable of representing moving bodies in aeroacoustic simulations. For simulation of TS-waves, poor agreement of the second order BDIM with the reference was found despite a significantly smoother and more accurate representation of the base flow compared to the first order framework.

4.2 Validation of Structural Solver

The newly implemented structural solver was validated independently of the fluid solver. The reference data was obtained from the analytical solution for the Euler-Bernoulli beam theory. As initial test case a steady state solution for a prescribed constant pressure load was considered under the steady state condition, equation 2.15 simplifies to

$$0 = \Delta p - E_s I_s \frac{\partial^4 w_s}{\partial s^4} \,. \tag{4.10}$$

This equation can be integrated analytically with four integration constants that need to be determined. At the clamped end, the deflection and its slope are zero and at

the free end bending moments and transverse forces have to vanish as they cannot be supported. These requirements result in the following set of boundary conditions:

$$w_s\Big|_{s=0} = 0,\ \frac{\partial w_s}{\partial s}\Big|_{s=0} = 0,\ \frac{\partial^2}{s^2}\Big|_{s=L_s} = 0,\ \frac{\partial^3 w_s}{\partial s^3}\Big|_{s=L_s} = 0\,. \tag{4.11}$$

Using these boundary conditions, it is possible to evaluate the four integration constants. Hence, the deflection at location s under the steady and uniform load can be expressed with

$$w(s) = \frac{\Delta p\, s^2(6L_s^2 - 4L_s s + s^2)}{24E_s I_s}\,. \tag{4.12}$$

The largest deflection occurs at the free end for $s = L_s$ and can be expressed with

$$w_s(L_s) = \frac{3\Delta p\, L_s^4}{24E_s I_s}\,, \tag{4.13}$$

which is a linear function in Δp.

In order to force the time dependent simulation to a steady state, an additional viscous damping term $-c_d\, \partial w/\partial t$ was included on the right hand side of equation 2.15. The $\partial w/\partial t$ term was evaluated with values from the preceding timestep. This causes a lag in time of the damping term. However, as this is only a tool to achieve a steady state, and the dynamic behaviour is not important for this testcase, such a lag is reasonable.

Figure 4.20 shows the averaged deflection for the quasi-steady state after 1.5×10^6 timesteps. The damping constant c_d was time dependent and varied from $c_d = 5 \times 10^{-5}$ at the beginning to $c_d = 5 \times 10^{-7}$ at the end. This allowed for the adaptation of the damping depending on the amplitude of oscillations around the mean value. At the end of the simulations with different pressure loadings minor oscillations could still be observed. Therefore, an averaged value over the last 1×10^5 timesteps was used in figure 4.20. The bending rigidity and density parameters of the structure in this validation case were set to $EI = 6.5 \times 10^{-3}$ and $\rho_s = 400$, respectively. The results presented in figure 4.20 show very good agreement with the analytical solution. The deviation between simulations and analytical solution for all loads is 0.28%.

The previous results show that the model represents the deflection as a response to an external force accurately in the limit of steady state. However, when coupled to the unsteady fluid simulation, the dynamic behaviour is very important and vibrations are expected to occur. The unsteady properties of the implemented model are evaluated by the response to a prescribed initial deflection of the beam. The shape of the initial deflection was a superposition of the first six bending modes, where the maximum amplitude $A_{max,j}$ of each mode j was decreased as $A_{max,j} = \frac{A_{glob}}{2j}$ beginning from the global maximum amplitude A_{glob}. The free vibrations that follow the initial deflection

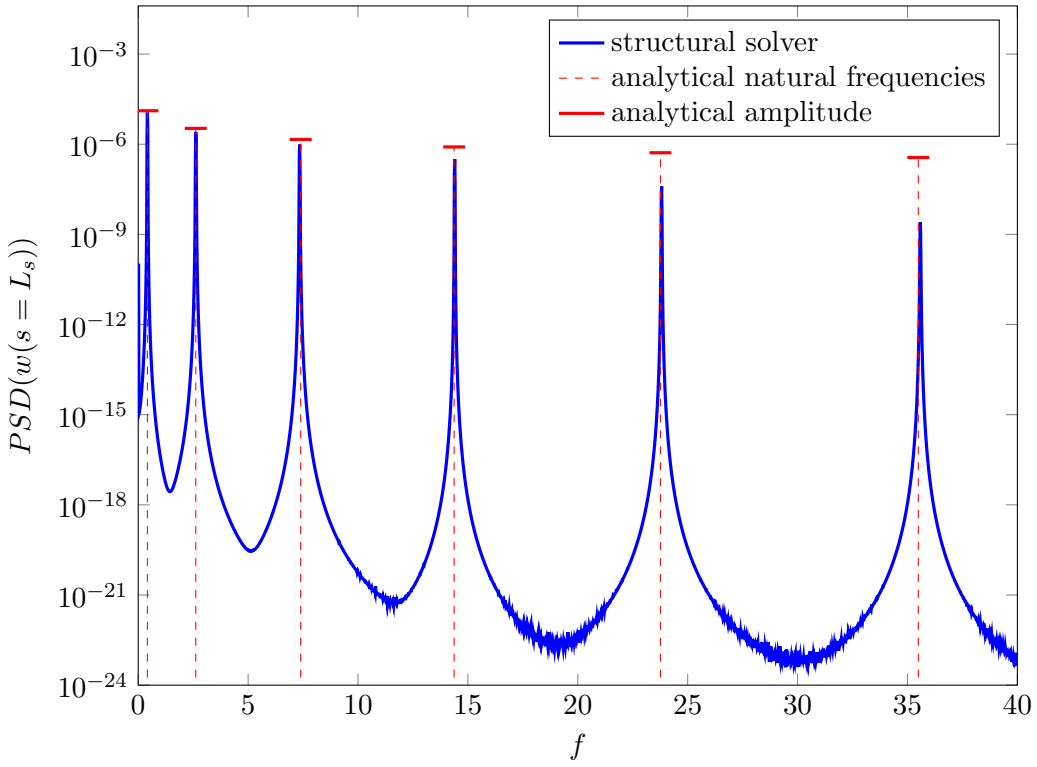

Figure 4.21: Comparison of natural frequencies and amplitudes obtained from the structural solver compared to the analytical solution. The vertical dashed lines indicate the value of the natural frequency and the horizontal lines the amplitude.

were sampled. During postprocessing, the time history of the deflection at the free end was then converted to a spectral power density.

Figure 4.21 compares this power spectral density from the simulation to the analytically calculated natural frequencies, employing equation 2.18, indicated by the vertical dashed lines. The overall agreement for the values of the natural frequencies is very good. The amplitudes of the different modes were calculated from the initial condition and are validated in addition. The agreement of the simulation results and the analytical reference is very good for the first three modes. For higher modes the deviation is increasing. However, in the coupled simulations the excitation frequency from the pressure loading will be within the range of the first three natural frequencies. Hence the results show that the implemented model is suitable to represent an elastic TE extension in a fluid-structure interaction simulation.

Chapter 5

Trailing-Edge Noise from an Airfoil at Angle of Attack

This study investigates the effect of an elastic flat plate extension on the acoustic noise radiation of a NACA0012 airfoil profile at angle of attack AoA=5° with two dimensional simulations. Firstly, the influence of the TE extension itself is assessed in section 5.1. Secondly, elastic TE extensions using two different material parameter sets will be compared to the rigid case in section 5.2

5.1 Effect of a Rigid TE Extension

In most studies found in the literature where TE noise reduction through serrations is considered the TE of the airfoil profile itself is not modified. Instead, a flat plate extension with a serration profile is attached to the TE (Oerlemans *et al.*, 2009; Gruber *et al.*, 2010*a*,*b*, 2011; Chong *et al.*, 2011; Moreau *et al.*, 2012*a*; Sandberg & Jones, 2011; Jones & Sandberg, 2012; Arina *et al.*, 2012; León *et al.*, 2016). Only relatively few studies are available for so-called non-insertion type serrations Chong *et al.* (2012, 2013*a*). Therefore, the effect of TE elasticity will be studied employing elastic TE extensions and this section will investigate how the rigid TE extension influences the flow around the airfoil.

5.1.1 Computational Setup

The domain under consideration for this study features the cross-section of a NACA0012 airfoil at angle of attack AoA=5°. In order to discretize the geometry a body-fitted C-mesh is employed around the airfoil. The overall grid topology is illustrated in figure 5.1 showing two blocks: the C-mesh type block for the airfoil which has two interfaces with

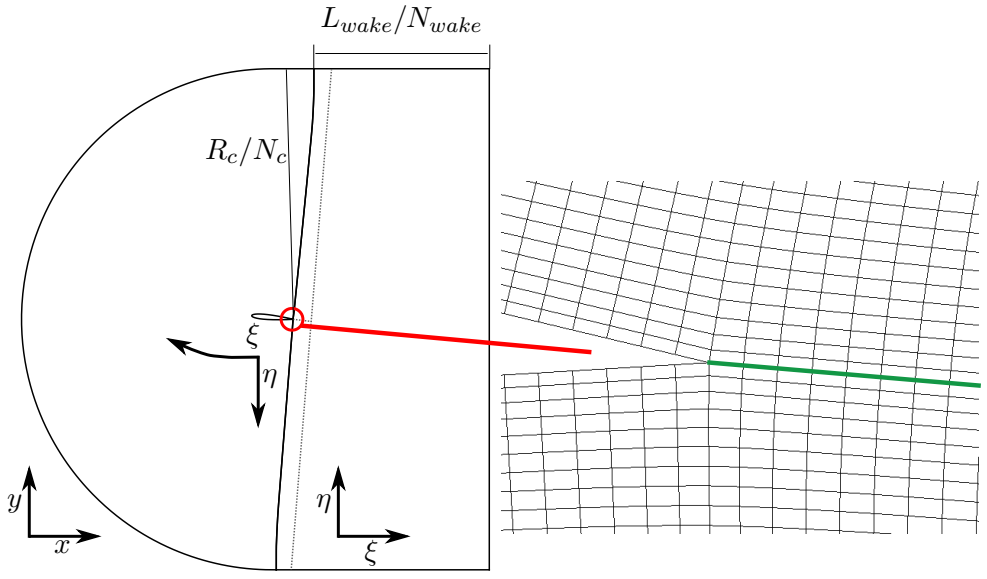

Figure 5.1: Schematic of the computational setup with two blocks employing a C-mesh and a wake block. The actual number of grid points and dimensions can be found in table 5.1. The green line in the close up of the TE indicates the extension of 10% chord length represented by body-fitted boundary conditions. The directions ξ and η indicate the directions of the grid indices. The directions of the physical coordinate system are given with x and y with the origin at the TE point.

L_{wake}/N_{wake}	$R_c/N_{c\xi}$	$\Delta\eta$ at LE	$\Delta\eta$ at TE	$\Delta\xi$ at LE and TE
5.0/752	7.25/1066	2.428×10^{-4}	3.771×10^{-4}	1×10^{-3}

Table 5.1: Spatial and grid dimensions of the airfoil setup. $N_{c\xi}$ is the number of grid points on the surface of the airfoil. L_{TE} and N_{TE} are the thickness and the number of grid points of the TE, respectively. The definition of the other parameters can be found in figure 5.1. Furthermore the wall grid spacings at the leading-edge (LE) and TE are given.

the block used to discretize the wake. Due to the airfoil geometry the grid metrics are not continuous over these interfaces. In order to avoid numerical oscillations from these metric discontinuities characteristic interface conditions as presented by Kim & Lee (2003) are employed to couple the flow information between both blocks.

The TE was considered to be infinitely sharp, as shown in the close up of figure 5.1. To study the effect of the extension the wake block is split in the vertical direction at the TE location for the length of the extension, which is 10% of the chord. This length is in the range of typical lengths used for serrated TE's in literature (Chong *et al.*, 2010; Jones & Sandberg, 2012; León *et al.*, 2016). The resulting 4 block topology is indicated by the grey dashed lines in figure 5.1. This allows the application of body-fitted boundary conditions at the newly created block boundaries which represent the extension.

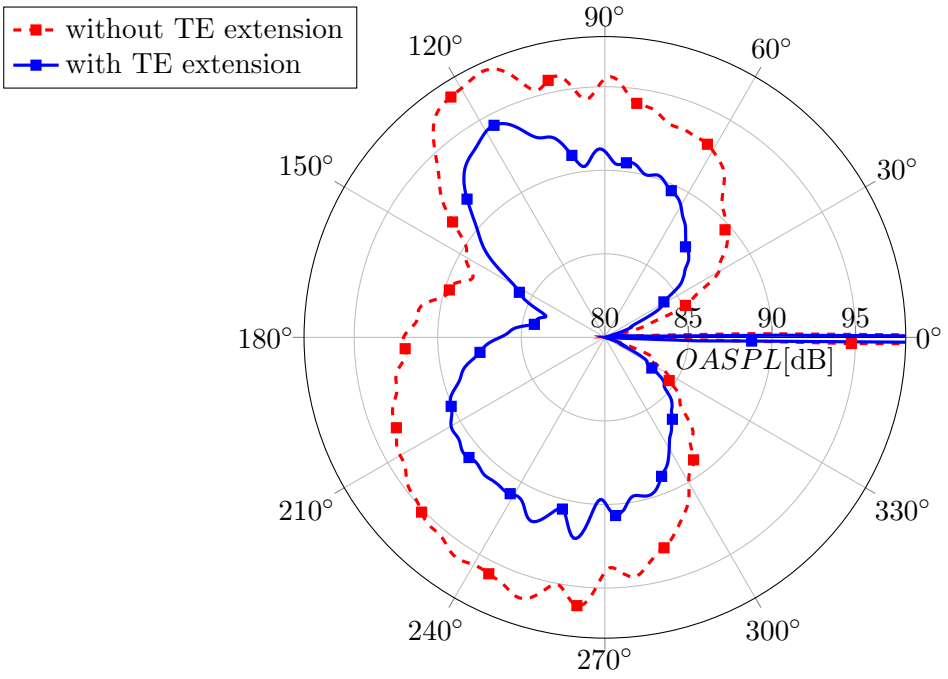

Figure 5.2: Directivity of the overall sound pressure level at a radial distance of $r = 5$ from the TE for an airfoil with and without a rigid TE extension using body-fitted boundary conditions only.

The grid spacing is based on the grid that was used by Jones *et al.* (2008) where the resolution requirements were determined using an iterative approach. The values of the wall grid spacings at the leading-edge (LE) and TE are given in table 5.1. In addition to these grid spacing constraints on the airfoil surface the resolution tangential to the wall was refined around mid-chord on the suction side to $\Delta\xi = 8 \times 10^{-4}$ in order to resolve the laminar separation bubble that is expected to form.

The inflow boundary conditions were imposed by the integrated characteristic boundary condition (Jones, 2008) with the fluid density ρ, the streamwise velocity u_1 and the freestream temperature T being prescribed as unity. The whole outer boundary of the C-mesh block was treated as an inflow boundary. The upper and lower boundaries of the wake block were both treated as freestream boundaries employing non-reflective characteristic boundary conditions. The outflow of the wake block was prescribed with the zonal characteristic boundary condition (Sandberg & Sandham, 2006) using 65 points for the zone. As initial condition a uniform flow field conforming with the inflow boundary conditions was prescribed throughout the domain. The chord based Reynolds number was $Re_c = 5 \times 10^4$ and the freestream Mach number was $M = 0.4$.

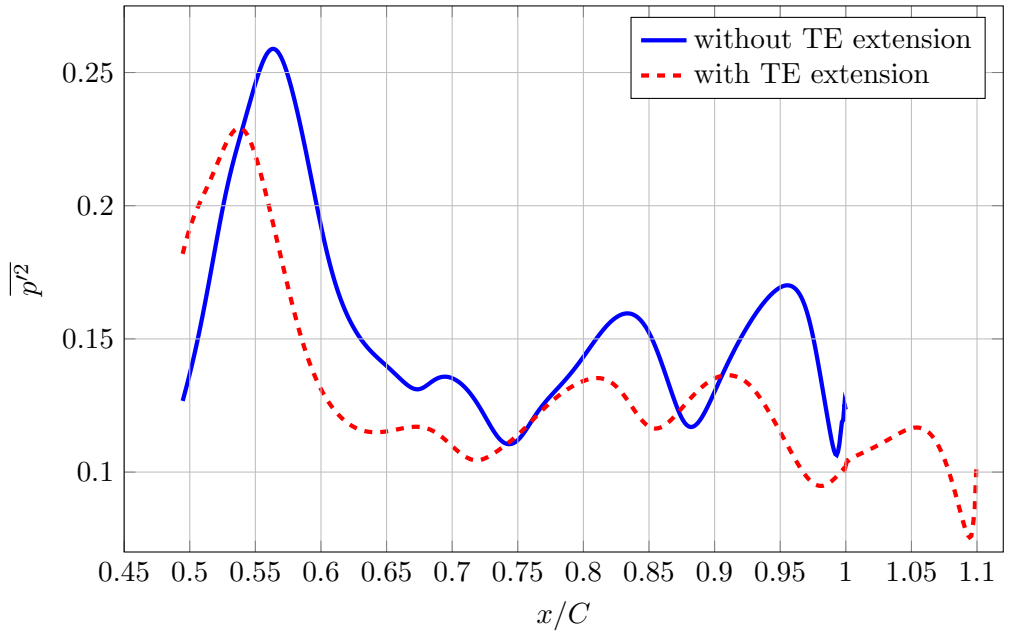

Figure 5.3: Wall pressure fluctuations on the suction side of the airfoil using configuration one from a simulation with and without a TE extension using body-fitted boundary conditions only.

5.1.2 Results – Statistical Analysis of the Acoustic Field

To assess the effect of a rigid TE extension attached to an airfoil the overall sound pressure level in the acoustic far field is compared in figure 5.2 at a radial distance of $r = 5$ from the original TE location. It can be seen clearly that both directivity patterns show a similar asymmetric shape. The higher noise level on the suction side can be attributed to the formation of a laminar separation bubble which was investigated in detail by Jones *et al.* (2008). Despite the similarities of the pattern the actual noise level for the airfoil with a rigid TE extension is significantly reduced by up to 5.5dB compared to the airfoil without any extension.

5.1.3 Results - Examination of the Hydrodynamic Source Region

Since wall pressure fluctuations are the input for the TE noise mechanism they can give indications about the source of the different noise levels found in the overall sound pressure level directivity. Note, however, that they were only gathered as time-averages and therefore the fluctuations also contain the contribution from the scattered acoustic field making a distinction, as outlined in section 2.1.4, impossible. Figure 5.3 compares the variance of pressure on the suction side of the airfoil for the two cases with and without extension. Both cases feature a peak after the mid-chord location which is likely to be caused by the reattachment of the laminar separation bubble at that location. Furthermore, both cases feature the lowest level of wall pressure fluctuations just before the

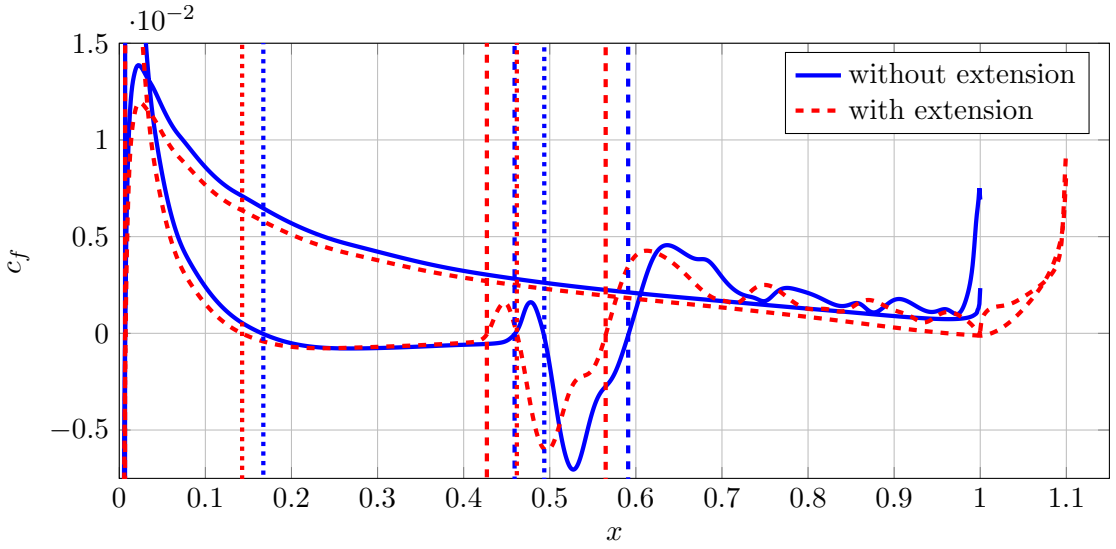

(a) The skin-friction distribution around airfoil, where the vertical dotted lines indicate the start of a separated flow region and the dashed lines the end of it.

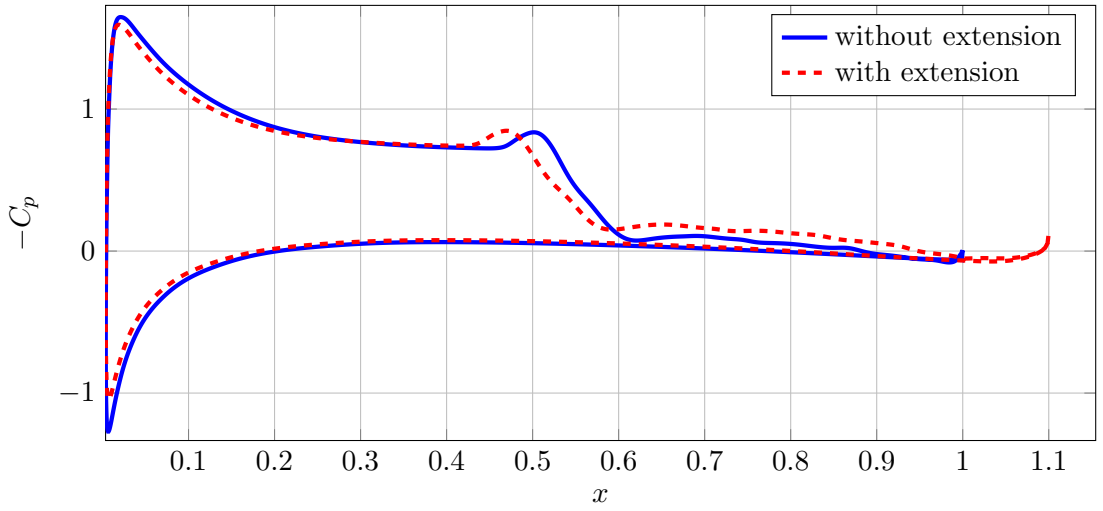

(b) pressure distribution around airfoil

Figure 5.4: Comparison of the pressure distribution around the airfoil with and without the TE extension.

respective TE location which is then followed by a sharp increase towards the TE. For the case with the TE extension it can be seen that the peak in the pressure fluctuations from the laminar separation bubble is shifted slightly upstream. Most important is that the amplitude of the peak is significantly lower compared to the case without the extension. Consequently, the case with the extension shows a decreased overall level of the fluctuations further downstream. This is most notable in the region of the TE and the extension. Since the sharp increase in the wall pressure fluctuations towards the TE location is also significantly less pronounced with the extension, it is consistent with the resulting reduction in noise level.

To further assess the change of the flow in the vicinity of the separation bubble, figure 5.4a compares the skin-friction c_f distribution around the airfoil for the case with and without extension. The start of the separation bubble on average can be identified by the zero-crossing at approximately 15% of the chord and is visualized by a vertical dotted line in the figure. It shows only a minor difference between both cases. The reattachment points of both cases are visualized by the vertical dashed lines. It shows a shift in the upstream direction when the TE extension is employed. Downstream of the reattachment point is a second separated flow region in both cases featuring comparatively high magnitudes of skin-friction. From visual inspection of the instantaneous flow fields it can be concluded that this second separated flow region is associated with the vortex shedding from the separation bubble and is therefore denoted vortex shedding region. In this vortex shedding region the skin-friction shows slightly lower magnitudes when the TE extension is employed. Thus, the changes observed in the wall pressure fluctuations can indeed be related to a modification of the size and location of the separation bubble. This altered location of the separation bubble and the vortex shedding region has also influence on the overall pressure coefficient distribution presented in figure 5.4b. In fact, the change in the distribution of the pressure when employing the extension reduces the lift force generated by the airfoil by 2.5%, despite a longer effective chord length, due to the extension.

Besides the changes in pressure distribution and the reduced extent of the separation bubble the lower wall pressure fluctuations could also be caused by a higher distance of the convected vortices from the respective TE location. Figure 5.5 compares the three Reynolds stress components over the distance in the y-direction from the TE of the airfoil itself or the extension. For all three components it can be found that the level of the fluctuations are lower throughout the considered distances from the TE. For the τ_{11} and the τ_{22} components it can be noted that the profiles are shifted slightly towards the freestream.

It can be summarized that the airfoil with a rigid TE extension results in a significantly lower noise level. It can mainly be attributed to the fact that extension alters the pressure distribution around the airfoil and reduces the lift force generated. This change in the pressure distribution also influences the location and size of the separation bubble which is reduced when the extension is employed. Consequently, the incident pressure fluctuations are reduced and the distance of the passing vortices seems to be of secondary importance.

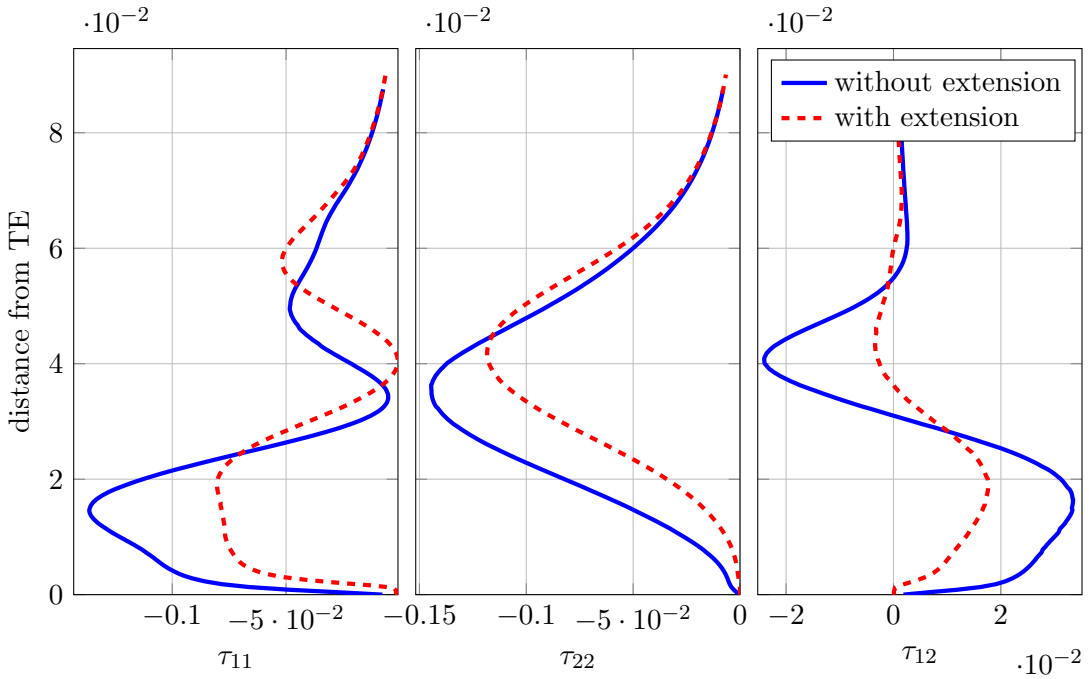

Figure 5.5: Comparison of the Reynolds-stresses as a function of the distance in the $y-$direction from the wall just before the respective TE for the case with and without a rigid TE extension using configuration one.

L_{wake}/N_{wake}	$R_c/N_{c\xi}$	h_{TE}/N_{TE}	$\Delta\eta$ at LE and TE	$\Delta\xi$ at LE and TE
4.7/755	6.0/1066	$2.458 \times 10^{-3}/11$	2.428×10^{-4}	1×10^{-3}

Table 5.2: Spatial and grid dimensions of the airfoil setup. $N_{c\xi}$ is the number of grid points on the surface of the airfoil. h_{TE} and N_{TE} are the thickness and the number of grid points of the TE, respectively. The definition of the other parameters can be found in figure 5.6. Furthermore, the wall grid spacings at the leading-edge (LE) and TE are given.

5.2 Effect of an Elastic TE Extension

Following the assessment of the effect of a rigid TE extension, this section investigates the noise radiation from elastic TE extensions of an airfoil. The computational setup is introduced in section 5.2.1 and the results are discussed in 5.2.3.

5.2.1 Computational Setup

The grid topology and configuration from the setup introduced in section 5.1 was modified to facilitate the TE extension in a smoother way. A particular aim was to enable a simulation with body-fitted boundary conditions for a rigorous validation of the BDIM, requiring the grid to be aligned with the surface of the extension. Furthermore, this topology keeps the interaction between BDIM and characteristic interface conditions to

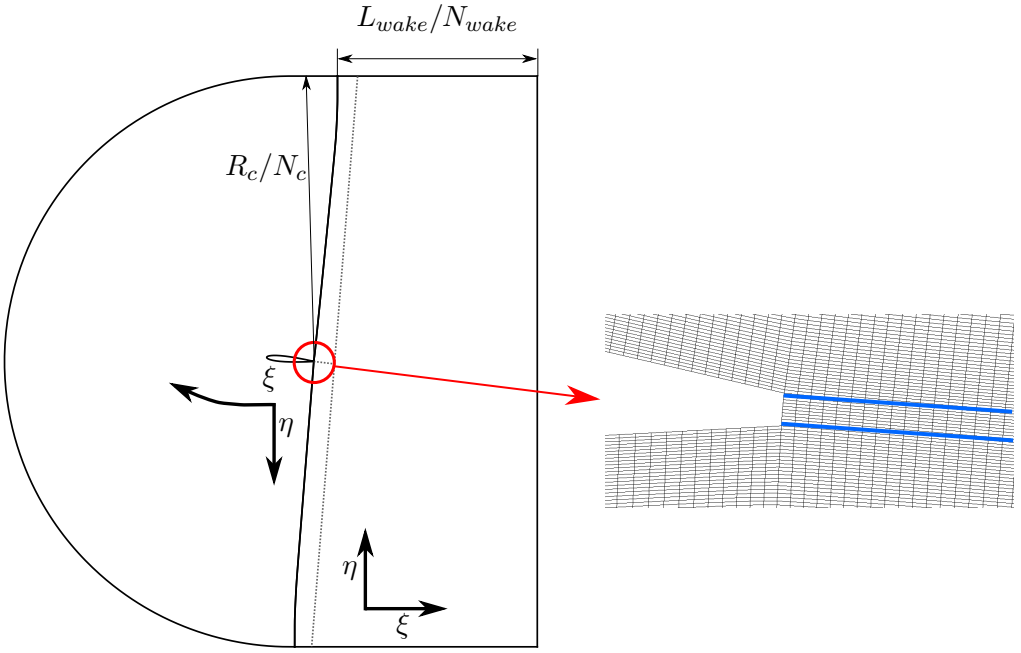

Figure 5.6: Schematic of the computational setup with two blocks employing a C-mesh and a wake block. The actual number of grid points and dimensions can be found in table 5.1. The dashed grey lines indicate the additional block boundaries when the rigid flat plate extension with body-fitted boundary conditions is considered. The blue lines in the close up of the TE indicate the extension when using the BDIM.

a minimum, avoiding issues with numerical instabilities. Overall, the two block grid topology is the same as in section 5.1. However, the grid resolution was increased and less stretching was applied to the first grid points in the wall normal direction of the airfoil to ensure the motion of the elastic extension was resolved appropriately. The values of the wall grid spacings at the leading-edge (LE) and TE are given in table 5.2. In addition to these grid spacing constraints at the respective domain boundaries the resolution tangential to the wall was refined around mid-chord on the suction side to $\Delta\xi = 8\times10^{-4}$ in order to resolve the laminar separation bubble that is expected to form.

The boundary conditions and initialization are unchanged in comparison to section 5.1. For the elastic TE extension the two different parameter sets with a high and a reduced bending rigidity were chosen and are listed in table 5.3. In addition the first two natural frequencies of the structure f_1 and f_2, as defined in equation 2.18, are listed alongside with the added mass factor μ_m which is negligibly low in both cases. The vortex shedding frequency f_s, used to normalize the natural frequencies of the structure, was obtained from the precursor simulations of the previous section 5.1 and has a non-dimensional value of $f_s = 3.46$. For the remainder of this chapter, all frequencies will be normalized by this vortex shedding frequency.

	E_s	ρ_s	f_1/f_s	f_2/f_s	μ_m
set 1	2.18×10^5	1019	0.172	1.09	0.040
set 2	1.91×10^5	1319	0.142	0.89	0.043

Table 5.3: Parameters describing the flat plate extension and specifying the structural properties of the elastic extension with two different parameter sets with the Youngs modulus E, the structural density ρ_s. The length of the structure is $L_s = 10\%C$ and the height is given in table 5.2. Using equation 2.18 the first and second natural frequencies of the structure f_1 and f_2 can be calculated and are normalized by the vortex shedding frequency f_s, obtained from precursor simulations. Furthermore, the added mass factor μ_m, as defined in equation 2.20, is presented. The structural parameters are non-dimensionalized with freestream quantities or combinations thereof.

5.2.2 Results – Validation

This paragraph gives a first overview of the hydrodynamic and the acoustic far field. Furthermore, the accuracy of the BDIM when representing a TE extension will be examined.

Figure 5.7 shows two instantaneous snapshots obtained from simulations where the BDIM is employed to represent the TE extension. In the contours of the spanwise vorticity component presented in figure 5.7a it can be clearly seen that the flow separates before mid-chord forming a laminar separation bubble. The vortices shed from there are then convected downstream along the airfoil over the TE extension. As the vortices convect along the suction side they generate pressure fluctuations on the airfoil surface that cause noise radiation from the surface which scales $\sim M^6$ according to the acoustic analogy (Curle, 1955). When these pressure fluctuations convect over the TE additional noise radiation can be observed which scales with $\sim M^5$ (Ffowcs Williams & Hall, 1970). Thus, for low Mach number flows it is expected that the TE noise dominates the overall noise radiation. However, since this flow is at a moderate Mach number of $M = 0.4$, contributions from both sources might be relevant. The resulting acoustic field is visualized in figure 5.7b using the dilatation contours at an arbitrary instant of time. It can be appreciated that the acoustic field is very clean with distinctive wave fronts. No signs of reflections from the outflow or any other boundary of the computational domain into the region of interest can be found. The noise predominantly originates from the trailing-edge and the scattering is the strongest in the upstream direction with an increased noise level on the suction side which is likely to originate from the surface dipole caused by the interaction of the wall and the pressure fluctuations from the separation bubble and the associated vortex shedding.

Figure 5.8 shows the directivity of the overall sound pressure level at a radial distance

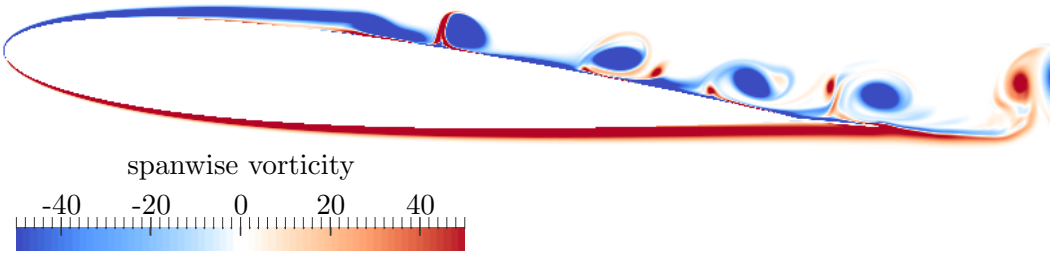

(a) Contours of the spanwise vorticity component around the airfoil.

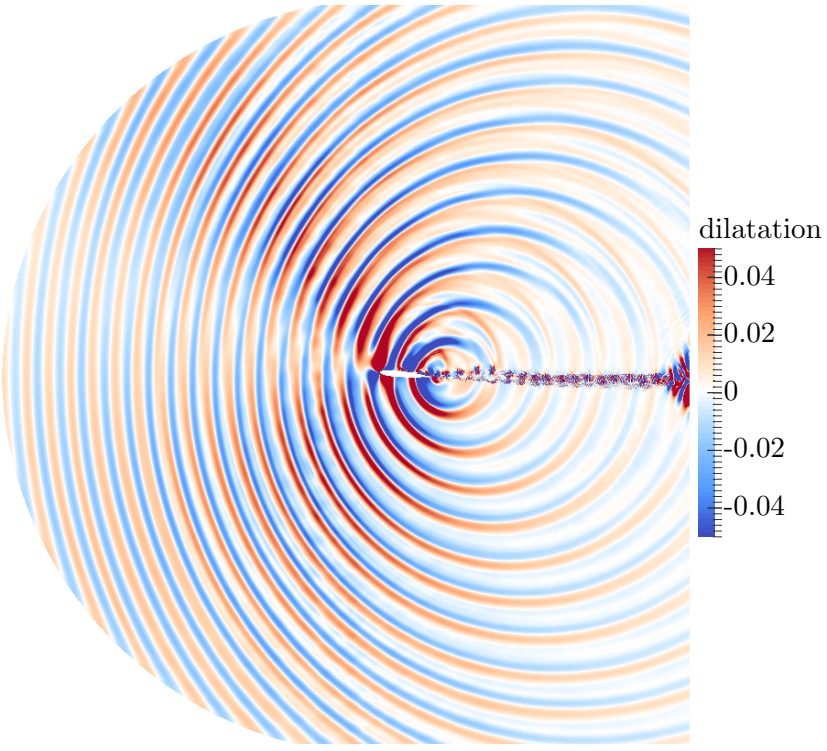

(b) Contours of dilatation showing the acoustic field.

Figure 5.7: Instantaneous snapshots showing the hydrodynamic and acoustic field from simulations with a rigid TE extension.

of $r = 3.5$ from the aft of the airfoil with a rigid extension which is represented by body-fitted boundary conditions and the BDIM. For the BDIM cases two different resolution levels were considered where level 1 refers to the baseline resolution as documented in table 5.2. For the higher resolution level 2 the grid was refined by a factor of two relative to the grid spacings detailed in table 5.2 at the TE in both directions. It can be appreciated that the sound levels of both cases employing the BDIM are in very close agreement. In fact the maximum difference between the two below the airfoil is 0.25dB. Consequently, the required grid resolution that was determined by Jones *et al.* (2008) for body-fitted simulations is also sufficient to resolve the TE noise mechanism with the BDIM and only resolution level 1 will be considered for the remainder of this chapter. When comparing the two data sets obtained employing the BDIM to the body-fitted case good agreement can be found with a slight over-prediction of a maximum of 0.42dB

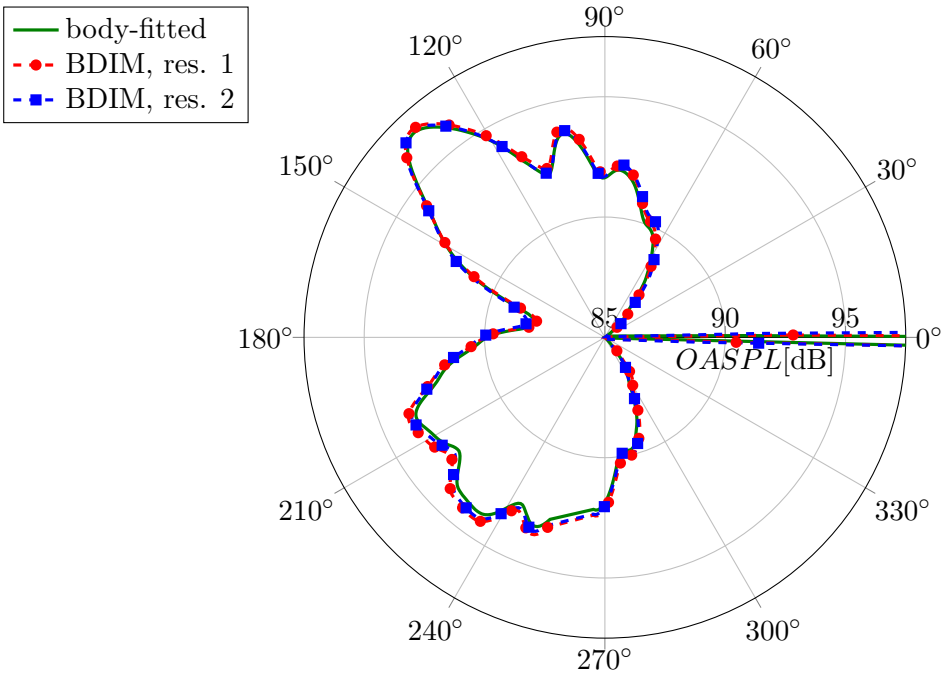

Figure 5.8: Directivity of the overall sound pressure level at a radial distance of $r = 3.5$ from the aft of the airfoil comparing the body-fitted with the BDIM cases. For the BDIM cases two different resolution levels, abbreviated with res., are shown where level 1 refers to the baseline resolution as documented in table 5.2 and 2 to a refined grid.

and 0.2dB for resolution level 1 and 2, respectively.

Figure 5.9 compares the power spectral density of the pressure signal for the body-fitted and the BDIM case with a rigid extension. The virtual microphone position is located on the pressure side upstream of the airfoil at a radial distance of 3.5 and an angle of $\theta = 217°$ in the directivity pattern. The dominant peak in the spectrum is at the frequency of the vortex shedding from the laminar separation bubble which was also used to normalize the frequency of the spectrum. It can be observed that the exact location is in perfect agreement for both cases. For the BDIM the amplitude is slightly over estimated and since the amplitudes of this dominant peak and the subsequent harmonics are decades above all the other peaks in the spectrum they govern the overall fluctuation level. Hence, the findings are consistent with what has been found in the directivity plot in figure 5.8. There is an additional peak in the spectrum that is not a harmonic of the dominant peak at a frequency of $f/f_s \approx 0.26$. The agreement of the peak's location is very good. However, the amplitude when employing the BDIM is roughly two decades higher than in the body-fitted case. Regarding the contribution to the overall energy contained in the spectrum this difference is unlikely to influence the integral noise level. Nevertheless, this overestimation of this first peak can also explain the higher amplitudes for all following non-dominant peaks since they are either higher harmonics or non-linear interactions between the dominant peak and this first peak. It

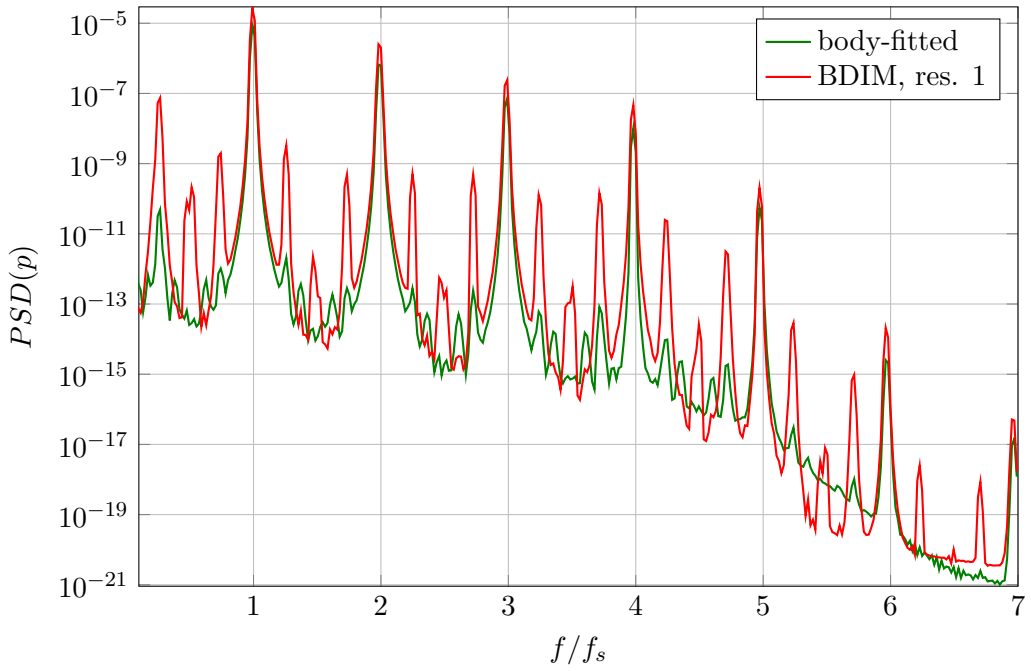

Figure 5.9: Power spectral density of pressure at a radial distance of $r = 3.5$ with an angle of $\theta = 217°$ from the TE comparing the body-fitted with the BDIM case on the pressure side.

is speculated that this frequency is linked to an instability in the wake which would be a quadrupole-like source according to the acoustic analogy and was also found by Sandberg *et al.* (2007).

The validity of the hypothesis about the additional noise source originating from the wake can be evaluated by calculating the power spectral density of the acoustic far-field as a plane. To that end planes of the far-field were captured skipping different numbers of grid points in varying grid regions to reduce the overall amount of data. The power spectral density was calculated by averaging over 7 Hanning windows each containing 26.25 vortex shedding cycles with an overlap of 50%. Figure 5.10 shows the contour of the power spectral density of pressure from the simulation employing the BDIM to represent the rigid extension for the hypothetical frequency of the wake instability $f/f_s = 0.26$. In addition contour lines of time averaged $\frac{\partial \widetilde{u_1}}{\partial x_2}$ are presented to visualize the shear of the wake. When examining the wake region it is apparent that there are multiple noise sources that radiate into the far-field. The first one is located at $x = 1.25$ and radiates predominantly towards the suction side. The second strong source can be identified with a center at approximately $x = 2.5$ and the radiation is towards the pressure side.

As increased fluctuations at this frequency can also be observed in the vicinity of the separation bubble it is speculated that the initial disturbances are introduced at this location. They are then convected downstream where they are amplified in the wake.

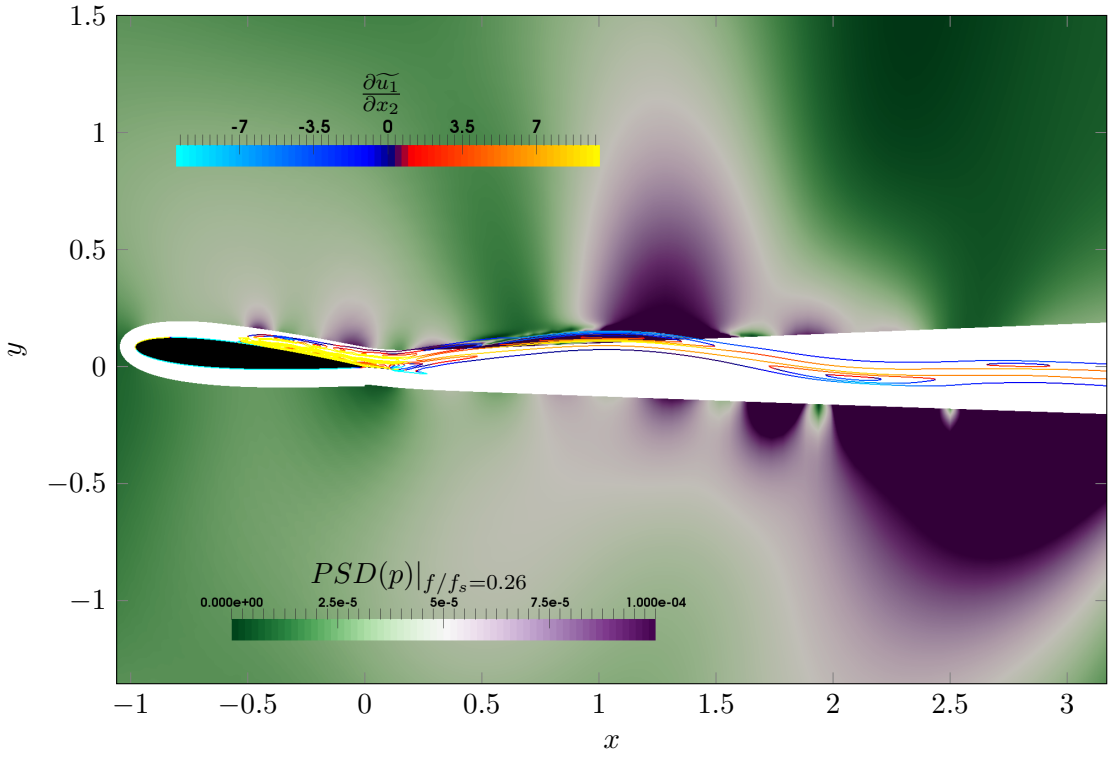

Figure 5.10: Contours of $PSD(p)_{f/f_s=0.26}$ from the simulation using the BDIM. The contour lines visualize the shear in the wake with $\frac{\partial \widetilde{u_1}}{\partial x_2}$ from the time averaged statistics.

Figure 5.11 shows the contours of the power spectral density of the streamwise velocity component on the surface of the airfoil for the frequency of the wake instability. It is speculated that the instability is of Kelvin-Helmholtz type that is typically found in wakes (Yaglom, 2012). The comparison between the velocity fluctuations of the airfoil's suction side between the BDIM and body-fitted cases shows that the fluctuations with this frequency originate from the vicinity of the reattachment point of the separation bubble. They are more pronounced in the case using the BDIM and seem to be amplified as they convect downstream, whereas in the body-fitted case the overall level of the fluctuations is significantly lower and also confined to the reattachment point. It is suggested that the initial disturbances at this frequency originate from the vicinity of the reattachment point of the separation bubble and are amplified in the wake. When the BDIM is employed this amplification is stronger than with the body-fitted boundary conditions. The growing instabilities eventually radiate noise which is strong enough to trigger an amplification of the initial disturbance in the vortex shedding region and thus establish an acoustic feedback loop.

The differences in the amplification of the inital disturbance in the wake and the hypothesized feedback loop that follows can likely be explained with differences in the velocity profiles in the wake. Therefore, figure 5.12 shows the velocity, velocity gradient and Reynold stress profiles for the case with a TE extension represented by body-fitted

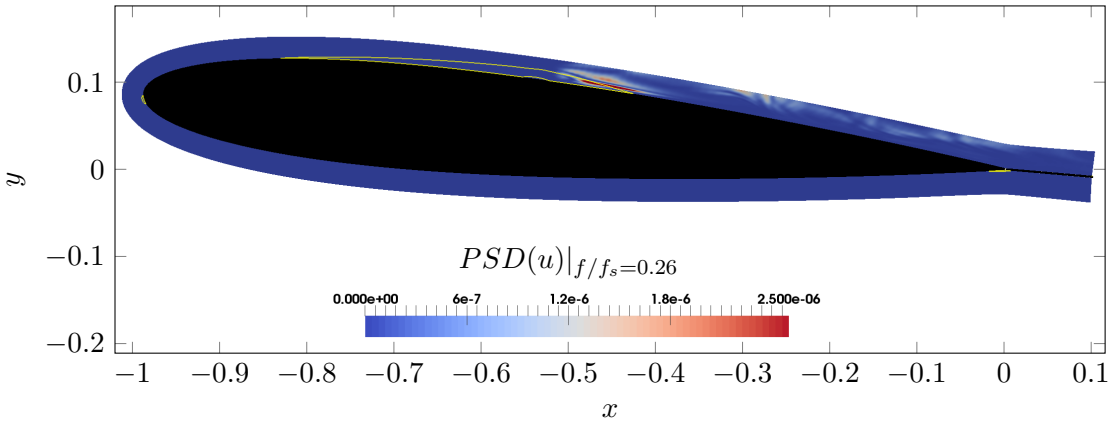

(a) extension is represented by body-fitted boundary conditions

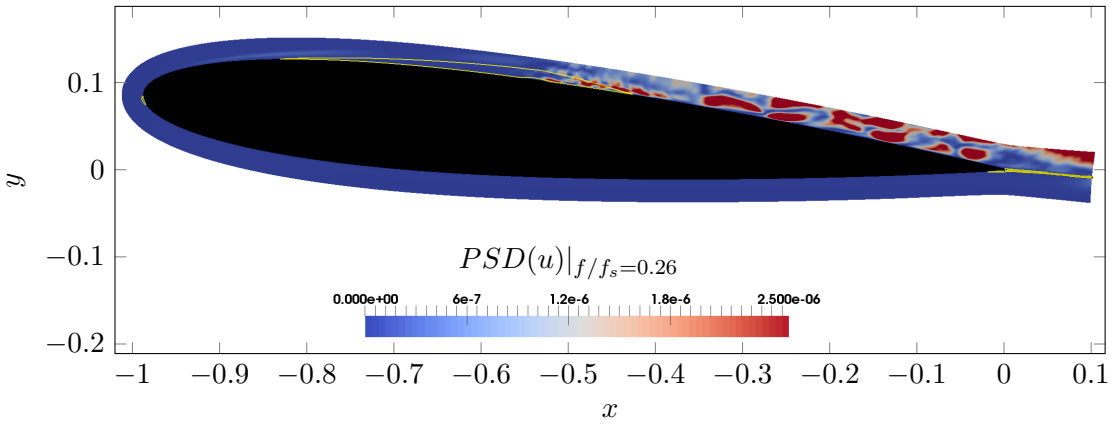

(b) extension is represented by the BDIM

Figure 5.11: Contours of $PSD(u)_{f/f_s=0.26}$ comparing body-fitted boundary conditions and the BDIM. The contour line visualize the streamwise velocity component for $u_1 = 0$.

boundary conditions and the BDIM at a location 2.5 chord lengths downstream of the TE extension. It can be noticed that the mean streamwise velocity profiles and its lateral derivative agree very well. However, the lateral velocity component and its derivative show a qualitatively different shape. In contrast to the streamwise velocity component, the shape of the lateral velocity profile depends on the streamwise location in the wake when coherent vortex shedding is considered. Therefore the lateral velocity component is an indicator for a difference in the phase of the wake development, possibly explaining the qualitative difference between body-fitted and BDIM case. The τ_{11} and τ_{22} Reynolds stress components show the same trend, but the amplitudes are higher in the BDIM case and are also slightly shifted. Furthermore, the τ_{12} Reynolds stress component shows a lower correlation level of the streamwise and lateral velocity fluctuations which again indicates a different phase of the wake development. It seems that the slightly different representation of the TE extension for the two different boundary conditions leads to a shift in the wake development. These differences can hardly be noticed closer to the TE but are accumulating in the downstream development. It is argued that the higher amplitude of the wake noise source and the hypothesized feedback loop in the BDIM

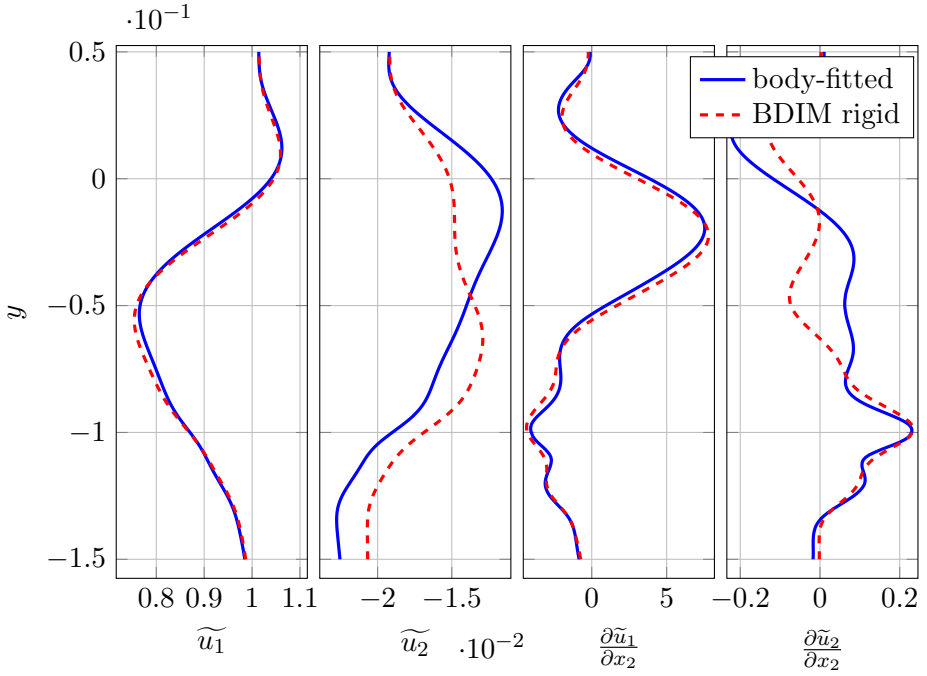

(a) profiles of the velocity and its gradients in the lateral direction

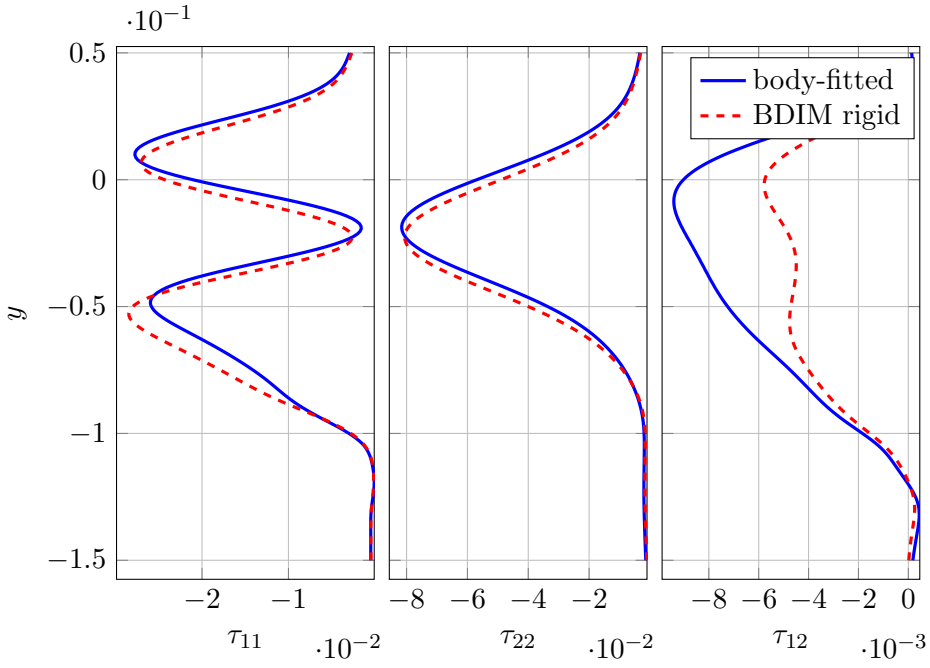

(b)

Figure 5.12: Comparison of the velocity and Reynolds-Stresses 4 chord lengths downstream of the TE extension for the rigid TE extension represented by body-fitted boundary conditions and the BDIM.

case can be explained with these differences.

Overall it can be stated, that the data from simulations where the TE extension is represented by the BDIM are in very good agreement with results obtained with the body-fitted boundary conditions. The differences in the exact representation of the extension's shape between body-fitted boundary conditions and the BDIM seem to result in slightly altered mean profiles in the wake that lead to an amplification of velocity disturbances that seem to originate from the reattachment point of the separation bubble. However, the contribution of that frequency to the overall noise level can be neglected. For the following investigation of the effect of TE elasticity the rigid TE extension will always be represented by the BDIM for a consistent comparison.

5.2.3 Results – The Elastic TE Extension

The following paragraphs consider two elastic TE extensions with different material properties in comparison to a rigid TE. Firstly, the structural motion will be analysed in section 5.2.3.1. The acoustic noise radiation is examined in section 5.2.3.2 and is followed by an investigation of the hydrodynamic source region is section 5.2.3.3.

5.2.3.1 The Structural Behaviour

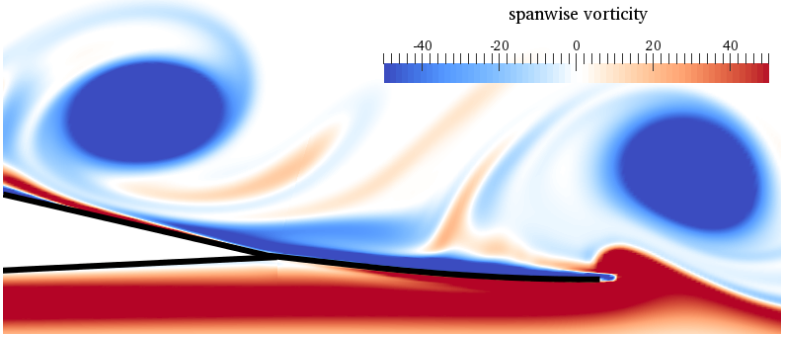

Figure 5.13: Contours of spanwise vorticity showing the flexible TE extension in a deflected state.

Figure 5.13 shows the instantaneous spanwise vorticity field around the elastic flat plate extension of the airfoil with parameter set 1 at an arbitrary instant of time. The vortices that were found to originate from the laminar separation bubble in figure 5.7a can be clearly identified. The coherent vortex shedding leads to strong pressure disturbances that drive the motion of the elastic TE extension. The resulting deflection of the extension with the shape of bending mode two can be found when the plot is examined carefully.

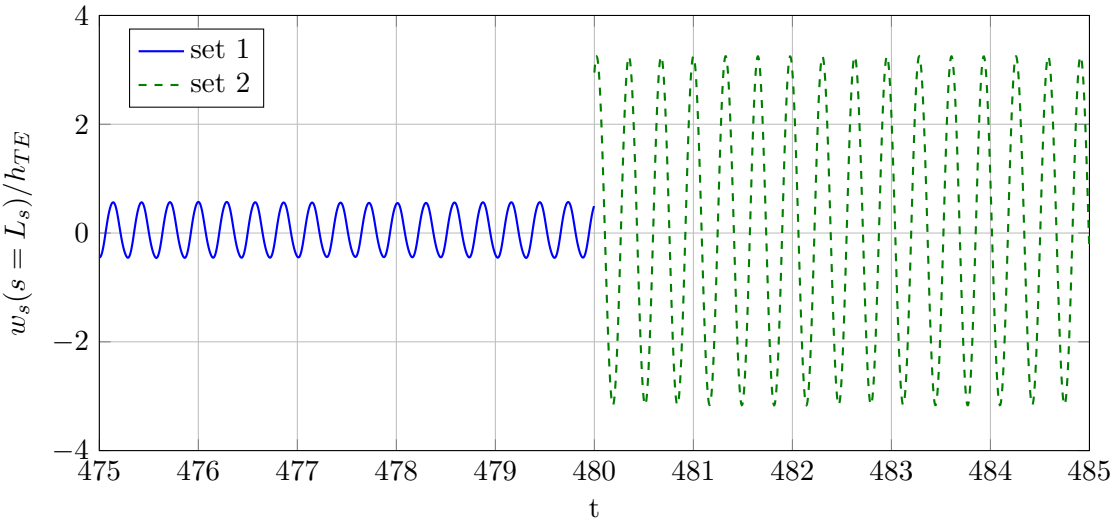

Figure 5.14: Time history of the deflection w_s of the free end at $s = L_s$ of the elastic TE extensions for both parameter sets normalized by the height of the TE h_{TE}.

A representative sequence of the time history of the deflection w of the TE extensions' end point after it has reached a quasi-periodic state is presented in figure 5.14 for both parameter sets. The fact that they are not shown for the same period of time is purely for illustration purpose and enhanced readability. It can be appreciated that the deflections are periodic with one dominant frequency and a constant amplitude. This can be attributed to the very coherent vortex shedding from the laminar separation bubble that generates a periodic loading on the plate.

The time averaged deflection $\overline{w_s}$ of the extension in units of the plate thickness h_{TE}, shown in figure 5.15a, is positive, which indicates a mean deflection towards the suction side. In both cases the mean deflection shows the shape of bending mode 1, as also shown in figure 2.2 for comparison. Consequently, the net pressure force is bending the extension towards the suction side. The mean deflection at the free end is approximately $0.53\Delta y$ and $0.44\Delta y$ for parameter set 1 and 2, respectively. Thus the effect of this mean deflection is likely to be negligible. The standard deviation of the deflection w_{rms} is plotted in figure 5.15b over the length of the extension. For both parameter sets the shape is a pronounced bending mode shape 2, as also shown in figure 2.2 for comparison. The shape features two nodes, one at the mounting point and one at 3/4 of the extensions' length. The bending mode 2 shape can be explained with the fact that the second natural frequency of the structure is closest to the frequency of the pressure loading. As expected the lower bending rigidity of parameter set 2 leads to significantly higher fluctuations of the deflections. If the amplitude of the sinusoidal time signals are calculated with the standard deviation by multiplying it with $\sqrt{2}$ the deflection amplitude can be quantified with $5.2\Delta y$ and $33\Delta y$ for parameter set 1 and 2,

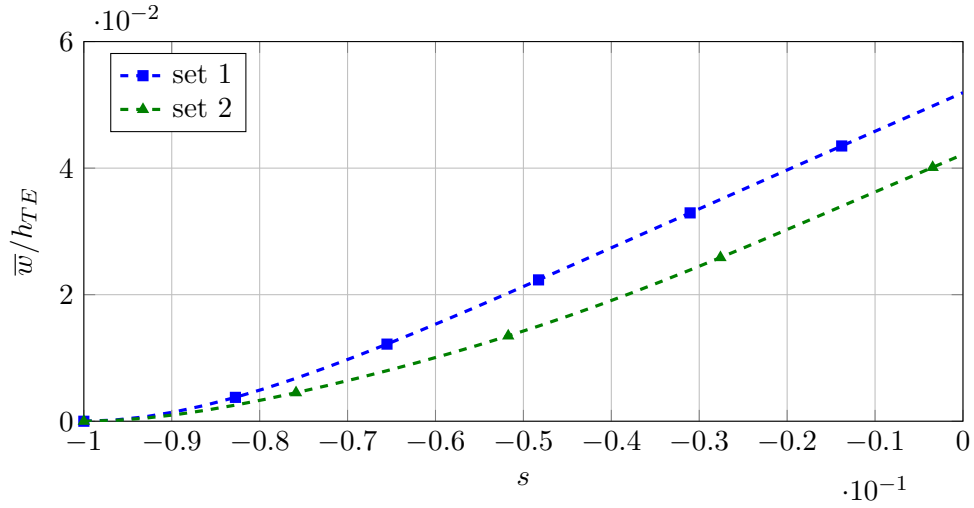

(a) Mean deflection, $\overline{w}$

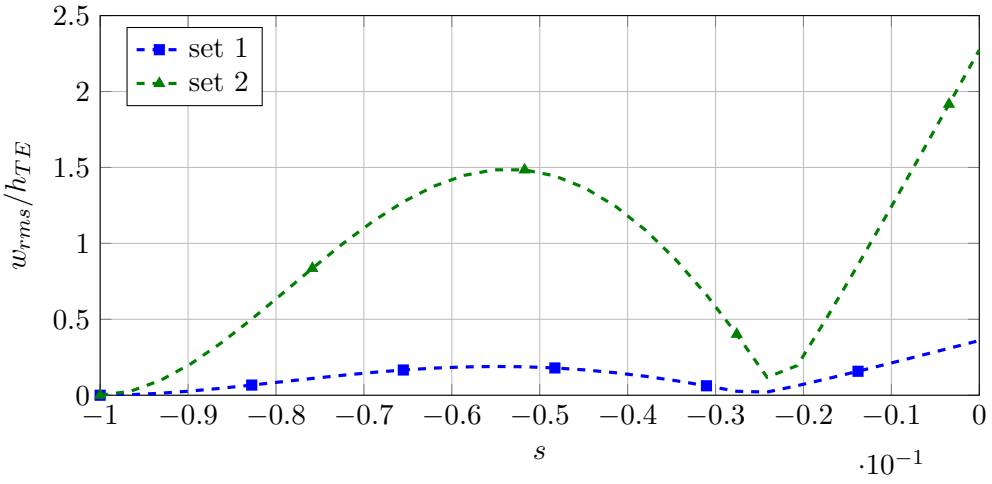

(b) Standard deviation of the deflection, w_{rms}

Figure 5.15: Mean and standard deviation of the deflection time history of the TE point as function of the coordinate s parameterizing the length of the extension for the two different structural parameter sets.

respectively. Both are amplitudes that can be accurately represented by the BDIM.

Figure 5.16 presents the power spectral density of the extensions' free end deflection, shown as time history in figure 5.14, to evaluate the important frequencies that govern the structural behaviour. The spectrum was calculated using 5 segments employing Hanning windows with a length of 65.6 vortex shedding cycles and an overlap of 53%. For parameter set 1 the spectrum is dominated by the vortex shedding frequency with comparatively low amplitudes in other frequency ranges. Additional peaks can be found at the second and third natural frequencies of the structure but in terms of contribution to the overall energy they are insignificant. Thus, the response of the structure to the external forcing is governed by the forcing frequency itself and its harmonics. For parameter set 2 the vortex shedding frequency and the second natural frequency of the

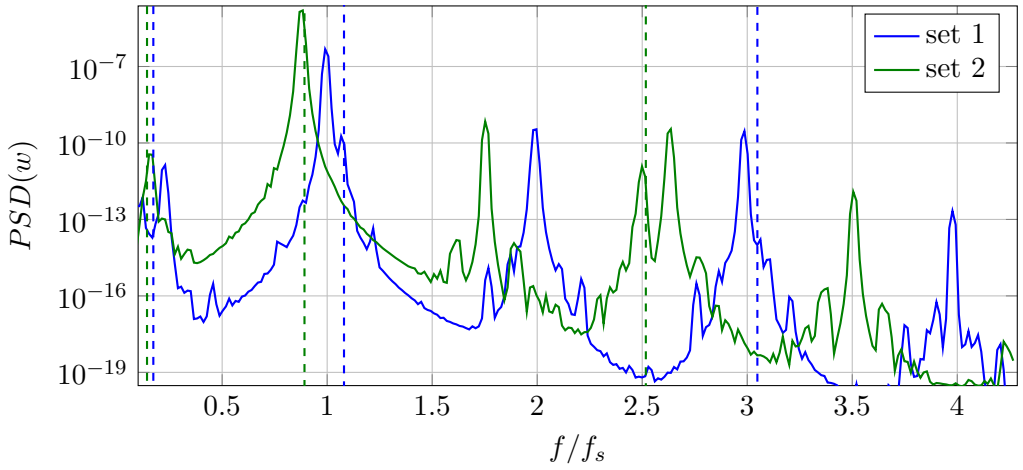

Figure 5.16: Power spectral density of the deflection time history w of the TE point for the two different structural parameter sets. The respective natural frequencies are indicated with vertical dashed lines with the same color and are normalized with the vortex shedding frequency f_s.

structure seem to be locked as the only peak that can be identified in this frequency range is at the natural frequency. Thus the structural movement might be close to resonance. Apart from that the qualitative behaviour is similar to the one of parameter set 1 but the peaks at the natural frequencies are more pronounced.

5.2.3.2 Statistical Analysis of the Acoustic Field

For an assessment of the integral performance of the elastic TE extensions figure 5.17 compares the overall sound pressure level of the rigid and the two elastic cases at a radial distance of 5 chord lengths from the mounting point of the TE extension. All directivity patterns feature the aforementioned asymmetric shape with the higher noise level on the suction side due to the laminar separation bubble. For the elastic extension with parameter set 1 the directivity shape appears to be the same as for the rigid TE. In contrast to that the three lobes on the suction side of parameter set 2 are pronounced. Furthermore, the noise radiation appears to be directed more towards the vertical direction. However, in general both the elastic TE extensions are significantly noisier than the rigid case. When parameter set 1 is used the maximum noise increase is 3.6dB in the $\theta = 210°$ direction. For parameter set 2 the maximum noise increase is 11.2dB in the same direction.

The spectral analysis of the pressure signal from three cases can give further insights about the distribution of the energy in the pressure fluctuations and in which frequency ranges the noise amplification occurs. To that end, figure 5.18 shows the power spectral density of the pressure signal from upstream of the airfoil on the suction side calculated from an average of 7 Hanning windows and an overlap of 50%. When parameter set 1 is considered the first thing to note is that the dominant peak of the spectrum and its

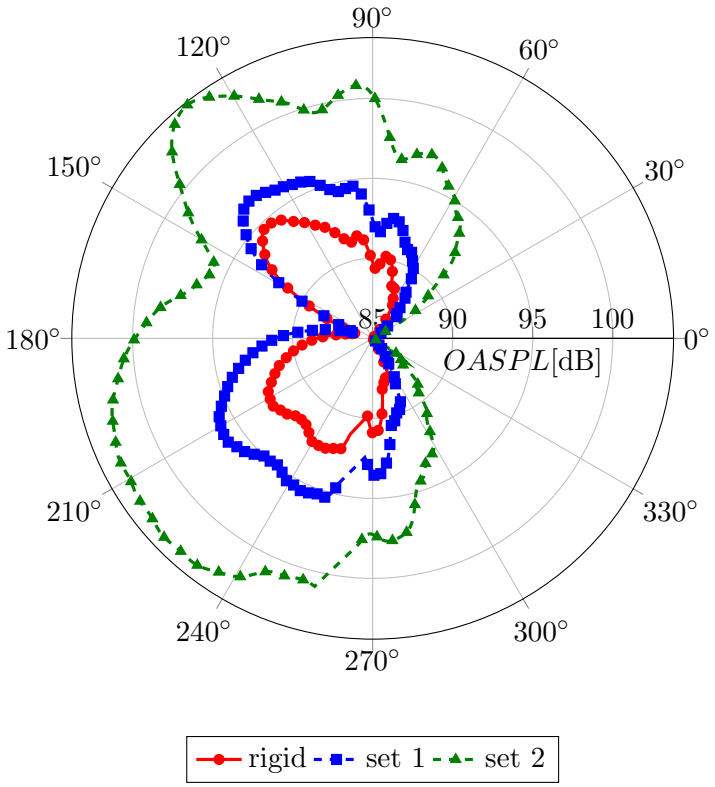

Figure 5.17: Directivity of the overall sound pressure level SPL at a radial distance of $r = 5$ from the TE for the rigid and elastic TE extensions.

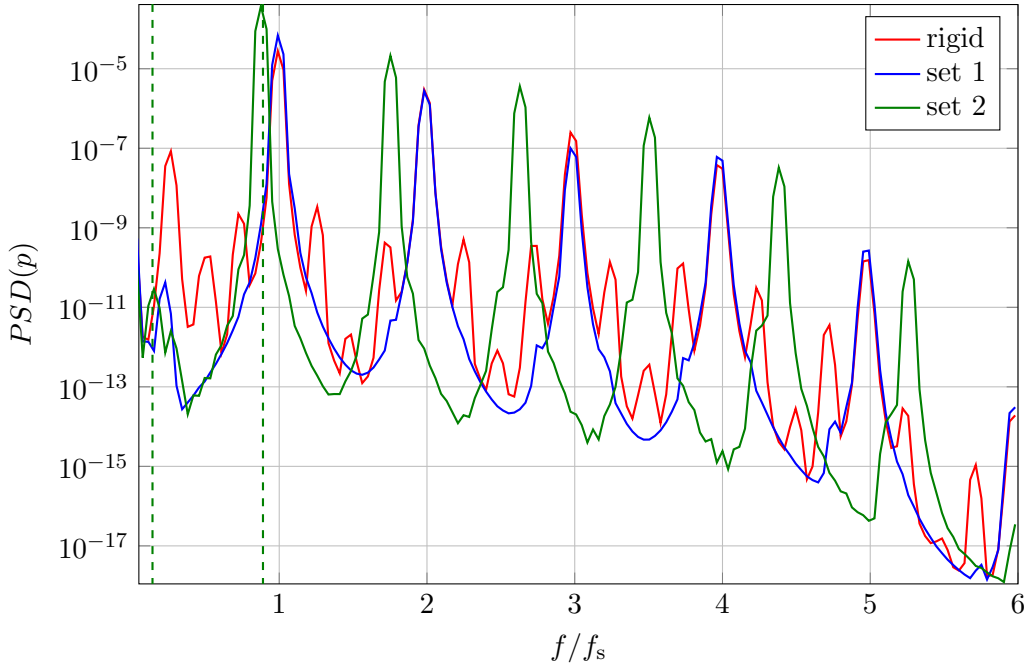

Figure 5.18: Power spectral density of pressure at a radial distance of $r = 3.5$ with an angle of $\theta = 216°$ from the TE comparing the elastic and rigid TE extensions. The vertical dashed green lines indicate the first and second natural frequency of the structure of parameter set 2.

harmonics occur at the same frequencies, i.e. $f/f_s = 1$ and $f/f_s = 2$, as in the rigid case. Hence, the frequency of the vortex shedding from the laminar separation bubble is not affected by this elastic TE extension. Furthermore, the amplitudes of these peaks are significantly higher. In contrast to the amplitudes of these dominant peaks the amplitudes of the aforementioned hypothetical wake source are several decades lower in the elastic case.

For parameter set 2 the dominant peak and its harmonics are shifted towards lower values. The exact frequency is in good agreement with the second natural frequency $f/f_s = 0.89$ of the structure indicated by the vertical dashed line. This is consistent with the spectrum of the structural deflection presented in figure 5.16 where the same shift could be identified and the spectrum was dominated by the peak at the second natural frequency. Consequently, the vortex shedding frequency seems to be changed by locking in to the second natural frequency of the structural motion. It is speculated that the noise generated by the motion of the structure acted as acoustic excitation in the current application and thus led to the observed global changes. Similar observations were made by Pröbsting & Yarusevych (2015) who reported changes in the overall separation bubble characteristics and lock in of the vortex shedding frequency to that of the acoustic excitation. The low frequency noise source from the wake appears to be shifted alongside and collapses with the first natural frequency. However, no interaction of higher harmonics of the instability can be found for the elastic case.

In summary, the elastic TE extensions are noisier than the rigid one in this application and for the chosen structural parameters. The excess noise seems to be generated by the interaction of the structural vibration with the incident pressure field. Furthermore the vortex shedding frequency from the separation bubble seems to change when parameter set 2 is used.

5.2.3.3 Near Field Effects of the Elastic Extension

This section investigates if and how the flow around the airfoil is affected by the elastic TE extension to explain the noise amplification found in the previous section 5.2.3.2. To that end, figure 5.19a compares the skin-friction distribution around the airfoil for the rigid and elastic TE extensions. It can be found that in the first 40% of the chord there is no difference between the cases. However, further downstream pronounced differences can be found on the suction side which is magnified in figure 5.19b. For parameter set 1 the agreement with the rigid TE is good initially with slight differences in the exact amplitude of the peaks around mid-chord. However, further downstream the amplitudes and location of the skin-friction peaks differ. Considering parameter set 2 it can be found that the end of the separation bubble is shifted upstream and the positive and

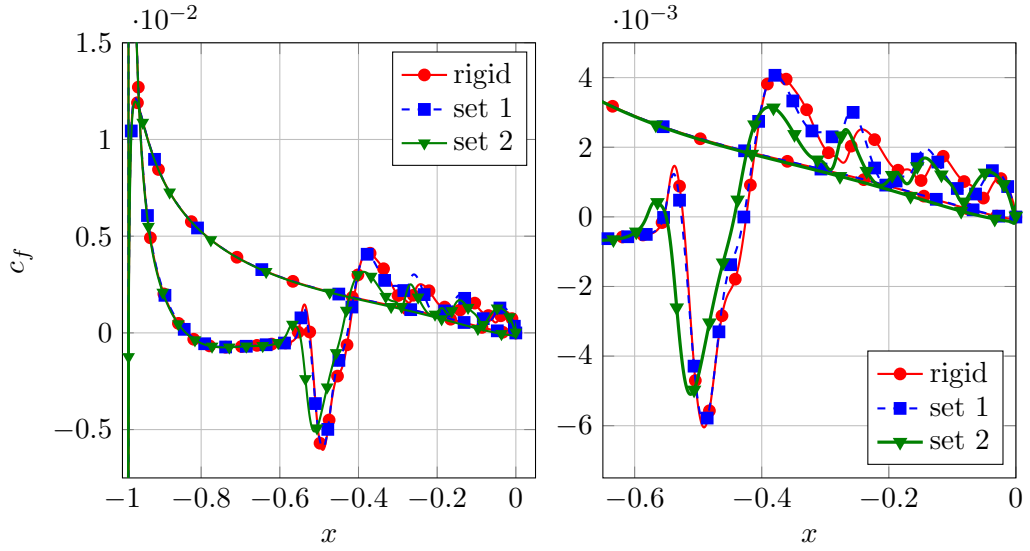

(a) skin-friction distribution around airfoil

(b) skin-friction distribution in vicinity of the separation bubble

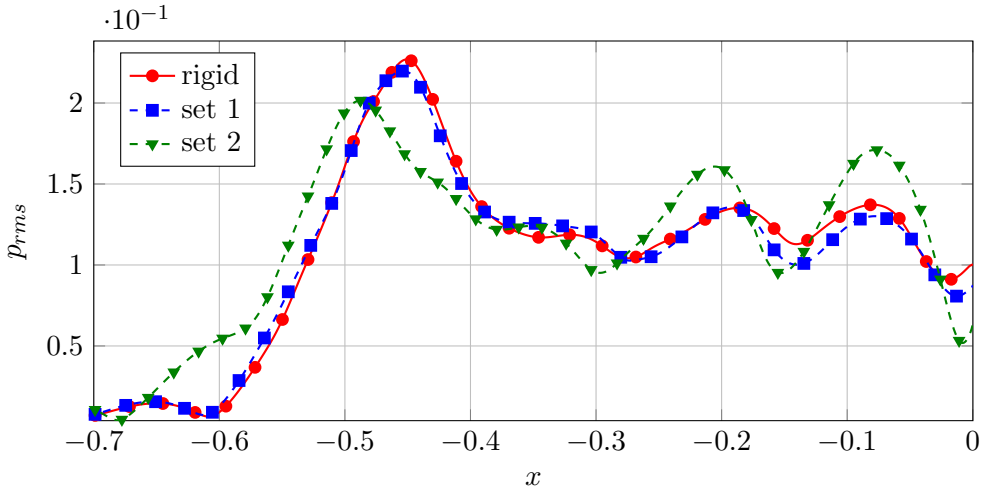

(c) distribution of pressure fluctuations around airfoil

Figure 5.19: Comparison of the skin-friction and pressure fluctuation distribution around the airfoil upstream of the extension between the rigid and elastic TE extensions.

negative peak values downstream of that show significantly lower amplitudes. The same differences can also be found downstream of the reattachment point, indicated by the zero crossing to positive values, at $x = -0.45$. The results of the changed location and intensity of the separation bubble on the pressure fluctuations on the wall are presented in figure 5.19c. It is apparent that the pressure fluctuations are initially lower than the other two cases for parameter set 2. However, further downstream and in particular towards the TE they are significantly amplified. For parameter set 1 the opposite is true, but the differences to the rigid TE are notably smaller. As the pressure fluctuations at the wall contain the input to the TE noise mechanism a higher noise level is expected for higher pressure fluctuations.

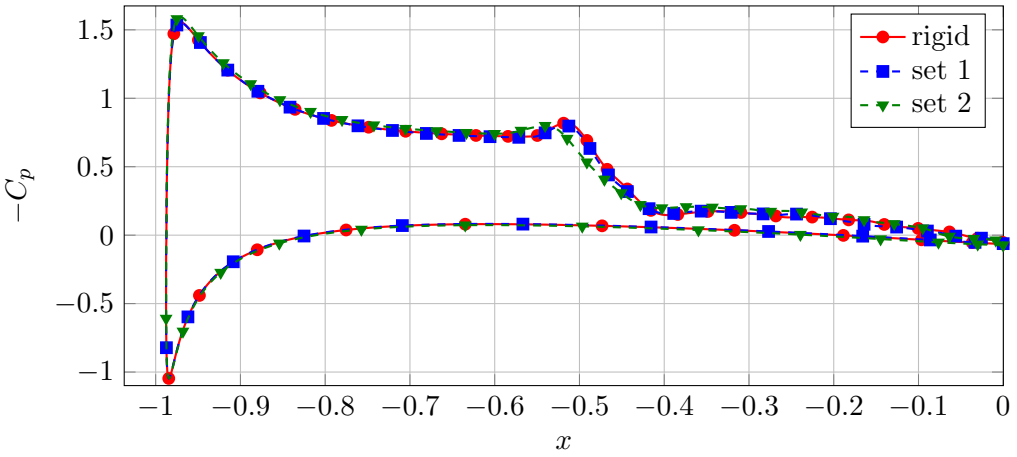

(a) global distribution of pressure coefficient

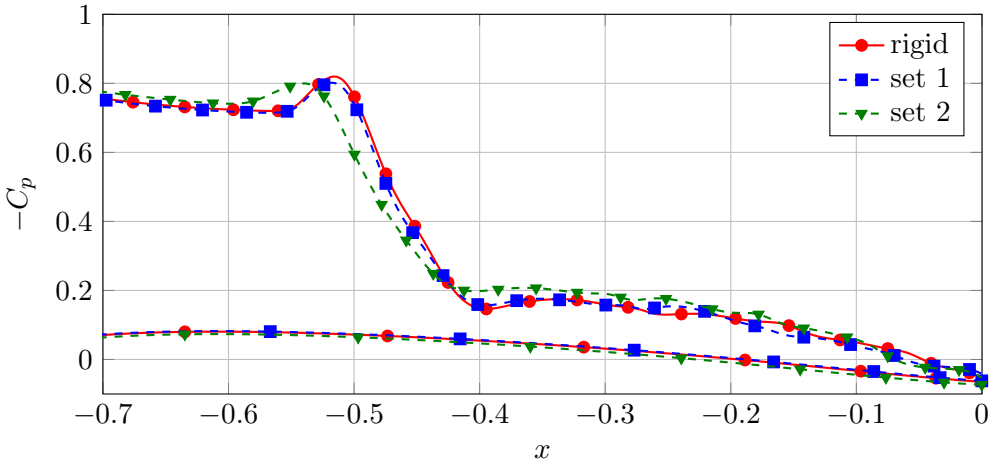

(b) distribution of pressure coefficient in vicinity of the separation bubble

Figure 5.20: Comparison of the pressure coefficient distribution around the airfoil upstream of the extension between the rigid and elastic TE extensions.

Finally, figure 5.20 compares the pressure coefficient distribution defined by (Anderson, 2001)

$$C_p = \frac{p - p_\infty}{\frac{1}{2}\rho_\infty U_\infty^2}\,, \tag{5.1}$$

around the airfoil body, where the density ρ, pressure p and velocity U with the subscript ∞ refer to freestream quantities. The most notable difference is at the location of the reattachment of the separation bubble around mid-chord and the region downstream of that. Here, the elastic TE extension with parameter set 3 shows lower pressure values on the suction side, i.e. a higher $-C_p$ for $x > -0.4$. This results in a change of the lift generated by the airfoil. For parameter set 2 the lift is increased by 3.23% relative to the case with the rigid TE extension. The opposite is true for parameter set 1 where the lift is reduced by 1.1%.

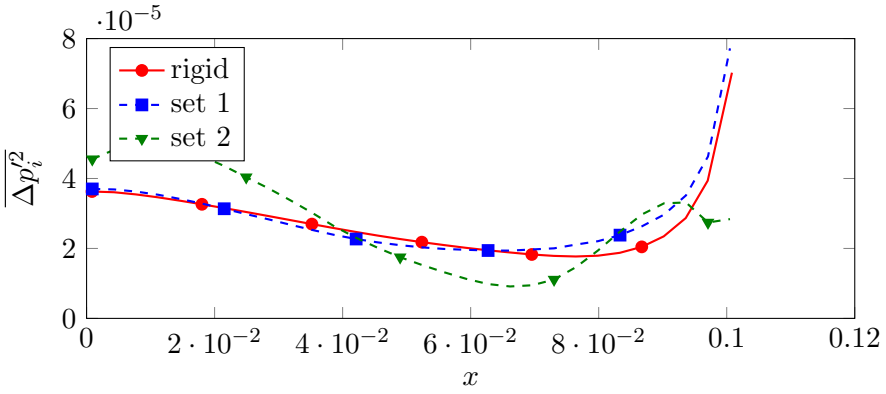

(a) incident pressure difference fluctuations

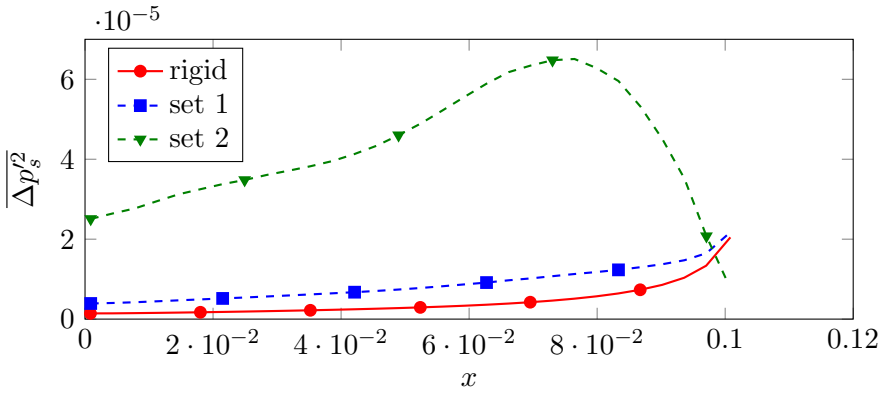

(b) scattered pressure difference fluctuations

Figure 5.21: Comparison of the variance of the pressure difference $\Delta p'$ for the elastic and rigid TE extensions.

In summary, the noise increase can be partly related to a global change of the flow around the airfoil. In particular for parameter set 2 the location and intensity of the separation bubble changes qualitatively which also results in an increase of the lift that is generated. Thus, a fair comparison between rigid and elastic TE extensions is difficult. However, the analysis of the incident and scattered pressure differences following in the next paragraph will be used to develop some initial indications of the physical mechanisms responsible for the increased noise level.

Figure 5.21 presents the comparison of the variance of the incident and scattered pressure difference for the two elastic and rigid TE's. For the incident pressure field it can be appreciated that parameter set 1 seems to have little effect on the pressure field in the first half of the extension. Towards the end of the extension it is amplified more strongly compared to the rigid case, leading to a higher peak at the TE location. This also leads to a higher amplitude of the scattered pressure fluctuations presented in figure 5.21b. Thus, the increased noise level can be attributed to an amplification of the incident pressure field which then leads to a higher noise radiation. When parameter set 2 is used the incident field is modified significantly which is consistent with the amplification

of the wall pressure fluctuations on the suction side found in figure 5.19c. However, the scattered pressure fluctuations at the TE are significantly reduced which is in contrast to the far-field observations. Thus, the significantly increased noise level must originate from another noise source and it is speculated that it is the motion of the structure itself.

5.3 Summary of the Findings

The chapter first investigated the effect of a rigid TE extension on its noise radiation and the flow around the airfoil. The simulated data showed that a rigid TE extension reduces the noise radiation. This noise reduction was attributed to changes in the location and strength of the vortex shedding which also resulted in a reduced loading.

For the two parameter sets investigated as elastic TE extensions, it was found that the structural motion was dominated by the vortex shedding frequency. In the acoustic far-field higher noise levels in comparison to the rigid TE were found at the vortex shedding frequency for both parameter sets. For the case with the highest deflections the vortex shedding frequency was found to lock in with the second natural frequency. This led to a global change of the flow with different location and intensity of the separation bubble. As the incident pressure fluctuations were reduced with that parameter set it is argued that the high excess noise originates from the structural motion. Pröbsting & Yarusevych (2015) reported changes in the overall separation bubble characteristics and lock in of the vortex shedding frequency to that of the acoustic excitation. It might well be that the noise generated by the motion of the structure acted as acoustic excitation in the current application and thus led to the observed global changes. The elastic extension with smaller deflections was found to amplify the incident pressure fluctuations which led to an increased noise level as well.

In general, a fair comparison between the rigid and elastic TE extensions was found to be challenging as changes in the hydrodynamic near-field were found far upstream of the actual TE locations. Therefore, a greater focus of this work was put on an alternative setup of a flat plate with a vortex generator and an elastic TE that is introduced in the following chapter 6.

Chapter 6

Trailing-Edge Noise from an Elastic Flat Plate

In the following chapter TE noise from a flat plate with an elastic TE is considered in two dimensions. The computational setup of the case is described in section 6.1. Section 6.2 gives a first overview of the acoustic field and the hydrodynamic sources region. It is followed by an investigation of the motion of the elastic fraction of the TE in section 6.4. The comparison of the rigid and elastic TE's are split into a discussion about the influence of different structural parameters (6.5.1) and the effect of structural damping (6.5.2). Finally the findings of this chapter are summarized in section 6.6.

6.1 Computational Setup

The computational domain for this study is visualized in figure 6.1. It incorporates the TE of a flat plate and its associated wake region. The plate divides two laminar boundary layers that are prescribed at the inflow boundary symmetrically with a displacement thickness of $\delta^* = 7.243 \times 10^{-3}$ using an integrated characteristic boundary condition. The boundary layer grows as it convects along the plate to a displacement thickness of $\delta^* = 2.360 \times 10^{-2}$ at the TE. The freestream Mach number was $M = 0.4$. The global Reynolds number was $Re = 7.5 \times 10^4$ based on unit freestream velocity and unit length scale. It can be considered as the inverse of the non-dimensional viscosity. This results in a Reynolds number at inflow and trailing-edge based on displacement thickness of $Re_{\delta^*} = 543.21$ and $Re_{\delta^*} = 1770.26$, respectively.

The TE thickness was set to $h_{TE} = 2.5 \times 10^{-3}$ which results in a thickness parameter of $h_{TE}/\delta^* = 0.106$. Considering the findings of Brooks & Hodgson (1981), the TE can be considered thin and noise from vortex-shedding due to TE bluntness is expected not

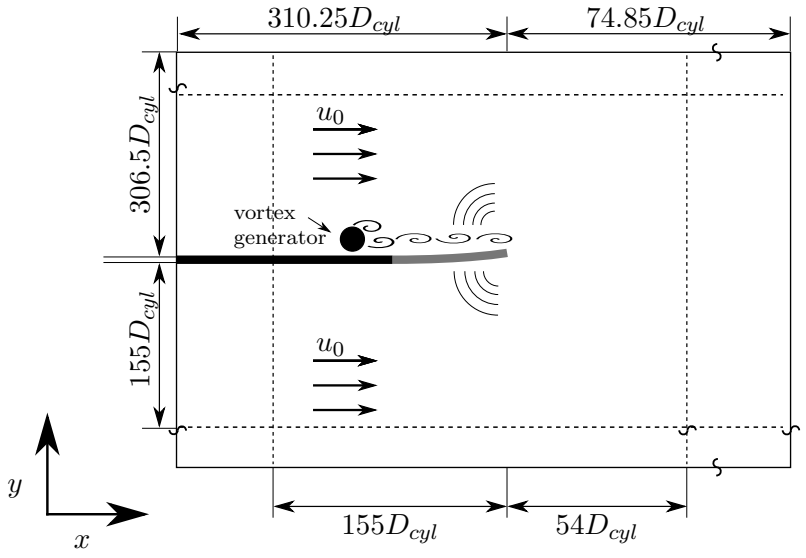

Figure 6.1: Schematic of the computational setup with the elastic part of the flat plate in grey with a length of $L_s = 8.816 D_{cyl}$. The domain is symmetric to the flat plate and the dimensions in the upper half denote the lengths of the entire domain and the dimensions in the lower half those of the measurement region. Note that the origin is located at the TE and the axis in the sketch only indicate the directions.

to occur as the current case is below the threshold of $h_{TE}/\delta^*_{TE} \approx 0.3$.

In order to create pressure fluctuations that scatter from the TE and drive the structural motion when an elastic TE is considered, a cylinder acting as a vortex generator was inserted upstream of the elastic fraction of the plate on the upper side of the flat plate. Singer *et al.* (2000) employed a similar approach using a vortex generator plate at 98% chord of a NACA airfoil. Physically the strong vortices that will shed from the vortex generator are intended to imitate the vortex shedding from the laminar separation bubble of a NACA0012 at angle of attack $AoA = 5°$ for a Reynolds number of 5×10^4 (Jones *et al.*, 2008). The cylinder has a diameter of $D_{cyl} = 0.04$ and the origin is located at $(x = -0.4946, y = 0.0275)$. For the remainder of this and the following chapter all length scales will be normalized by this diameter unless stated differently. Note, the time is not scaled alongside. Thus, all derived quantities will be calculated with the original length scale to stay consistent with the original non-dimensionalization. In relation to the boundary layer the vortex generator reached from $0.324\delta^*$ to $2.051\delta^*$ of the undisturbed flow. The streamwise location is $12.37 D_{cyl}$ upstream of the TE. Using the global Reynolds number as dimensionless viscosity the Reynolds number based on the cylinder centreline velocity $2D_{cyl}$ upstream of the cylinder is $Re_{cyl} = 682$. Since the cylinder is within the boundary layer it can not be considered as a canonical cylinder flow and due to the vicinity to the wall or as canonical cylinder in a shear flow. However, despite the uncertainty about the exact value for Re_{cyl} it is most likely in the subcritical regime which is defined by $350 < Re_{cyl} < 200,000$ (Froehlich *et al.*, 1998). That means that the boundary layer of the cylinder remains laminar between stagnation and separation

point and the transition to turbulence occurs in the wake of the cylinder. However, since the simulations in this chapter were two-dimensional this prediction can only be verified in chapter 7.2 with three-dimensional simulations.

The dimensions of the computational domain illustrated in figure 6.1 are symmetric with respect to the flat plate. The dimensions of the whole domain are indicated in the upper half of the figure and the dimensions of the measurement area with a fine resolution in the lower part.
A common challenge in aeroacoustic simulations is the disparity of the length scales of the source region and the acoustic wave length which is expressed by the very large measurement and domain size compared to the cylinder radius D_{cyl} or the thickness of the TE ($D_{cyl} = 16h_{TE}$). A priori the beginning of the acoustic far field can be estimated by $R_{source} \geq \lambda_a$, where the distance from the source region is R_{source} and the acoustic wave length is λ_a. The acoustic wave length for a given frequency f can be calculated with $\lambda_a = c/f$, where c is the speed of sound. In general, the domain size has to be as small as possible due to limited computational resources. In the current setup the grid was designed such that the measurement region where the grid is well resolved ends at a distance of approximately λ_a for the frequency $f/f_{in} \approx 0.45$, where $f_{in} = 0.94$ is the frequency of the dominant peak in the spectrum of the far-field (determined from preliminary simulations). This means that the measurement region covers $155D_{cyl}$.
The advantage of the infinite extent of the plate in the upstream direction is that there is no circulation around the plate such that a meaningful comparison between the rigid and elastic TE‘s is possible. In addition, with the design of this setup, the noise that will be observed on the lower side of the plate will only originate from the TE and not be contaminated by other noise sources such as the vortex shedding from the cylinder.

At the freestream boundaries above and below the plate and at the outflow zonal characteristic boundary conditions (Sandberg & Sandham, 2006) were applied to allow acoustic waves and vortical structures in the wake to leave the computational domain without spurious reflections. For the freestream boundary the number of points employed for the zonal ramp was 40 and for the outflow 140. A constant pressure and density level was maintained by combining the zonal boundary condition with an approach suggested by Poinsot & Lele (1992), as described in section 2.1.3 at the outflow. In addition, it was found that a high resolution of at least $\Delta x = 8.5 \times 10^{-3}$ was needed at the outflow in order to avoid reflections. This is in contrast to the most common strategies where grid stretching is employed.
From figure 6.1 it is apparent that the dimensions of the measurement area in the upstream direction are only half of the dimensions of the domain, approximately. This was necessary to eliminate spurious reflections from the integrated characteristic inflow boundary condition and the zonal boundary conditions at the freestream. Along with

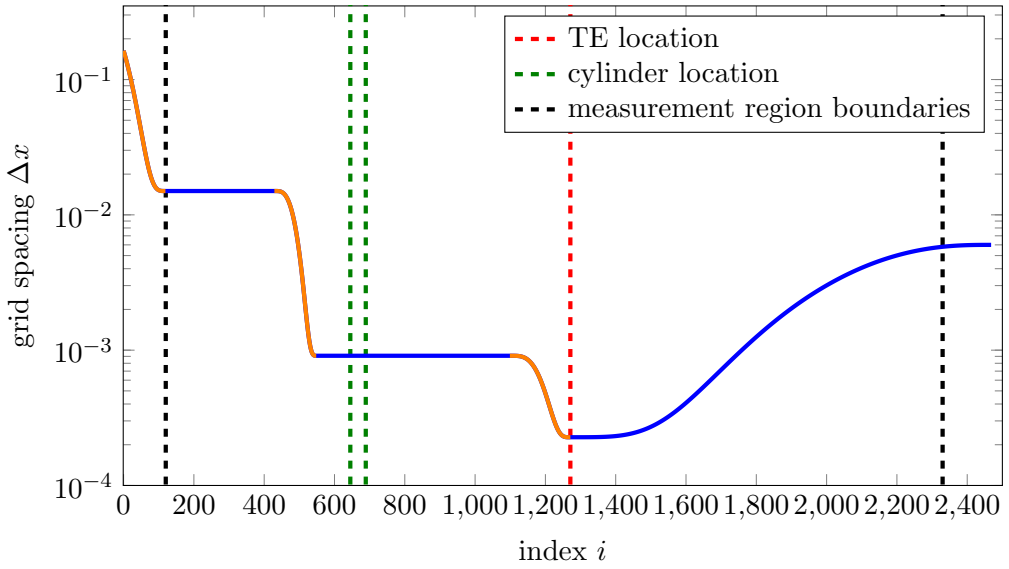

(a) grid spacing in x-direction for intermediate resolution level

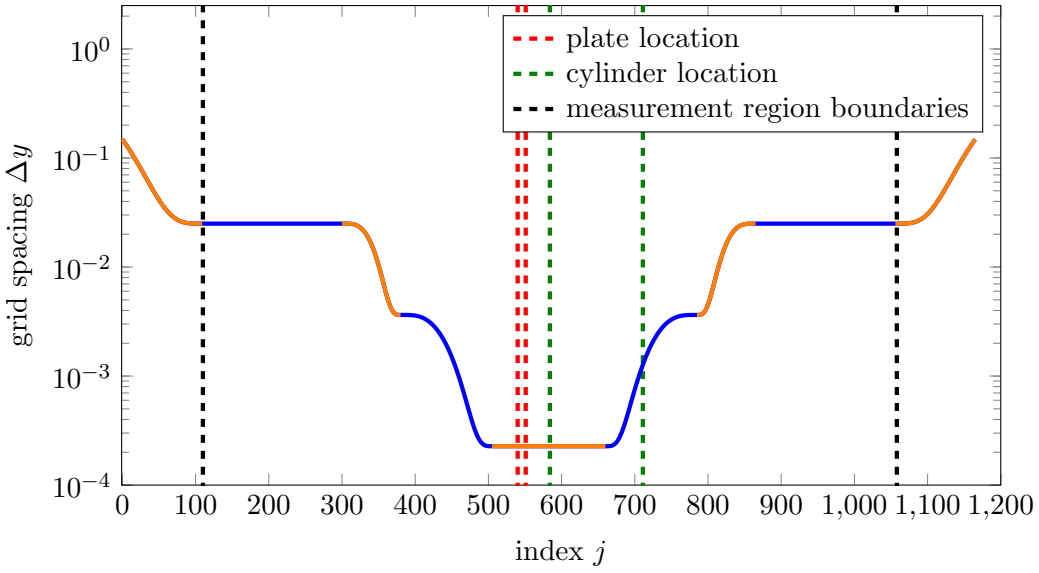

(b) grid spacing in y-direction for intermediate resolution level

Figure 6.2: Distribution of grid spacing $\Delta h_{i+1} - \Delta h_i$ where the individual segments are coloured in orange and blue.

the coverage of a large spatial area where the acoustic waves continue to decay the grid resolution was reduced severely.

6.1.1 Grid Resolution, Distribution and Generation

Figure 6.2 shows the distribution of the grid spacing for the whole domain over the grid points in the streamwise (6.2a) and the wall normal (6.2b) directions, respectively. The location of the TE/plate, cylinder and boundaries of the measurement region are indicated with dashed lines. The grid resolution that was chosen is motivated and justified

resolution	N_{TE}	Δx_{TE}	Δy_{TE}	N_x	N_y	N_{tot}
1 – low	12	4.546×10^{-4}	2.27×10^{-4}	2140	1167	2.497×10^6
2 –intermediate	12	2.273×10^{-4}	2.27×10^{-4}	2470	1167	2.882×10^6
3– high	12	1.136×10^{-4}	2.27×10^{-4}	2600	1167	3.034×10^6

Table 6.1: Number of grid points and spacing at the TE, number of grid points in each direction and the total number of points for each resolution level. The resolution of the vortex shedding cylinder and the acoustic far-field is the same for all cases.

in the following paragraphs.

The thickness of the TE was discretized with 12 grid points to avoid effects of surface coupling through the filtering which uses a stencil with a width of 10. In order to keep the discretization of the TE constant over time for the moving body, the grid spacing was equidistant for $-0.25D_{cyl} < y < 0.625D_{cyl}$. This is in contrast to the domain size not symmetric and ensures that points are only clustered where the structure moves.. For the baseline case the grid had an aspect ratio of $\Delta x_{TE}/\Delta y_{TE} = 1$ at the TE.

In the hydrodynamic source region the resolution around the cylinder was set to $D_{cyl}/\Delta x = 44$. Considering the relatively high Reynolds number of $Re_{cyl} = 653$ this resolution is likely not to be sufficient to fully resolve the flow around the cylinder. However, the vortex shedding from the cylinder is considered as input to the TE noise mechanism only and the focus of this study is the effect of TE elasticity on the radiated noise. Since this input will not change between the elastic and rigid TE's a comparison is valid and conclusions can be drawn from it.

Table 6.1 summarizes the number of grid points and the resulting grid spacing at the TE and the resulting total number of grid points for three different resolution levels. The aforementioned baseline case refers to the intermediate resolution level. It is apparent that the levels differ in the streamwise grid spacing at the TE only. The aim of the grid convergence study here is to ensure that the TE noise mechanism is represented accurately. As mentioned earlier the vortex shedding from the cylinder is likely to be under-resolved and therefore the vortex shedding might change with resolution. For an appropriate comparison between the three different resolution levels the grid spacing around the cylinder was therefore kept constant. Due to the fully-structured grid, this also implies that the wall normal grid resolution at the TE remains constant. However, the strongest gradients are expected in the streamwise direction imposed by the geometric singularity at the TE. If these streamwise gradients can be represented accurately it is expected that the resolution in the wall normal direction is also sufficient.

In order to make the simulations computationally affordable, the grid resolution had to be adapted according to the important length scales in the different regions of the domain. In the source region around the cylinder and the trailing-edge the relevant length scale is the cylinder diameter. In the outer region, hereafter denoted by acoustic field, the acoustic wave length λ_a is the relevant length scale. As $\lambda_a = c/f$ it is apparent that this length scale depends on the frequency considered. When discussing the resolution of the acoustic field the highest frequency that should be resolved is relevant as it is associated with the shortest acoustic wave lengths. In the current setup acoustic waves are resolved with a minimum of $n_{p/\lambda_a} = 10$ grid points per acoustic wave length up to a frequency of $f_a/f_{in} = 10.64$. In the direction normal to the mean flow the resulting resolution is $\Delta y = c/f_{res}/n_{p/\lambda_a} = 0.625 D_{cyl}$ for the acoustic field. Due to the mean flow in the opposite direction of the upstream noise radiation direction the acoustic wave propagation speed in that direction is reduced to $c = u_\infty/M - u_\infty$ which results in a grid spacing of $\Delta x = 0.375 D_{cyl}$.

The resolution at the inflow and freestream was $\Delta x_{\text{inflow}} \approx 4 D_{cyl}$ and $\Delta y_{\text{freestream}} \approx 3.7 D_{cyl}$, respectively. This coarse grid spacing was required in order to damp acoustic waves travelling towards the inflow and freestream boundary. It is in contrast to the resolution required at the outflow, where it was found that a high resolution of $\Delta x_{\text{outflow}} = 0.2125 D_{cyl}$ was needed. The difference between these requirements is likely to be due to the difference of the flow features passing the boundary. For the inflow and the freestream, acoustic waves have to leave the domain without reflections. Trailing-edge noise radiates predominantly in the upstream direction and therefore the amplitudes of the acoustic waves passing the outflow boundary are significantly lower. In addition the energy transported by acoustic waves is orders of magnitude lower than for the vortical structures in the wake that also pass the outflow boundary.

The grid was generated combining polynomial functions that were defined independently in each of the intervals visualized by the alternating blue and orange line colour in figure 6.2 as a function

$$f: \ \text{index}_{i,j} \rightarrow \text{location}_{x,y} \qquad .$$

The order of the polynomials was adapted to the number of boundary conditions, i.e. the location, the grid spacing and the conditions needed to match the higher derivative of the neighbouring segments. They were matched exactly up to the fourth derivative, i.e. the third derivative of the grid spacing. In principle, the higher derivatives could take arbitrary values, however, it was found more practical to set these higher derivatives to zero. This grid generation strategy has the advantage that the grid point distribution can be optimized independently of other segments and the grid resolution can be controlled conveniently. Apart from the grid resolution itself, it was found that grid stretching can lead to non-physical effects such as internal reflections from grid regions

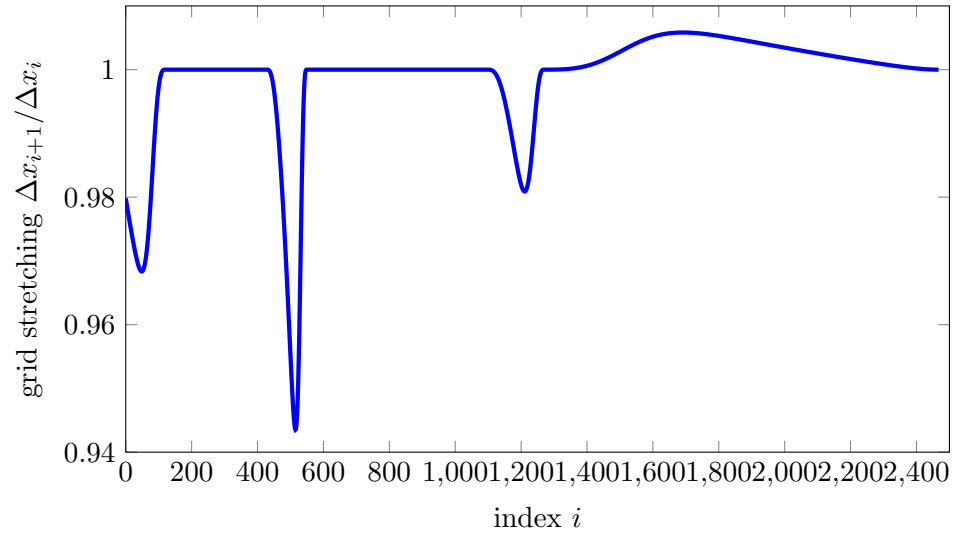

(a) grid stretching in x-direction

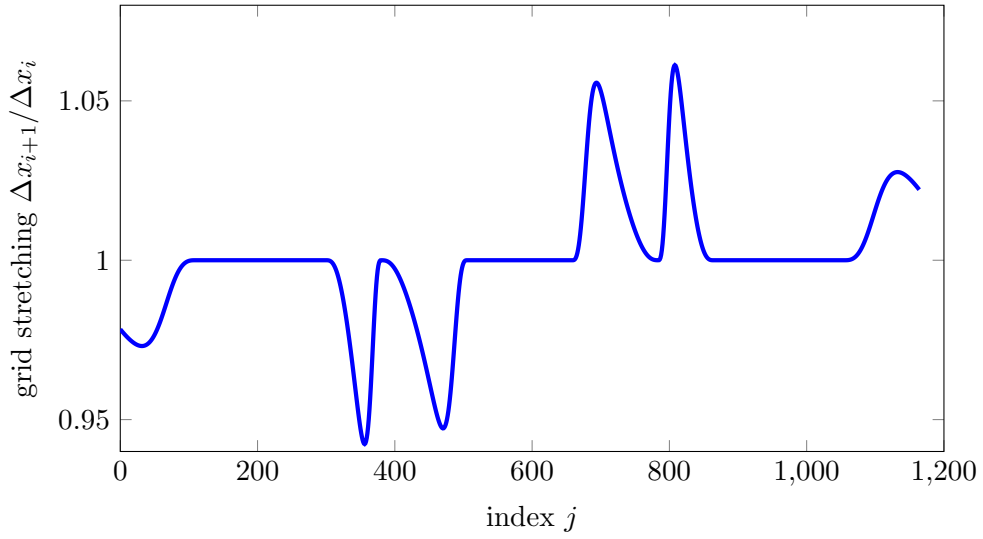

(b) grid stretching in y-direction

Figure 6.3: Stretching $\Delta h_{i+1}/\Delta h_i$ of the computational grid.

with high stretching. Figure 6.3 shows the grid stretching $\Delta h_{i+1}/\Delta h_i$ for both grid directions. Care was taken that the grid stretching was lower than 6% which proved to avoid any spurious influence on the flow field. In principle, even lower values might be desirable but the number of grid points needed to further reduce the grid stretching rendered the overall grid count computationally unaffordable.

The setup with a rigid TE was also simulated with body-fitted boundary conditions for the plate as reference. In that case the BDIM was only employed to represent the vortex generator cylinder. For the body-fitted reference case a multi-block topology with 3 blocks using characteristic interface conditions was used. The block boundaries were aligned with the TE, i.e. $x = 0$, resulting in one block above and below the plate and

one for the wake. It should be mentioned that the exact representation of the geometric singularity at the TE had a significant effect on the resulting acoustic field. The same geometry was also simulated with a five block setup using a halo cell approach for the connection of the blocks but it was impossible to obtain consistent results for different grid resolutions due to the difficulties of the exact representation of the TE such as which finite difference stencils to choose, filtering, etc.

In all cases where the BDIM was employed to represent the rigid and elastic flat plates the smoothing region half-width was set to $\epsilon/\Delta y_{TE} = 2$. The cylinder was located on a grid that was not equidistant and in addition coarser compared to the TE. In order to enable a reasonable smooth representation of the cylinder the smoothing region half-width was set to $\epsilon/\Delta y_{TE} = 9$ which resulted in $\epsilon/\Delta y_{\text{cylinder top}} = 0.5$ at the location with the coarsest grid resolution around the cylinder.

6.1.2 Structural Parameters

	E_s	ρ_s	f_1/f_{in}	f_2/f_{in}	μ_m
set 1	9.05×10^6	600	0.46	2.86	0.24
set 2	9.05×10^7	400	1.77	11.08	0.35
set 3	1.82×10^6	400	0.25	1.57	0.35
set 4	9.05×10^5	600	0.14	0.90	0.24

Table 6.2: Structural parameters which are given by the Youngs modulus E_s and the structural density ρ_s, which are both non-dimensionalized with freestream quantities or combinations thereof. In all cases the length of the elastic fraction was $L_s = 8.816 D_{cyl}$ and the thickness of the plate $h_{TE} = 1/16 D_{cyl}$. Furthermore, the first two natural frequencies f_1 and f_2 of the structure in vacuo are listed. They are normalized by the frequency of the most energetic pressure fluctuations f_{in} on the plate. The added mass coefficient is given with μ_m as defined in equation 2.20.

The structural parameters for the simulations employing an elastic TE are summarized in table 6.2. The Youngs modulus E_s determines together with the height of the TE h_{TE} how stiff the elastic fraction is and thus how high the deflections with a given pressure load from the fluid will be. Furthermore, it determines the natural frequencies of the structure as detailed in equation 2.18. The natural frequencies are normalized by the frequency of the most energetic pressure fluctuations f_{in}, which was determined from precursor simulations and will be investigated in detail in section 6.2. When the ratio f_1/f_{in} and f_2/f_{in} is an integer, resonance is expected to occur. The value of the ratio also determines if the structure can react to pressure fluctuations in the flow, i.e. how high the inertia is. The parameter set 1 was chosen such, that measurable deflections, which can be resolved appropriately by the BDIM, could be expected. Furthermore, care was taken that the first two natural frequencies of the structure were in the range

of the dominant frequency of the pressure disturbances to ensure that the relevant time scales of the structural forcing and motion match. This is also one of the reasons why only a fraction of the flat plate was considered to be elastic. All together this results in a ratio $f_1/f_{in} = 0.46 < 1$ and $f_2/f_{in} = 2.86 > 1$, which ensures that there is no resonance but the structure can follow pressure fluctuations in the flow reasonably well. Based on this reference case the structure was stiffened significantly for the parameter set 2. In combination with the reduced structural density this leads to natural frequencies that are higher than the input frequency, i.e. $f_1/f_{in} = 1.77 > 1$ and $f_1/f_{in} = 11.08 \gg 1$. Furthermore, smaller deflection amplitudes are expected in that case. The opposite is true for parameter sets 3 and 4 where the Youngs modulus was set to low values such that large deflections could be expected. As the natural frequencies relative to the forcing from the fluid are low, the plate is expected to follow the fluid forcing only partly.

During the elastic TE simulations the surface pressure values were gathered from all adjacent processes at the beginning of each time step. Then the structural deflection and velocity were calculated by the structural solver for the centre line of the structure on an independent equidistant grid with 53 grid points. Since the resolution of the structure grid is much coarser than that of the fluid domain the deflection and velocity between the structural points were interpolated linearly. This is acceptable since the changes between two adjacent structural points are minute and the BDIM introduces a certain level of smoothing. After calculating the deflection and velocity of the structure the BDIM was reinitialized at the end of each timestep. The fluid and the structural solver both use the same Runge-Kutta integration scheme for time-integration. Therefore a stronger coupling can be achieved by synchronizing both solvers in each Runge-Kutta sub-step. However, in a testcase no differences in the statistics could be found between the two levels of coupling. Since the stronger coupling increases the computational cost it was not employed in the simulations discussed below. Due to the efficiency of the implemented algorithms the runtime between simulations with elastic and rigid TE's did not show any reproducible differences.

6.2 Results – Overview

This section gives a first overview of the acoustic and the hydrodynamic near field. Figure 6.4 presents the instantaneous dilatation contours obtained from a simulation with an elastic TE to give a first overview of the acoustic field. The TE at $x = 0$ can be clearly identified as the origin of the acoustic waves. The change of the acoustic wavelength λ_a in the upstream direction due to the mean flow can also be observed. On the upper surface of the plate the noise level seems to be lower, most likely due to the interaction of the vortex generator with the TE noise. When the plot is examined closely, one can also find quadrupole noise sources in the wake. According to the acoustic analogy they

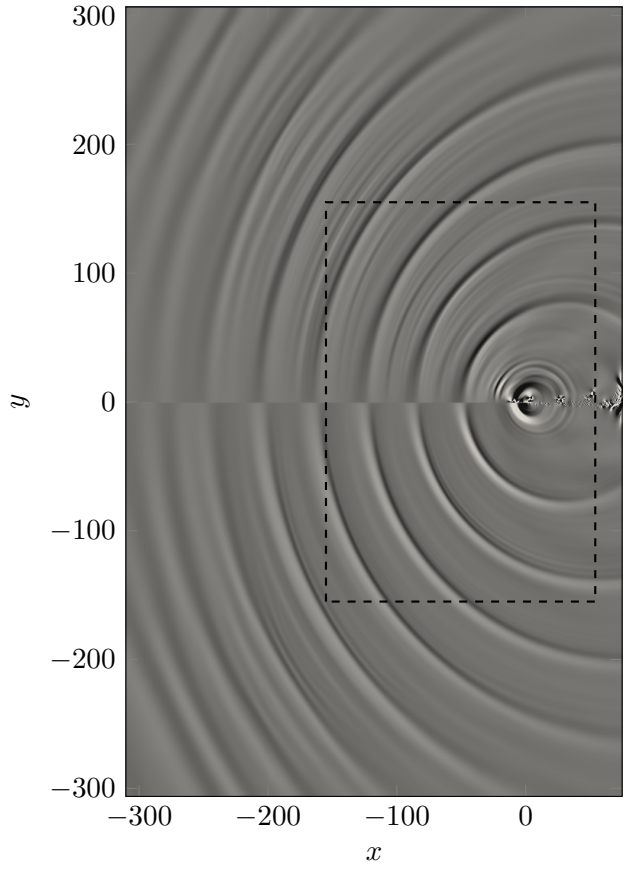

Figure 6.4: Instantaneous contours of dilatation $\nabla \cdot u$ showing the acoustic field of the simulation with the rigd TE using contour levels $0.07 < \nabla \cdot u < 0.07$. The dashed box indicates the boundary of the measurement region.

are weaker than the TE noise mechanism for low Mach numbers. However, Wolf *et al.* (2012*a*) showed that quadrupole sources can have a significant contribution for medium high frequencies at a moderate Mach number of $M = 0.4$. This can be confirmed from the dilatation field as there are only high wave number acoustic waves visible that originate from the sources in the wake. Overall it can be appreciated that there are no noticeable reflections from the domain boundaries or from the zones of the characteristic boundary condition at the inflow and outflow as well as the freestream boundaries. The measurement region is indicated with the dashed line.

Figure 6.5 visualizes the instantaneous flow field at an arbitrary snapshot in time in the vicinity of the vortex generator and the TE. The vortex generator produces strong, and from visual inspection, non-periodic vortices that are convected over the TE. The symmetry-breaking effect of the wall can be clearly seen by considering the shear layer above and below the cylinder and the structure of the shed vortices. Furthermore, the wake of the cylinder seems to strongly interact with the wall, which is apparent from the vortex topology when considering the streamwise locations $x = -8$ and $x = -2$. The region containing the vortex generator cylinder and the TE is the hydrodynamic source

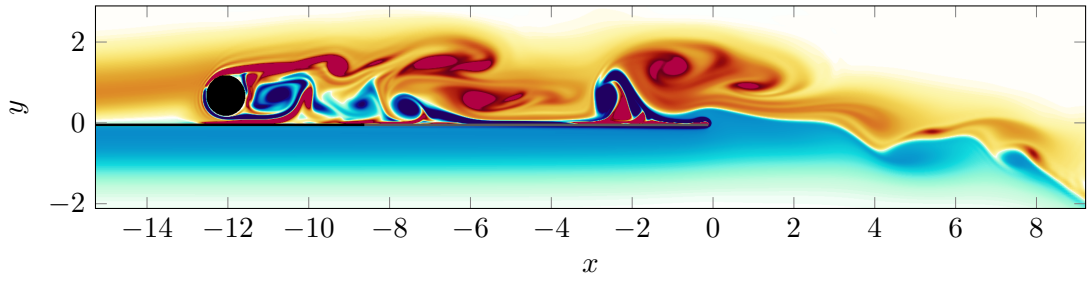

Figure 6.5: Contours of spanwise vorticity for $-50 < \omega_z < 50$ showing the vortex generator cylinder and the TE.

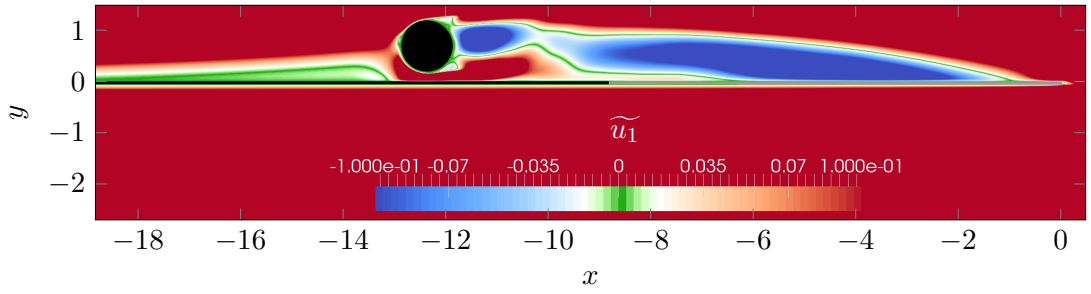

Figure 6.6: Contours of the favre averaged streamwise velocity component $\widetilde{u_1}$ in the vicinity of the rigid TE. The fraction of the plate that will be considered elastic later is coloured in grey.

region of the sound perceived in the far-field. In particular, the pressure fluctuations from the vortices are the incident pressure field for the TE noise mechanism. Therefore, the type of noise, i.e. tonal or broadband, will be determined by the characteristics of the pressure disturbances at the wall.

The following paragraphs will characterize the flow features present in the aforementioned source region statistically. Figure 6.6 presents the Favre averaged streamwise velocity component $\widetilde{u_1}$ in the vicinity of the vortex generator and the TE. The green contour color is representing the value $\widetilde{u_1} = 0$ and thus is the dividing line for recirculation regions. From the contours it is apparent that there is a narrow but elongated recirculation bubble upstream of the vortex generator which is likely to be caused by its blockage effect in the boundary layer. Downstream of the cylinder is a recirculation region, which is expected to be caused by the separating flow from the cylinder. In contrast to a canonical flow around a cylinder it is not symmetric with respect to the centreline but shifted and also inclined away from the wall. At the fraction that will be considered elastic in later cases, i.e. the part of the plate indicated in grey in figure 6.1, a long separation bubble adjacent to the wall can be identified. Taking the findings from the instantaneous flow field in figure 6.5 into account it seems that large scale vortices are shed from this separation bubble and interact with the vortex shedding from the cylinder.

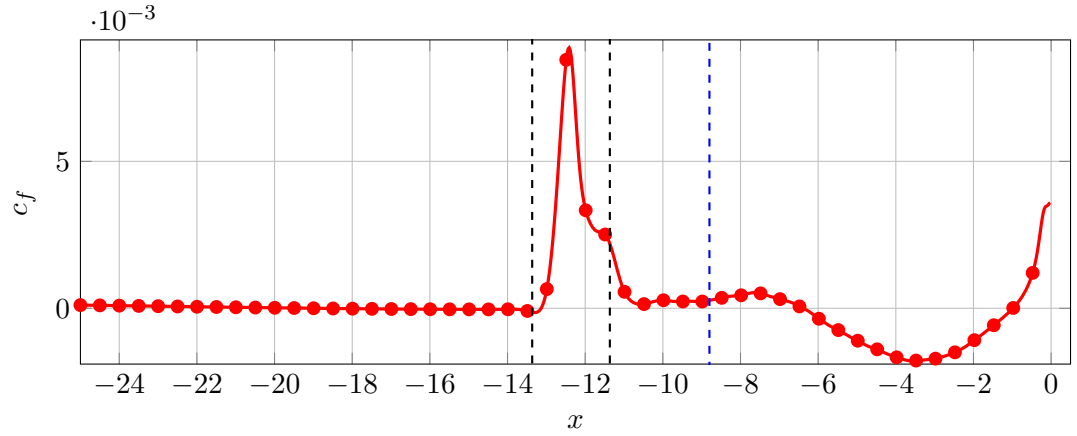

(a) skin friction coefficient over streamwise position upstream of the TE

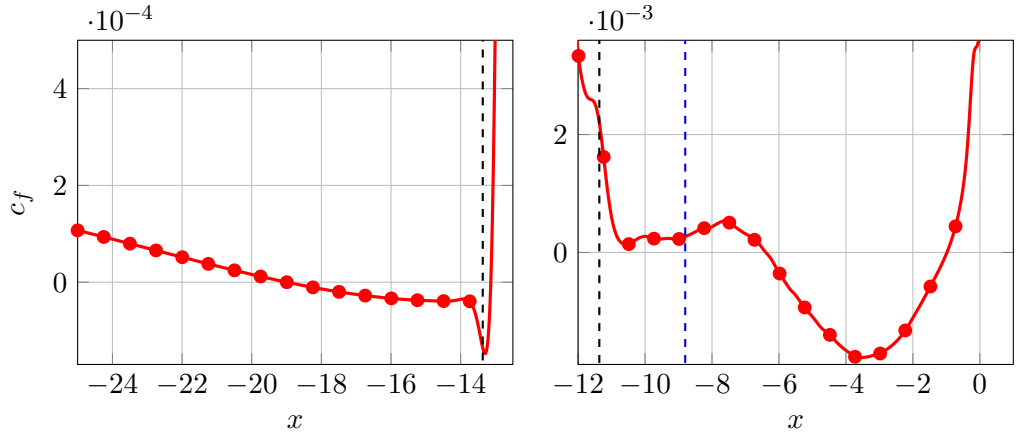

(b) skin friction coefficient upstream of the cylinder (c) skin friction coefficient between cylinder and TE

Figure 6.7: skin friction c_f as a function of the streamwise location for the rigid TE. The location of the cylinder is indicated by the black dashed lines and the fraction that will be considered elastic by a blue dashed line.

To further examine the recirculating regions adjacent to the wall in the flow and determine the extent of the these regions figure 6.7 presents the skin friction coefficient as a function of the streamwise location. From the overview in figure 6.7a, it can be seen that the unperturbed flow upstream of the cylinder shows a significantly lower magnitude of the skin friction than the flow affected by the presence of the cylinder. In the gap between wall and cylinder the flow is accelerated relatively close to the wall which leads to a very high skin friction in that region, clearly visible as the global maximum in figure 6.7a. Figure 6.7b examines the flow upstream of the cylinder in more detail. The negative value of the skin friction for $-19 < x < -13.1$ indicates the location of the recirculation region. Further downstream figure 6.7c focusses on the large separation bubble on the fraction that will be considered elastic and the TE region. On average the flow separates here $1.5D_{cyl}$ downstream of the start of the elastic fraction until $1D_{cyl}$ upstream of the TE.

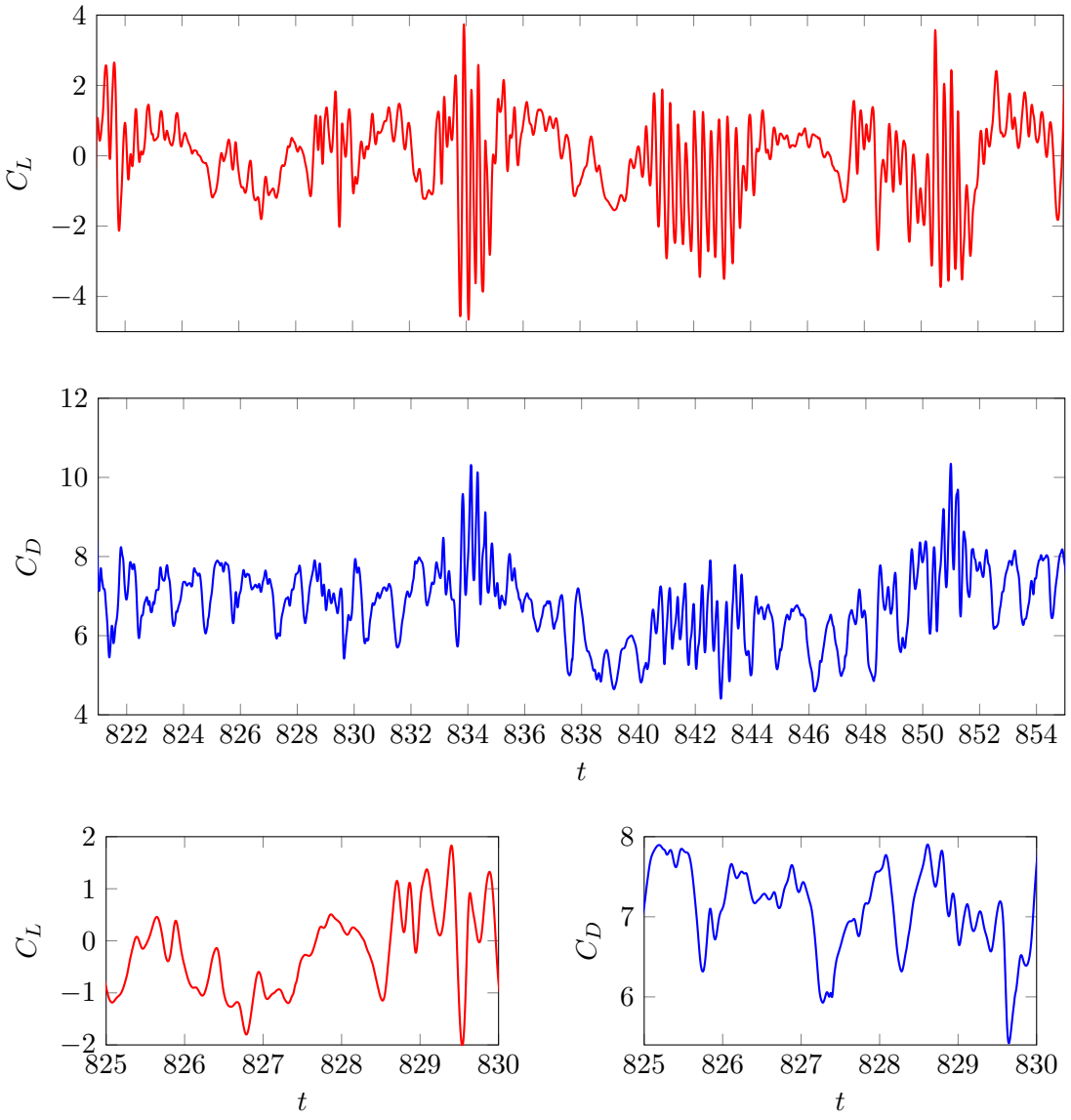

Figure 6.8: Lift and drag coefficient C_L and C_D of the vortex generator cylinder over time obtained from the simulations with the rigid TE.

Figure 6.8 shows the time history of lift and drag coefficients C_L and C_D from the vortex generator cylinder. Both show packets of high frequency fluctuations that are approximately 4 time units apart. Furthermore, relatively large fluctuations of low frequency are superimposed by small amplitudes with high frequency, which can be observed in more detail in the magnified window of time in figure 6.8c. To find the relevant frequencies of the force fluctuations on the cylinder and therefore determine the important frequencies in the system figure 6.9 presents the power spectral density of the lift (6.9a) and drag (6.9b), respectively. The dominant peak of the C_L spectrum is at a non-dimensional frequency of $f = 3.65$. It is expected that this is the frequency of the vortex shedding. With the cylinder diameter and the freestream velocity U_∞ this would result in a Strouhal number of $St = fD_{cyl}/U_\infty = 0.146$ which is slightly lower than the expected

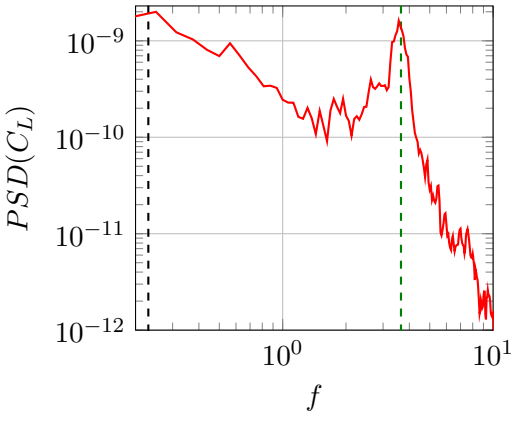

(a) power spectral density of C_L, the black dashed line marks a frequency of $f = 0.23$ and the green dashed line a frequency of $f = 3.65$

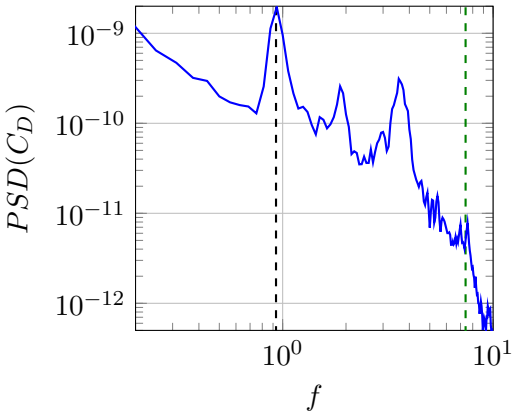

(b) power spectral density of C_D, the black dashed line marks a frequency of $f = 0.92$ and the green dashed line marks a frequency of $f = 7.4$

Figure 6.9: Power spectral density of lift and drag coefficient C_L and C_D from the vortex generator cylinder obtained from the simulations with the rigid TE. The green dashed lines mark frequencies that are expected to be related to the vortex shedding from the cylinder.

value of $St \approx 0.17$ for a cylinder in a uniform flow (Henderson, 1995). When the centerline velocity $2D_{cyl}$ upstream of the cylinder is used instead as relevant velocity scale, $St = 0.64$. In addition, a significant peak is in the very low frequency range, most likely related to the "packets" of fluctuations observed in the time-history. Indeed, a peak at a non-dimensional frequency $f = 0.23$ which equals a period of 4.34 non-dimensional time-units can be identified in the spectrum. In the spectrum of the drag coefficient the highest peak is at $f = 0.92$ and its first and second harmonic. The peak at $f = 7.4$ which is marked with a dashed line could potentially be related to the dominant peak of the spectrum of C_L as in theory f_D should be $2f_L$ for the vortex shedding from a cylinder. However, the fact that this peak is at very low amplitudes indicates that the main peak of the drag coefficient fluctuations is not originating from the vortex shedding itself.

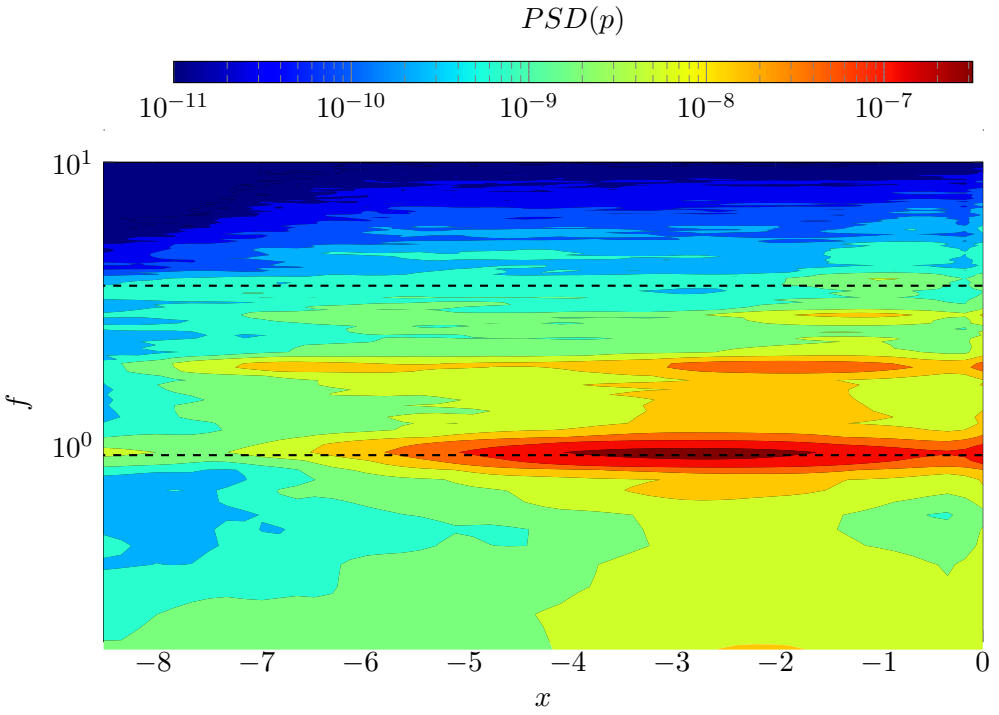

Figure 6.10: Power spectral density of the surface-pressure p on the upper side of the rigid plate as a function of the streamwise location. The dashed lines indicate the frequencies of the two dominant peaks in the power spectral density of the lift and drag coefficient presented in figure 6.9.

Figure 6.10 presents the power spectral density of the surface pressure on the upper surface as a function of streamwise location. With that it can be assessed where the dominant peak of force fluctuations originate and which frequencies will force the structural motion as well as being the input into the TE noise mechanism. The contours feature a peak at a frequency of $f = 0.92$ which is dominant at all locations along the plate and marked with a black dashed line. However, it is strongest for $-4 < x < -1.5$ which coincides with the end of the recirculation bubble. In addition the harmonics of this frequency can be identified. This indicates that the frequency that was found to contain most energy in the power spectral density of C_D can be attributed to the separation bubble on the upper surface and not to the vortex shedding of the cylinder. In fact, the frequency containing the most energy in the power spectral density of C_L (also marked with a black dashed line) can only be identified as a peak with very little energy close to the TE. Hence the most energetic input to the TE noise mechanism and the forcing for the elastic motion seems to be the pressure fluctuations induced from the vortex shedding from the separation bubble. In the remainder of this chapter all frequencies will be normalized by this $f_b = 0.916$ and will be denoted recirculation or bubble frequency. Since the interaction of the vortex shedding from the cylinder and the separation bubble is likely to interact with the noise radiated from the TE the analysis of the acoustic field in the following sections will focus on the lower side where only TE

noise or noise sources from the wake should be present.

The further statistical examination of the simulation results is split into three parts where the first section, 6.3, reports the results from a grid independence study and validates the BDIM with results from a body-fitted simulation for a rigid TE. In the second section, 6.4, the structural behaviour is analysed for different material parameters. Finally the rigid and elastic TE's are compared to each other in section 6.5.

6.3 Results – Grid Independence and Validation

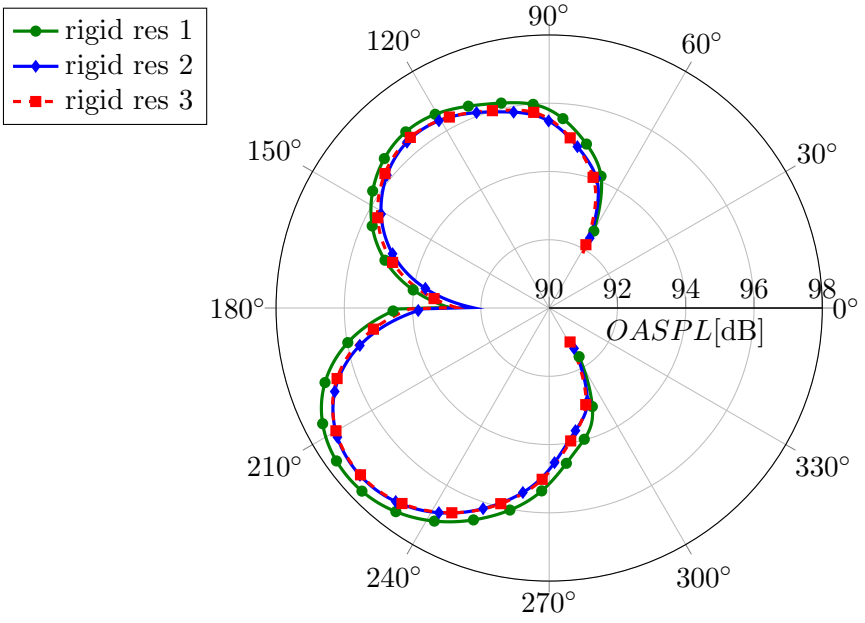

(a) Rigid TE: three different resolution levels.

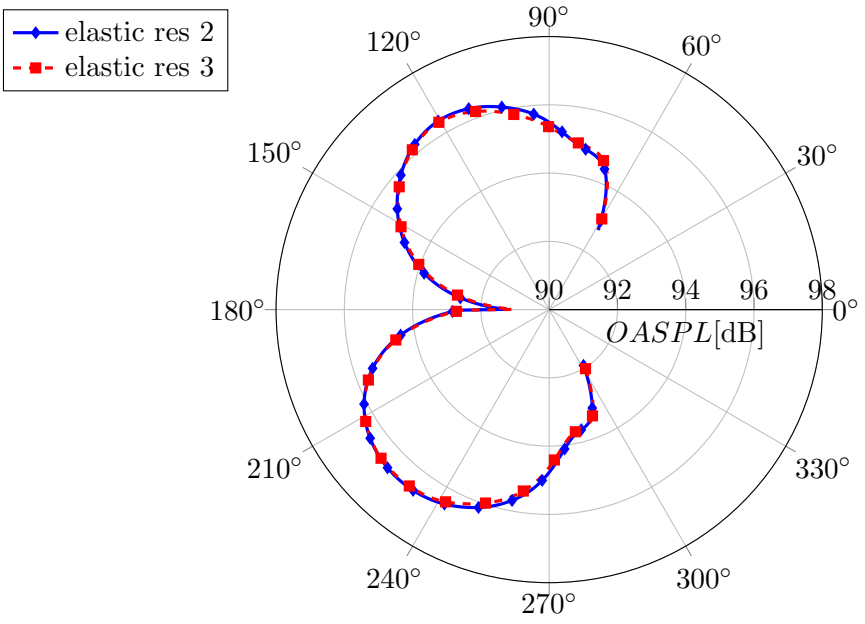

(b) Elastic TE: two different resolution levels using parameter set 1 .

Figure 6.11: Comparison of the directivity of the overall sound pressure level $OASPL$ at a radial distance of $r = 150D_{cyl}$.

A grid independence study has been carried out with three different resolution levels detailed in table 6.1. The overall sound pressure level directivity at a radial distance of $150D_{cyl}$ is shown in figure 6.11a for the rigid TE represented by the BDIM. It can be appreciated that all three resolution levels show the typical dipole shape with a higher overall sound pressure level in the upstream direction. The amplitude of resolution level

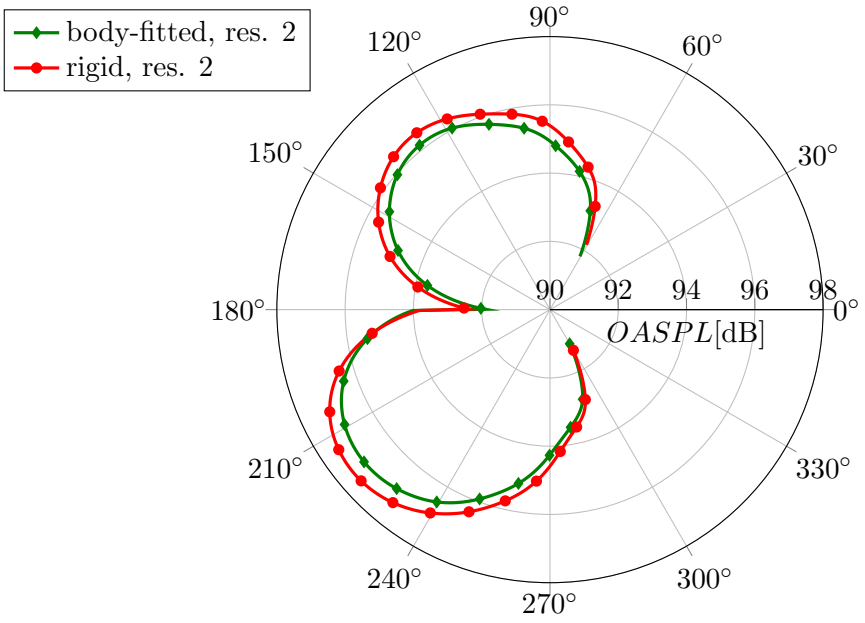

Figure 6.12: Comparison of the overall sound pressure level directivity at a radial distance of $r = 150D_{cyl}$ for rigid TE between the BDIM and body-fitted boundary conditions.

1 is $0.17dB$ higher than in the other two cases. Resolution level 2 and 3 can hardly be differentiated and indeed the maximum difference is only $0.02dB$, which is negligible. Thus, it can be concluded that grid-independence for TE noise is achieved with resolution level 2.

For the elastic TE the challenge is to represent the TE noise mechanism of a moving body accurately. Since grid resolution level 1 was not sufficient for the rigid TE it was not tested for the elastic TE. For resolution levels 2 and 3 the overall sound pressure level of the elastic TE is presented in figure 6.11b. It can be appreciated that the agreement between the two cases is as good as in the rigid case. In conclusion, grid resolution 2 can be considered sufficient to represent the TE noise from a moving TE as well.

Figure 6.12 compares the noise directivity obtained from simulations employing grids with resolution level 2 where the plate and TE were represented by body-fitted boundary conditions and the BDIM. Both cases show the same directivity pattern in terms of shape. However, the amplitude when employing the BDIM is overestimated by a maximum of $0.4dB$ on the lower side of the plate.

In order to ensure that the higher noise level in the BDIM case is indeed caused by the TE noise mechanism, figure 6.13 compares the wall pressure fluctuations between the BDIM and the body-fitted cases on the upper and lower side. Since the wall pressure fluctuations on the upper side can be considered as the input to the TE noise mechanism

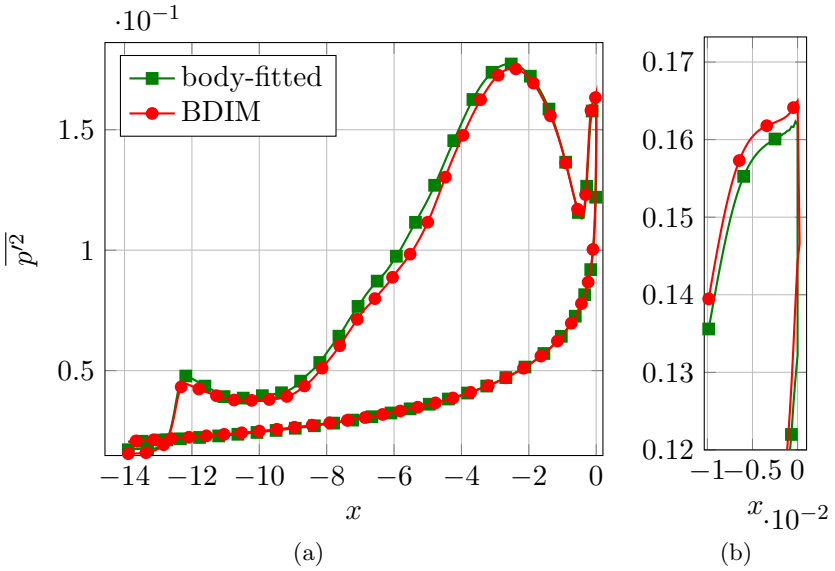

(a) (b)

Figure 6.13: Comparison of the wall pressure fluctuations between the body-fitted boundary conditions and the BDIM representing the plate. The upper side can be identified by the peak towards the end of the separation bubble at $x = -2$ and the higher amplitudes. The figure on the right shows a magnified view of the wall pressure fluctuations at the TE.

and are the scattered noise on the lower side of the plate, the peak at the TE should show the same trend as the noise level in the far field. The data was obtained at a wall normal distance equal to the smoothing region halfwidth ϵ to ensure that the data is physically meaningful and not influenced by the smoothing between the solid body and fluid domain in the BDIM cases. The pressure fluctuations on the upper surface can be identified by the higher amplitudes upstream of the TE in both cases. The location of the vortex generator cylinder can be clearly identified in the plot at $x = -13$ as it induces a distinct peak in the pressure fluctuations on the wall. The amplitude of this peak is lower in the cases where the plate is represented by the BDIM indicating that the interaction between the vortex generator cylinder and the rigid wall is represented in a slightly different way. At a location of approximately $x = -2.5$, the wall pressure fluctuations show a maximum that is slightly higher than the sharp increase at the TE location. However, the TE noise will be the dominant noise source for low Mach numbers (M^5 scaling) and the peak of the wall pressure fluctuations (M^6 scaling) will only have little contribution to the radiated noise. Overall, the pressure fluctuations on the upper surface are slightly higher when body-fitted boundary conditions are employed upstream of the TE. The opposite is true for the sharp increase and the peak of the wall pressure fluctuations towards the TE. This is consistent with the noise levels found in the far-field in the directivity pattern presented in figure 6.12 as the BDIM case shows a higher peak at the TE and exhibited a higher overall sound pressure level. This shows that the differences in the noise amplitude can be attributed to the exact representation of the TE using different boundary conditions. However, the difference between both

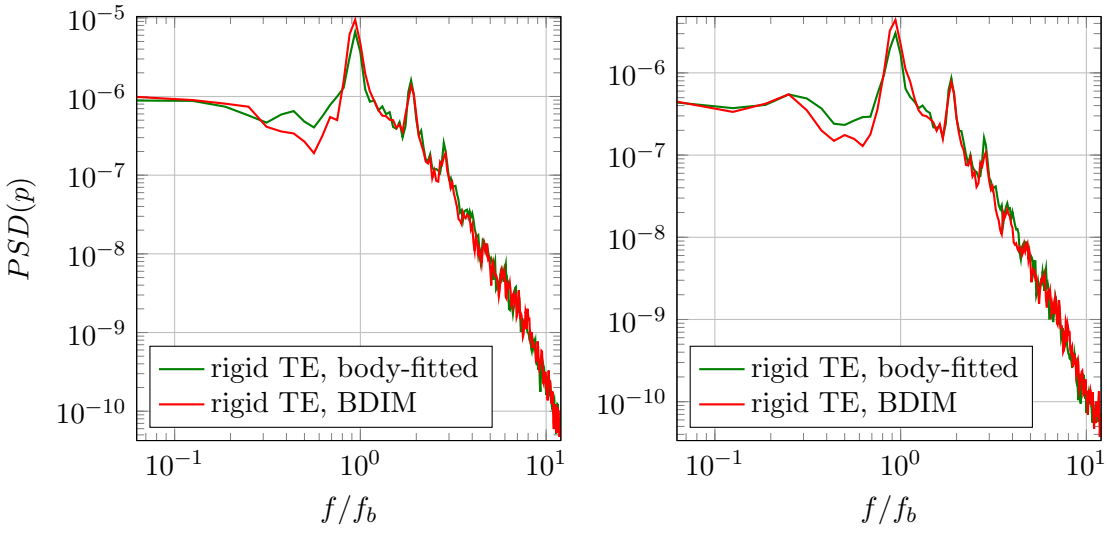

(a) $PSD(p)$ at a radial distance of $150D_{cyl}$ and an angle of $\theta = 225$

(b) $PSD(p)$ at a radial distance of $150D_{cyl}$ and an angle of $\theta = 270$

Figure 6.14: Comparison of the power spectral density of pressure in the acoustic far-field at a radial distance of $r = 150D_{cyl}$ for rigid TE between the BDIM and body-fitted boundary conditions with the resolution level 2. The azimuthal positions relate to the directions from the directivity in figure 6.12.

methods is small and it is argued that the BDIM is able to represent the physical mechanism of the TE noise radiation.

Figure 6.14 compares the power spectral density of pressure for the body-fitted and the BDIM cases at two different locations. They were calculated by averaging over 20 Hanning windows that had a length of 14.6 recirculation bubble cycles and an overlap of 57%. These parameters are used throughout the rest of this chapter unless stated differently. It can be appreciated that both spectra show peaks at the same frequencies. No peaks from spurious oscillations can be identified in the spectrum of the BDIM. Overall the amplitudes agree well. The most relevant deviation can be found at the recirculation bubble frequency where the amplitudes in the BDIM case are higher at both locations. Since this frequency is clearly related to the TE noise mechanism this behaviour is consistent with the findings from the surface pressure fluctuations presented in figure 6.13. In the frequency range below the recirculation frequency f_b the data obtained with body-fitted boundary conditions shows higher amplitudes than the BDIM case. However, the level of these amplitudes is more than an order of magnitude lower that the dominant peaks in the spectrum.

Considering the large uncertainty of the precise TE treatment in the case of the body-fitted boundary conditions the minor deviations found are reasonable. In addition the results from the grid independence study for the TE represented by the BDIM suggest

maximum frequency	[%] of total energy	grid points per acoustic wave-length λ_a
$f/f_b < 5$	97.659	20
$f/f_b < 7.5$	99.534	15
$f/f_b < 10$	99.870	10
$f/f_b < 12.5$	99.956	7.5

Table 6.3: Comparison of how much energy is contained in the spectrum for different cut-off frequencies at a location $-6.25D_{cyl}$ upstream of the TE and a distance of $2.4D_{cyl}$ above the plate. The last column is based on the far-field grid resolution. The energy was integrated by summing over the contribution from the individual frequency bins and multiplying by the width of the bin.

that there is no lack of resolution.

Table 6.3 summarizes the energy contents of the pressure signal for different cut-off frequencies at a location $-6.25D_{cyl}$ upstream of the TE and a distance of $2.4D_{cyl}$ above the plate. This location is above the wake with the vortices shed from the cylinder and the grid resolution is comparatively high. From the TE to this location acoustic waves with a frequency $f/f_{cyl} < 26.28$ are resolved with a minimum of 40 points per wave length. The second column of the table shows that when the energy content of the signal is integrated in the interval of $0 < f/f_b < 7.5$ the energy that is not contained in that frequency range is less than 0.5%. For the grid resolution chosen in the far-field it follows that the acoustic waves which contain more than 99.5% of the energy are resolved by at least 15 grid points per acoustic wave-length λ_a.

6.4 Results – The structural behaviour

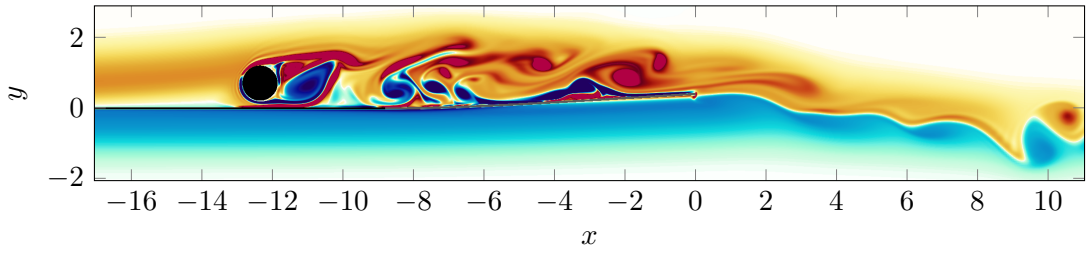

(a) parameter set 1

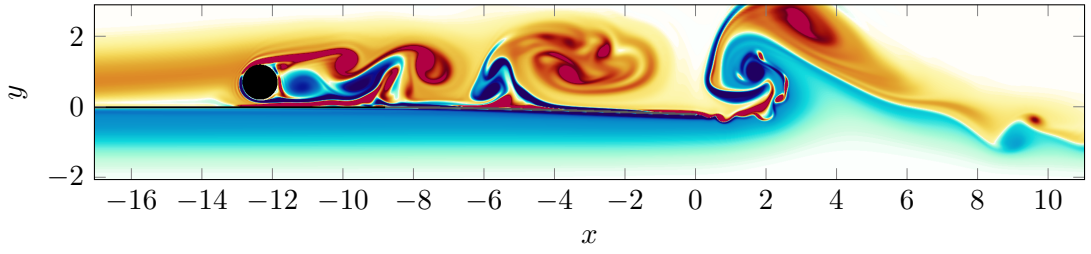

(b) parameter set 2

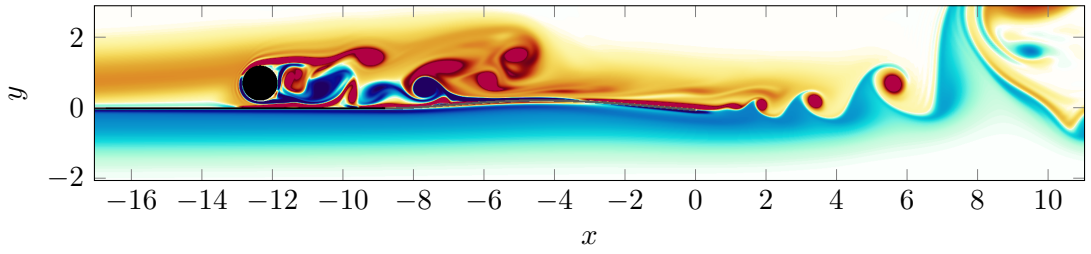

(c) parameter set 3

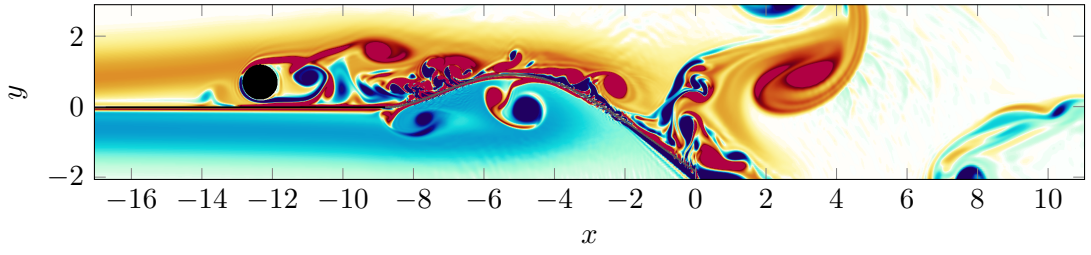

(d) parameter set 4

Figure 6.15: Contours of spanwise vorticity for $-50 < \omega_z < 50$ showing the vortex generator cylinder and the TE.

This section analyses the structural motion for the different structural parameter sets. Figure 6.15 gives a first impression of the instantaneous flow field around the elastic fraction of the flat plate and the vortex generator for different parameter sets. For parameter set 1 (6.15a) and 2 (6.15b) the deflection is of shape of bending mode 1 based on the visual impression of the shape of the TE deflection. Furthermore the amplitudes are moderate. The deflection of parameter set 3 (6.15c) is of mode shape 2 which is expected since the first natural frequency for this parameter set is significantly lower

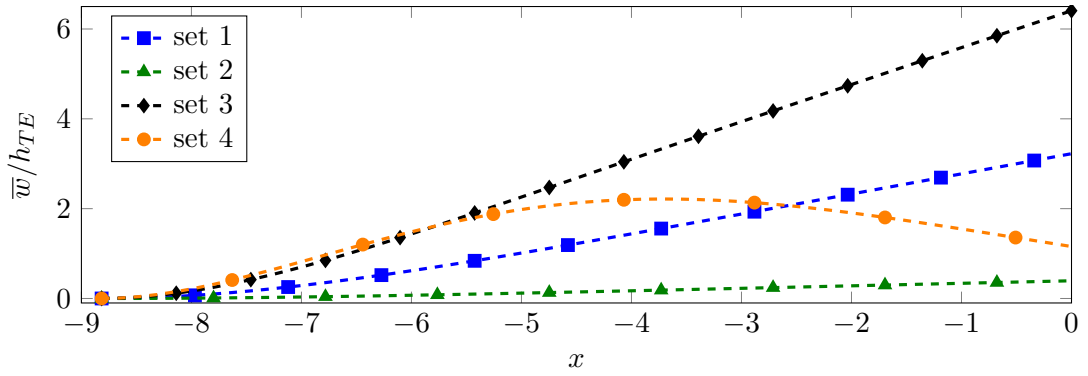

(a) Mean deflection $\overline{w}/h_{TE}$

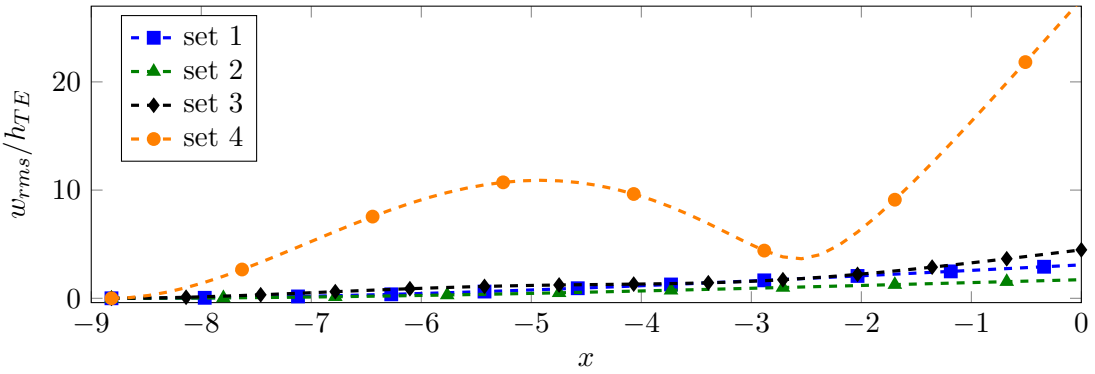

(b) Standard deviation of the deflection w_{rms}/h_{TE}

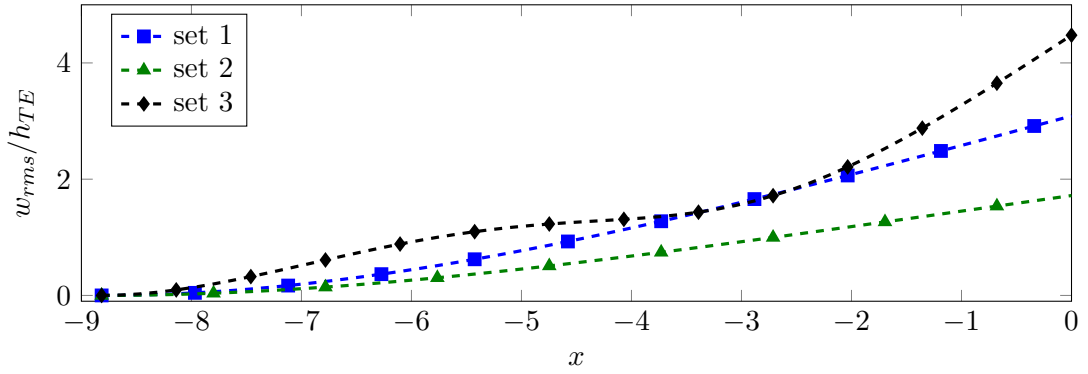

(c) Standard deviation of the deflection w_{rms}/h_{TE} without parameter set 4

Figure 6.16: Mean and fluctuations of the deflection time history of the TE point as function of the streamwise location for the four different structural parameter sets. Note that subfigure c) is a magnified view of the fluctuations for parameter set 1 to 3.

than the recirculation frequency and the second one closest to the forcing. Finally, figure (6.15d) shows very large deflections of mode shape 2 for parameter set 4.

In order to quantify the initial impressions, figure 6.16 compares the mean deflection $\overline{w}$ and its standard deviation w_{rms}. In addition the values at the free end are reported in table 6.4. The positive mean values of the averaged deflection in figure 6.16a and table 6.4 for all parameter sets shows that on average the TE of the plate is bent in the upper

parameter set	$\overline{w_s}/h_{TE}$	$\overline{w}/L_s$	w_{rms}/h_{TE}	w_{rms}/L_s
set 1	3.22	0.0228	3.01	0.0213
set 2	0.39	0.0028	1.72	0.0122
set 3	6.41	0.0454	4.48	0.0317
set 4	1.16	0.0082	27.62	0.1956

Table 6.4: Mean $\overline{w_s}$ and standard deviation w_{rms} of the deflection of the free end of the elastic TE's. The deflection was normalized by the TE thickness h_{TE} and the length L_s.

direction. For set 1 to 3 the mean deflection increases monotonically towards the TE. For these cases the maximum mean deflection increases with decreasing bending rigidity. The maximum value can be found for parameter set 3 with $6.41h_{TE}$ which is equivalent to $0.4D_{cyl}$. The lowest mean deflection of the free end can be found for parameter set 2 with $0.39h_{TE}$ which equals $4.68\Delta y$. In case of the most flexible parameter set 4 the mean deflection is qualitatively different and the maximum deflection is approximately at the half length of the plate and decreases towards the free end. The bending-beam model does not account for stretching and assumes that the deflection is only perpendicular to the equilibrium position. Hence effectively the TE length is greater with high deflections.

Figure 6.16b shows the standard deviation of the deflection for the same cases. Parameter sets 1 and 2 show qualitatively the same behaviour of the mean deflection with a monotonic increase towards the TE with the shape of bending mode 1. The lowest standard deviation of all cases, found for parameter set 2, is equal to $20\Delta y_{TE}$ which is significantly larger than what is needed for the BDIM to represent the structural motion appropriately on the background grid. In contrast to parameter sets 1 and 2 the standard deviation of parameter set 3 features a saddle point at $x \approx -4D_{cyl}$. This indicates that the second bending mode has a notable contribution to the overall structural motion. This is consistent with the second natural frequency which is relatively close to the recirculation frequency. Adding the mean deflection and the standard deviation for that case results in $0.68D_{cyl}$. As the grid is equispaced for $0.25D_{cyl} < y < 0.625D_{cyl}$ the structural motion also reaches into grid regions with a slightly lower resolution. However, the resolution decreases very slowly outside the equispaced region and a reasonable representation of the structural motion is expected. This is not the case for the parameter set 4 where the standard deviation is $1.7D_{cyl}$ which means that independent of the mean location the structure will move in a region with reduced resolution for a significant amount of time. The shape of the standard deviation profile for this case shows a pronounced bending mode 3.

In summary, all elastic cases feature a mean deflection in the upper direction and for parameter sets 1 to 3 the mean and standard deviation of the deflection increase with decreasing bending rigidity. For these cases the structure is moving within well resolved

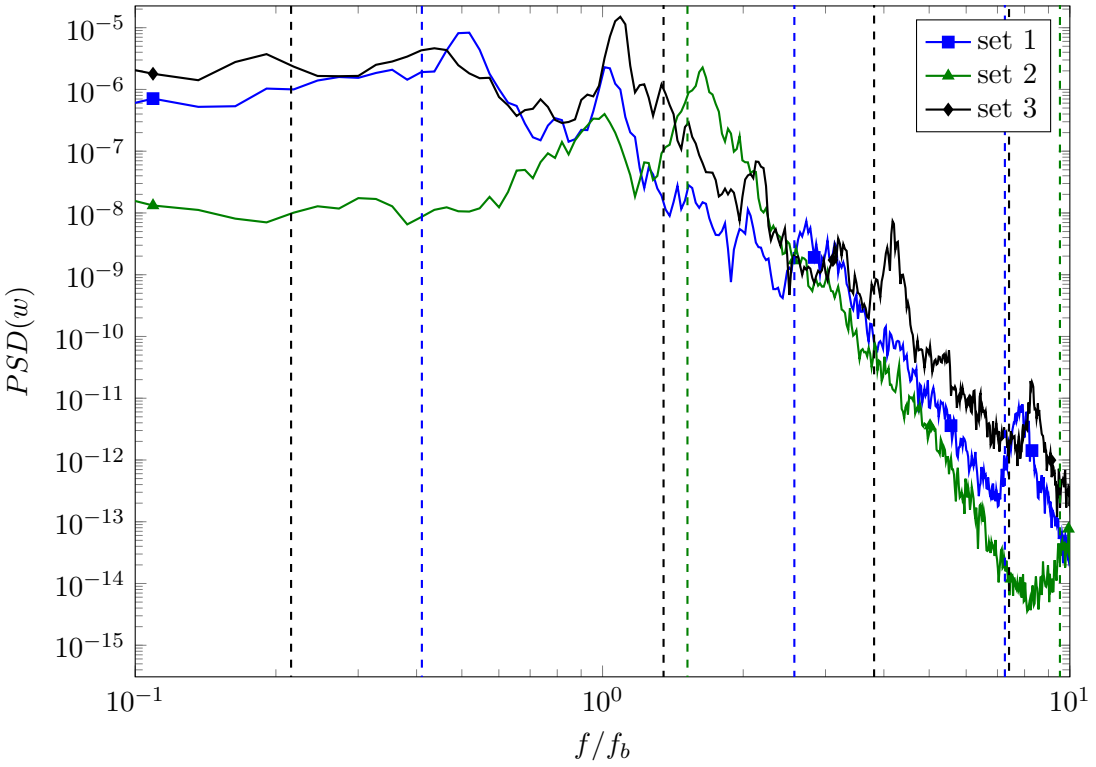

Figure 6.17: Power spectral density of the deflection time history of the free end of the structure for the three different parameter sets. The vertical dashed lines indicate the natural frequencies of the structural motion corrected by the effect of added mass as detailed in equation 2.21.

regions of the grid. Since this is not the case for parameter set 4 this case will be mostly ignored for the following comparison. Furthermore, the very large deflections in this case violate the assumptions made for the governing equation of the structure assuming small deflections.

Figure 6.17 compares the power spectral density of the free end deflection for parameter set 1 to 3. To increase the resolution in the low frequency range the window length was 43.7 recirculation cycles. This results in 9 Hanning windows with an overlap of 57%. As a reference the natural frequencies corrected for the effects of added mass are plotted as vertical dashed lines in the colors of the respective parameter set. It can be appreciated that for all parameter sets significant peaks can be found at the recirculation frequency. For parameter set 3 this frequency is slightly shifted to higher frequencies. The amplitude of the peak at this frequency reduces with increasing stiffness of the structure, i.e. it is lowest for parameter set 2 and highest for parameter set 3. The first harmonic of the recirculation frequency can also be identified by a distinct peak for parameter sets 1 and 3. However, it is at comparatively low energy levels.

case	$f_{1,\mathrm{sim}}/f_b$	$f_{1,\mathrm{analytical}}/f_b$	$f_{2,\mathrm{sim}}/f_b$	$f_{1,\mathrm{analytical}}/f_b$	$f_{3,\mathrm{sim}}/f_b$	$f_{3,\mathrm{analytical}}/f_b$
set 1	0.51	0.41	2.74	2.57	7.88	7.26
set 2	1.64	1.52	10.9	9.52	31.10	26.88
set 3	0.2	0.21	1.35	1.35	4.20	3.81

Table 6.5: Comparison of the analytical and simulated frequencies of the structural motion.

Considering the natural frequencies of the structure, the peaks of the simulated motion show differences to the theoretical predictions. Possible reasons for these deviations include inaccurate modelling of the added mass effects, locking in of the structural frequencies at higher harmonics of the recirculation frequencies and, for the low frequency range, a lack of averaging. In addition, the viscous fluid surrounding the structure results in damping also influencing the motion of the structure. Apart from the shift in the spectrum parameter set 3 also features an additional hump at $f/f_b = 0.41$ which is approximately the first harmonic of its first natural frequency (not its second natural frequency, though).

For the later comparison and further analysis of the acoustic far-field, the frequencies of the peak indicating the actual structural motion were evaluated from the spectrum. They are listed in table 6.5 and are for reference also compared to the analytical value. Any reference to structural or natural frequencies hereafter refers to the values actually simulated and not the analytical values.

Considering the energy distribution between the recirculation frequency f_b and the structural frequencies in the spectrum the recirculation frequency is not the dominant peak for parameter sets 1 and 2. For these two parameter sets most of the energy is attributed to the first structural frequency, where the difference is more significant for parameter set 2. For parameter set 3 in contrast, the spectrum is dominated by the peak at the recirculation frequency. In terms of energy content it is followed by the two peaks in the low frequency range and the second natural frequency. The comparable level of energy in the first and second natural frequency for this parameter set is consistent with the shape of the standard deviation presented in figure 6.16b.

6.5 Results – Comparison Between Rigid and Elastic Trailing-Edge

The following comparison of the elastic and rigid TE's first considers the influence of the structural parameters in section 6.5.1. The effect of structural damping on the radiated noise and the hydrodynamic near-field is investigated in section 6.5.2

6.5.1 Influence of Elasticity and Different Structural Parameters on Trailing-Edge Noise Generation

This section is split into the analysis of the acoustic far-field (6.5.1.1) and an investigation of the hydrodynamic near-field (6.5.1.2).

6.5.1.1 Statistical Analysis of the Acoustic Field

The directivity of the overall sound pressure level in the acoustic far-field at a radial distance of $r = 150D_{cyl}$ is considered in figure 6.18 as an initial measure of the effect of the different structural parameters on the noise from elastic TE's. In figure 6.18a the noise from all structural parameter sets introduced in table 6.2 is shown. It is apparent that parameter set 4 is significantly louder than all other cases under consideration. Compared to the rigid TE it shows a noise increase of approximately 15dB below the plate. As mentioned in the analysis of the structural motion in section 6.4, the violent motion and large deflections are not resolved appropriately by the current grid. Therefore, this case will not be analysed further in the following sections. In order to allow a better comparison of the other elastic TE's with the rigid TE the data of figure 6.18a without parameter set 4 is replotted in figure 6.18b. The comparison reveals that the elastic TE with the second lowest bending rigidity, i.e. set 3, also shows a significant noise increase with a maximum of 2.7dB for $\theta = 195°$. Furthermore, indications of an additional lobe in the directivity can be found in the direction pointing slightly downstream from the TE. This lobe is also present in the directivity of parameter set 4. Thus, it can be speculated that this lobe can be associated with large to very large deflections. However, an increase in noise can not only be related to the magnitude of the deflections as the stiffest plate, i.e. parameter set 2, with the smallest deflections also results in a noise increase. The higher noise level can be observed in the upstream direction below the plate and shows a maximum of 0.6dB compared to the rigid plate. In contrast to that, a noise reduction of up to 1dB can be observed above the plate and in the downstream direction. The opposite is true for parameter set 1 where the elastic TE leads to an increased noise level of up to 0.3dB above the plate. However, in the upstream direction below the plate, where the noise level is the highest in the rigid case, a noise reduction of 0.75dB can be achieved with the elastic TE using this parameter set. In summary,

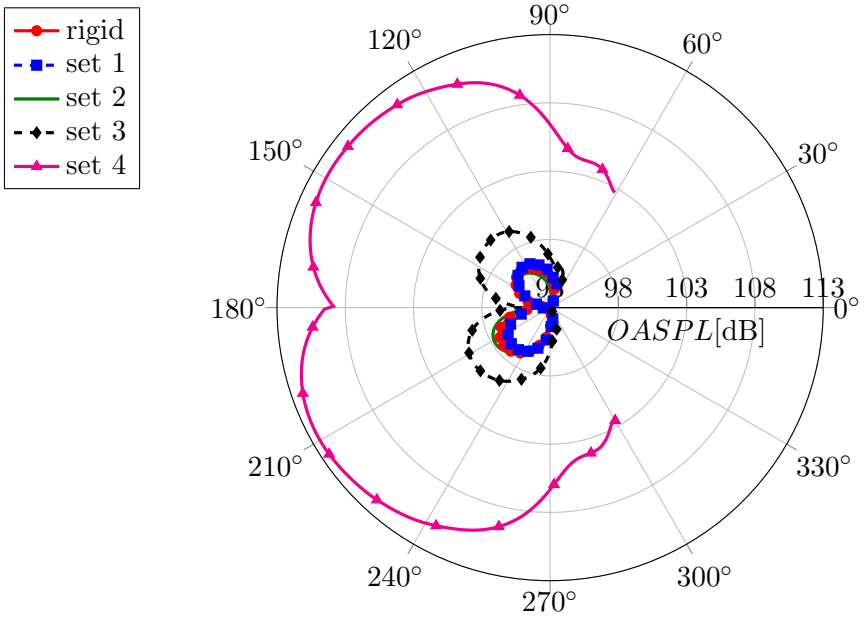

(a) comparison of all elastic TE parameter sets with the rigid TE

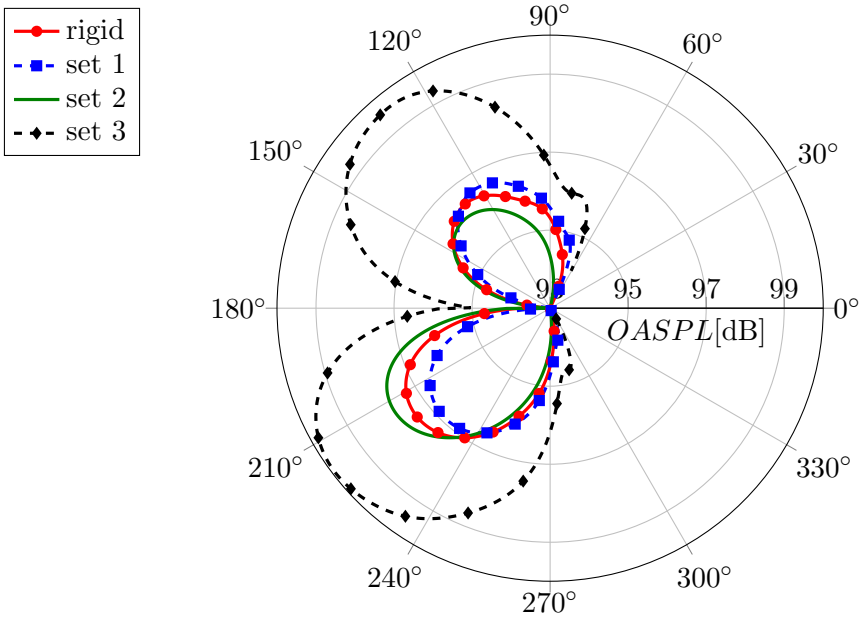

(b) comparison of elastic TE parameter sets with the rigid TE without set 4

Figure 6.18: Directivity of the overall sound pressure level at a radial distance of $r = 150D_{cyl}$ from the TE comparing the rigid with the elastic TE's.

the structural parameters which lead to an intermediate deflection and for which the recirculation frequency f_b is in between the first two natural frequencies appear to be the most beneficial for noise reduction. This is true for the upstream direction below the plate which has the highest noise level in the rigid case and is not influenced by noise from the vortex shedding, recirculation or any shielding effects of the cylinder.

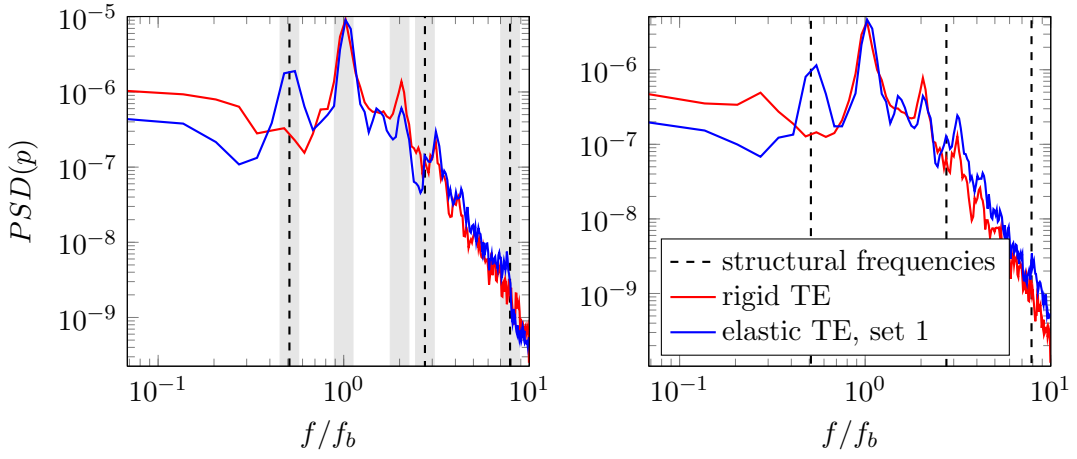

(a) parameter set 1 at $r = 150D_{cyl}$ and $\theta = 225°$ (b) parameter set 1 at $r = 150D_{cyl}$ and $\theta = 270°$

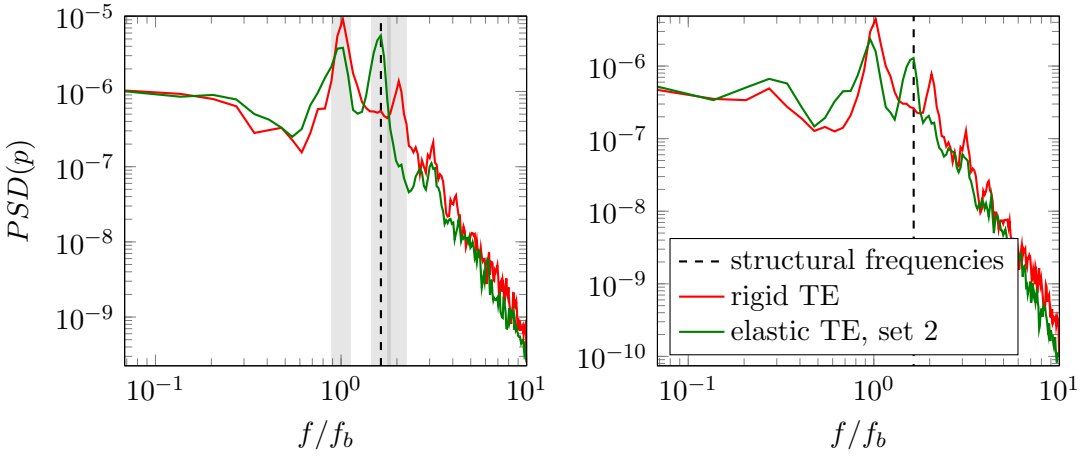

(c) parameter set 2 at $r = 150D_{cyl}$ and $\theta = 225°$ (d) parameter set 2 at $r = 150D_{cyl}$ and $\theta = 270°$

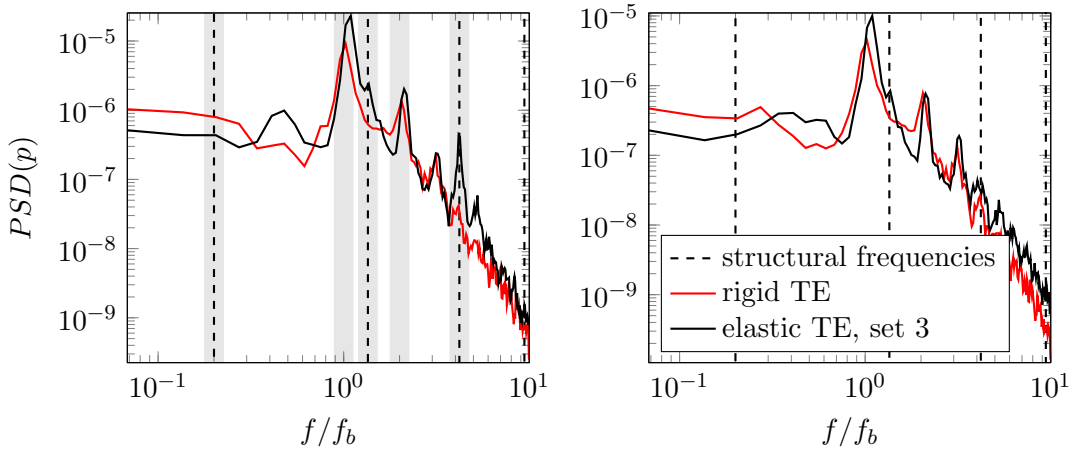

(e) parameter set 3 at $r = 150D_{cyl}$ and $\theta = 225°$ (f) parameter set 3 at $r = 150D_{cyl}$ and $\theta = 270°$

Figure 6.19: Comparison of the power spectral density of pressure between the rigid represented by the BDIM and the elastic TE's for two different positions. All data is taken at a radial distance of $r = 150D_{cyl}$ and the left and right column refer to the azimuthal directions $\theta = 225°$ and $\theta = 270°$ which are consistent with the directions used in figure 6.18. The vertical dashed black lines are the structural frequencies as determined from the PSD of the deflection in figure 6.17 and documented in table 6.5. The shaded areas mark the one-third octave bands discussed in the text.

The analysis of the pressure time history in frequency space can give further insight into the physical origin of the different noise levels observed in figure 6.18. To that end, the power spectral density was computed using Welch's method with 21 Hanning windows that had a length of 14.6 recirculation cycles and an overlap of 50%. All frequencies in the following spectral analysis were normalized with the recirculation frequency f_b of the rigid TE as it was determined in section 6.2. Figure 6.19 presents the results at two locations below the plate at the same radial distance $r = 150D_{cyl}$ as analysed in figure 6.18 for an azimuthal position of $\theta = 225°$ (a,c,d) and $\theta = 270°$ (b,d,f). The direction $\theta = 225°$ is pointing upstream with an inclination of 45° relative to the plate and showed the highest overall sound pressure levels in the rigid case. The second direction $\theta = 270°$ is perpendicular to the TE and is therefore not influenced by the mean flow. As both locations are below the plate, it is expected that the noise originates predominantly from the TE and is not influenced by the vortex shedding from the cylinder. Each of the elastic TE's are compared to the rigid TE in a separate figure so the natural frequencies of the elastic TE can be plotted in addition. Table 6.6 quantifies the energy distribution of the spectra in the left column of figure 6.19, i.e. for the position below the plate at $r = 150D_{cyl}$ at $\theta = 225°$, relative to the rigid TE. The overall sound pressure level is calculated in one-third-octave bands around center frequencies f_c which are the recirculation frequency and its first harmonic. In addition the first three structural frequencies are considered. The octave bands are visualized by the shaded area in figures 6.19a, 6.19c, 6.19e. In addition to the noise increase or reduction the contribution of the frequency band to the overall energy in the spectrum of the elastic and rigid TE, respectively, are given in percentage.

The first row, i.e. figure 6.19a and 6.19b presents the power spectral density of the pressure comparing the data from the elastic TE with parameter set 1 and the rigid TE. This is the parameter set for which the vortex shedding frequency f_b is between the first two natural frequencies of the structure. At the most dominant peak in the spectrum, which is at the vortex shedding frequency, the elastic TE slightly increases the noise by 0.4dB. The opposite is true for the first harmonic of this frequency with a noise reduction of −6.6dB employing an elastic TE. However, the amplitude of this peak is significantly lower and the contribution to the overall energy in the spectrum is small. On a comparable amplitude level a significant noise reduction is achieved for the very low frequency range. On the other hand the elastic TE shows a distinct peak at $f = 0.51$ which is close to the simulated first frequency of the structural motion which featured the highest amplitude in the power spectral density of the TE deflection. In addition a linear interaction between the first structural frequency and the recirculation frequency can be observed in the spectrum featuring an additional peak at $f = 1.5$ in the spectrum of the elastic TE. The variations of the characteristics of the spectrum between both locations are minute. In general, the elastic TE tends to higher amplitudes at the wall

t

f_c		set 1			set 2			set 3	
f_b	0.4dB	49.5%	44.3%	−6.2dB	20.8%	44.3%	7.2dB	54.2%	44.3%
$2f_b$	−6.6dB	6.0%	12.0%	−14.9dB	2.1%	12.0%	1.6dB	7.7%	12.0%
$f_{1,s}$	16.4dB	9.3%	1.3%	16.7dB	39.2%	6.0%	−5.2dB	0.6%	1.9%
$f_{2,s}$	−1.9dB	2.7%	3.1%	−3.0dB	0.0%	0.0%	7.7dB	11.0%	8.5%
$f_{3,s}$	3.2dB	0.2%	0.1%	−4.5dB	0.0%	0.0%	14.5dB	2.4%	0.9%

Table 6.6: Energy distribution of the power spectral density for the elastic TE's in comparison with the rigid TE below the plate relating to the spectra in the first column of figure 6.19. The power is calculated in third octave bands around center frequencies f_c. The difference to the rigid TE is given in dB where a positive sign indicates a noise increase and a negative sign a noise reduction. The second and third number in each column indicate the contribution of frequency range to the total energy in % for the elastic and rigid TE, respectively.

normal position.

The spectra in the second row (figure 6.19c and 6.19d) compare the rigid to the elastic TE with the parameter set, where the first natural frequency $f_1 1$ is higher than the recirculation frequency f_b and the bending rigidity is comparatively high. It is apparent that the energy in the frequency band containing the recirculation frequency is reduced when the elastic TE is employed. With a reduction of 6.2dB, this reduction is significant in particular because the contribution of this third octave band to the overall energy in the spectrum is high. However, the directivity plot showed a noise amplification for this parameter set. The reason for that is the additional peak at the first structural frequency, which occurs at both locations considered. The increase in noise level at the upstream position is 16.7dB. This peak has a higher amplitude than the peak at the recirculation frequency in the upstream direction. The importance of the peaks in the spectrum matches the spectrum of the structural motion. Thus, the dominant noise source in this case is not the TE noise induced by the pressure fluctuations of the recirculation but a physical mechanism related to the first natural frequency of the structural motion. It can be speculated that the excess noise is generated by an excitation of the separation bubble by the motion of the structure. In addition, the motion of the structure is a noise source of dipole type (Manela, 2011). At the location perpendicular to the TE the peak at the first structural frequency is reduced in amplitude which explains the noise reduction that was observed in this direction. In the elastic case, the first harmonic of the recirculation frequency from the cylinder can not be identified in the upstream direction and is hardly visible in the direction normal to the TE. At both locations the elastic TE has an increased noise level in the very low frequency range. However, considering the energy level this is only of secondary importance.

Finally, spectra of the elastic TE with parameter set 3 featuring a very low bending stiffness are compared to the rigid TE in figure 6.19e and 6.19f. The most apparent difference between the spectra of the rigid and elastic case is the significant increase of the amplitudes at the recirculation frequency for the elastic TE. In addition to the increased noise level the recirculation frequency is also slightly higher than in the rigid case, which is consistent with the shift of the peak in the spectrum of the structural motion found in figure 6.17. The noise increase for this frequency, which has a very high contribution to the overall energy in the spectrum, is 7.2dB. In the upstream direction the first harmonic of the recirculation frequency is also amplified in the elastic case which is not the case in the wall normal direction. At a much lower level in energy the spectrum of the elastic TE features a significantly higher peak at the third harmonic of the recirculation frequency which coincides roughly with the third natural frequency of the structure leading to a very significant noise increase of 14.5dB, that does not contribute significantly to the overall energy in the spectrum though.

The point spectra presented in figure 6.19 showed that the noise reduction and the amplitudes of the excess noise at the structural frequencies depend on the azimuthal location. To evaluate the directivity pattern at different frequency bands of interest the power spectral density of a plane covering most of the far-field was calculated. To that end, planes were captured, skipping points in different grid regions to reduce the amount of the data captured. The power spectral density was then calculated using Welch's method with 21 Hanning windows with a length of 14.6 recirculation cycles and an overlap of 55%. Figure 6.20 presents the directivity in the third octave frequency band centred at the recirculation frequency f_b. The elastic TE's with different parameters are compared to the rigid case in figure 6.20a and it can be found that the qualitative difference between each elastic parameter set and the rigid TE does not change in the azimuthal direction. To investigate the differences in the directivity shape itself, each parameter set is considered in a separate figure (6.20b-d). Parameter set 1 is presented in figure 6.20b and the qualitative comparison shows the same behaviour as the integral directivity presented in figure 6.18b. It is apparent that the noise reduction occurs predominantly in the upstream direction and a slight noise increase can be found in the range of $\theta = 240°$. In addition, the data from the rigid TE is rescaled, i.e. multiplied with a factor, such that it matches the amplitude of the elastic case in the upstream direction. The direct comparison of the shape of the directivity reveals that the noise radiation in the elastic case has a higher contribution in the direction where the noise increase was found. It is speculated that this deviation from the directivity shape of the rigid TE noise is due to the noise from the structural motion. The opposite behaviour can be observed for parameter set 2 considered in figure 6.20c, where the noise radiation seems to be directed slightly more strongly in the upstream direction. Parameter set 3 is presented in figure 6.20c and the directivity pattern in the elastic case seems unchanged compared to the rigid TE when comparing the rescaled data.

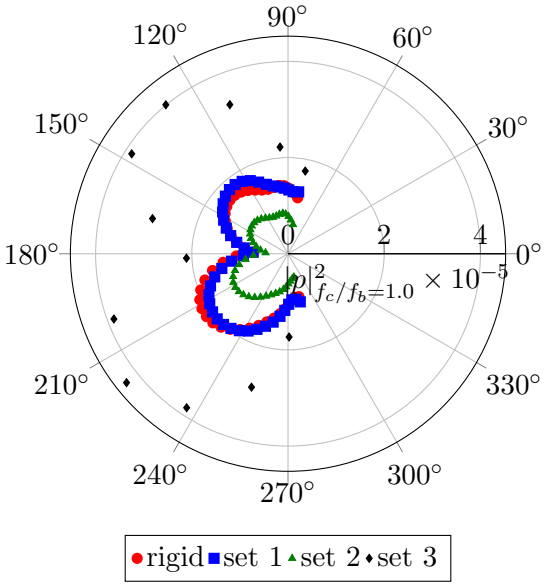

(a) directivity shape of all parameter sets in comparison to the rigid TE

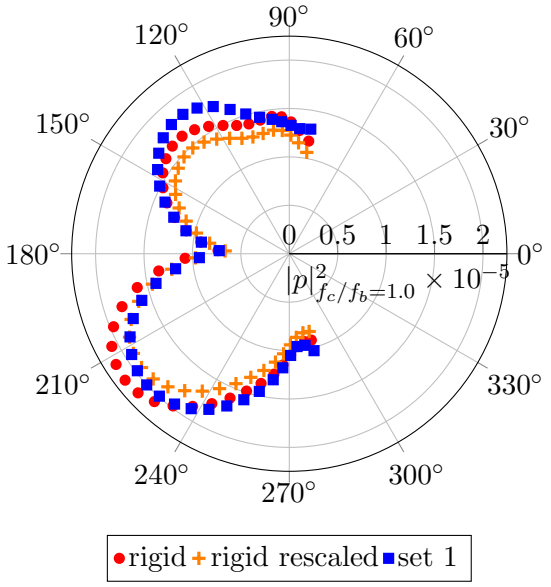

(b) directivity shape of parameter set 1 with rescaled data from rigid case

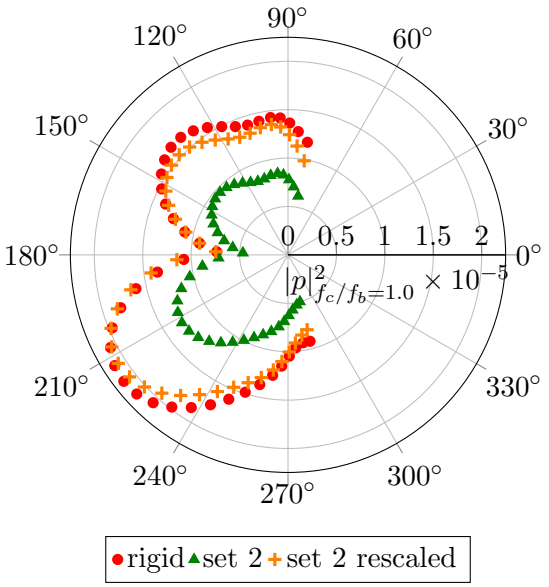

(c) directivity shape of parameter set 2 with rescaled data form rigid case

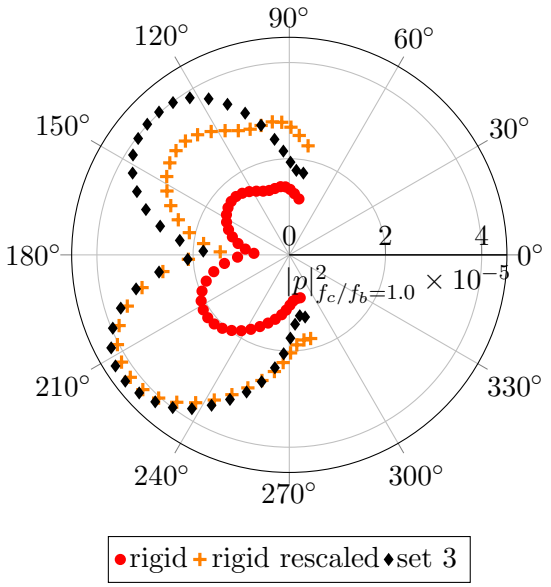

(d) directivity shape of parameter set 3 with rescaled data form rigid case

Figure 6.20: Comparison of the directivity of the power spectral density of pressure for the rigid and elastic TE's in one-third-octave bands centred on the recirculation frequency f_b. As explained in the text, the rescaled data was obtained by multiplication with an arbitrary factor such that the amplitudes match the case the data is compared to.

Figure 6.21 considers the one-third-octave bands centred around the structural frequencies that contain the most energy, the first for parameter sets 1 and 2 and the second for set 3. It is apparent that for all parameter sets the elastic TE is noisier in all directions in the chosen frequency bands. To enable a comparison of the shape the data from

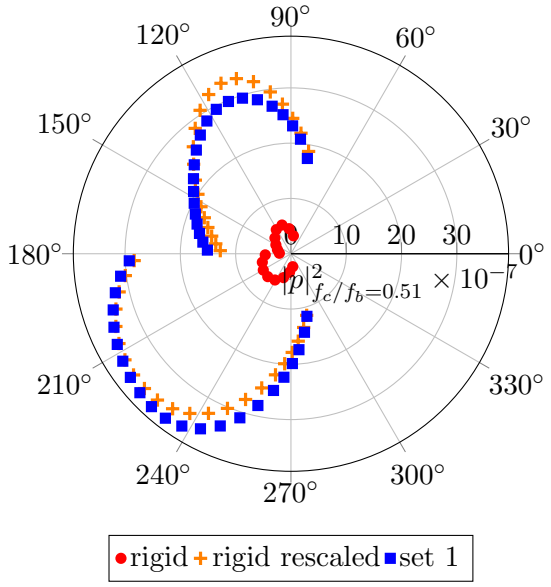

(a) one-third-octave band based on first structural frequency of parameter set 1

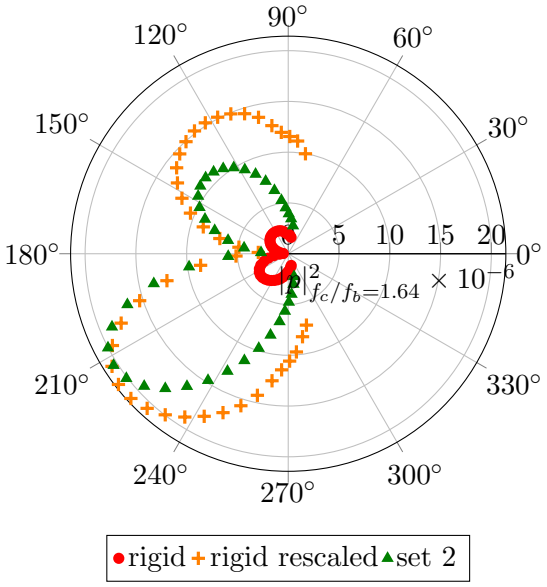

(b) one-third-octave band based on first structural frequency of parameter set 2

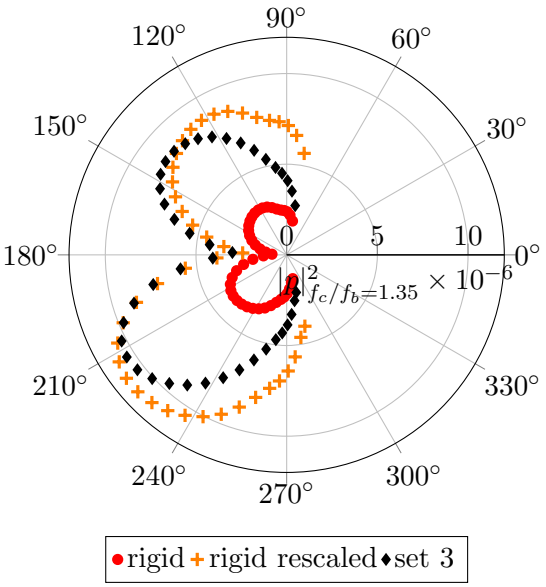

(c) one-third-octave band based on second structural frequency of parameter set 3

Figure 6.21: Comparison of the directivity of the power spectral density of pressure for the rigid and elastic TE's in the one-third-octave band centred on the structural frequency containing most energy.

the rigid TE was again rescaled, as explained in the previous paragraph, to match the amplitude of the elastic case in the upstream direction. Similarly to the recirculation frequency in the case using parameter set 1, considered in figure 6.21a, this case also shows a slightly higher relative noise increase in the $\theta = 240°$ direction. The opposite is true for parameter sets 2 and 3. In both cases the noise radiation in the upstream direction is significantly more pronounced in the rigid case than for the elastic TE.

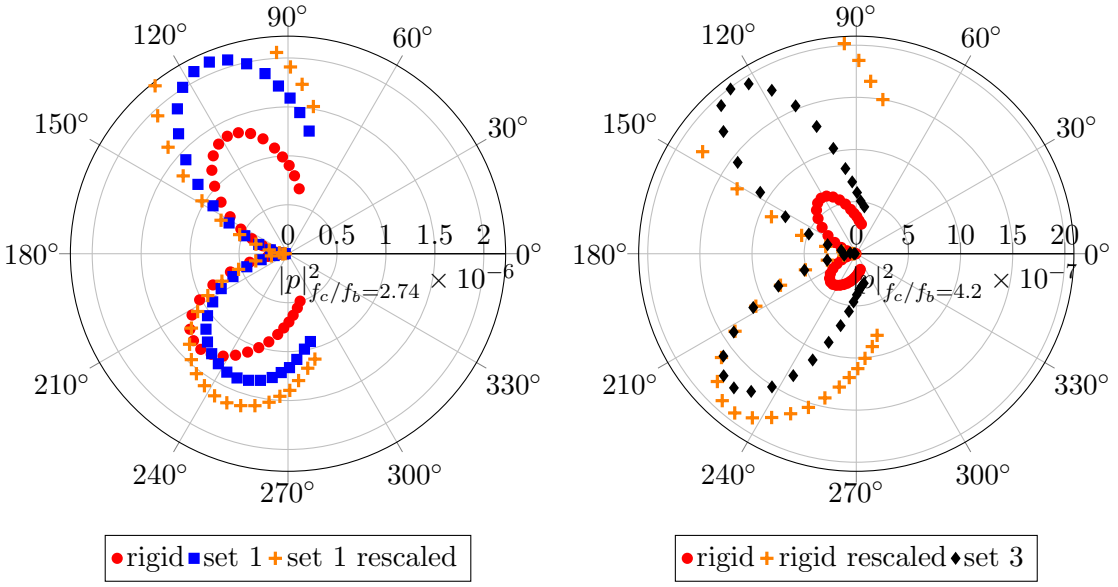

(a) one-third-octave band based on second structural frequency of parameter set 1

(b) one-third-octave band based on third structural frequency of parameter set 3

Figure 6.22: Comparison of the directivity of the power spectral density of pressure for the rigid and elastic TE's in the one-third-octave band centred on the structural frequencies associated with higher modes.

Figure 6.22 shows the directivity for parameter sets 1 and 3 in frequency bands centred around structural frequencies that are associated with distinct peaks not present in the spectra of the rigid TE but do not contribute significantly to the overall energy of the fluctuations. For parameter set 1 the frequency band is centred around the second structural frequency and the comparison of the unscaled directivity shows that the elastic TE leads to a higher noise level in the wall normal direction and a noise reduction in the upstream direction. The rescaled data from the elastic plate confirms this trend showing a stronger noise radiation in the wall normal direction. The opposite is true for the third structural frequency of parameter set 3 presented in figure 6.21c. In this case the noise is radiated almost entirely in the $\theta = 225°$ direction. The observations for both parameter sets are consistent with the findings from the two point spectra presented in figure 6.19.

In summary, a potential for noise reduction from an elastic TE was found. For the overall sound pressure level a noise reduction was only found for one of the three parameter sets and the other two amplified the noise. However, the spectral analysis of the far-field revealed that in certain frequency bands significant noise reductions can be found for all parameter sets. In many cases these reductions were overpowered by excess noise found at the structural frequencies and the recirculation frequency. Even though no formal correlation was presented, the amount of excess noise or noise reduction was found to

be closely related to the distribution in the power spectral density of the structural deflections.

6.5.1.2 Analysis of the Hydrodynamic Near-Field

The following section will investigate the influence of structural elasticity on the hydrodynamic near-field in the vicinity of the TE. Since this is the source region of the noise radiated into the far-field, which was discussed in the previous section 6.5.1.1, this should give further insight into the origin of the frequency-dependent excess noise or noise reductions found in the far-field.

Before the source region is analysed, potential mechanisms for noise attenuation and amplification are discussed in this paragraph. On the one hand, the noise reductions found in certain frequency ranges could be due to a modification of the input to the TE noise mechanism. On the other hand, the noise amplification in the one-third-octave bands centred on the structural frequencies could originate from the motion of the structure itself which is of dipole type. Alternatively, the structural motion could amplify the input to the TE noise mechanism by exciting instabilities in the separation bubble.

The recirculation bubble on the upper side of the TE was found to create the most energetic pressure fluctuations as input for the TE noise mechanism and the structural motion in section 6.2. To assess how it is changed by the moving TE's, the recirculating flow regions of the different cases are presented in figure 6.23. For all elastic TE's, the recirculating flow regions in the vicinity of the vortex generator cylinder and upstream of the elastic fraction of the TE seem not to be changed by the motion of the solid body. The elastic TE's with the largest deflection, i.e. parameter sets 1 and 3, show a shortened separation bubble, which in turn extends further upstream for parameter set 3. These changes are likely to be an effect of the mean deflection. For parameter set 2 the changes compared to the rigid TE are small and only a minor shift towards the freestream can be observed at the end of the separation bubble.

Figure 6.24 compares the skin friction downstream of the vortex generator cylinder for the elastic and the rigid TE's. The skin friction values were calculated during the runtime of the simulation and gathered as a time history in the moving frame of reference with an offset of one smoothing region half-width 1ϵ. The sampling locations were independent of the computational grid of the fluid with a significantly reduced resolution compared to the fluid grid. The skin friction confirms that the elastic TE with parameter set 3 leads to an upstream shift of the separation bubble which ends $2.2D_{cyl}$ upstream of the TE in contrast to $1D_{cyl}$ for the rigid case. For parameter sets 1 and 2 the differences

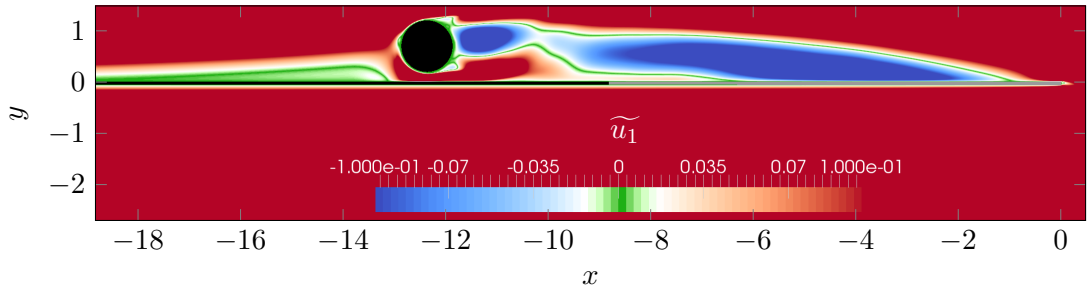

(a) rigid TE

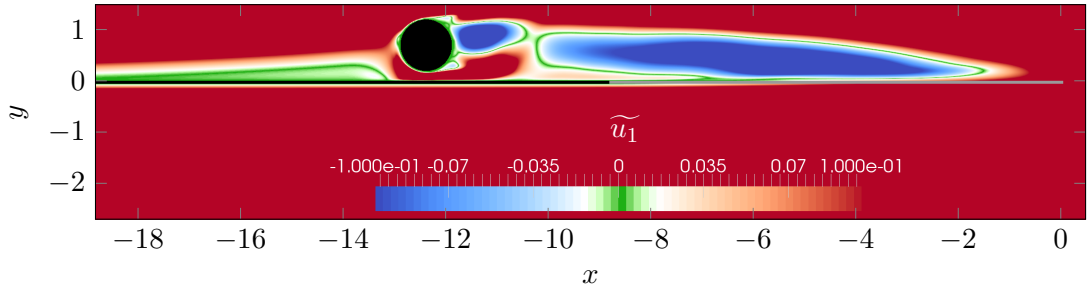

(b) elastic TE with parameter set 1

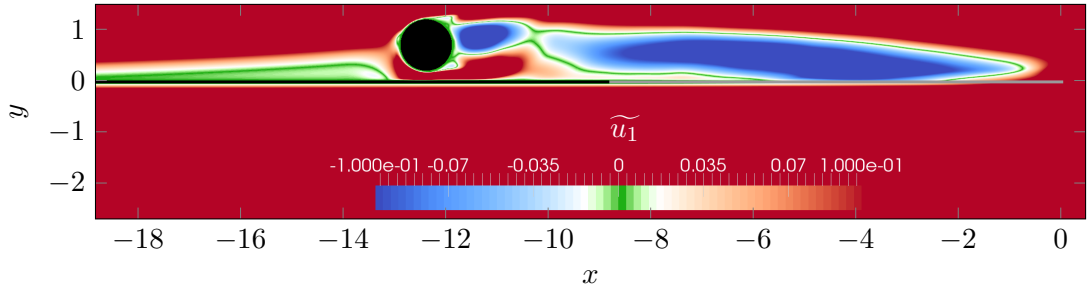

(c) elastic TE with parameter set 2

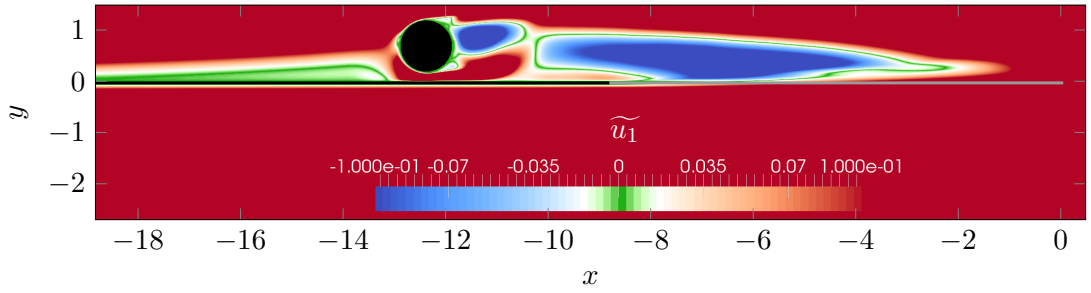

(d) elastic TE with parameter set 3

Figure 6.23: Contours of the Favre averaged streamwise velocity component $\widetilde{u_1}$ in the vicinity of the TE for the rigid and elastic TE's. The fraction of the plate that is considered elastic is coloured in grey.

in the location of the separation to the rigid TE are moderate with a slight upstream and downstream shift, respectively.

Figure 6.25 assesses the influence of the change in separation bubble on the velocity and Reynolds stress profiles upstream of the elastic fraction of the plate. In the streamwise

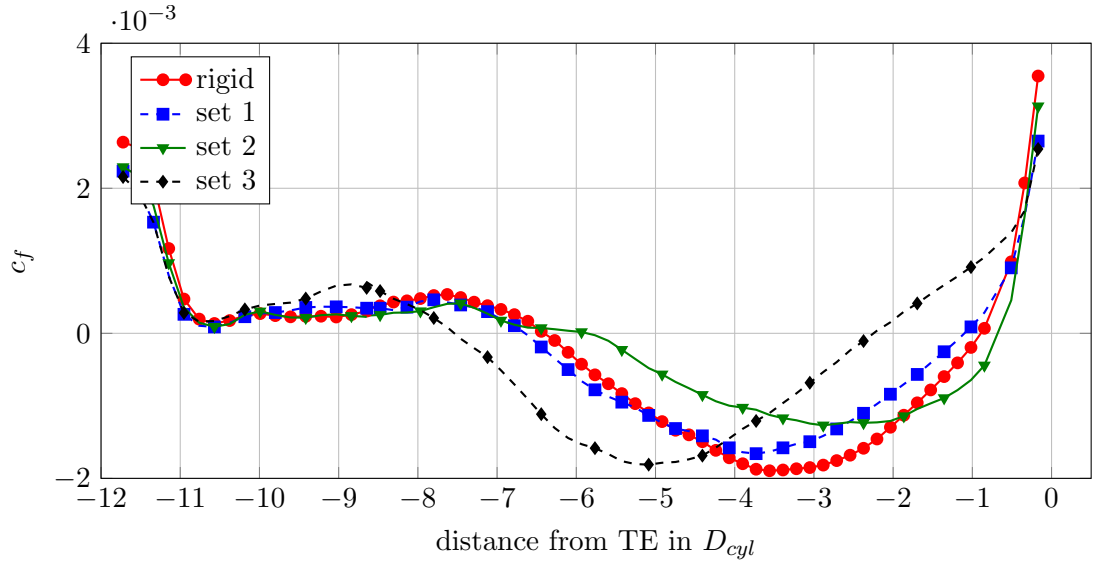

(a)

Figure 6.24: Skin friction coefficient along the upper side of the plate for the different elastic and rigid TE's.

velocity $\widetilde{u_1}$ profiles in figure 6.25a the recirculation region, which is not connected to the wall at this location, does not seem to be significantly influenced by the motion of the TE downstream. This confirms the findings from the contours of the streamwise velocity component, where the shape of the recirculation bubble is comparable at the start of the elastic fraction. Only parameter set 3, featuring the largest deflection amplitudes, shows slightly increased velocity amplitudes in the upstream direction. The differences are more pronounced for the wall normal velocity $\widetilde{u_2}$ where the average in the rigid case shows a flow towards the wall for $y < 0.2$ where the flow is in the opposite direction for the elastic TE's. Towards the freestream the profiles of this velocity component show quite different shapes. This is consistent with the varying position of the separation bubble in the different cases which means that the start of the elastic fraction is at different locations relative to the separation bubble for each case. The same is true for the Reynolds stresses compared in figure 6.25b. For the streamwise and wall normal component τ_{11} and τ_{22}, respectively, the amplitudes are proportional to the deflections of the elastic fraction, i.e. parameter set 3 shows the highest amplitude, in particular close to the wall and parameter set 2 and the rigid case the lowest. These increased Reynolds stresses can most likely be attributed to the upstream shift of the separation bubble for parameter sets 1 and 3 found in the skin friction in figure 6.24 that might cause a higher level of flow unsteadiness in this region.

The TE location is considered in figure 6.26. The most apparent differences between the rigid and the elastic TE's can be observed in the streamwise velocity component $\widetilde{u_1}$ and the associated Reynolds stress components τ_{11} and τ_{12}. Considering $\widetilde{u_1}$, it can be appreciated that the elastic TE reduces the wake deficit significantly. This effect

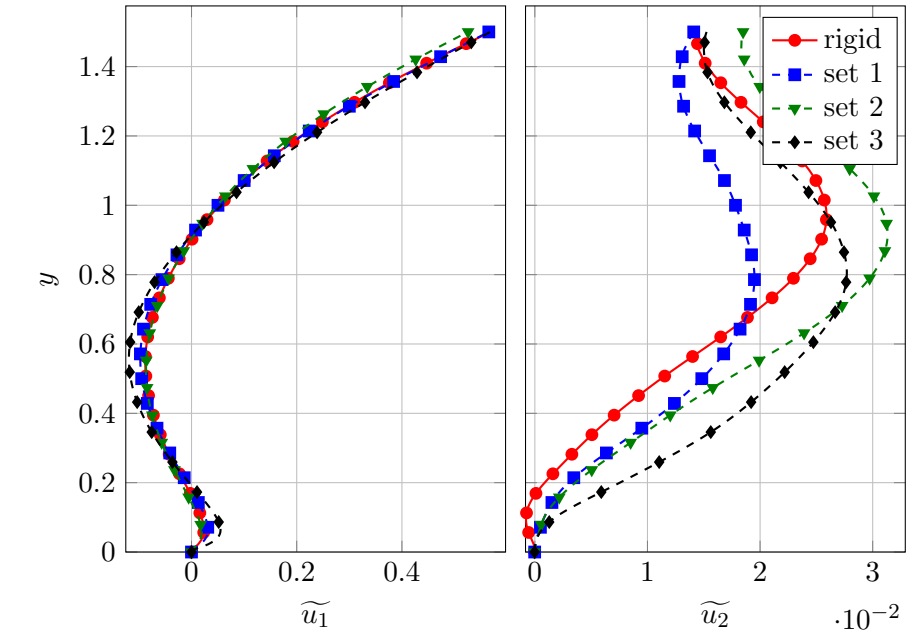

(a) velocity profiles

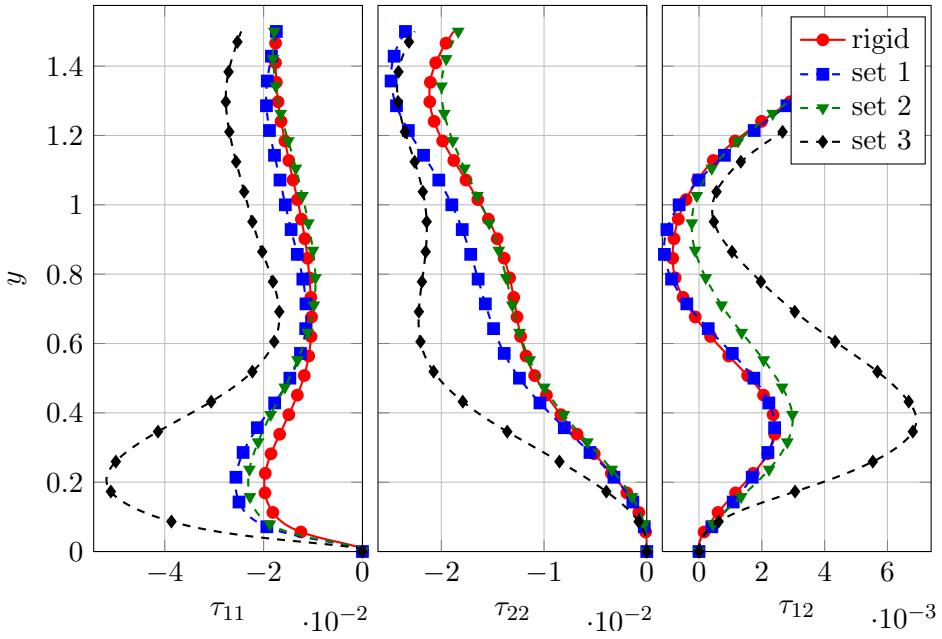

(b) Reynolds stress profiles

Figure 6.25: Comparison of the Favre averaged velocity and Reynoldsstress profiles at the beginning of the elastic fraction ($x = -8.75 D_{cyl}$) for the rigid and elastic TE.

is more pronounced for cases with a higher deflection. Furthermore, the wall normal location of the maximum wake deficit varies for the different parameter sets. Since it is shifted furthest towards the free stream for parameter set 2, which featured the lowest mean and standard deviation of deflection, it seems unlikely that this is an effect of the one of these two statistical moments. The streamwise Reynolds stress components τ_{11} of parameter sets 1 and 3 show significantly reduced amplitudes compared to the rigid case and parameter set 2 for $0 < y < 0.75$. This could indicate that the fluctuations

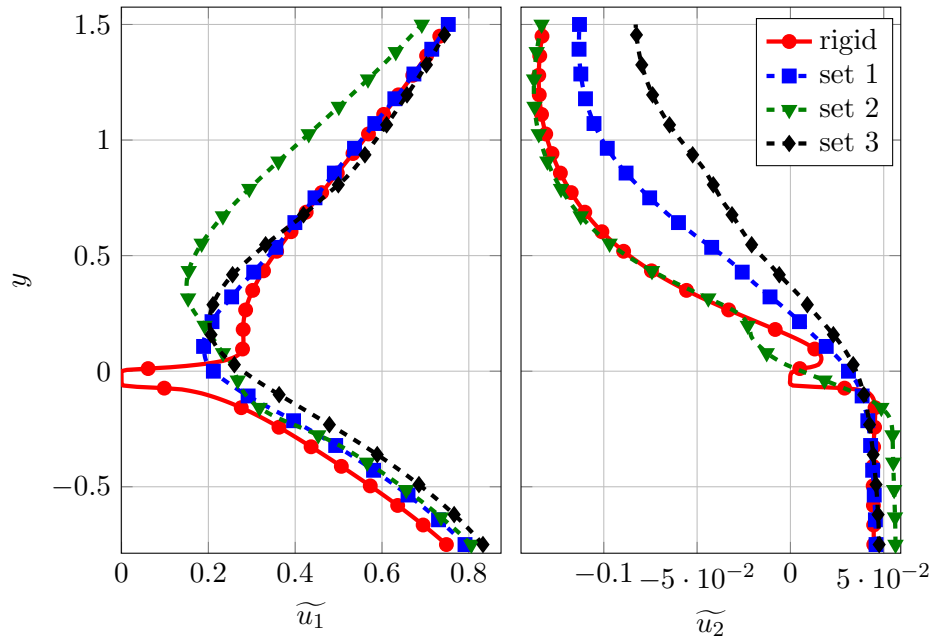

(a) velocity profiles

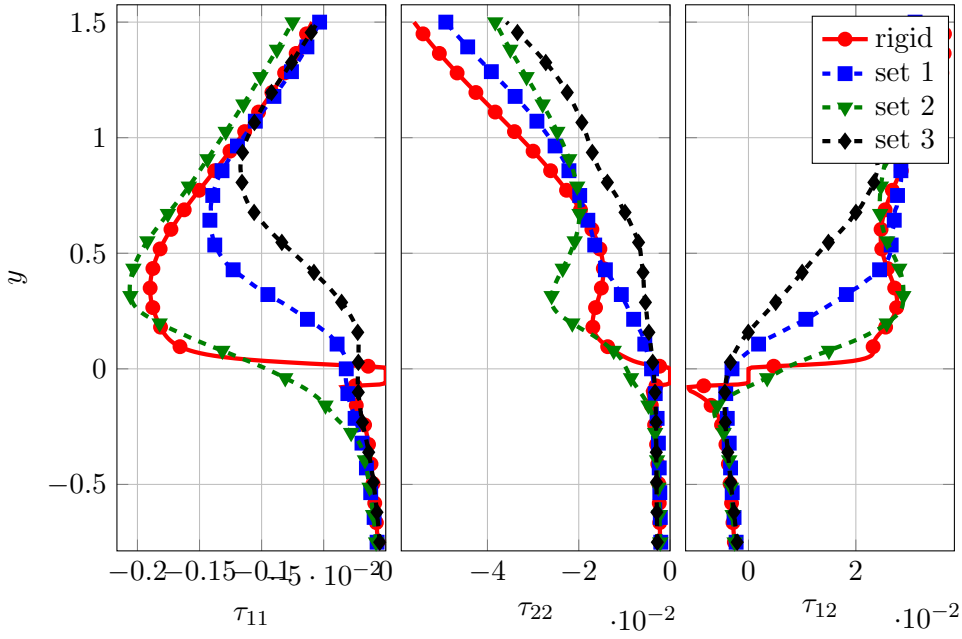

(b) Reynolds stress profiles

Figure 6.26: Comparison of the velocity and Reynoldsstress profiles at the TE ($x = 0.0$) for the rigid and elastic TE's.

in the flow field are mitigated by the structural motion in these cases, leading to lower incident amplitudes of pressure fluctuations to the TE noise mechanism. It can be speculated that the earlier wake development is achieved by smearing out the position of the TE through the moving boundary. This is supported by the profiles of both mentioned Reynolds stress components τ_{11} and τ_{12} which indicate that the wake of the elastic TE is more developed already at the TE. Thus, the elastic TE allows a smoother streamwise

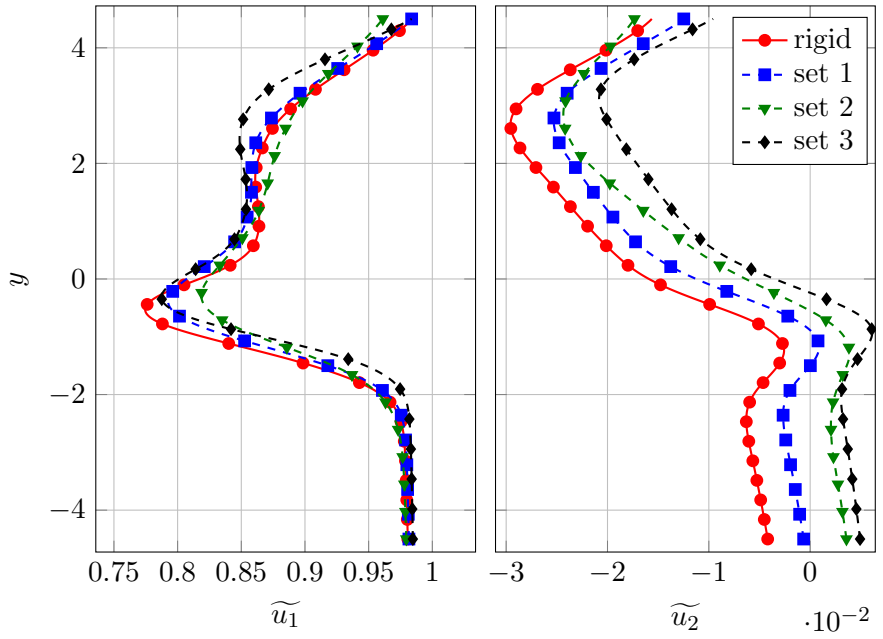

(a) velocity profiles

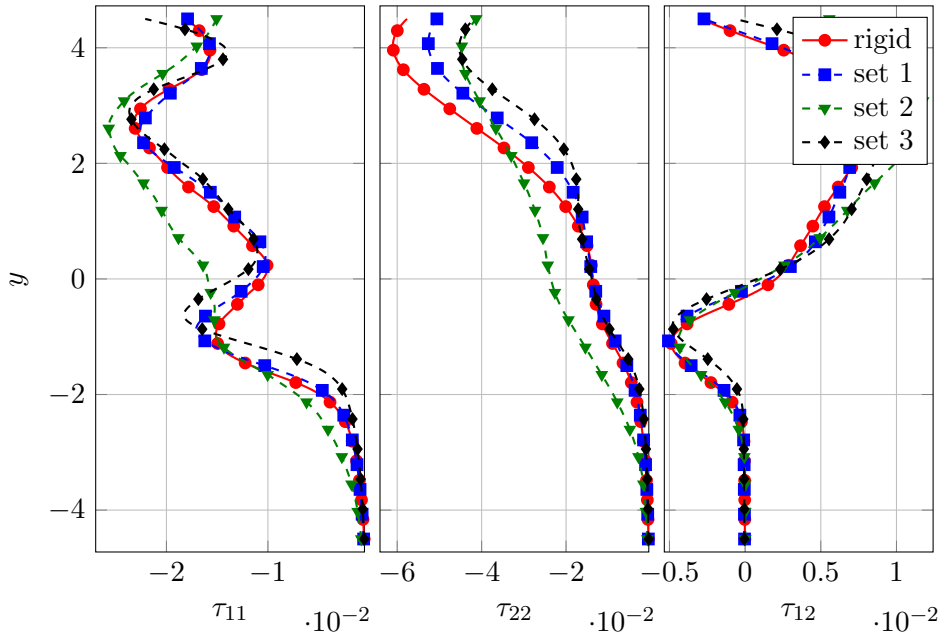

(b) Reynolds stress profiles

Figure 6.27: Comparison of the velocity and Reynoldsstress profiles $12D_{cyl}$ downstream of the TE for the rigid and elastic TE's represented by the BDIM.

evolution of the flow and it can be hypothesized that it mitigates the incident pressure fluctuations.

Figure 6.27 compares the velocity and Reynolds stress profiles in the wake $12D_{cyl}$ downstream of the TE. From the streamwise velocity profile $\widetilde{u_1}$ it can be seen that the differences of the momentum deficit are reduced compared to those at the TE location.

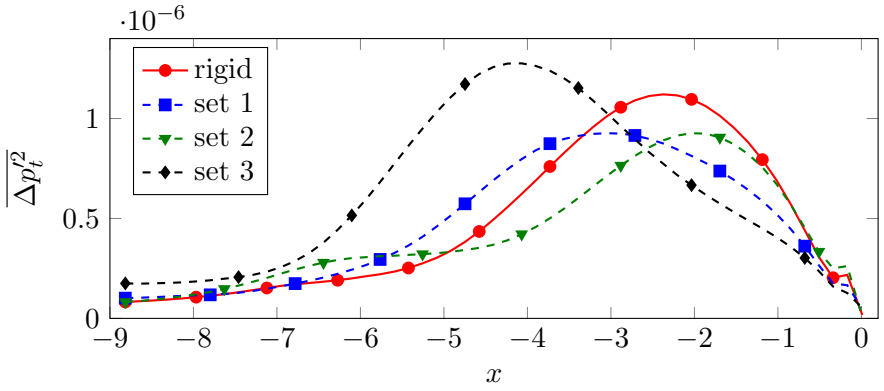

(a) total pressure difference fluctuations

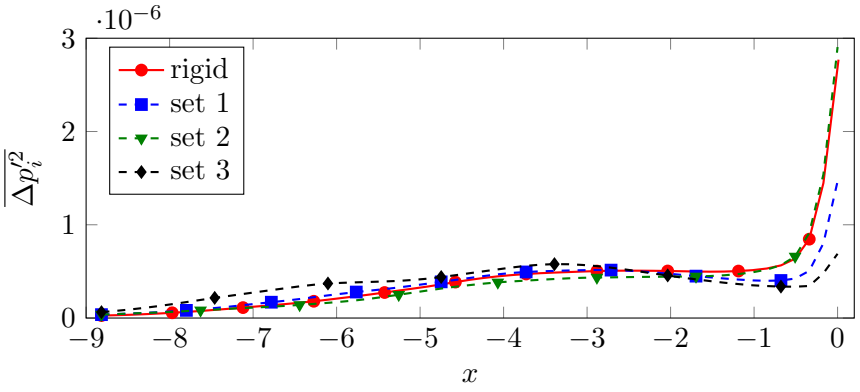

(b) incident pressure difference fluctuations

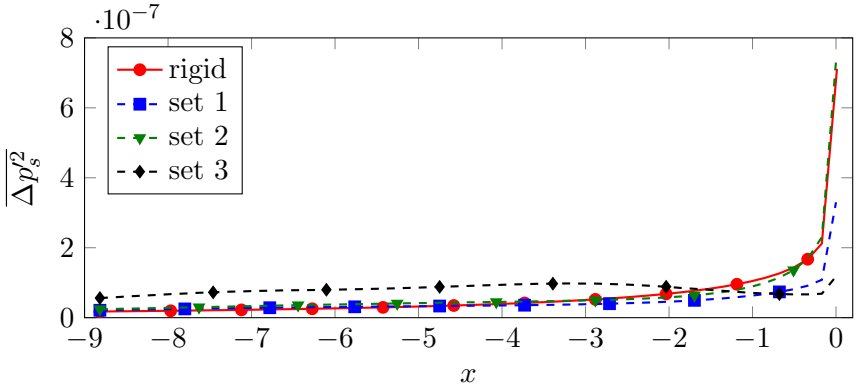

(c) scattered pressure difference fluctuations

Figure 6.28: Comparison of the variance of the pressure difference fluctuations $\Delta p'$ for the elastic and rigid TE.

Surprisingly, parameter set 3 shows the lowest wake deficit of all cases despite the relatively high deficit at the TE location. A possible explanation for this behaviour could be the high amplitudes in the Reynolds stresses at the TE (figure 6.26b) for this case which leads an enhanced momentum exchange in the lateral direction. For the Reynolds stresses the differences between parameter sets 1 and 3 are less pronounced but parameter set 2 is qualitatively different with a more uniform profile and higher amplitudes.

Figure 6.28 presents the variance of the pressure difference for the elastic and rigid TE's as a function of the streamwise position. From the variance of the total pressure difference shown in figure 6.28a it is apparent that the elastic TE's influence the amplitude and the location of the peak of the pressure fluctuations upstream of the TE. Consistent with the findings from the skin friction coefficient presented in figure 6.24 the elastic plate with parameter set 2 shows the least deviations from the rigid TE and parameter set 3 the largest. As found by Sandberg *et al.* (2007) and Sandberg & Sandham (2008) as well, the total pressure differences at the TE are non-zero but small in all cases.

The incident field $\Delta p_i'$ is presented in figure 6.28b and features the typical sharp rise of the pressure fluctuations towards the TE. For the elastic plate with parameter set 2 the peak at the TE is higher than for the rigid plate. This indicates that the increase in noise level that was found for this case can be attributed to an amplification of the TE edge noise mechanism. In contrast to that the two elastic TE's with the lower bending stiffness show a lower amplitude at the TE. In fact the case with the lowest bending rigidity, i.e. with the highest deflections, yields the lowest peak at the TE location. Since this case was the noisiest in the acoustic far-field it was considered that significant noise must be produced by the structural motion or other noise sources. These findings correlate directly with the amplitudes of the streamwise Reynolds stress τ_{11} at the TE presented in figure 6.26b.

Figure 6.28c presents the scattered and motion induced pressure fluctuations Δp_s and shows consistent trends with the incident pressure field at the TE location. However, it should be noted that this quantity also contains the contribution of pressure fluctuations imposed on the fluid through the structural motion itself. This additional contribution to the scattered field leads to an increasing Δp_s when considering locations upstream of $x = -2$ for parameter set 3 that featured the largest deflections.

In order to investigate the frequency dependence of the noise amplification and attenuation, the power spectral density in one-third-octave bands of the incident pressure fluctuations will be considered in the following paragraph. It was calculated using 21 Hanning windows containing 14.6 recirculation cycles with an overlap of 55%. Figure 6.29a presents the energy of the incident pressure fluctuations at the recirculation frequency and its first harmonic. For parameter sets 1 and 2 the energy at the TE is lower than for the rigid plate in both frequency bands. This is consistent with the noise reduction in these two frequency bands found in table 6.6. In contrast, parameter set 3 showed a significant noise augmentation in the far-field but features the lowest peak at the TE thus confirming the findings from the overall variance presented in figure 6.28b.

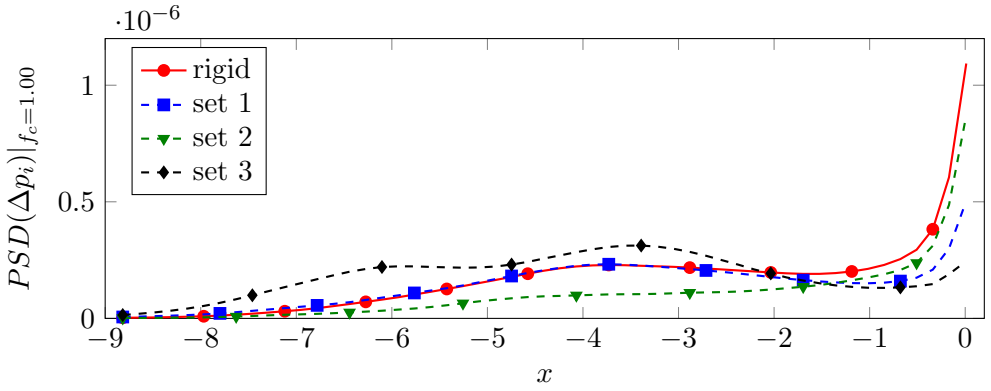

(a) recirculation frequency

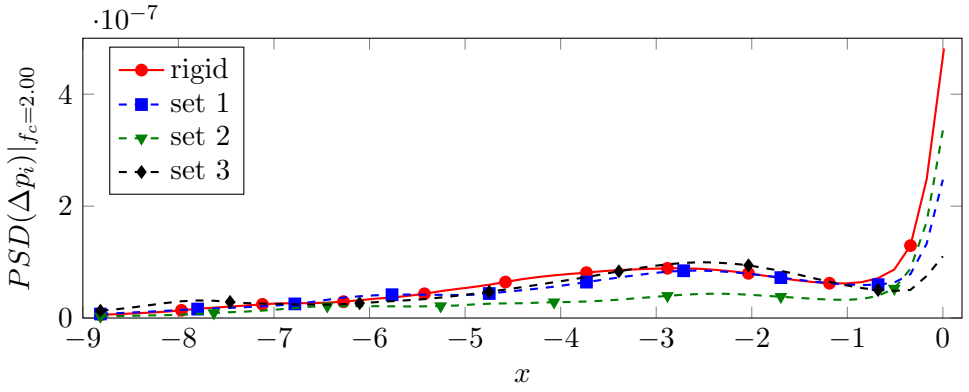

(b) first harmonic of the recirculation frequency

Figure 6.29: Comparison of the incident pressure difference fluctuations $\Delta p_i'$ at the recirculation frequency f_b and its first harmonic $2f_b$ for the elastic and rigid TE.

Figure 6.30 shows the incident pressure fluctuations at the respective structural frequency with the highest excess noise listed in table 6.6. For parameter sets 1 and 2 this is the first and for set 2 the second structural frequency, respectively. Parameter set 1 is presented in figure 6.30a and despite a noise increase of 16.4dB for this one-third-octave band the peak at the TE has less energy than in the rigid case. The higher fluctuation level of the elastic plate upstream of the TE at $x = -4$ indicates that the fluctuations in the separation bubble are amplified by the structural motion. However, this is not the dominating noise source that causes the excess noise, as this would predominantly radiate into the upper part of the domain. In figure 6.21a an increased noise level was found in all directions, which in fact was more pronounced on the lower side.

The energy of the incident pressure fluctuations for the elastic TE with parameter set 2 is shown in figure 6.30c. Similarly to parameter set 1 the pressure fluctuations in the separation bubble seem to be amplified by the structural motion. Moreover, the sharp increase towards the TE is significantly amplified in the elastic case. This is consistent with the directivity in that frequency band, presented in figure 6.21b, showing a very strong upstream radiation directivity. Furthermore higher Reynolds stress amplitudes

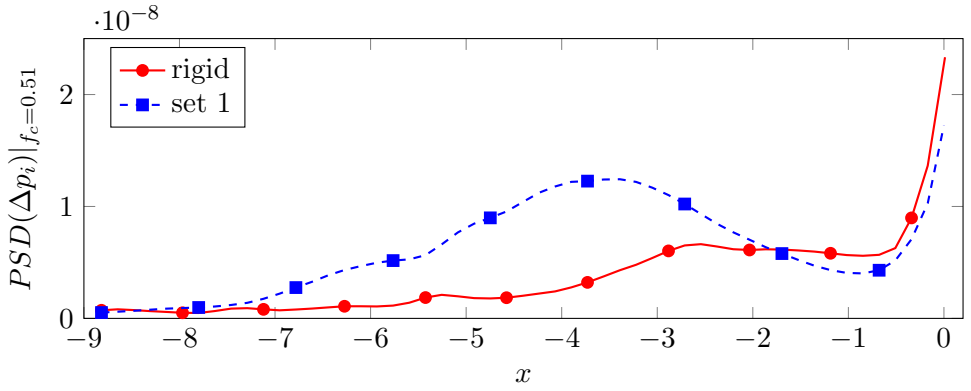

(a) total pressure difference fluctuations

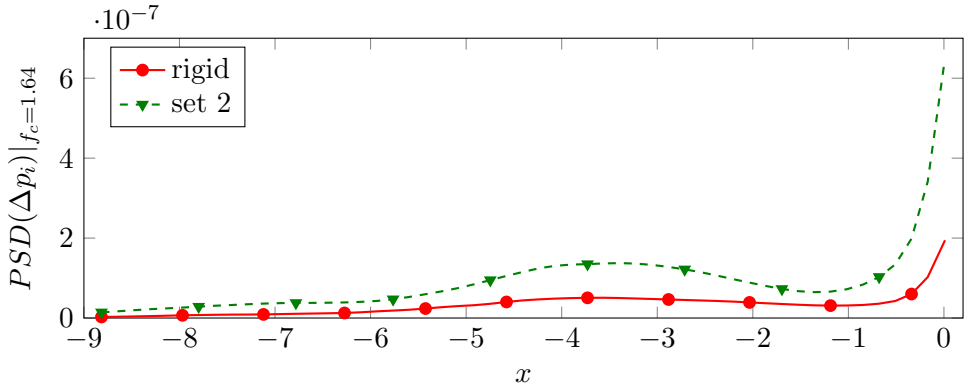

(b) parameter set 1 for $f = 0.51$

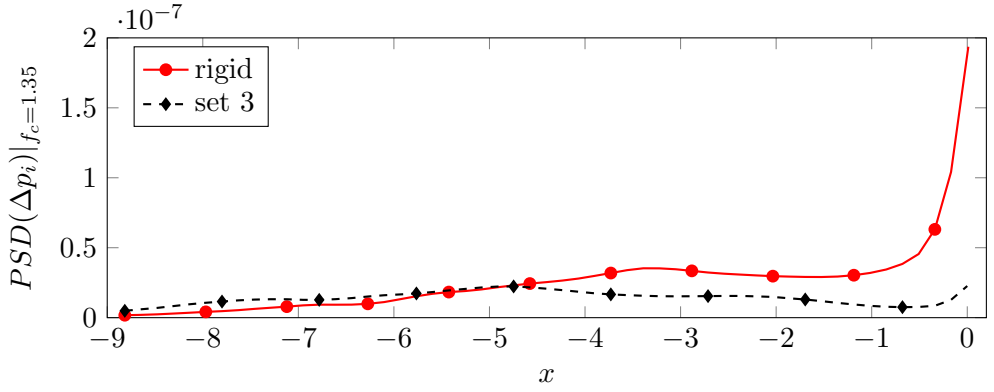

(c) total pressure difference fluctuations

Figure 6.30: Comparison of the incident pressure difference fluctuations $\Delta p'$ at structural frequencies with the highest excess noise comparing the elastic and rigid TE's.

were found at this location in figure 6.26b. It should be mentioned that the third structural frequency of the parameter set 1 qualitatively shows a similar behaviour. Due to the insignificant energies contained in the related frequency band it is not discussed separately here.

Finally, the elastic plate with parameter set 3 featuring the lowest bending rigidity of the elastic cases is considered in figure 6.30c. The behaviour at the TE is comparable

to parameter set 1. However, along the plate the fluctuations in the separation bubble are damped instead of amplified.

In summary, it was found that the motion of the elastic TE does change the length of the separation bubble and therefore also the input to the TE noise mechanism. Considering the excess noise of the elastic TE found in certain frequency bands, indications for the following mechanism was found: The excess noise does not originate from the TE as the sharp increase of the incident pressure field is significantly lower than for the rigid case. In that case the most likely source of the excess noise is the structural motion itself. This mechanisms was also represented in the amplitudes of the streamwise Reynolds stress profiles at the TE location.

6.5.2 Influence of Structural Damping on Trailing-Edge Noise Generation

The results from the previous section 6.5.1 showed that the potential for a noise reduction of an elastic TE can be mitigated or destroyed by the noise amplification or excess noise found at the structural frequencies. From a physical point of view the elastic TE's redistribute the energy of the flow between the main recirculation frequency and the natural frequencies of the structure. This redistribution can lead to an overall noise reduction as found for parameter set 1. However, the elastic structure in the discussed simulations does not absorb energy as the governing equation 2.15 does not account for that physical mechanism. This section investigates the influence of structural damping on the TE noise generation. Damping of vibrations in structures usually not only depends on its material properties, but also on the surrounding medium and on the boundary conditions. Furthermore, structural damping varies with the vibration frequency, amplitude and mode as well as temperature. To conceptionally investigate the effect of damping on the noise from an elastic TE, a mathematical formulation commonly presented in textbooks is employed in this work (Thomsen, 2004). To that end the governing equation of the bending beam is reformulated to

$$\rho_s A_S \frac{\partial^2 w_s}{\partial t^2} = \Delta p - E_s I_s \frac{\partial^4 w_s}{\partial s^4} - c_d \dot{w}_s \qquad , \tag{6.1}$$

where c_d is the viscous damping constant and $\dot{w}$ the velocity of the structure, i.e. $\partial w/\partial t$. The damping constant was set to $c_d = 0.01$. It was chosen such that a significant reduction of the structural deflections could be observed but still be represented appropriately by the BDIM. The mathematical formulation to represent structural damping chosen in equation 6.1 is often denoted air damping (Baker *et al.*, 1967; Banks & Inman, 1989), i.e. damping through viscous forces in the surrounding fluid of the structure. Through the direct coupling of the structural solver and the fluid solver this physical mechanism is implicitly accounted for, even if $c_d = 0$. Despite this physical interpretation, the model was chosen for a conceptional study due to its ease of implementation. Even if other models, such as the Kelvin-Voigt strain rate damping model or the time hysteresis model, might represent the physics of the vibrating beam more accurately, the additional damping introduced with the current model is able to show the principal effect of damping. With this updated structural model the simulations for parameter sets 1 and 3 were repeated.

6.5.2.1 Statistical Analysis of the Acoustic Field

Figure 6.31 compares the overall sound pressure level of damped and undamped elatic TE's with the rigid TE in the far-field. For parameter set 1 the difference between undamped and damped cases are up to 1.6dB in the $\theta = 225°$ direction below the plate.

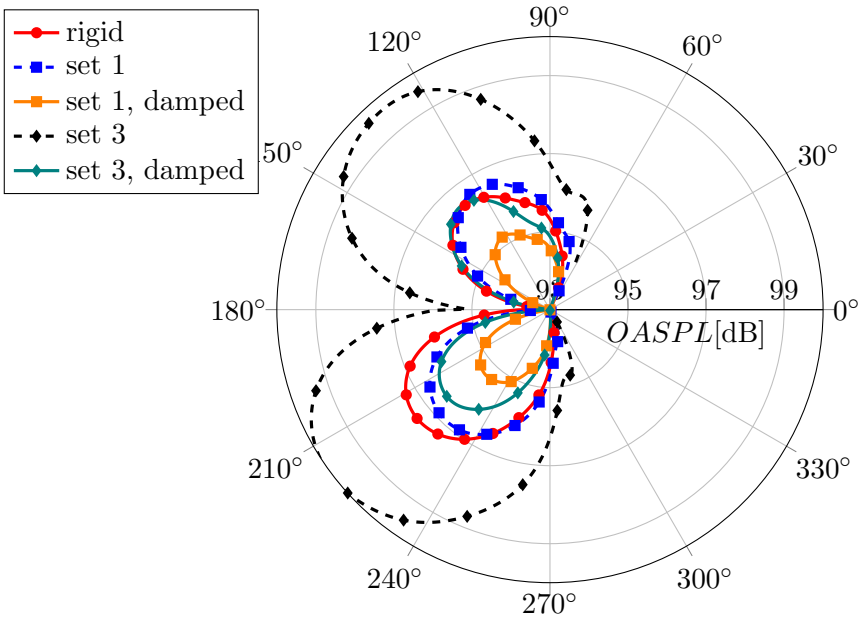

Figure 6.31: Directivity of the overall sound pressure level $OASPL$ at a radial distance of $r = 150D_{cyl}$ from the TE comparing the damped and undamped elastic TE's with the rigid TE. The linestyles with the same marker type relate to the same parameter set with and without damping.

The noise reduction compared to the rigid TE is up to 2.4dB. The influence of the structural damping is most significant for parameter set 3 where the damping leads to a noise reduction of up to 3.7dB below the plate in the $\theta = 225°$ direction relative to the undamped case with the same structural parameters. Indeed with the damping this parameter set can also lead to a noise reduction of 1.1dB relative to the rigid TE where the undamped case showed an increase in noise.

To analyse the influence of the structural damping on the spectral content of the elastic TE in the far-field, figure 6.31 presents the power spectral densities comparing the undamped and damped cases with the rigid TE's. The first row (figure 6.32a and 6.32a) considers parameter set 1 at the two reference locations used in the previous section. At the recirculation shedding frequency, which is at the most relevant energy level, the damping leads to a noise reduction at both locations. In the upstream direction it is a 3.5dB reduction compared to a 0.4dB increase for the damped and undamped TE, respectively. Since this third-octave band contributes 44% to 50% to the overall energy of the spectrum this difference is highly relevant for the additional noise reduction employing the damping. Minor difference can be observed at the first harmonic of the recirculation, where the damping leads to an increase in noise of 1.1dB compared to the undamped elastic TE. The second largest contributor to the overall energy in the spectrum of the undamped elastic TE is the first structural frequency with 9%. When damping is considered this contribution decreases to 1.8% and yields a noise reduction of

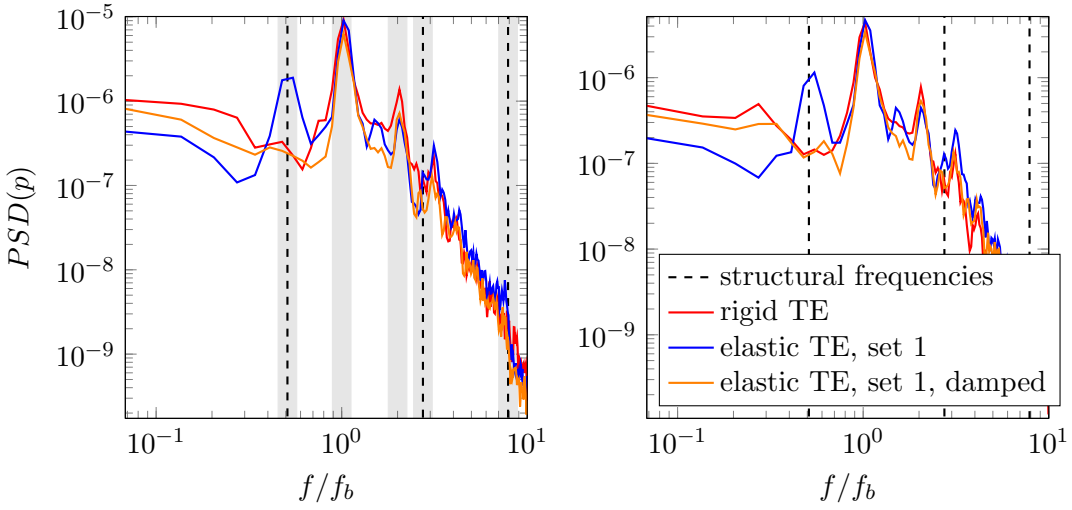

(a) parameter set 1 at $r = 150D_{cyl}$ and $\theta = 225°$ (b) parameter set 1 at $r = 150D_{cyl}$ and $\theta = 270°$

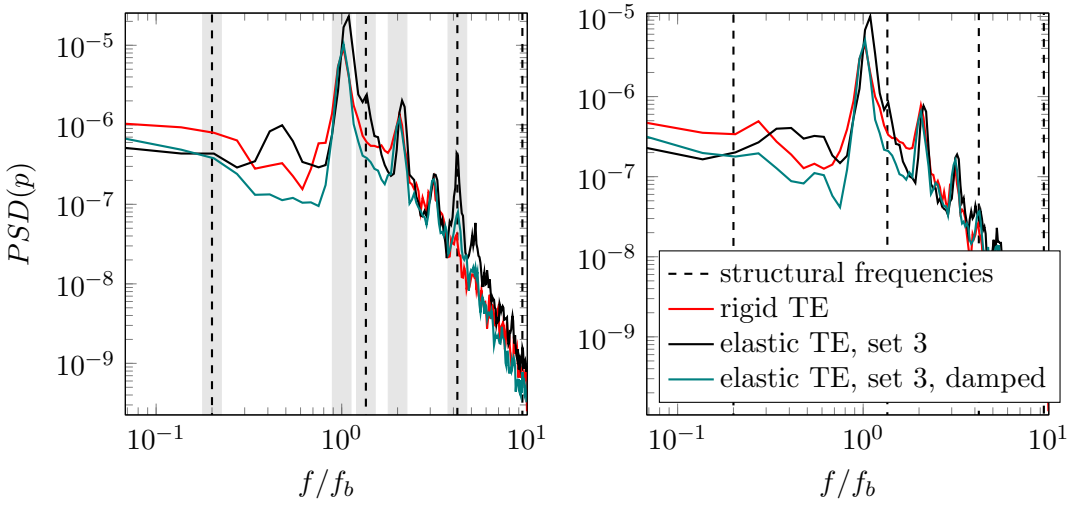

(c) parameter set 3 at $r = 150D_{cyl}$ and $\theta = 225°$ (d) parameter set 3 at $r = 150D_{cyl}$ and $\theta = 270°$

Figure 6.32: Evaluation of the influence of structural damping on the far-field power spectral density of pressure between the rigid and elastic TE's for two different positions and two different parameter sets. The vertical dashed black lines are the structural frequencies as determined from the PSD of the deflection in figure 6.17 and documented in table 6.5. The shaded areas mark the one-third octave bands discussed in the text.

17.6dB and 1.5dB relative to the undamped and rigid TE, respectively. The interaction between recirculation frequency and first structural frequency seems to be suppressed when the elastic TE is damped. For the other frequency ranges the damping reduces the energy in the spectra, however, their contribution to the overall energy is small.

The effect of damping on the spectrum of the elastic TE with parameter set 3 with a lower bending rigidity than set 1 is considered in the second row of figure 6.32. It is apparent that the damping reduces the peak at the recirculation frequency significantly at both locations under consideration. The reduction in the upstream direction is 7.7dB

f_c		set 1			damped	
f_b	0.4dB	49.5%	44.3%	−3.5dB	47.1%	44.3%
$2f_b$	−6.6dB	6.0%	12.0%	−5.5dB	10.1%	12.0%
$f_{1,s}$	16.4dB	9.3%	1.3%	−1.2dB	1.8%	1.3%
$f_{2,s}$	−1.9dB	2.7%	3.1%	−5.4dB	2.7%	3.1%
$f_{3,s}$	3.2dB	0.2%	0.1%	−3.2dB	0.1%	0.1%

f_c		set 3			damped	
f_b	7.2dB	54.2%	44.3%	0.5dB	57.3%	44.3%
$2f_b$	1.6dB	7.7%	12.0%	−1.7dB	12.1%	12.0%
$f_{1,s}$	−5.2dB	0.6%	1.9%	−6.4dB	1.1%	1.9%
$f_{2,s}$	7.7dB	11.0%	8.5%	−4.9dB	5.9%	8.5%
$f_{3,s}$	14.5dB	2.4%	0.9%	4.3dB	1.7%	0.9%

Table 6.7: Energy distribution of the power spectral density for the elastic TE's with and without damping in comparison with the rigid TE below the plate relating to the spectra in the first column of figure 6.32. The power is calculated in third octave bands around center frequencies f_c. The difference to the rigid TE is given in dB where a positive sign indicates a noise increase and a negative sign a noise reduction. The second and third number in each column indicate the contribution of frequency range to the total energy in % for the elastic and rigid TE, respectively.

relative to the undamped case. It should be mentioned that this reduction is biased by the slight shift of this peak towards higher frequencies in the undamped elastic case. As a result the frequency band does not cover the whole peak. Thus the actual noise reduction is higher. However, overall the damped elastic TE still leads to a minor increase in noise compared to the rigid case in this frequency band. In contrast to that the damping reduces the noise level at the first harmonic of the recirculation frequency by 3.3dB and 1.7dB compared to the undamped and rigid TE, respectively. In the low frequency range below the recirculation frequency the damping leads to noise reduction and the additional hump found in the undamped elastic TE at $f/f_b = 0.47$ can not be identified in the damped case. The same is true for the second structural frequency where a reduction in the damped case is 12.6dB and 6.4dB relative to the undamped and rigid TE, respectively. At the third structural frequency the excess noise found in the undamped elastic TE is also reduced significantly. However, the contribution of that frequency to the overall noise is comparatively small.

Figure 6.33 compares the directivity of the power spectral density for the damped and undamped cases. For easier comparison the data from the body-fitted simulations is not plotted here as it was presented and discussed in figure 6.20. At the recirculation frequency the comparison of undamped cases with the rescaled data from the damped cases shows signs of an additional lobe present in these cases. It can only be speculated at this stage whether they originate from a physical mechanism that is only present in the cases with damping or whether it is due to the significant reduction of the noise from the TE and the structural motion that this lobe can now be identified. Since the

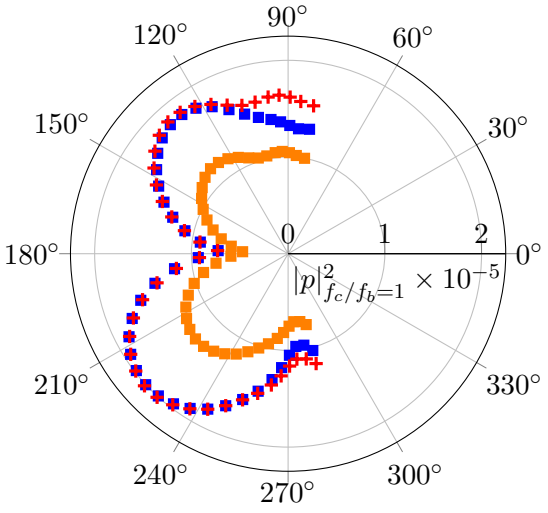

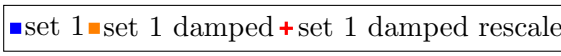

(a) directivity of parameter set 1 at the recirculation frequency $f_c/f_b = 1$

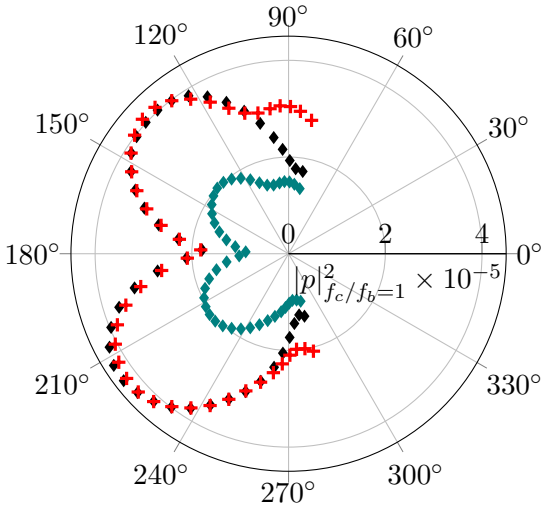

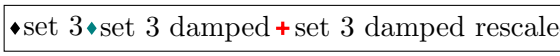

(b) directivity of parameter set 3 at the recirculation frequency $f_c/f_b = 1$

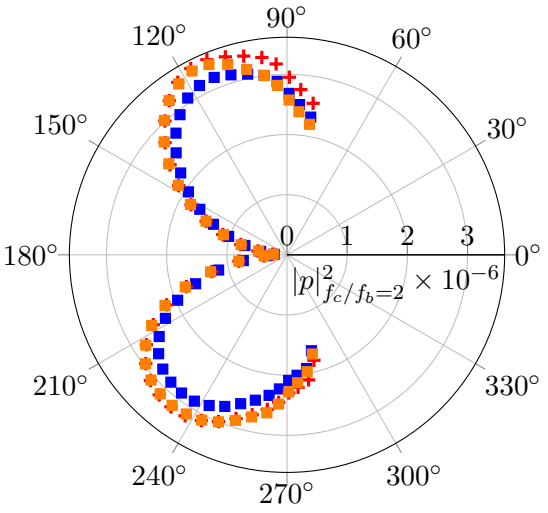

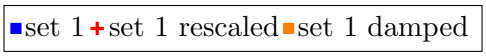

(c) directivity of parameter set 1 at the first harmonic of the recirculation frequency $f_c/f_b = 2$

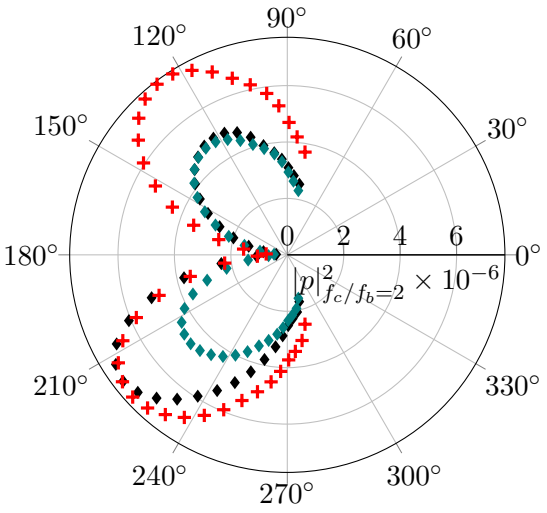

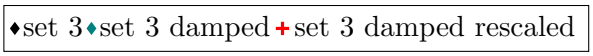

(d) directivity shape of parameter set 3 at the first harmonic of the recirculation frequency $f_c/f_b = 2$

Figure 6.33: Comparison of the directivity of the power spectral density of pressure for the damped and undamped elastic TE's in the third octave band centered on the recirculation frequency and its first harmonic.

undamped cases, in particular parameter set 1 on the lower side of the plate, show indications of this lobe as well, the latter option seems, however, to be more reasonable. At the first harmonic of the recirculation frequency presented in figure 6.33c the rescaled data for parameter set 1 matches the undamped case exactly with respect to shape. This is not the case for parameter set 3 shown in figure 6.33d where the noise radiation of the damped TE seems to be relatively stronger in the wall normal direction.

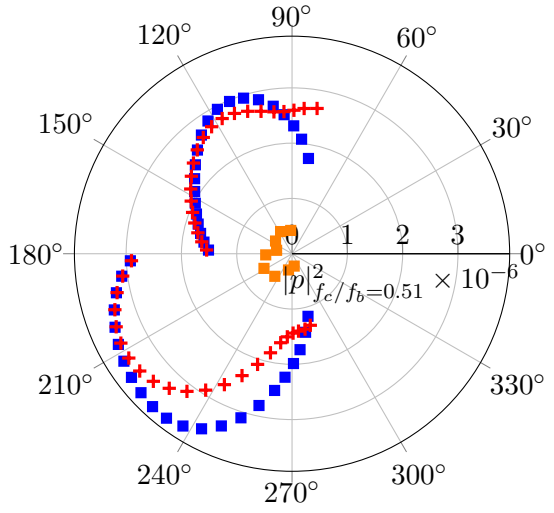

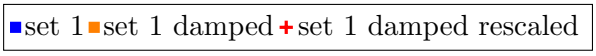

(a) directivity shape at the first structural frequency of parameter set 1 $f_c/f_b = 0.51$ with rescaled data from rigid case

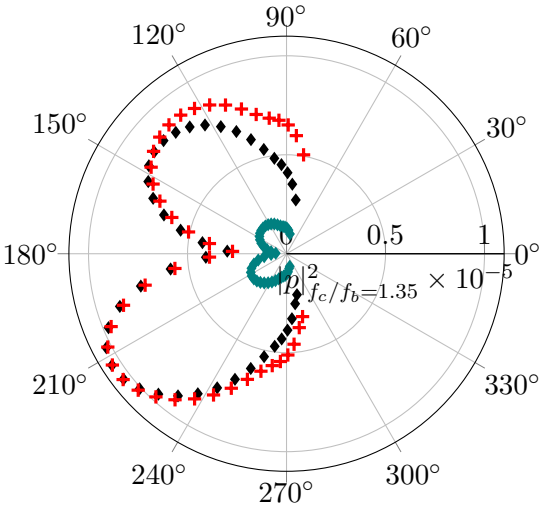

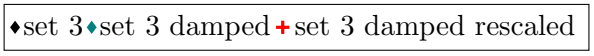

(b) directivity shape at the second structural frequency of parameter set 3 $f_c/f_b = 1.35$ with rescaled data from rigid case

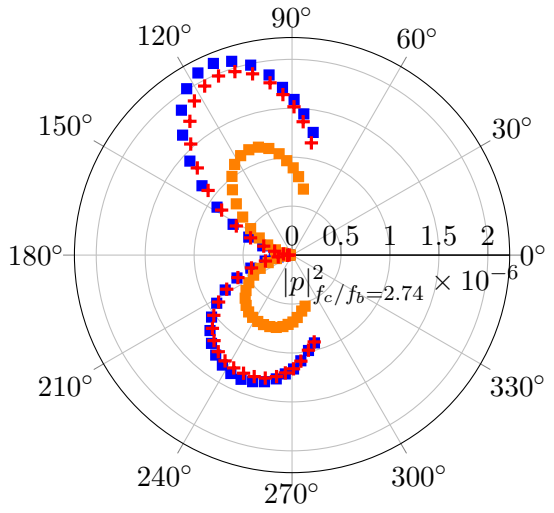

(c) directivity shape at the second structural frequency of parameter set 1 $f_c/f_b = 2.74$ with rescaled data from rigid case

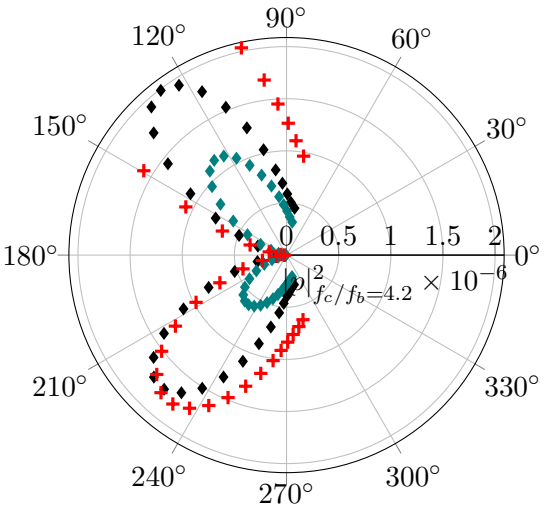

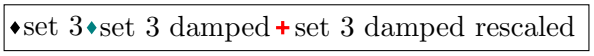

(d) directivity shape at the third structural frequency of parameter set 3 $f_c/f_b = 4.2$ with rescaled data from rigid case

Figure 6.34: Comparison of the directivity of the power spectral density of pressure for the rigid and elastic TE's in the third octave band centred on the structural frequencies where significant excess noise was observed.

Figure 6.34 shows the directivity in frequency bands where significant excess noise was found in the undamped cases. In all cases and frequency bands considered here the structural damping reduces the noise in all directions significantly. For the first structural frequency the directivity of parameter set 1, presented in figure 6.34a shows a relative decrease of the noise radiation in the wall normal direction. The opposite is true for

parameter set 3 presented in figure 6.34b. In the frequency band of the second structural frequency the shapes of the damped and undamped cases match closely. Considering the third structural frequency of parameter set 3 in figure 6.34d the relative change of the directivity pattern is similar to the second structural frequency of the same case where the wall normal direction is relatively more pronounced.
Overall the changes in the directivity indicate that the radiation in the wall normal direction becomes relatively more important when employing damping in parameter set 3. For parameter set 1 only minute changes or a tendency to decrease the noise radiation in the wall normal direction could be observed. As a result the change in the directivity shape relative to the rigid TE can not be attributed to the directivity shape of the noise from the structural motion as this source is eliminated by the damping.

In summary the damping leads to a significant noise reduction compared to the undamped cases and also the rigid TE. From the spectral analysis the noise attenuation could be attributed to a reduced energy level at the recirculation frequencies. Moreover the damping attenuates or eliminates the unfavourable excess noise related to the structural frequencies.

6.5.2.2 Analysis of the Hydrodynamic Near-Field

This section investigates the changes in the hydrodynamic near-field when structural damping is employed in order to find the reason for the noise reduction compared to the undamped cases and the rigid TE. The first question is whether the significant modification of the acoustic far-field by structural damping can be related to changes in the structural motion itself. To assess the structural motion figure 6.35a compares the time-averaged deflection for the two parameter sets 2 and 3 with and without damping. On the one hand, the damping does not change the shape of the mean deflection for both parameter sets. On the other hand, the amplitude of the deflection is slightly increased by the damping. The opposite is true for the standard deviation of the structural motion presented in figure 6.35b. Firstly, the damping changes the shape of the standard deviation of parameter set 3 to be dominated by bending mode 1. Secondly, the deflection amplitudes are reduced significantly for both parameter sets when the damping is employed.

The spectral content of the free end deflection for the damped and undamped cases is presented in figure 6.36. For both parameter sets the amplitude of the peak at the recirculation frequency is reduced when damping is employed. This is consistent with the reduction of the noise in the far field discussed earlier. In contrast to that, its first harmonic contains slightly more energy in the cases with damping which is what was found in the far-field spectra as well. In the frequency range below the recirculation frequency the energy containing peaks found in the undamped case can not be identified

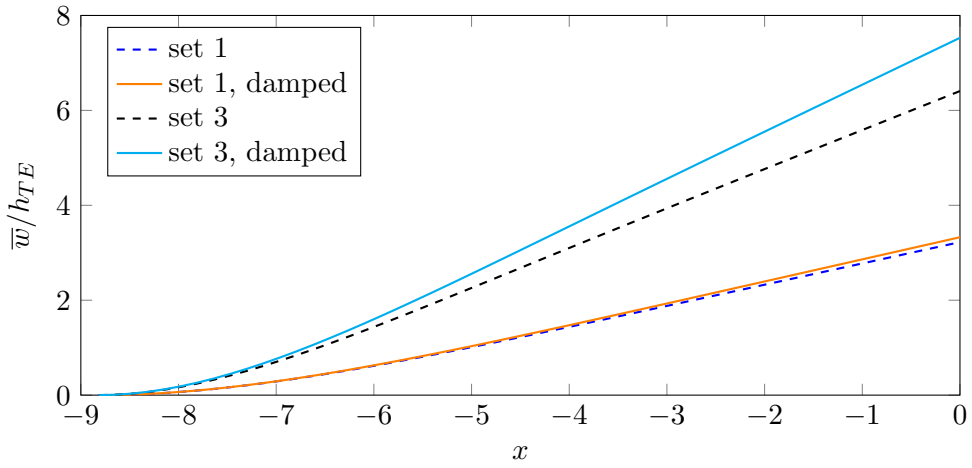

(a) Mean deflection $\overline{w}$

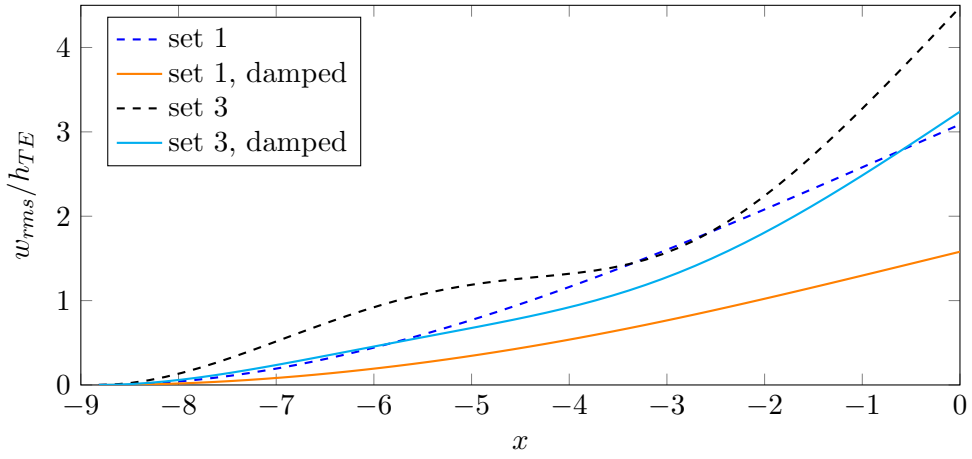

(b) Standard deviation of the deflection w_{rms}

Figure 6.35: Mean and standard deviation of the deflection time history of the TE point as function of the streamwise location comparing the undamped and damped TE.

in the cases with damping. The same is true in the frequency range above the recirculation frequency, where the damping attenuates or eliminates the peaks at the natural frequencies of the structural motion.

In conclusion, the damping reduces the vibration amplitude globally. Qualitatively, the spectra are changed at the natural frequencies of the structure where the amplitudes of the motion are significantly reduced or completely damped. This is consistent with noise reductions observed in the far field power spectral density presented in figure 6.32.

As the pressure fluctuations from the separation bubble on top of the plate represents one of the major inputs into the TE noise mechanism and were found to be slightly altered by the elastic (undamped) TE's, the contours of the streamwise velocity component are considered first in figure 6.37. The rigid and undamped TE's are replotted here again to enable a better comparison. For both parameter sets the damping leads to a

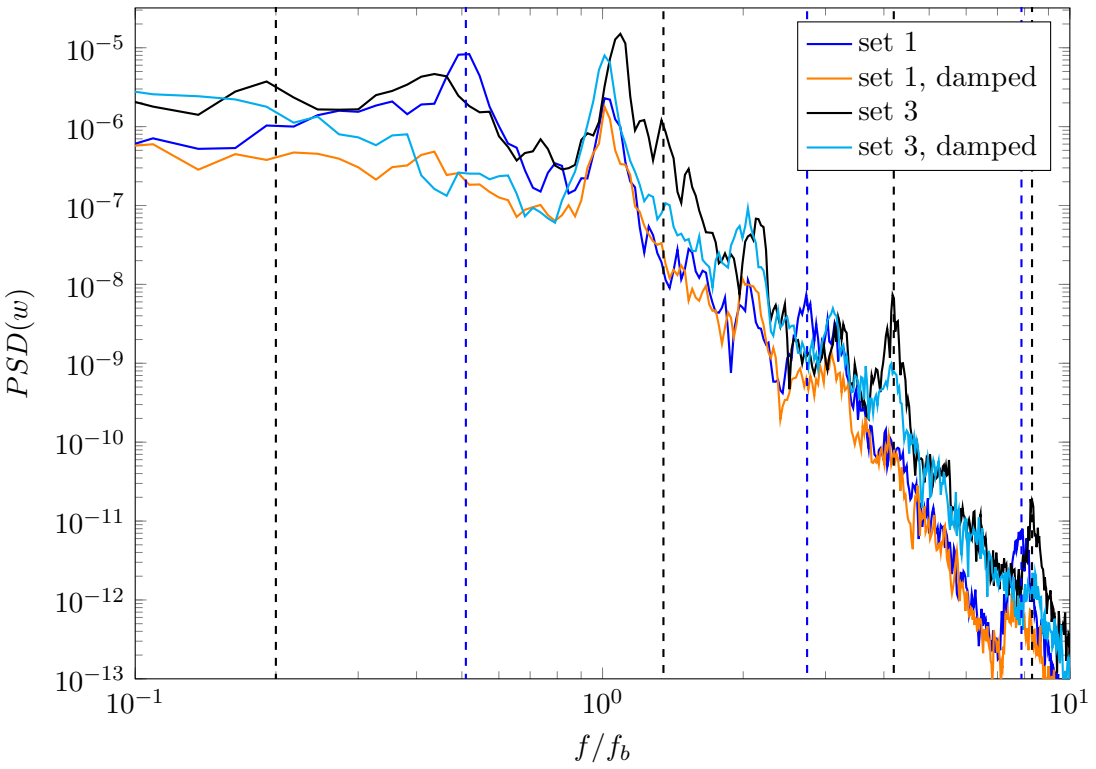

Figure 6.36: Power spectral density of the free end deflection w of the structure for two different parameter sets with and without damping. The vertical dashed lines indicate the actual frequencies of the undamped structural motion that were determined from figure 6.17 and listed in table 6.5

longer separation bubble on top of the plate. In terms of shape, the separation bubbles in the damped cases more closely resemble that of the rigid case. It is likely that this can be attributed to the smaller fluctuations of deflection of the plate despite the larger mean as shown in figure 6.35b.

Figure 6.38 shows the time averaged skin-friction to determine the start and end of the separation bubble under the influence of structural damping. The first visual impressions from the velocity contours are confirmed when the zero-crossings are considered which show that for both parameter sets the damping leads to a downstream shift of the separation bubble. For parameter set 1 with damping, the onset and end of the bubble closely agree with the rigid TE. For parameter set 3 the damping results in a separation bubble that is shifted upstream compared to the rigid TE.

Figure 6.39 compares the velocity and Reynolds stress profiles of the damped and undamped elastic cases with the rigid TE upstream of the elastic fraction. As discussed in figure 6.25a, the changes in the streamwise velocity profiles are minute. For parameter set 3 the damping reduces the higher recirculation velocity observed in the undamped

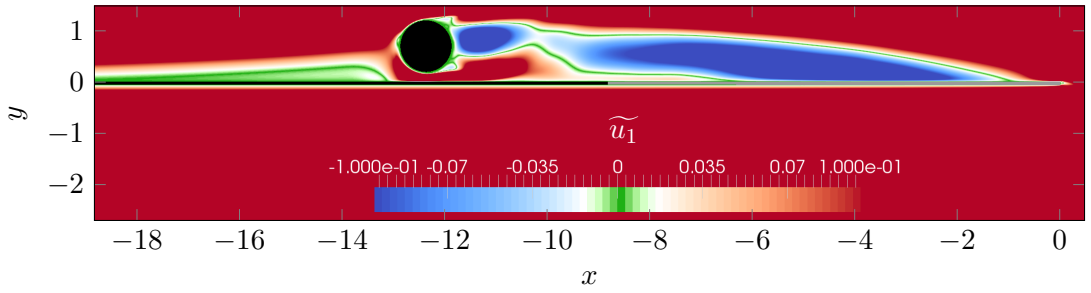

(a) rigid TE

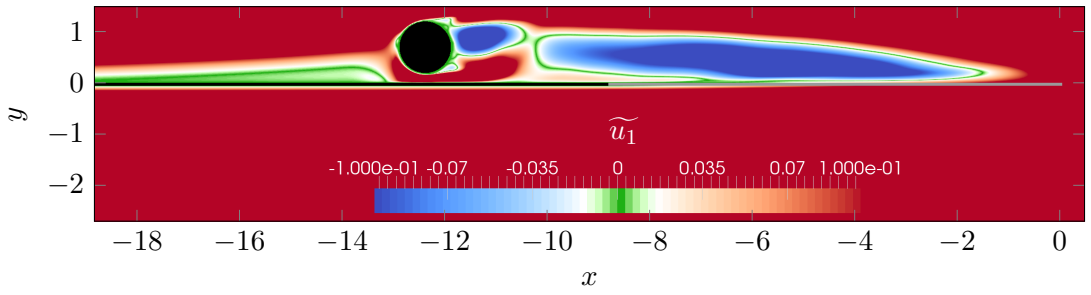

(b) elastic TE with parameter set 1

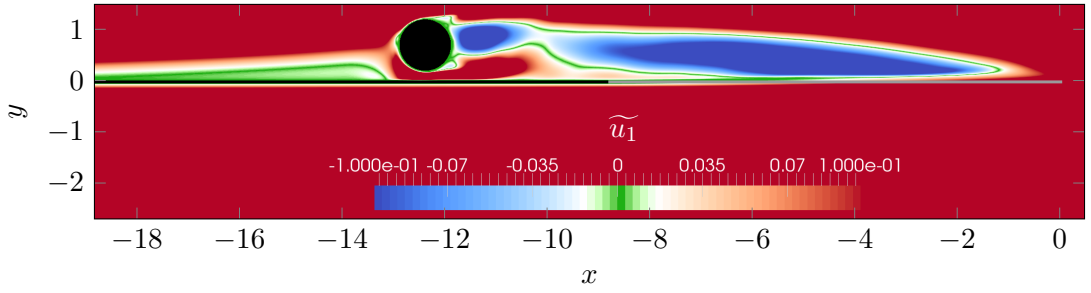

(c) elastic TE with parameter set 1 with damping

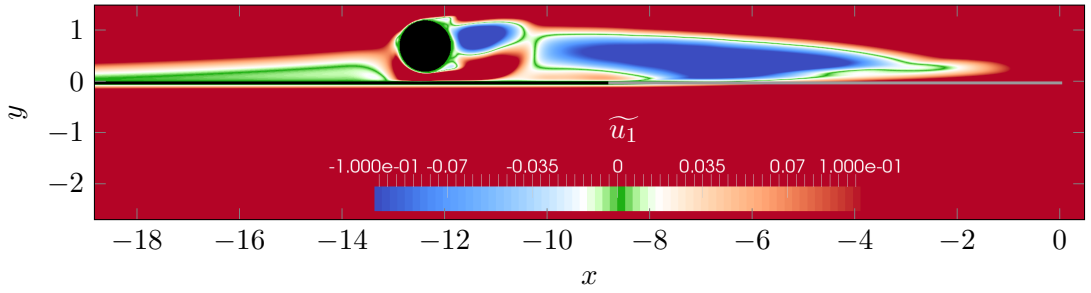

(d) elastic TE with parameter set 3

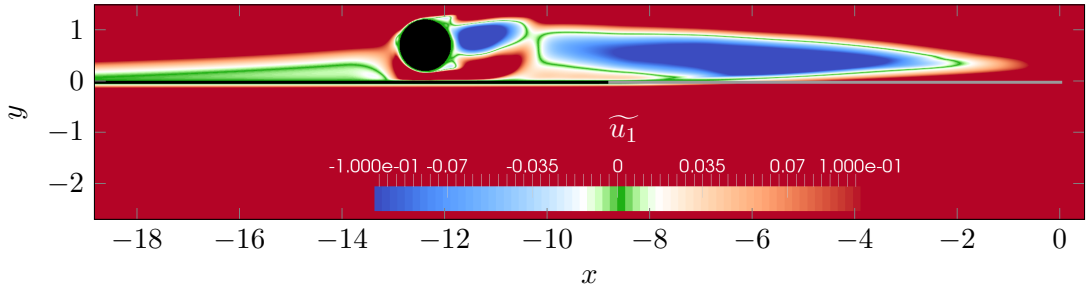

(e) elastic TE with parameter set 3 with damping

Figure 6.37: Contours of the Favre averaged streamwise velocity component $\widetilde{u_1}$ in the vicinity of the vortex generator and TE. The elastic fraction is visualized in the undeflected state in gray color.

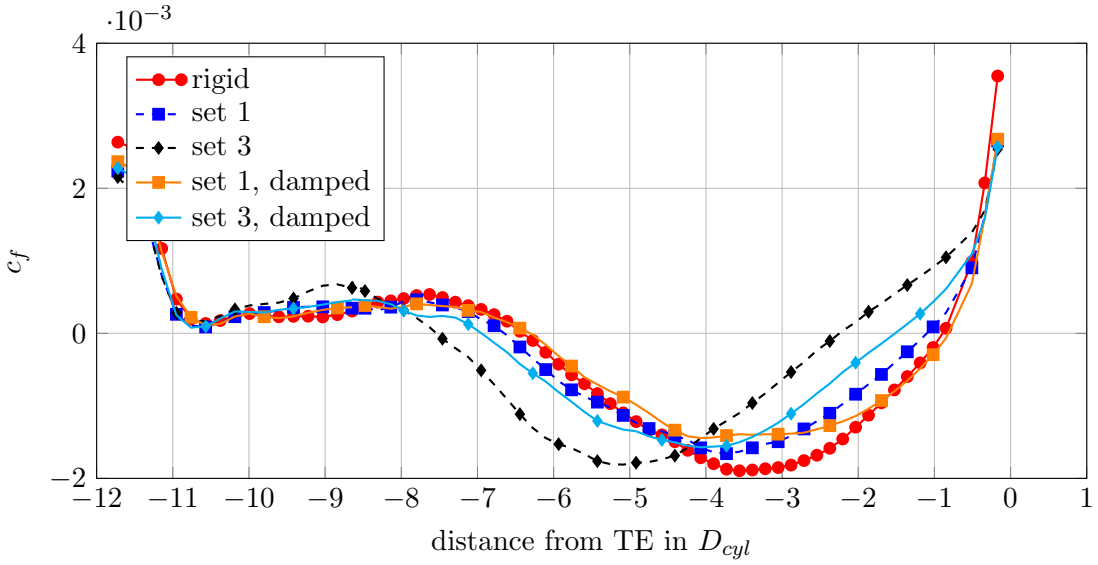

(a)

Figure 6.38: Skin friction along the upper side of the plate for the different damped and undamped elastic and rigid TE's.

case, leading to a profile very similar to the other cases. In particular for parameter set 1, the damping leads to a close agreement with the rigid TE, which is consistent with the similar location and extent of the separation bubble determined from figure 6.38. For both parameter sets the damping reduces the amplitudes of the Reynolds stresses τ_{11} and τ_{22} at this location, which can be related to the downstream shift of the separation bubble.

At the TE location, shown in figure 6.40, the smaller amplitude fluctuations of the body structural motion with damping lead to a slightly increased momentum deficit compared to the undamped cases. The Reynolds stress components seem to be reduced in amplitude close to the wall and increased towards the freestream when comparing the damped to the undamped elastic plate cases.

The variance of the total pressure difference presented in figure 6.41a shows the same trend as the skin friction. For parameter set 1 the maximum amplitude of the variance is not altered by the damping. This is in contrast to parameter set 3 where the maximum amplitude of the variance is decreased to a similar level as for parameter set 1. The variance of the incident pressure difference, shown in figure 6.41b, shows greater amplitude peaks at the TE for the damped TE's compared to the undamped cases. The same trend can be found in the variance of the scattered pressure difference. This trend is surprising as it is not consistent with the noise received in the far-field, as presented in figure 6.31. In the far-field, the damping leads to a significant noise reduction in all cases and it is expected that the peak of the variance of incident pressure field at the TE is proportional to the noise in the far-field. It can be speculated that on the one

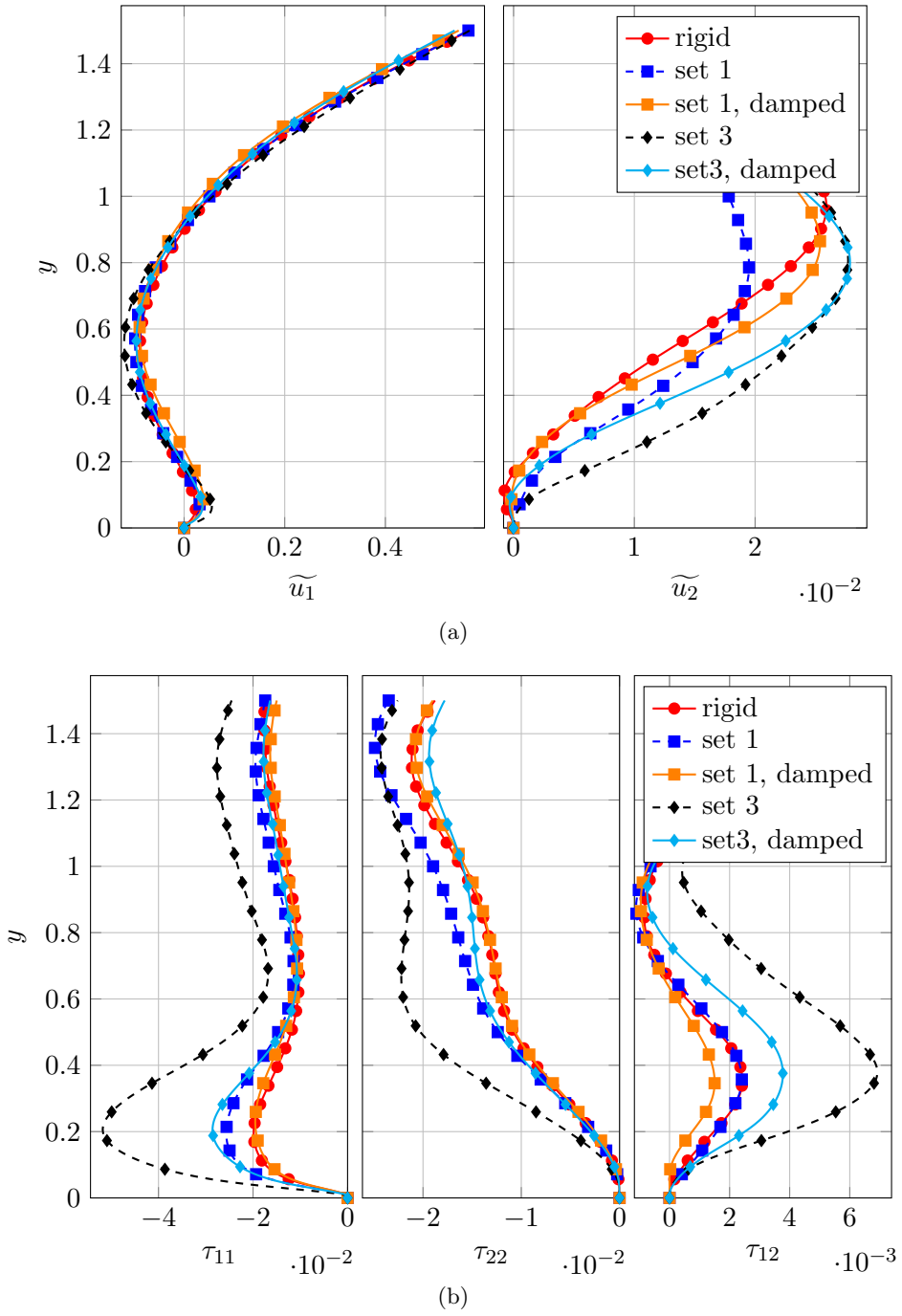

Figure 6.39: Comparison of the Favre averaged velocity and Reynolds stress profiles at the beginning of the elastic fraction ($x = -8.75D_{cyl}$) for the damped and undamped elastic and rigid TE's.

hand the slower reaction of the plate to the forcing from the fluid reduces the ability of the elastic TE to attenuate the TE noise radiation. On the other hand, this effect is overcompensated by the significant reduction of the excess noise generated by the structural motion at the recirculation and structural frequencies.

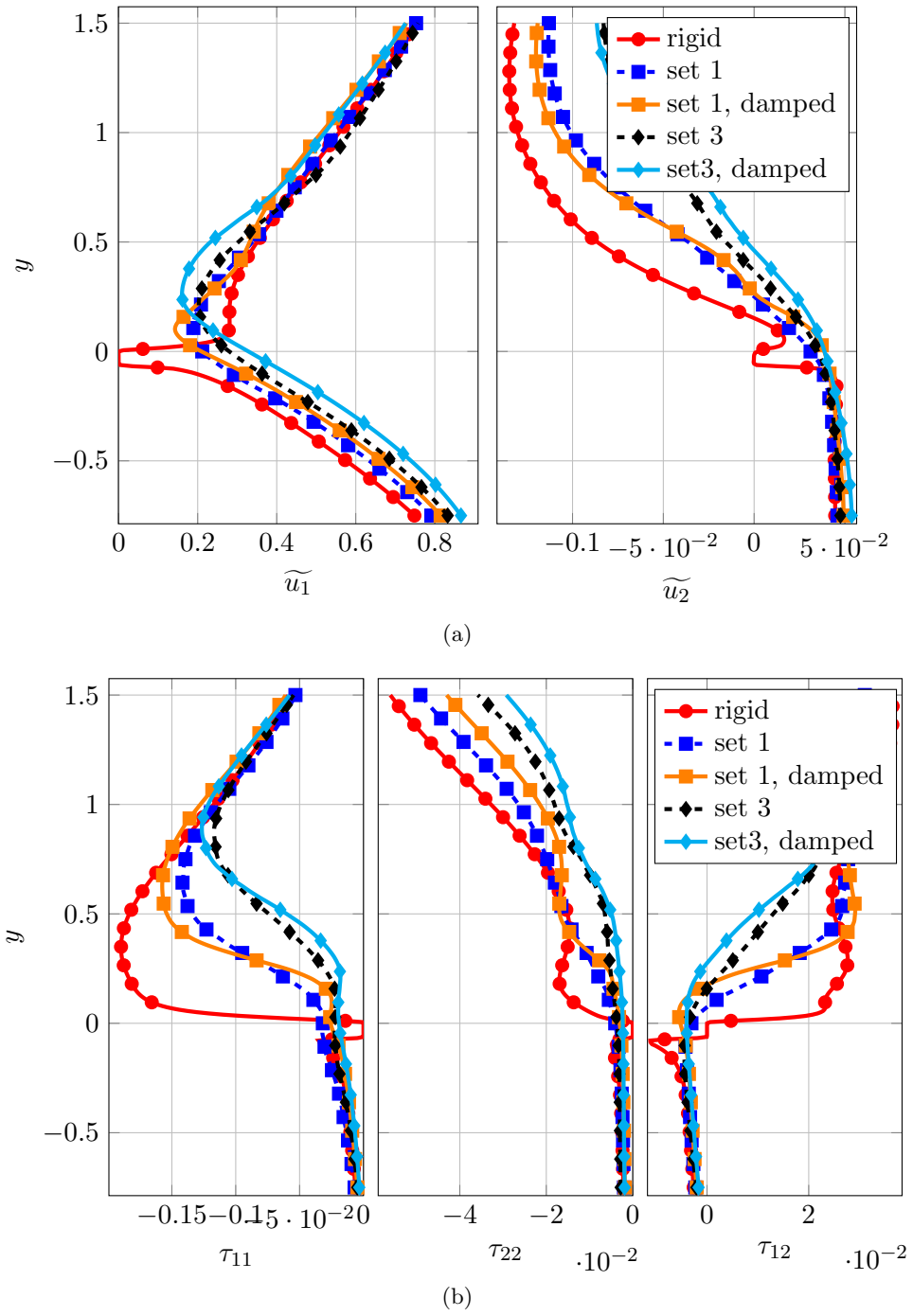

(a)

(b)

Figure 6.40: Comparison of the velocity and Reynolds stress profiles at the TE ($x = 0.4h_{TE}$) for the rigid and elastic TE represented by the BDIM.

The same trend can be observed in the power spectral density of the incident pressure difference at the recirculation frequency and its first harmonic shown in figure 6.42a and 6.42b, respectively. For parameter set 3 the amplitudes of the damped and undamped case are in very close agreement for $-1.7 < x < -0.4$, and only start to deviate very close to the TE. This indicates that the different peak values at the TE are not purely due to the slight differences of the separation bubble upstream of the TE but also due

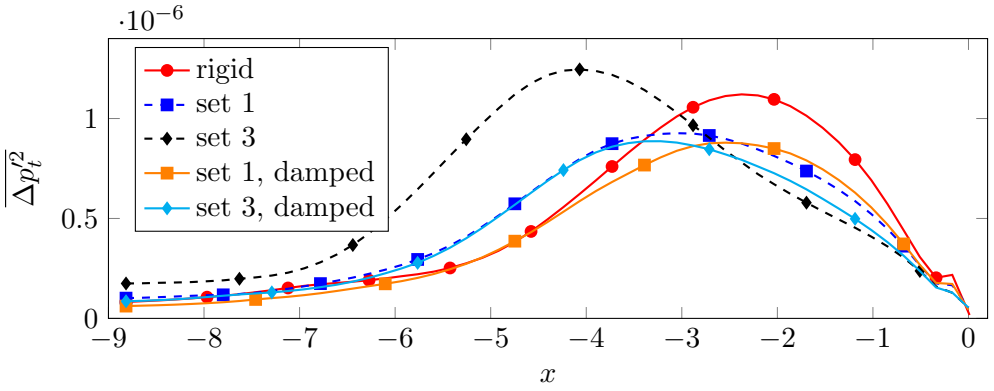

(a) variance of total pressure difference

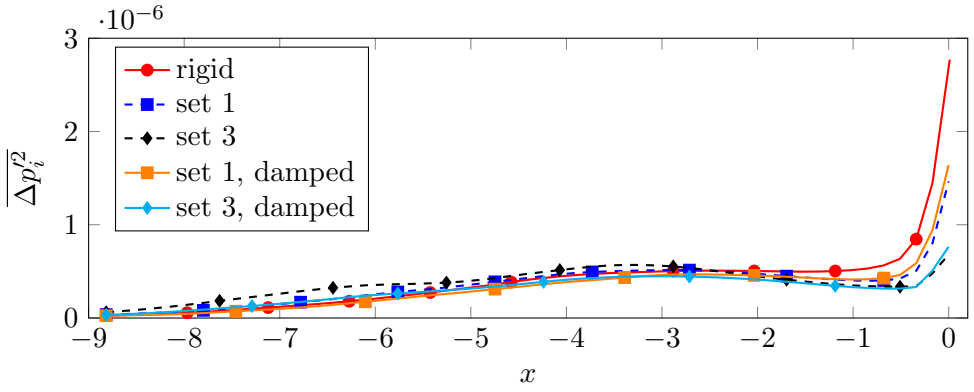

(b) variance of incident pressure difference

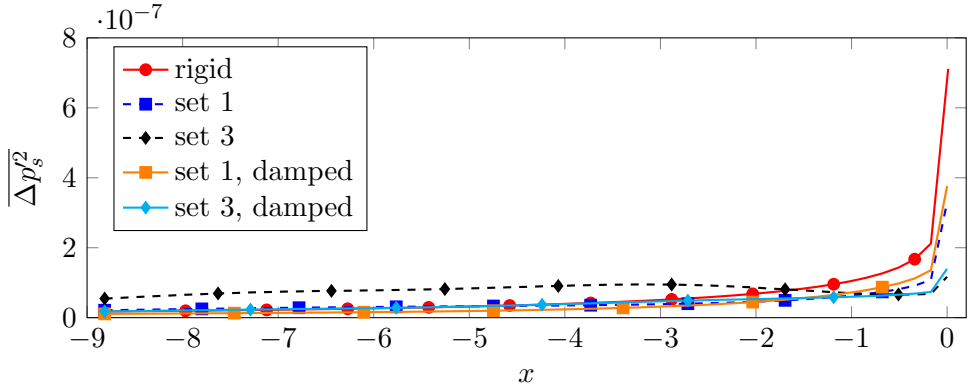

(c) variance of scattered pressure difference

Figure 6.41: Comparison of the total (a),incident (b) and scattered (c) pressure difference fluctuations $\Delta p'$ for the elastic and rigid TE.

to a stronger mitigation of the incident pressure field caused by the damping.

The sum of the scattered and motion induced pressure fluctuations is presented in figure 6.43 for the frequency bands with the most energy containing excess noise in the undamped elastic TE's. At the TE the same behaviour as in the figures of the incident pressure differences discussed previously can be observed. For the cases without damping significantly increased amplitudes of pressure fluctuations can be found upstream of

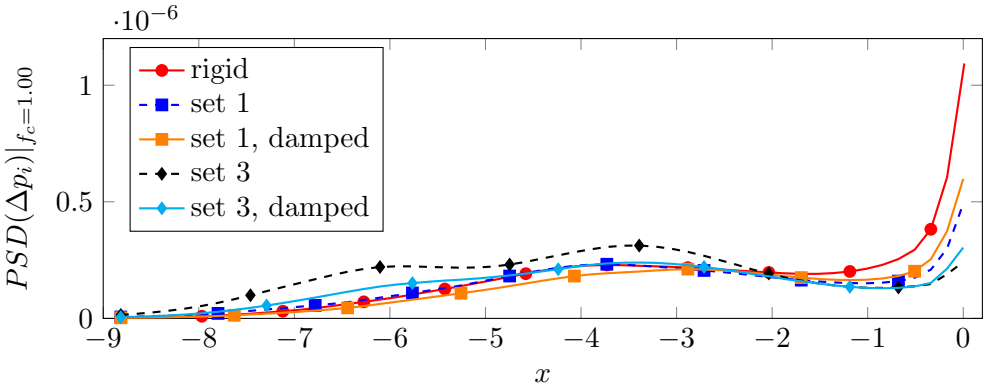

(a) recirculation frequency

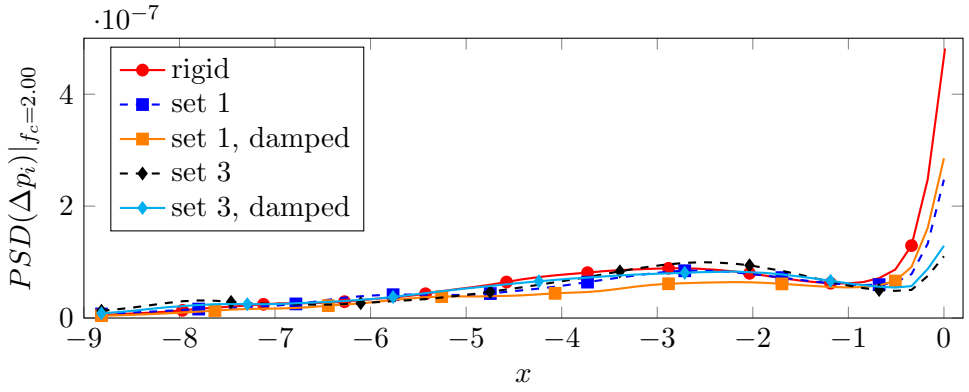

(b) first harmonic of recirculation frequency

Figure 6.42: Comparison of the incident pressure difference fluctuations $\Delta p_i'$ at the recirculation frequency f_b and its first harmonic $2f_b$ for the rigid and elastic TE's with and without damping.

$x = -2$. For both parameter sets with damping they are eliminated, which results in fluctuations lower than the rigid TE. This elimination can most likely be related to the significantly reduced fluctuations of the deflection at the structural frequencies.

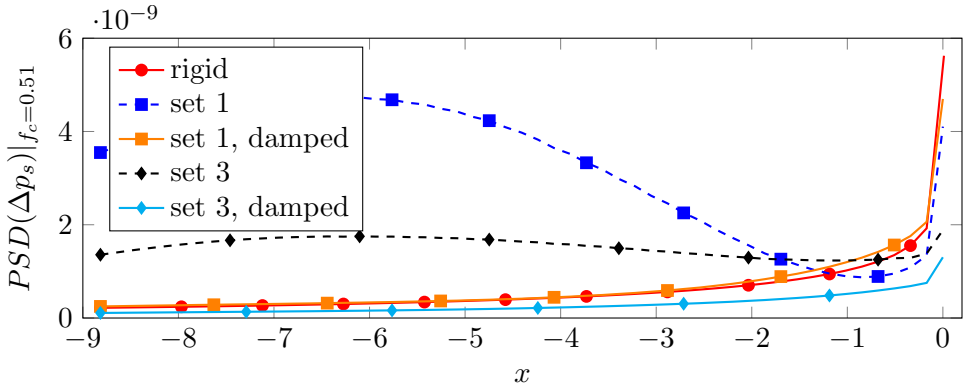

(a) scattered pressure differences at the first structrual frequency of parameter set 1

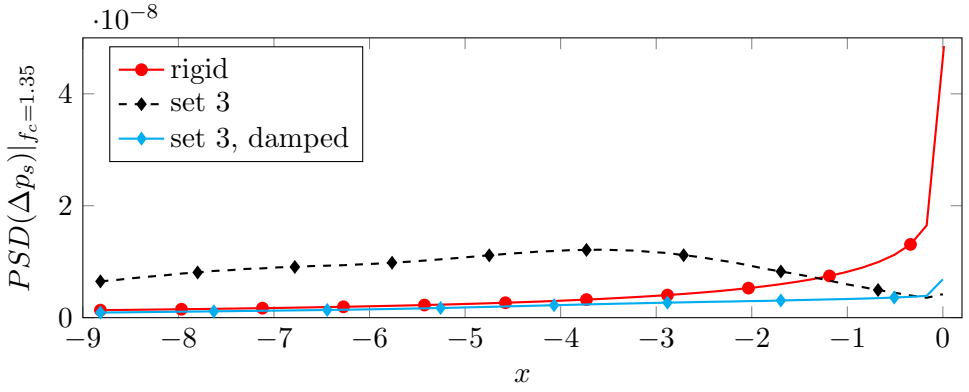

(b) iscattered pressure differences at the first structrual frequency of parameter set 3

Figure 6.43: Comparison of the sum of the scattered and motion induced pressure difference fluctuations $\Delta p'$ at the structural frequencies with the highest excess noise comparing the rigid and elastic TE's with and without damping.

6.6 Summary of the Findings

A generic setup to study the influence of TE elasticity on its noise radiation has been introduced and validated with a grid independence study and with body-fitted boundary conditions. Three different parameter sets for the elastic fraction of the TE have been considered. The effectiveness of a parameter set in reducing TE noise was found to be highly dependant on the response of the motion to the input loading from the flow, as the far field spectra of the elastic TE's featured excess noise at the structural frequencies. An examination of the hydrodynamic near field showed that this noise can originate from the TE as a result of an amplification of the incident field. However, in most cases the data showed no evidence that the excess noise is radiated from the TE and it is suggested that the excess noise is due to motion-induced sound from the elastic body. Finally, a reduction of the radiated noise was found in specific frequency ranges and for one parameter set also globally. This noise reduction was associated with two mechanisms: Firstly, the motion of the TE modified the incident pressure fluctuations and therefore the input to the TE noise mechanism. Secondly, the elastic TE was less efficient in transforming energy from hydrodynamic to acoustic pressure fluctuations.

The investigation of the effect of structural damping showed a potential for significant noise reductions compared to the undamped and the rigid cases. The investigated data indicated that this was achieved by reduced fluctuations of the deflections at the structural and the forcing frequencies. The higher amplitude peak of the incident pressure field at the TE suggests that some noise reduction potential of the elastic TE without damping is compromised. It is argued that this can be attributed to the less direct response of the elastic structure when damping is employed. However, this minor unfavourable effect is outweighed by the elimination of the excess noise at the structural frequencies which leads to an overall noise reduction of up to 2.4dB.

Chapter 7

Trailing-Edge Noise from a Fully Turbulent Flow Over an Elastic Trailing-Edge

After the studies considering noise radiation from two dimensional flows over elastic TE extensions of an airfoil and flat plate TE's a fully turbulent three dimensional flow over an elastic flat plate TE is investigated in this chapter. The computational setup is introduced in section 7.1 and is followed by an initial overview and validation in section 7.2. Finally, the rigid and elastic TE's are compared to each other in section 7.3.

7.1 Computational Setup

The setup for the three dimensional simulations is based on the grid and parameters from the previous two dimensional study introduced in section 6.1. As before the freestream Mach number was $M = 0.4$. The global Reynolds number was $Re = 7.5 \times 10^4$ based on unit freestream velocity and unit length scale. The displacement thickness of the boundary layer is $\delta^*_{TE} = 2.360 \times 10^{-2}$ at the TE. This results in a Reynolds number based on displacement thickness at the trailing-edge of $Re_{\delta^*} = 1770.26$. Furthermore, the Reynolds number based on the cylinder centreline velocity $2D_{cyl}$ upstream of the cylinder is $Re_{cyl} = 682$. However, as discussed before, the cylinder can not be considered as a canonical cylinder flow due to the vicinity to the wall. The reader is reminded that all spatial dimensions are scaled with the cylinder diameter D_{cyl}.

With the grid from section 6.1, it was found that significant reflections were originating from the outflow boundary when the turbulent wake was convected out of the domain.

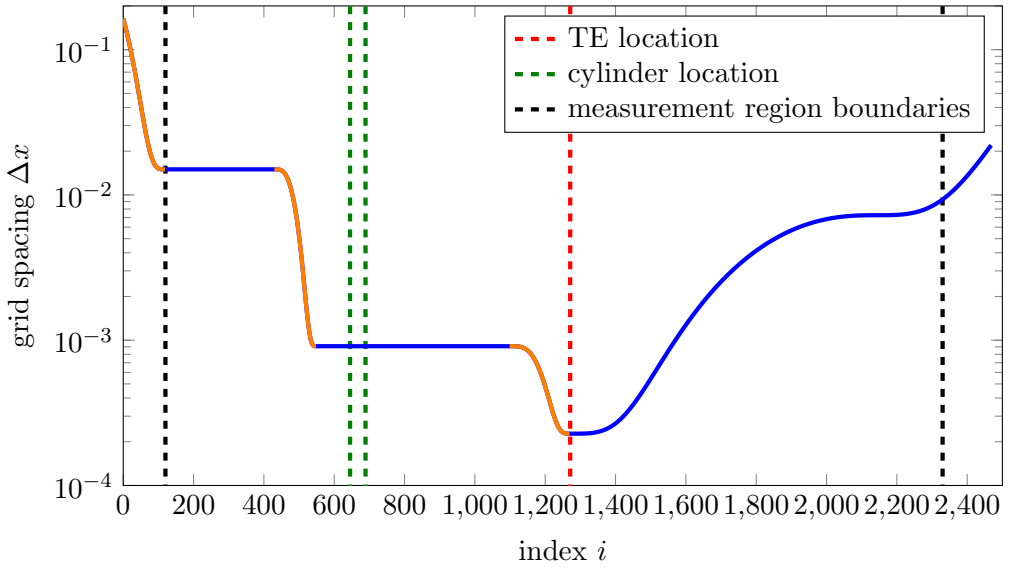

(a) grid spacing in x-direction for intermediate resolution level

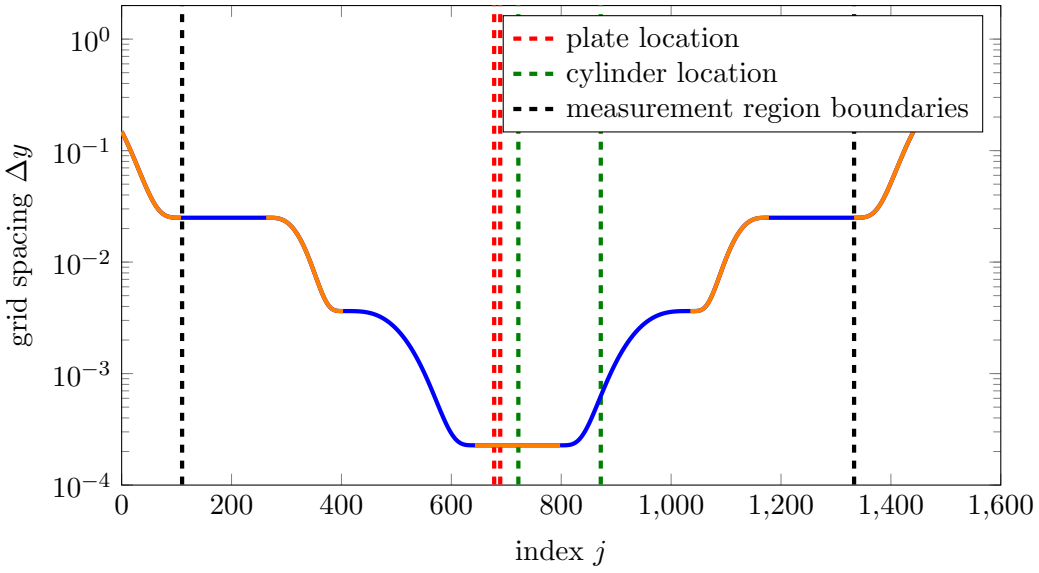

(b) grid spacing in y-direction for intermediate resolution level

Figure 7.1: Distribution of grid spacing $\Delta h_{i+1} - \Delta h_i$ where the individual segments are coloured in orange and blue.

In order to diminish the reflections the number of points for the zonal ramp was increased to $N_{\text{zone}} = 200$ and the physical dimensions increased from $L_{\text{zone}} = 20.85 D_{cyl}$ to $L_{\text{zone}} = 62.14 D_{cyl}$. Furthermore, the grid region with the higher near-field resolution was increased in the wall normal direction which resulted in a total grid size of $2470 \times 1443 \approx 3.564 \times 10^6$ in the two dimensional plane.

The spanwise domain width was set to $L_z = 3.6 D_{cyl}$ and discretized with to 48 Fourier modes, which results in 98 physical collocation points. With regard to the displacement thickness at the TE the domain width is $L_z = 6.1 \delta^*_{TE}$. Note, however, that on the

upper side of the plate the turbulent flow is governed by the vortex shedding of the cylinder and recirculation only. On the lower side of the plate a laminar boundary layer is expected to develop as there is no tripping or disturbances from the inflow. The total grid size including the spanwise direction is 3.4929×10^8 grid points. Periodic boundary conditions were used for the spanwise direction as the DNS code employs a spectral method to discretize this direction. Thus, the flat plate is modelled as infinitely long in the spanwise direction. The periodicity is also used to improve convergence of the gathered statistics by averaging over the spanwise direction in addition to the temporal average. The wake of the cylinder is expected to become turbulent. Based on the parameter ranges for the wake instabilities that can lead to transition introduced by Zhang *et al.* (1995), B mode instabilities should occur in the cylinder wake. Their wave-length is $\lambda_z \approx 1D_{cyl}$ and therefore is accommodated multiple times in the domain with the chosen width.

	E_s	ρ_s	f_1/f_b	f_2/f_b	μ_m
set 1	9.94×10^6	600	0.36	2.26	0.24

Table 7.1: Table describing the structural parameters for the elastic TE which are given with the Youngs modulus E and the structural density ρ_s which are both non-dimensionalized with freestream quantities or combinations thereof. The length of the elastic fraction was $L = 8.816D_{cyl}$ and the thickness of the plate $h_{TE} = 1/16D_{cyl}$. Furthermore the first two natural frequencies f_1 and f_2 of the structure in vacuo are listed. The added mass coefficient is given with μ_m.

As material properties of the elastic fraction the most efficient parameter set, that resulted in the highest noise reduction, from the two dimensional study of chapter 6, which is parameter set 1, was used. The parameters are listed in table 7.1 again for reference. The values of the first two natural frequencies differ to the values listed in table 6.2 due to a slight change in the recirculation frequency f_b of the separation bubble. Structural damping was not employed as the influence and the benefits were unknown at the time the simulations were carried out. It is assumed that spanwise extent of the structure is significantly larger than the streamwise length such that variations in the spanwise direction are small and the structure can be modelled with the two dimensional governing equation introduced in 2.2.1. The pressure loading of the structure Δp was calculated from the spanwise averaged pressure.

7.2 Results – Overview and Validation

Figure 7.2 shows an instantaneous snapshot of the Q-criterion from the DNS of a turbulent flow convecting over an elastic TE. In the background, the acoustic field is visualized with dilatation contours clearly originating from the TE. Furthermore, the deflection of

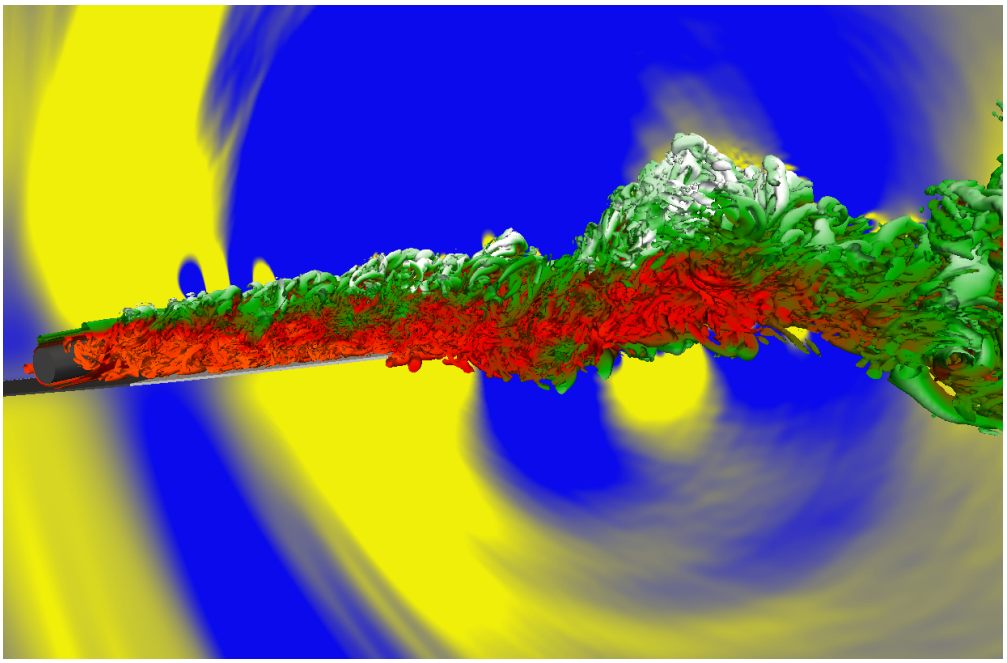

Figure 7.2: Instantaneous snapshot from the DNS with an elastic TE visualizing the turbulent flow with the Q-criterion for a threshold of $Q = 50$ coloured with the streamwise velocity component. In addition the acoustic field in the background is showing dilatation contours for $-0.001 < \nabla \cdot \vec{u} < 0.001$.

the elastic fraction of the TE in light grey can be seen when the figure is viewed carefully. The figure shows that the flow is becoming turbulent downstream of the cylinder with a wide range of sizes of the turbulent structures present. Upstream of the cylinder and on the lower side of the plate the flow appears to be laminar which has the advantage that on this side of the plate only the TE noise mechanism contributes to the overall noise and can be studied in isolation. Furthermore, the analysis of the surface pressure fluctuations can be decomposed into incident and scattered fluctuations as introduced in section 2.1.4.

The wake of the cylinder is visualized at an arbitrary instant of time in figure 7.3a with a view from the top. The turbulent structures are visualized with isosurfaces of the Q criterion and are coloured with the streamwise velocity component. Furthermore the location of the cylinder and the start of the elastic fraction of the TE are indicated with a vertical dashed line. The spanwise coherent vortices shed from the cylinder can be clearly identified up to approximately $2D_{cyl}$ downstream of the cylinder. Closer to the wall three dimensional structures already appear to exist further upstream. At the streamwise position of the start of the elastic TE the vortical structures that result from breakdown of the spanwise coherent structures can be identified. As estimated in section 7.1 the domain width is able to accommodate approximately 4 to 5 of these structures. Downstream of this location long streamwise elongated braid structures of similar diameter are visible and are followed by a broad range of vortex sizes indicating

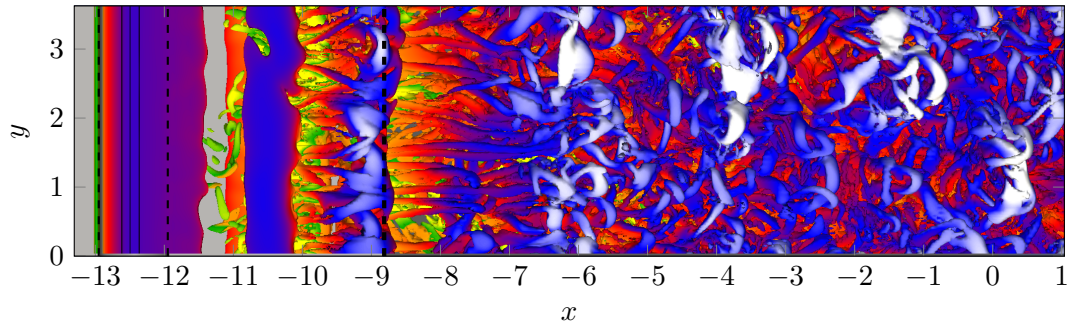

(a) Top view of the cylinder and its wake where the location of the cylinder and the start of the elastic fraction of the TE are indicated with dashed black lines.

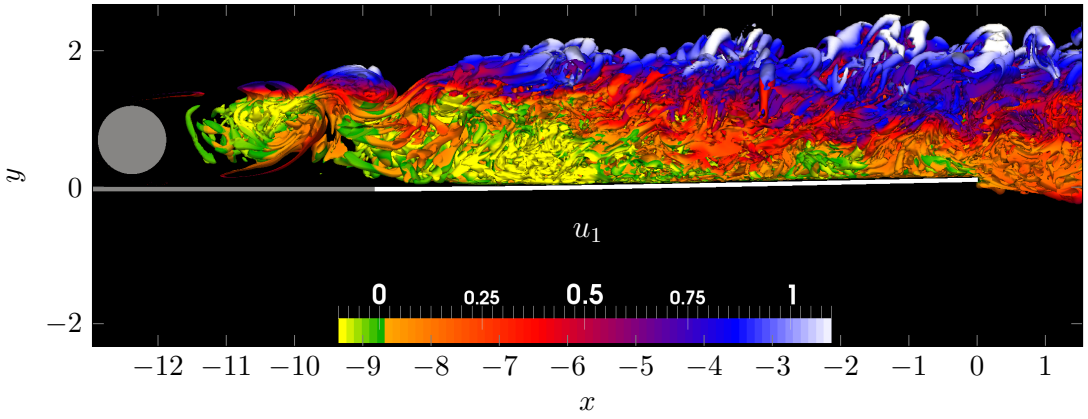

(b) side view of the cylinder and its wake with a slight deflection of the elastic fraction

Figure 7.3: Turbulent structures in the wake of the cylinder visualized with an isosurface of the Q-criterion of $Q = 100$ and coloured with the streamwise velocity component for $-0.1 < u < 1$. The colour legend in b) is also valid for figure a).

a further breakdown of the initial turbulent structures. The colouring of the isosurfaces indicates that there are recirculating flow regions closer to the wall. Overall, the visual observations of the instantaneous flow field in figure 7.3 are consistent with the estimation in section 6.1 that the boundary layer of the cylinder remains laminar and the transition to turbulence occurs in the wake of the cylinder.

A side view of the vicinity of the cylinder and the TE is presented in figure 7.3b at the same instance of time. It can be appreciated that there is a recirculating flow region $1D_{cyl}$ downstream of the cylinder where three dimensional structures are present which confirms the findings from the top view that three dimensional structures appear to develop later in the top shear layer than closer to the wall. The streamwise elongated braid structures that were identified in the top view can be observed from this view as well at the start of the elastic fraction of the TE. Furthermore, the colouring indicates a region of reversing flow in the first half of the plate. Compared to the size of the recirculation region in the two dimensional case discussed in section 6.2 the length appears to be shorter in the three dimensional case.

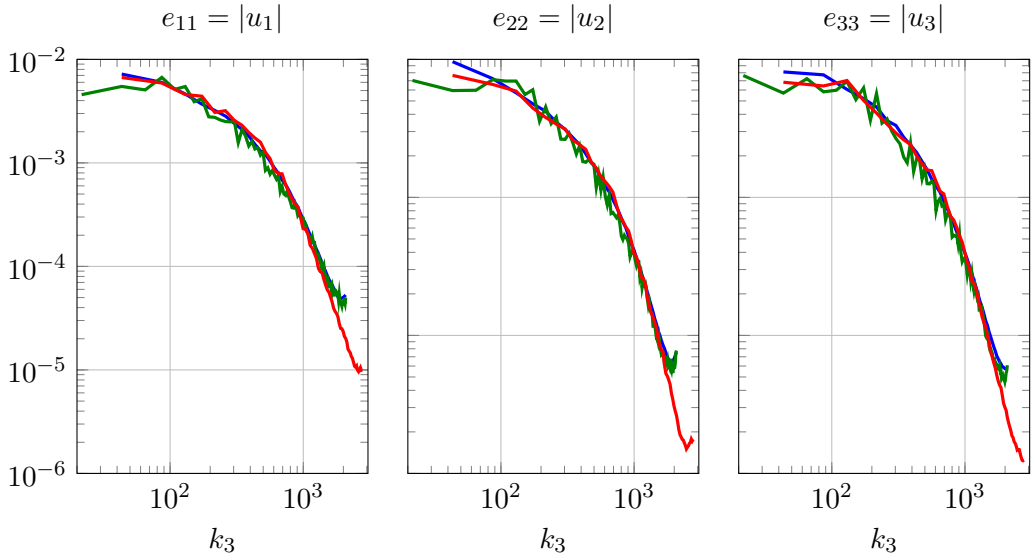

(a) Spanwise spectra at $0.364h_{\mathrm{TE}}$ downstream of the TE.

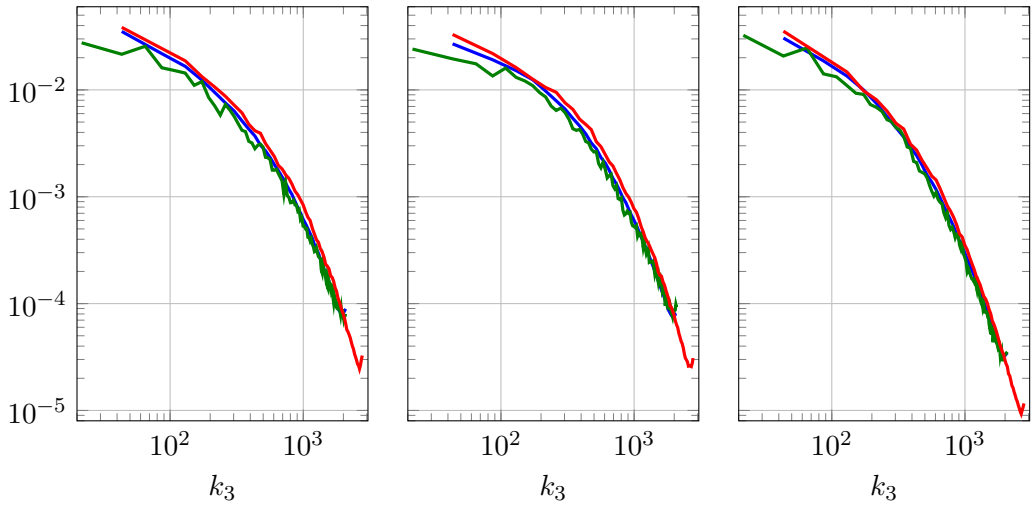

(b) Spanwise spectra at $12.54D_{\mathrm{cyl}}$ downstream of the TE.

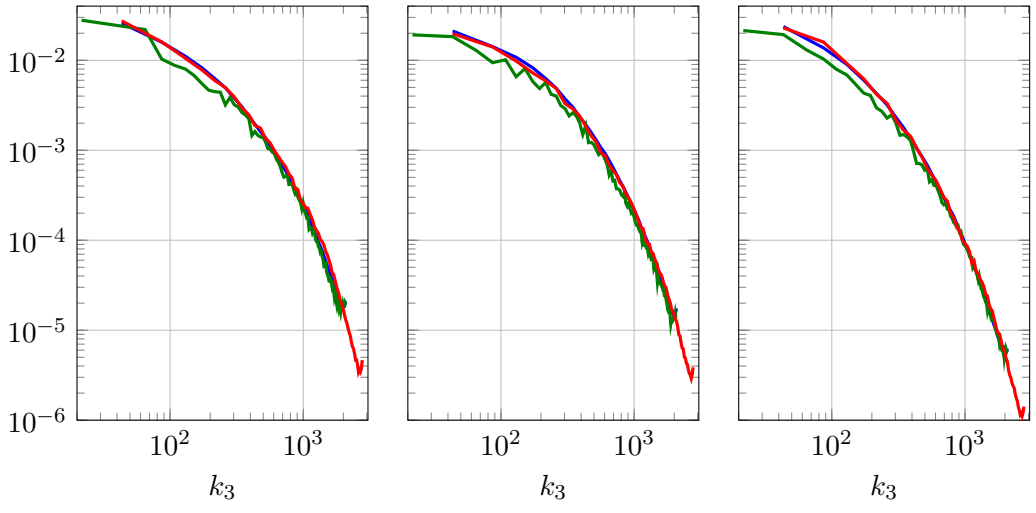

(c) Spanwise spectra at $24.97D_{\mathrm{cyl}}$ downstream of the TE.

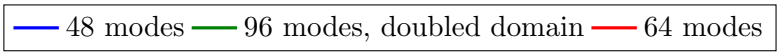

Figure 7.4: Spanwise spectra of the three velocity components at various locations downstream of the TE.

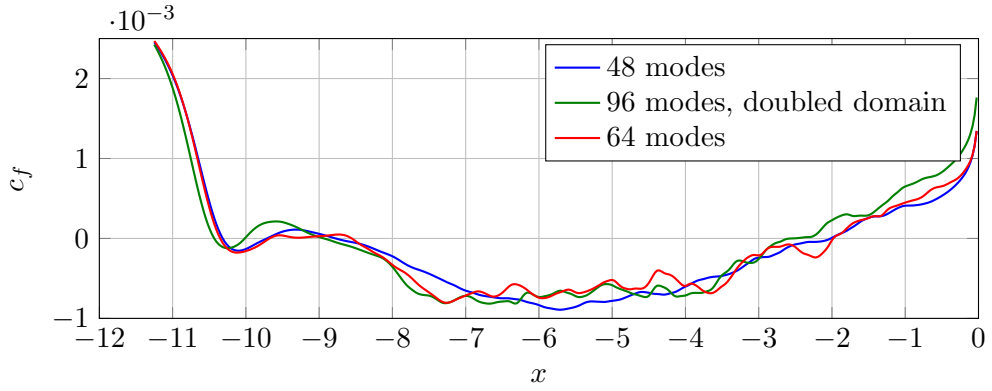

Figure 7.5: Time-averaged skin-friction c_f in the vicinity of the cylinder and TE on upper surface comparing the three different spanwise resolution and domain width.

For a statistical validation figure 7.4 shows the time-averaged spanwise spectra of the three velocity components at three different streamwise locations downstream of the TE. The first row is $0.364h_{\mathrm{TE}}$, the second $12.54D_{\mathrm{cyl}}$ and third $24.97D_{\mathrm{cyl}}$ downstream of the TE. In order to confirm that the spanwise resolution is sufficient an additional simulation was carried out where the resolution was increased to 64 Fourier modes and the results are plotted in the same figures. Furthermore, the results from a simulation with a doubled domain width of $7.2D_{cyl}$ using 96 Fourier modes are shown which yields the same spanwise resolution as the baseline case introduced in section 7.1. It is apparent that spanwise wave numbers with amplitudes ranging 2 to 3 orders of magnitude are present in the spectra of the baseline case. In comparison with the case using 64 Fourier modes minor variations in particular for the very low wave numbers can be found close to the TE. Further downstream the agreement is significantly better and at the location furthest downstream the spectra are barely distinguishable. The differences at low wavenumber are likely to be introduced by the relatively short time history available for averaging this higher resolution case. In the high wave number range differences can only be observed for the very last modes of the lower resolution case at the TE location and they vanish further downstream. This comparison indicates that the spanwise resolution is sufficient to represent the flow around the TE accurately. The case with the doubled domain width shows qualitatively good agreement with the other two cases at all locations. Quantitatively small differences can be found in the low wave number range in particular at the TE. It should be mentioned that due to the high computational cost and long initial transient this case could not be fully converged which is likely to cause some of these deviations.

The three cases presented in figure 7.4 are used to evaluate the sensitivity of the skin-friction c_f on the spanwise resolution and domain width in figure 7.5. The overall qualitative and quantitative agreement of the case with the higher resolution, i.e. 68 modes, with the base line case employing 48 modes is good. In particular, the location and size of the recirculation bubble show good correlation. However, the wiggles

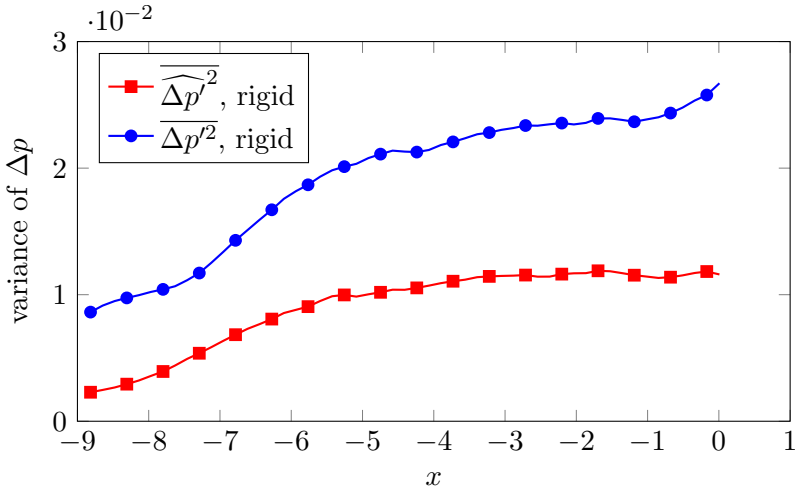

Figure 7.6: Variance of the pressure difference between upper and lower side of the plate in time and in the spanwise direction as a function of the streamwise position.

in the higher resolution case indicate that the statistics of the higher resolution case are not entirely converged. This is also the case for the data from the simulation with the doubled domain width. Additionally, the recirculation bubble seems to be shifted upstream with a higher skin-friction towards the TE and downstream of the cylinder. However, since the data is not entirely converged, a fair comparison is difficult. Overall the spanwise resolution appears to be sufficient, for the spanwise domain width there is a certain level of uncertainty. Nevertheless, with the given computational resources it was deemed more important to simulate a significant length of time to converge the spectra of the acoustic far-field in time.

In this study the structural motion was modelled with the one dimensional Euler-Bernoulli beam equation. Thus, it was assumed that the pressure loading Δp of the structure had little variation in the spanwise direction compared to the variation in time. To validate this assumption, figure 7.6 compares the variance of Δp in time with the variance in the spanwise direction. To calculate these quantities the overbar $\overline{\Phi}$ denotes a time average and the prime Φ' a fluctuation of the quantity Φ. Hence, Φ at a given instance of time can be decomposed as

$$\Phi = \overline{\Phi} + \Phi' \,. \tag{7.1}$$

Furthermore, the spatial average in the spanwise direction is introduced and indicated by the brackets $\langle\Phi\rangle$. A deviation from the spanwise average is $\hat{\Phi}$. Analogous to the temporal average this results in

$$\Phi = \langle\Phi\rangle + \widehat{\Phi} \,, \tag{7.2}$$

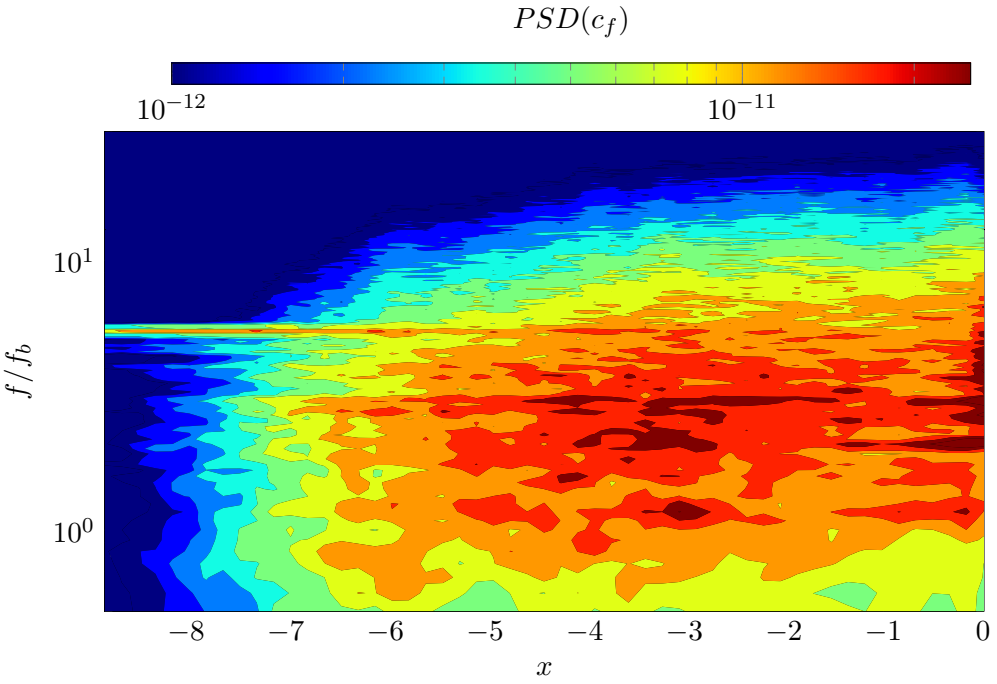

Figure 7.7: Contours visualizing the power spectral density of the skin-friction c_f as a function of the streamwise location on the upper side of the plate and the frequency.

for the quantity Φ at a certain spanwise location. Employing the introduced temporal average, the temporal variance of the pressure difference $\overline{\Delta p'^2}$ can be calculated with

$$\overline{\Delta p'^2} = \langle \overline{\Delta p \Delta p} - \overline{\Delta p}\ \overline{\Delta p} \rangle \,. \tag{7.3}$$

In this case the averaging over the spanwise direction is employed to improve convergence, exploiting the periodicity in the spanwise direction. The variance in the spanwise direction $\overline{\widehat{\Delta p'}^2}$ can be calculated with

$$\overline{\widehat{\Delta p'}^2} = \overline{\langle \Delta p \Delta p \rangle} - \overline{\langle \Delta p \rangle \langle \Delta p \rangle} \,. \tag{7.4}$$

It is apparent that the fluctuations in time are a factor of 2 to 3.5 larger than in the spanwise direction. For this parameter set the standard deviation of the deflection was $0.4 h_{TE}$ at the free end, approximately. Hence, the variation of the structural deflection in the spanwise direction is likely to be comparatively small and hence the assumption of a one dimensional governing equation for the structural motion appears reasonable.

In order to determine where the transition from laminar to turbulent on the surface of the plate takes place, figure 7.7 shows the power spectral density of the skin-friction c_f along the fraction of the plate that will be elastic in a later case on the upper side of the plate. The contours visualize the power spectral density and show that for the spectrum

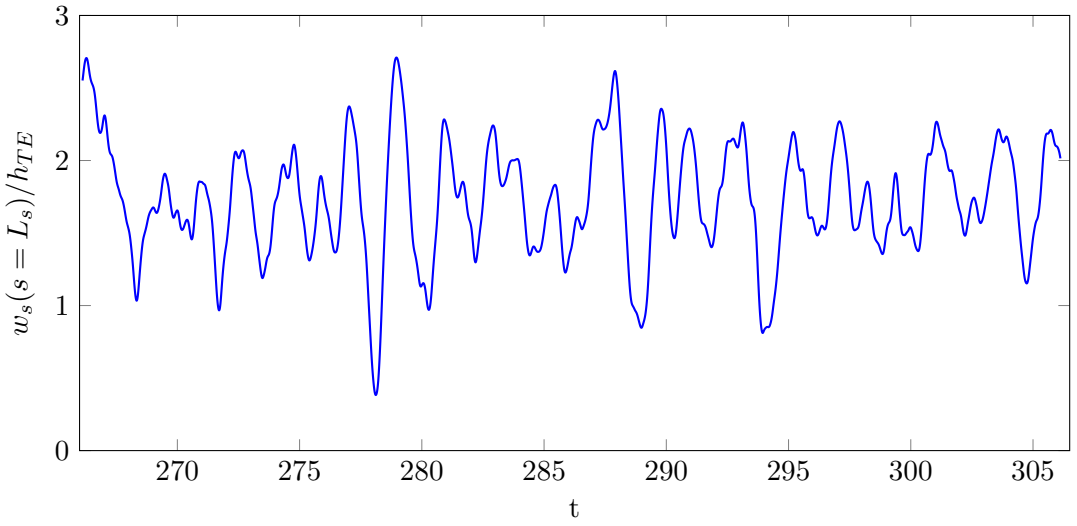

Figure 7.8: Time history of the deflection w_s of the free $s = L_s$ end of the elastic TE normalized by the TE thickness h_{TE}.

is dominated by one peak at a frequency of $f/f_b \approx 7.9$ represented by a thin line for $x < -7D_{cyl}$. The fluctuations increase significantly in amplitude over a wide range of frequencies along the streamwise direction. The widening of the spectrum and increase in amplitudes downstream of $x = -7D_{cyl}$ indicates the transition to turbulence and that the flow is turbulent when it reaches the TE. This confirms the observations from the visualization of the instantaneous flow field in figure 7.2 and 7.3 where a wide range of turbulent structures with different sizes could be seen.

7.3 Results – Comparison of the Rigid and Elastic Trailing-Edge

This section discusses the results from the simulation of the turbulent flow over an elastic TE in comparison to a rigid case. The structural motion of the elastic TE is assessed in section 7.3.1 first. It is followed by a comparison of the rigid and elastic TE in the acoustic far-field in 7.3.2 and the hydrodynamic near-field in 7.3.3

7.3.1 The Structural Behaviour

Figure 7.8 presents the structural motion in data sampling window of the DNS. It can be seen that the dominant period of approximately one time unit is super imposed with higher frequencies. Furthermore, the averaged deflection is positive and the plate is always bent above the position without loading.

The time averaged deflection of the plate is presented in figure 7.9a and shows the same qualitative behaviour of a positive mean deflection with bending mode shape one as the

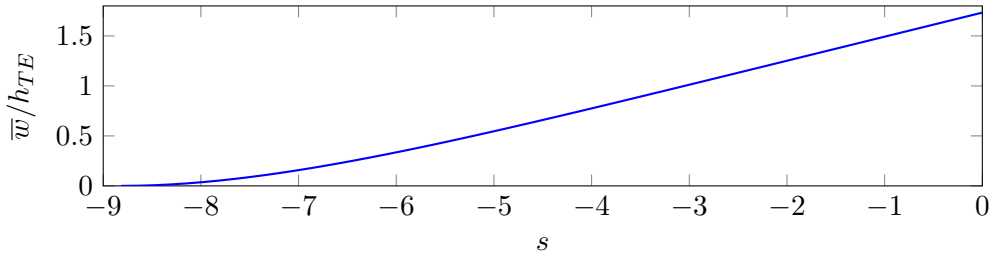

(a) Mean deflection $\overline{w}$ as function of the streamwise location.

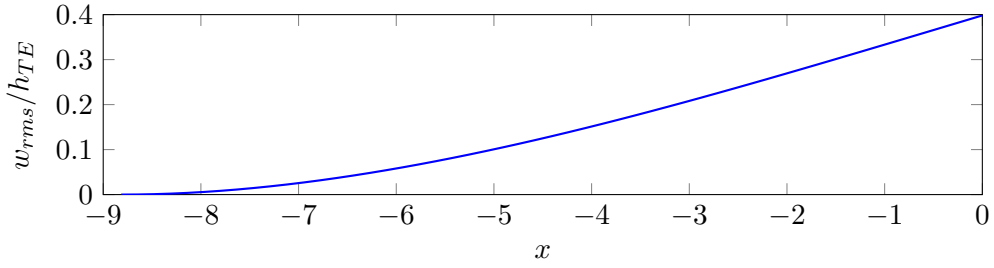

(b) Standard deviation of the deflection w_{rms} as function of the streamwise location.

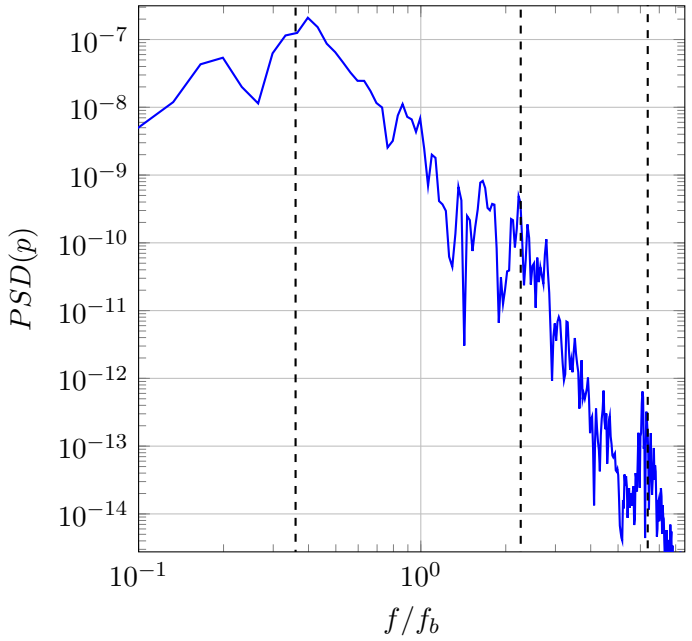

(c) Power spectral density of the deflection time history w of the TE point. The respective natural frequencies are indicated with vertical dashed lines.

Figure 7.9: Statistics of the deflection time history of the elastic plate.

elastic plate with the same parameters subject to loading from the two dimensional flow shown in figure 6.16a. Quantitatively, the mean deflections are reduced by a factor of 1.8 relative to the two dimensional cases. The same is true for the standard deviation plotted in figure 7.9b which is reduced by a factor of 7.8. The reduction of the mean deflection and the fluctuations around it can be explained with the less coherent vortex shedding and the breakdown of the quasi two dimensional into turbulent structures.

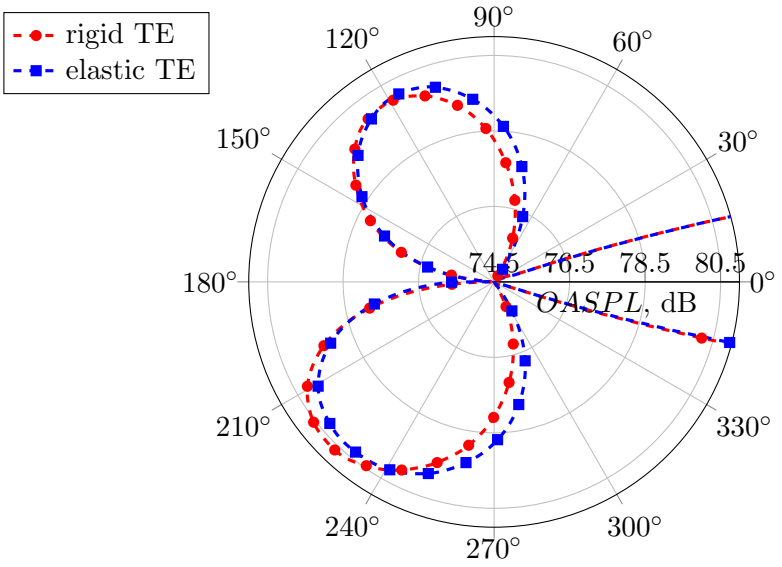

Figure 7.10: Overall sound pressure level at a radial distance of $r = 6D_{cyl}$ comparing the rigid and elastic TE cases.

Consequently, the pressure loading is reduced which then leads to smaller deflections.

The power spectral density of the structure's end point motion is presented in figure 7.9c. Due to the short time history available for averaging only two Hanning windows with a length of 22.4 periods of the recirculation and an overlap of 50%. Despite the fact that spectrum is not entirely converged qualitative estimations of the structural motion are possible. It can be found that the peak associated with the first natural frequency of the structure contains the most energy in the spectrum. It is followed by a peak at the sub-harmonic of this frequency. However, this is likely to be an artefact of the short averaging. The peaks at the recirculation frequency as well the higher natural frequencies of the structure contain less and less energy. In addition to recirculation and natural frequencies the spectrum also features a peak at $f = 1.8f_b$. In general the qualitative behaviour is the same as in the two dimensional case presented in figure 6.17.

7.3.2 Investigation of the Acoustic Far-Field

Figure 7.10 presents the overall sound pressure level (SPL) at a radial distance of $r = 150D_{cyl}$ from the TE comparing the rigid and the elastic TE cases. Note that on the upper surface, i.e. $0° < \theta < 180°$, the scattered noise is influenced by the presence of the cylinder and the recirculation whereas the noise observed below the plate should only originate from the TE or the wake. Therefore the following discussion will focus on observations on the lower side of the plate. The data shows that the elastic TE amplifies the noise in the direction perpendicular to the TE. The increase of the noise level is approximately 1 dB in that direction. In contrast to that the elastic TE shows

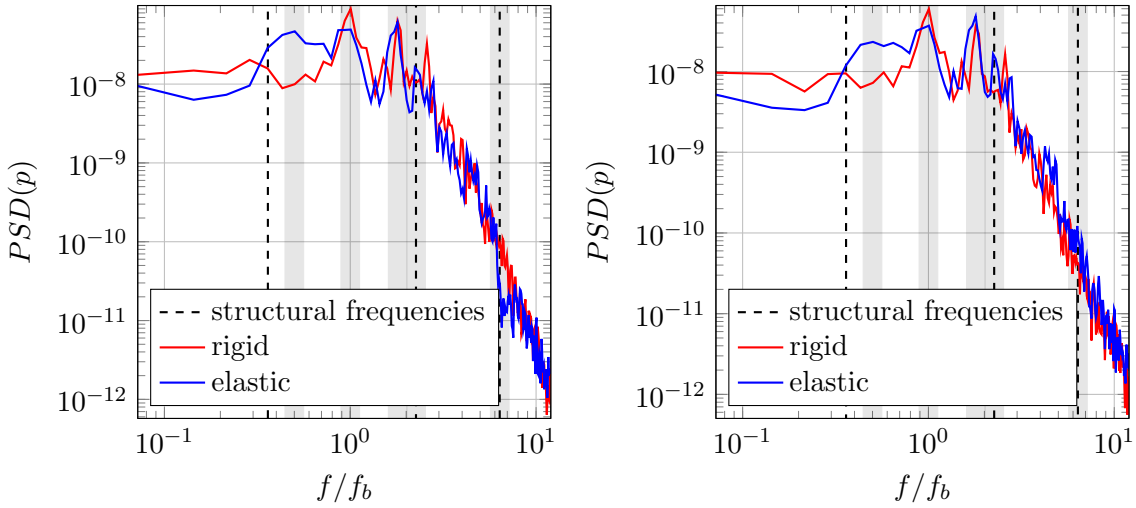

(a) radial distance from TE, $R = 150D_{cyl}$ at $\theta = 225°$ (b) radial distance from TE, $R = 150D_{cyl}$ at $\theta = 270°$

Figure 7.11: Power spectral density of pressure fluctuations in the acoustic far-field. The circumferential positions refer to the angles used in figure 7.10.

f_c	position 1			position 2		
f_b	−3.5dB	15.0%	21.9%	−2.7dB	14.9%	24.1%
$1.8f_b$	0.9dB	22.2%	19.7%	3.4dB	25.4%	20.5%
$0.5f_b \approx f_{1,s}$	13.4dB	5.4%	1.1%	10.1dB	3.7%	1.4%
$2.26f_b = f_{2,s}$	−1.7dB	7.7%	9.2%	3.3dB	9.9%	8.0%
$6.38f_b = f_{3,s}$	−4.9dB	0.1%	0.2%	3.1dB	0.2%	0.2%

Table 7.2: Energy distribution of the power spectral density for the elastic TE in comparison with the rigid case below the plate for the two locations considered in the spectra in figure 7.11. Position one refers to $R = 150D_{cyl}$ at $\theta = 225°$ and position two to $R = 150D_{cyl}$ at $\theta = 270°$. The power is calculated in third octave bands around center frequencies f_c. The difference to the rigid TE is given in dB where a positive sign indicates a noise increase and a negative sign a noise reduction. The second and third number in each column at each location under consideration indicate the contribution of frequency range to the total energy in % for the elastic and rigid TE, respectively.

a slight noise reduction of approximately 0.4 dB at an angle of $\theta = 45°$ in the upstream direction on the lower side of the plate.

A spectral analysis of the pressure time history can give further insight into the physical mechanisms that are responsible for the differences observed in the noise amplitudes and directivity shape. Figure 7.11 shows the power spectral density of pressure on the lower side of the plate at a radial distance of $r = 150D_{cyl}$ and an angle of $\theta = 225°$ (7.11a) and $\theta = 270°$ (7.11b). Both values for θ are consistent with the azimuthal directions in figure 7.10. The shaded areas visualize third octave bands in which the noise reduction and increase of the elastic TE relative to the rigid case is tabulated in table 7.2. The

spectra were calculated using Welch's method with 6 Hanning windows and an overlap of 53%. The frequencies in the spectra are normalized by the recirculation frequency f_b which can be clearly identified as the most dominant noise source in the rigid case at both locations. It can be noted that in this frequency range the elastic TE leads to a noise reduction of 3.5dB and 2.7dB in the upstream and wall normal direction, respectively. The first harmonic of this frequency can not be identified as a prominent peak at $2f_b$. Instead a peak of similar amplitude as the recirculation frequency can be found at $f = 1.8f_b$. A comparison of the elastic and rigid TE at this frequency shows a noise increase of 0.9dB and 3.4dB of the elastic case in the upstream and wall normal direction, respectively. Both the higher noise reduction and the lower increase in the upstream direction compared to the wall normal direction are consistent with the data from the directivity pattern presented in figure 7.10 where a noise increase was found for the elastic TE in the wall normal direction.

At a similar amplitude level significant excess noise of up to 13.4dB can be found for the elastic TE in the low frequency range close to the first structural frequency. As the octave band does not cover the whole frequency range featuring a higher noise level in the elastic case the actual excess noise is higher and the contribution to the overall energy in the spectrum is also underestimated in table 7.2. At a lower energy level the elastic TE leads to an increased noise level in the wall normal direction and noise reductions in the upstream direction for the higher modes of the structural frequencies.

The power spectral densities show that the distinct features in the spectra of the elastic TE vary in space and therefore show different behaviour depending on the azimuthal location. In order to investigate this variation in more detail and at all circumferential locations the power spectral density was calculated in the frequency domain from the time history of a sub-volume using the same parameters as mentioned above and averaged over the spanwise direction. Figure 7.12a shows the noise directivity at the recirculation frequency and confirms that the elastic TE reduces the noise in every direction. As a reference, the amplitudes obtained from the rigid TE were rescaled to match the level of the elastic TE. The comparison shows that the shape of the directivity pattern is not changed by the elastic TE but the amplitudes are reduced.

At the second dominant peak in the spectrum at $f/f_b = 1.8$, which is shown in figure 7.12b, the elastic TE is noisier in all directions. However, on the lower side the noise increase is less pronounced towards the upstream direction, which can also be observed when the rescaled directivity is considered. The higher excess noise in the wall normal direction is consistent with the observations made in the spectra at the two different locations presented in figure 7.11.

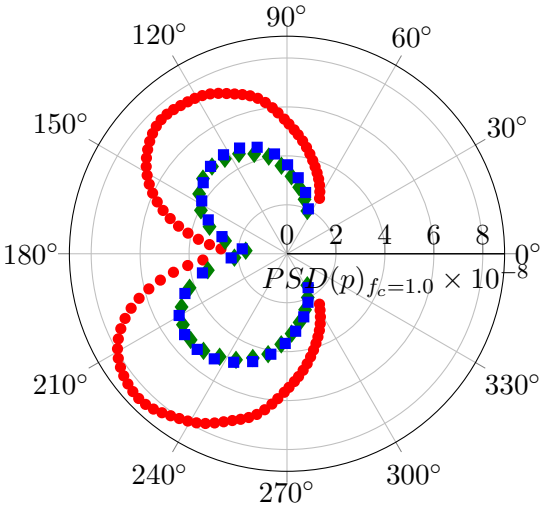

(a) recirculation frequency, $f/f_b = 1$

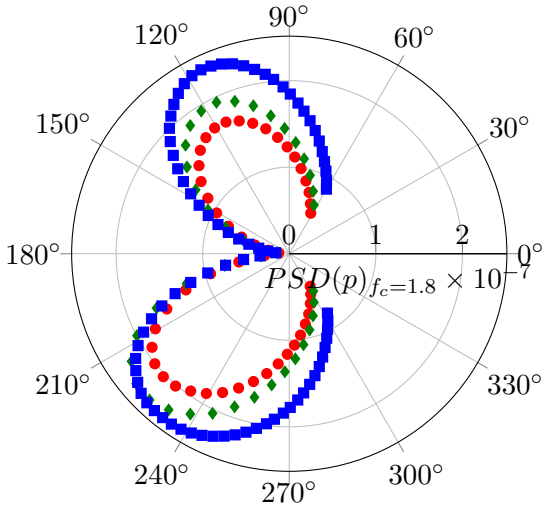

(b) first harmonic of recirculation frequency, $f/f_b = 1.8$

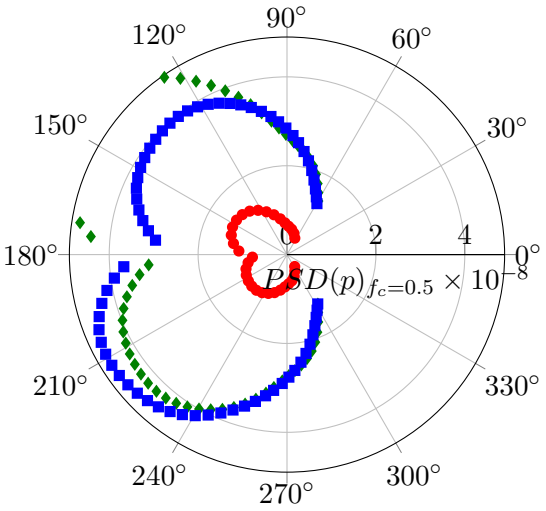

(c) low frequency excess noise close to first natural frequency $f/f_b = 0.5$

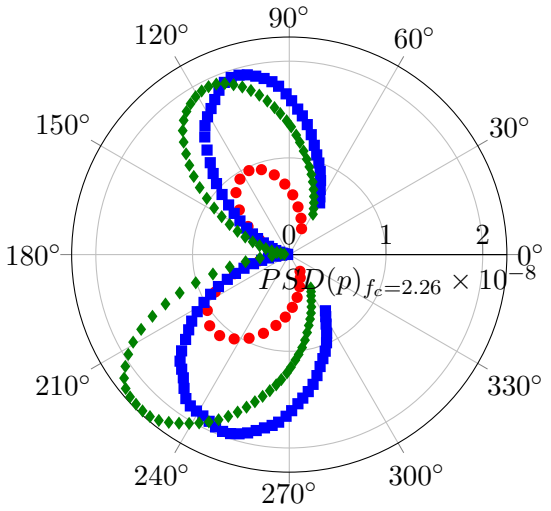

(d) second natural frequency of the structure, $f/f_b = 2.26$

Figure 7.12: Power Spectral Density of noise directivity at a radial distance of $r = 6D_{cyl}$ for different frequencies.

Figure 7.12c shows the noise directivity at the low frequency hump in the spectrum of the elastic TE which is close to the first structural frequency. Here, the noise level from the elastic TE is significantly higher than the rigid one in all directions with a maximum in the upstream direction. Furthermore, the upper side of the plate is noisier than the lower in the rigid case and the opposite is true in the elastic case. The comparison of the rescaled directivity of the rigid TE to the elastic TE shows that the noise is amplified more strongly in the upstream direction.

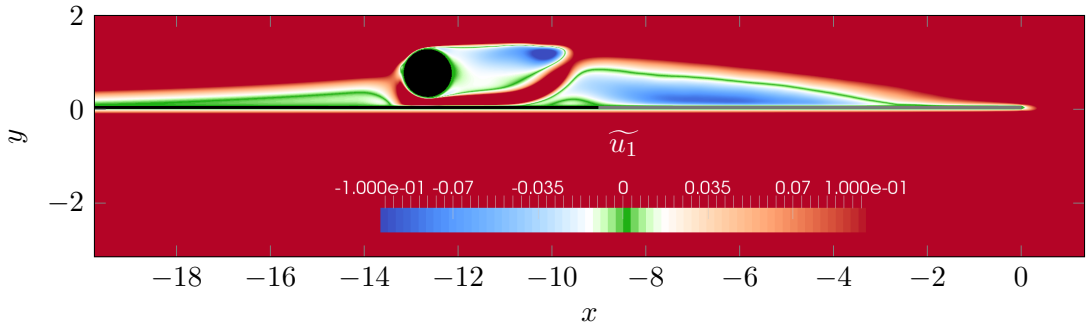

(a) rigid TE

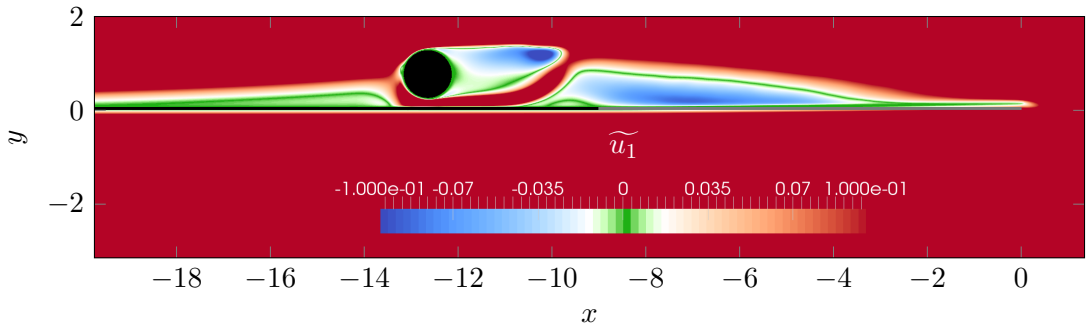

(b) elastic TE

Figure 7.13: Contours of the favre averaged streamwise velocity component $\widetilde{u_1}$ in the vicinity of the TE. The elastic fraction of the plate that is coloured in grey.

The directivity of the noise at the second structural frequency is compared in figure 7.12d. For this frequency the directivity shape seems to be changed when employing the elastic TE, which is in particular apparent from the rescaled directivity of the rigid case. The excess noise appears to radiate more strongly in the direction perpendicular to the plate which results in a noise increase. Towards the upstream direction the excess noise decreases subsequently and leads to a noise reduction in the wall parallel direction.

Overall, the change in directivity for the frequency range centred at $f_c = 1.8 f_b$ and at the second structural frequency $f = 2.2 f_b$ indicate that the excess noise is not caused by the TE noise mechanism. Assuming that the noise originating from the structural motion has a directivity that is more pronounced in the wall normal direction, it is likely that the excess noise is generated from the structural motion itself as the spectrum of the deflection in figure 7.9c also showed higher amplitudes at these frequencies.

7.3.3 Investigation of the Hydrodynamic Near-Field

For the two dimensional flat plate TE noise cases investigated in chapter 6 the recirculation bubble downstream of the cylinder was found to be the most energetic input to the TE noise mechanism and the structural motion. As it was previously found that

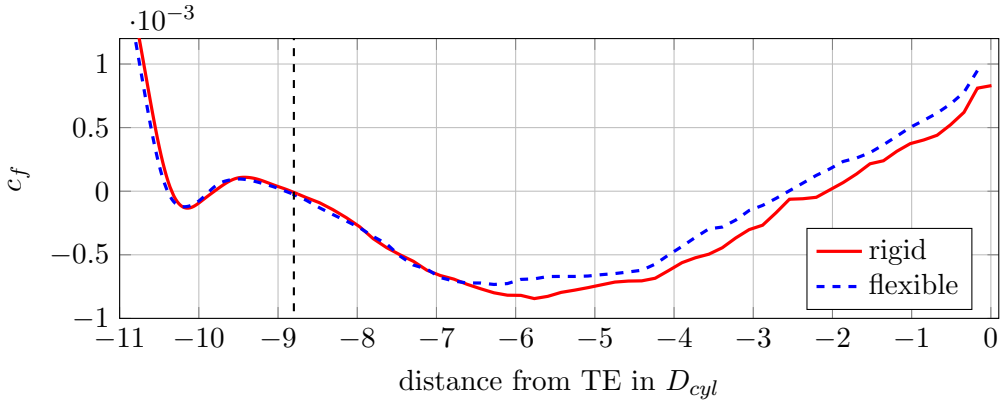

Figure 7.14: Time-averaged skin-friction c_f in the vicinity of the cylinder and TE on upper surface comparing the rigid and elastic TE. The vertical dashed line indicates the start of the elastic fraction.

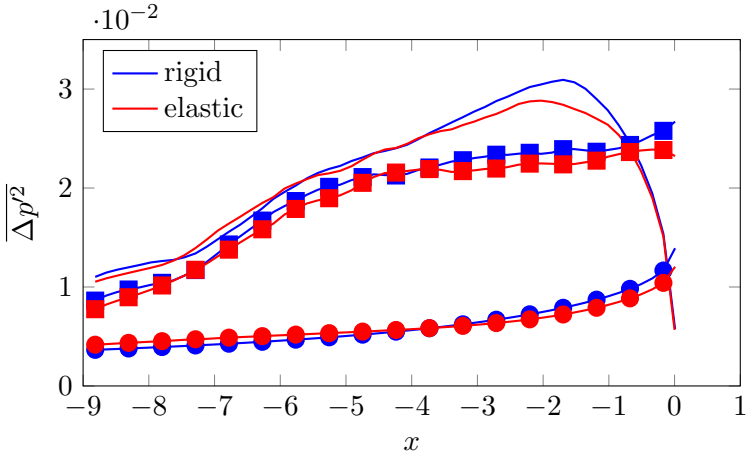

Figure 7.15: Fluctuations of the total (——), incident (—■—) and scattered (—●—) pressure differences between upper and lower surface.

the elastic TE changes the precise location and length of this recirculating flow region, figure 7.13 presents the streamwise velocity contours in the vicinity of the cylinder and the TE for the elastic and rigid plate. In general, the qualitative flow topology is very similar to the two dimensional case presented in figure 6.23. However, the length of the separation bubble on the plate appears to be shorter. These findings can be confirmed with the evolution of the skin-friction c_f in streamwise direction that are presented in figure 7.14. A negative value of skin-friction indicates a recirculation bubble in the time-average and can be found from $-8.9D_{cyl}$ to $-2.5D_{cyl}$ upstream of the TE, which is an overall upstream shift compared to the two dimensional case. The comparison of the rigid and elastic TE shows a small upstream shift of the end of the separation bubble. However, overall the differences are smaller than in the two dimensional case and the end of the separation bubble is further upstream. Therefore, it is expected that the input to the TE noise mechanism itself is comparable in both cases.

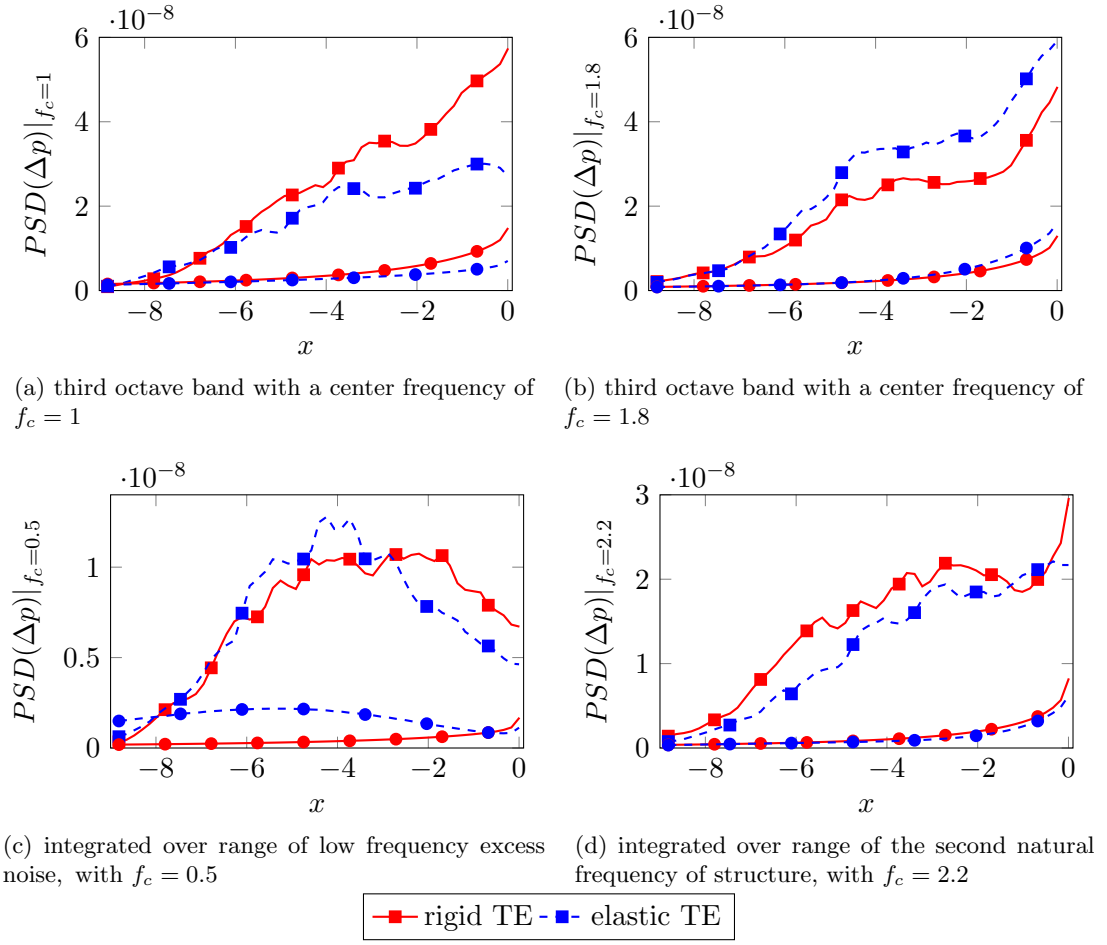

(a) third octave band with a center frequency of $f_c = 1$

(b) third octave band with a center frequency of $f_c = 1.8$

(c) integrated over range of low frequency excess noise, with $f_c = 0.5$

(d) integrated over range of the second natural frequency of structure, with $f_c = 2.2$

Figure 7.16: Fluctuations of the incident (—■—) and scattered (—●—) pressure differences between upper and lower surface.

Figure 7.15 shows a comparison of the total, the incident and the scattered pressure fluctuations for the rigid and elastic TE, calculated using the analysis leading to equation 2.14. The total pressure difference for both cases peak approximately $1.5D_{cyl}$ upstream of the TE at different values. However, downstream of that peak the differences are negligible. Considering the incident field the elastic TE leads to a decrease of the fluctuations from $-4D_{cyl}$ up to the TE. The scattered pressure field shows a similar overall behaviour in the vicinity of the TE. Upstream of $-3D_{cyl}$ the fluctuation level is higher than in the elastic case which is likely to be due to the structural motion.

The analysis of the incident field can be carried out in frequency space as well which allows a comparison for frequency bands of interest as identified in the power spectral densities presented in figure 7.11 and listed in table 7.2. The results can give valuable insight on whether noise amplification or damping can be related to the TE noise mechanism or to other noise sources. Furthermore, indications of the physical mechanism of the noise attenuation can be obtained. Considering the recirculation frequency presented

in figure 7.16a, differences between the rigid and elastic TE's are more significant than in the integral curves of figure 7.16. For the rigid TE the incident pressure fluctuations are increasing almost monotonically up until the TE location whereas they level off at $-4D_{cyl}$ for the elastic TE and thereby reduce the fluctuations at the TE. The scattered pressure fluctuations are also reduced. Both of these observations are consistent with the noise reduction that was found for this frequency range in the power spectral density of figure 7.11 and the spectral directivity shown in figures 7.12a. This indicates that the noise attenuation for the elastic TE can be attributed to the modification of the incident pressure field. For the frequency range of the second dominant peak at $f = 1.8f_b$ shown in figure 7.16b the incident and the scattered pressure fluctuations are more amplified when employing the elastic TE downstream of $-5D_{cyl}$. That means that the excess noise found in figure 7.11b and 7.12b can be related to the TE noise mechanism, which radiates more noise due to an amplification of the incident pressure field. Figure 7.16c considers the frequency range of the first additional hump in the spectrum of the elastic TE and it can be seen that the incident pressure fluctuations peak upstream of the TE in both cases. These fluctuations are reduced towards the end of the plate and the reduction is greater when employing the elastic TE. For the frequency range around the second structural frequency presented in figure 7.16d the incident pressure fluctuations are higher in the case of a rigid TE over the whole length of the measurement region. Both of the frequency ranges associated with the structural frequencies showed excess noise for an elastic TE when the power spectral density at a microphone position and the spectral directivity were considered. The analysis of the incident and scattered fields shows that this excess noise is not originating from the TE noise mechanism itself, as they cannot be related to an amplification of incident pressure fluctuations.

In summary, the elastic TE damps and amplifies the incident pressure fluctuations at the recirculation bubble frequency and its first harmonic, respectively. It is speculated that the elastic structure can react fast enough to pressure fluctuations allowing a conversion of the pressure force to kinetic energy of the structure, leading to a mitigation of the incident pressure fluctuations. However, the opposite process is possible as well which leads to an amplification of the incident pressure fluctuations. Concerning the extraneous noise found in the spectrum of the elastic TE, there is evidence that it does not originate from a noise source related to the TE noise mechanism itself.

The effect of the elastic TE on the statistics of the velocity field are presented in figure 7.17a at the streamwise position $x = 4h_{TE}$ just downstream of the TE. The most apparent difference between the rigid and elastic TE's is an upward shift in the wall normal direction. This is likely due to the mean deflection of the elastic TE which was approximately $1.73h_{TE}$. Considering $\widetilde{u_1}$, it can be found that the elastic TE also slightly reduces the wake deficit. It can be speculated that this is achieved by smearing out the

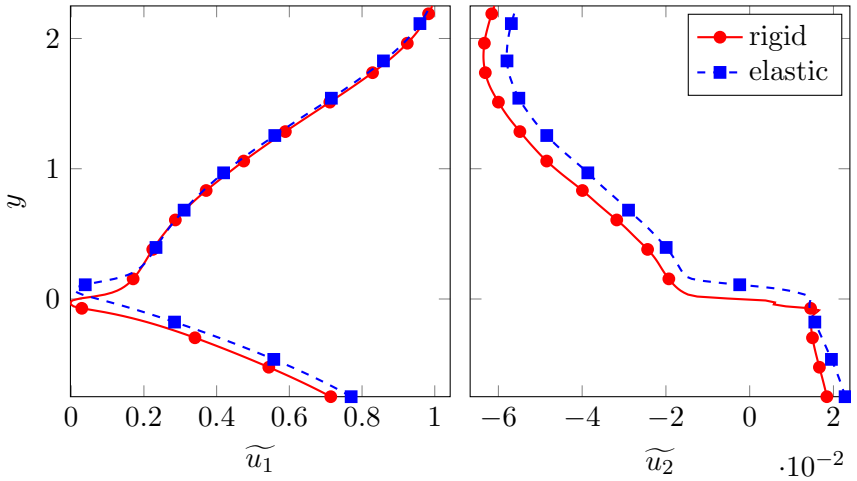

(a) Velocity profiles downstream of the TE.

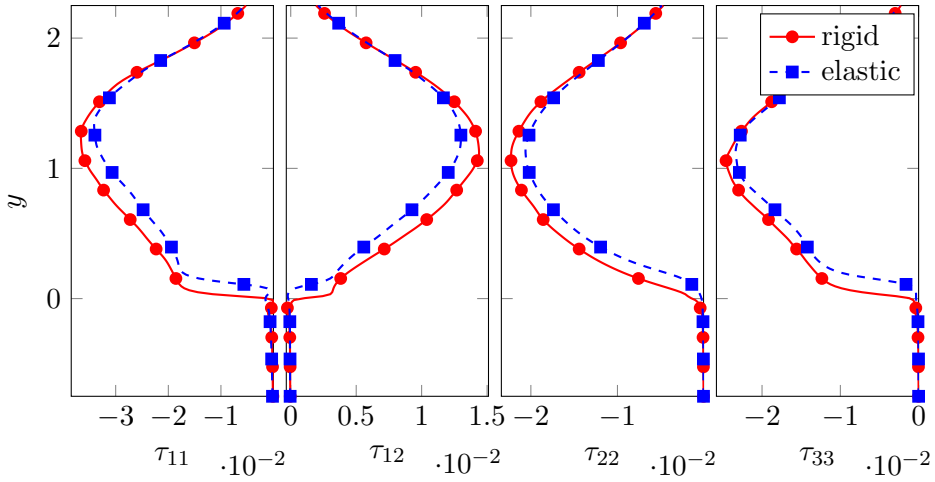

(b) Profiles of the Reynolds stress components downstream of the TE.

Figure 7.17: Velocity and Reynolds stress profiles $4h_{TE} = 0.25D_{cyl}$ downstream of the TE.

position of the TE through the movement of the boundary.
Figure 7.17b compares the Reynolds stress profiles obtained from the two simulations. It is apparent that the amplitudes of the Reynolds stresses are reduced in the free stream when employing the elastic TE. The TE noise reduction in that case can potentially be related to the reduction of the Reynolds stress amplitudes which results in reduced levels of turbulence. The lower turbulent fluctuations are likely to be related to the changes observed in the fluctuations of the incident pressure field in figure 7.16.

To assess the energy distribution in the spanwise direction when using the rigid and elastic TE's, figure 7.18 presents the spanwise energy spectra corresponding to the three velocity components downstream of the TE. In the near vicinity of the TE, at $x = 2.2 \times 10^{-2} D_{cyl}$, the spectral energy distribution shown in figure 7.18a differs significantly for the elastic and rigid TE. For all three velocity components the spectral

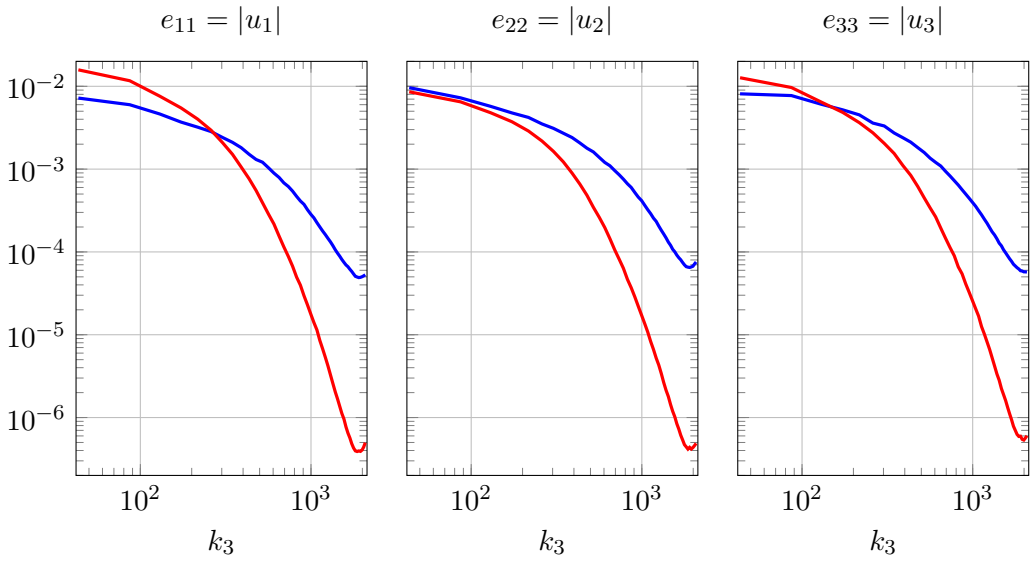

(a) Spanwise spectra at $2.2 \times 10^{-2} D_{cyl}$ downstream of the TE.

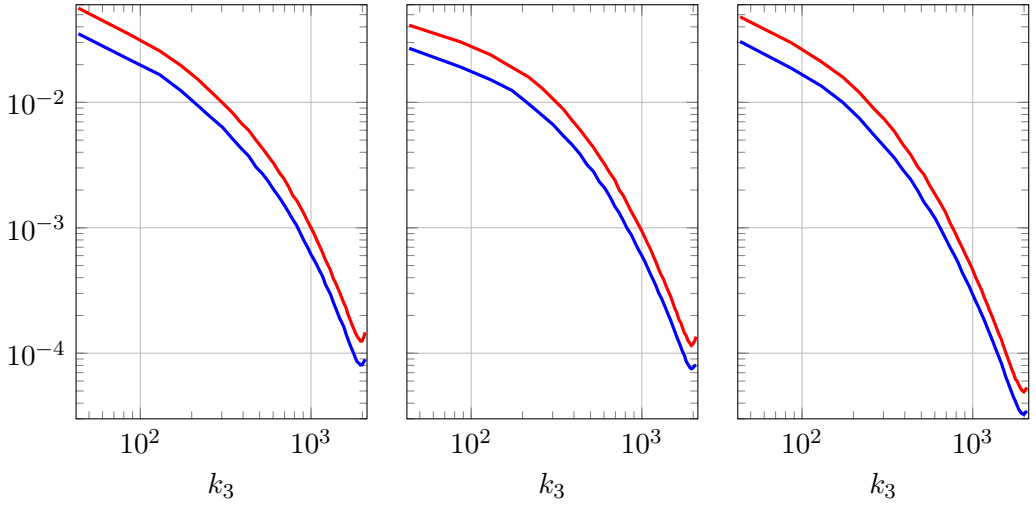

(b) Spanwise spectra at $12.54 D_{cyl}$ downstream of the TE.

rigid elastic

Figure 7.18: Spanwise spectra of the three velocity components at two locations downstream of the TE comparing the rigid and elastic TE.

energy of the highest wave numbers are two orders of magnitude lower in the elastic case. This indicates that the structural movement reduced the amount of structures with a small spanwise wave-length. For the low wave-number range, however, the streamwise and spanwise velocity components show a higher energy level. Consequently, spanwise coherent structures contain more energy than in the rigid TE case, which is likely to be caused by the spanwise coherent motion of the elastic TE.

Further downstream, at $x = 12.54 D_{\mathrm{cyl}}$, the spanwise spectra obtained from the flow over a rigid TE feature lower amplitudes for all velocity components in comparison to the

elastic TE case. It is suggested that the higher energy in the elastic case is due to the breakdown of the long wave-length structures at the TE. As discussed in the previous paragraph, it is speculated that the spanwise coherent motion of the elastic TE leads to higher amplitudes of low wave-number structures. These spanwise relatively coherent structures are then breaking down into smaller structures as they are convected downstream in the wake, leading to a broader distribution than at the TE and higher amplitudes than in the rigid case.

Finally, the influence of the TE motion on the turbulent structures in the flow is investigated. Jones & Sandberg (2012) used a metric based on the pressure gradient to analyse the influence of TE serrations on the turbulent structures in the wake of an airfoil at angle of attack. It is defined as

$$\Gamma = \frac{\overline{p_{xx}p_{xx}} - \overline{p_{zz}p_{zz}}}{\overline{p_{xx}p_{xx}} + \overline{p_{zz}p_{zz}}} \quad , \tag{7.5}$$

where p_{xx} and p_{zz} refer to the derivative of pressure in the streamwise and spanwise directions, respectively. When $\Gamma = 1$ the gradient in the streamwise direction is dominant and therefore the structures are oriented in the spanwise direction. The opposite is true for $\Gamma = -1$ where the dominant spanwise derivative of pressure indicates structures that are oriented in the streamwise direction. However, in this metric the time averaged pressure derivatives do not cancel out and it is therefore biased since strong mean gradients are expected to be present in the vicinity of the vortex generator and the TE. Instead of basing Γ on the pressure derivatives, Γ could also be computed based on gradients of the pressure fluctuations and thereby eliminate any influence of the mean. However, since the noise radiation from the TE is rather coherent in the spanwise direction the refined Γ-metric would also take differences in the noise radiation between two cases into account.

Due to the aforementioned problems when using a metric based on the pressure derivatives the vorticity vector $\omega = (\omega_x, \omega_y, \omega_z)$ was used to derive a similar quantity that can indicate the orientation of turbulent structures in the flow. We propose to calculate it as

$$\Pi_x = \overline{\left(\frac{\omega_x}{|\omega|}\right)'^2} \quad \text{and} \quad \Pi_z = \overline{\left(\frac{\omega_z}{|\omega|}\right)'^2} \quad . \tag{7.6}$$

This new metric is the variance of the respective normalized vorticity component. Since only fluctuations are taken into account the vorticity distribution in the mean flow does not influence the results.

Figure 7.19 shows the contours of the Π_x and Π_z metric for the rigid and elastic TE in the vicinity of the vortex generator cylinder, the TE and the wake. The contours of Π_x

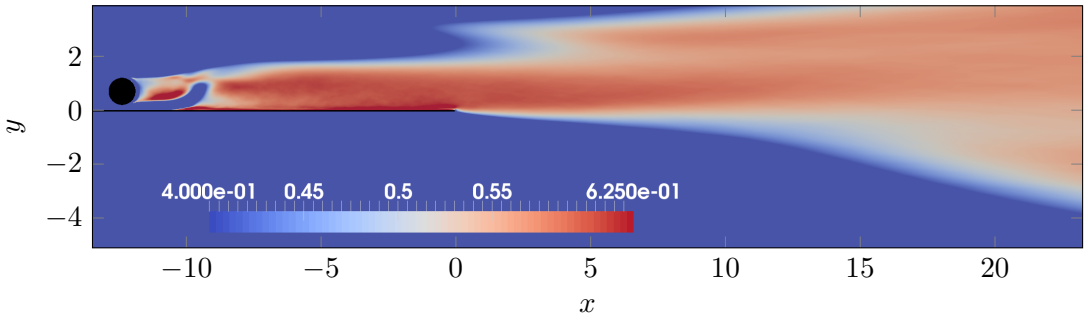

(a) Π_x for the rigid TE

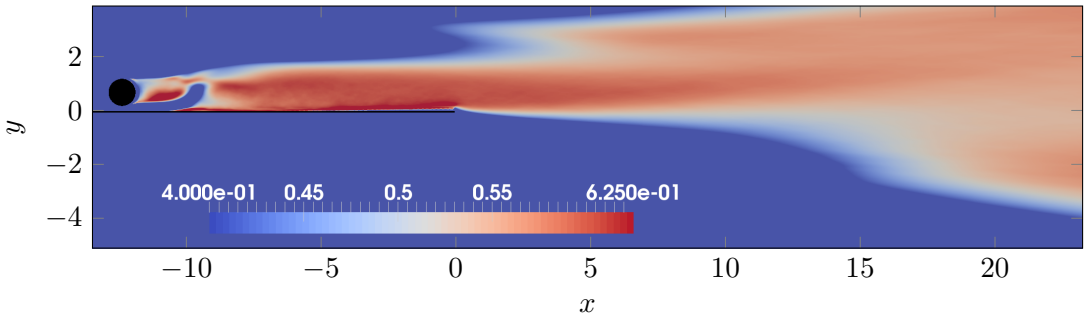

(b) Π_x for the elastic TE

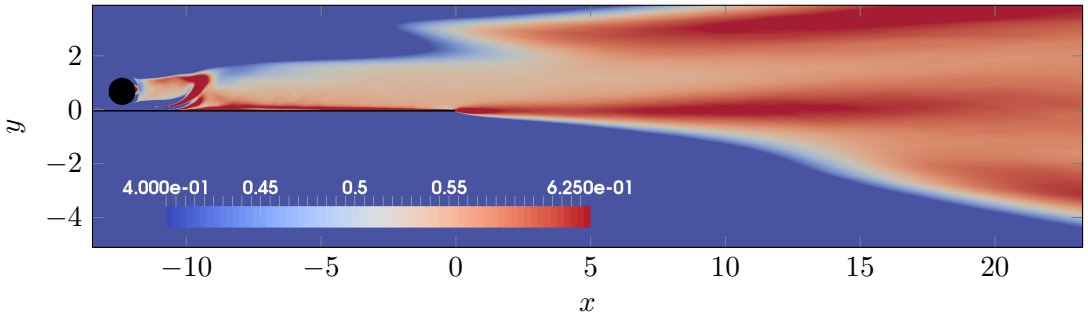

(c) Π_z for the rigid TE

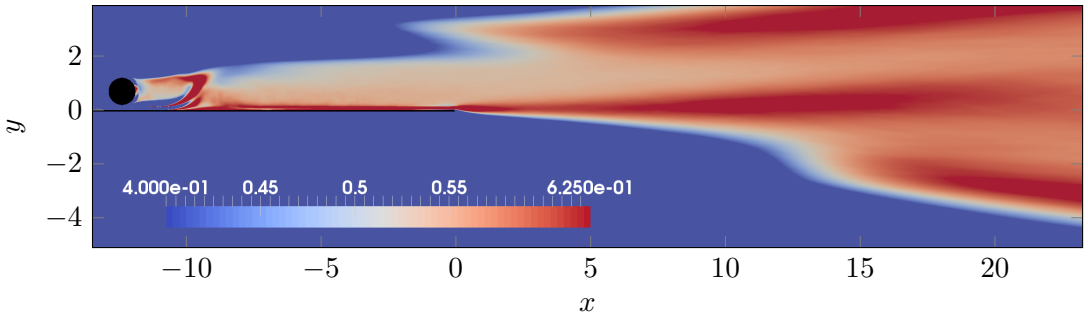

(d) Π_z for the elastic TE

Figure 7.19: Comparison of Π_x and Π_z in the vicinity of the vortex generator cylinder, the TE and the wake for the rigid and elastic TE.

are expected to be indicative of streamwise oriented turbulent structures that are commonly associated with wall bounded flows. Consistent with that, the highest contour levels are found in the turbulent region upstream of the TE. In the wake these high levels subsequently drop off. In the contours shown for the elastic case the mean deflection of the TE is visible when the figure is viewed closely. However, in comparison to the rigid TE no significant differences regarding the streamwise alignment of the turbulent structures are evident.

In the contours of the metric for spanwise oriented structures Π_z of the rigid TE a gradual reduction of the contour levels along the elastic fraction of the TE can be observed. This can most likely be linked to the separation bubble which leads to a recirculating flow that is averaged over time and thus coherent in the spanwise direction. Downstream of the TE the high contour levels of Π_z at the interface to the undisturbed free stream indicate a stronger spanwise orientation of the turbulent structures. A comparison of the rigid and elastic TE does not show a change in the overall topology.

7.4 Summary of the Findings

The aforementioned flat plate setup was extended to a three dimensional flow. The spanwise resolution and domain width was validated with a simulation with a higher resolution and a doubled domain width. The noise radiation from the fully turbulent flow over the elastic TE was found to be qualitatively similar to the two dimensional case. However, the noise from the structural motion was found to be relatively more important than in the two dimensional study and thereby reducing the advantage of the elastic TE. The analysis of the near field revealed that the motion of the TE increases the energy for long wavelengths in the spanwise direction at the TE location. Further downstream in the wake the distribution of energy in the spanwise direction is qualitatively similar in the rigid and elastic cases, although with a higher energy level in the elastic case. In addition a new metric to measure the dominant orientation of the turbulent structures was introduced and applied to the wakes of the rigid and elastic TE's. Apart from small differences no evidence of a topological change of the orientation of turbulent structures was found.

Chapter 8

Summary and Outlook

The principal findings and conclusions from this thesis are summarized in section 8.1. Furthermore an overview of future research that is enabled by the novel setup is given in section 8.2 .

8.1 Summary and Conclusions

The role of TE elasticity and its potential to achieve noise reductions has so far only been discussed in-depth analytically (Jaworski & Peake, 2013; Cavalieri *et al.*, 2016; Manela, 2011; Manela & Huang, 2013) and recently also experimentally (Das *et al.*, 2015). It was therefore the aim of this project to explore the effect of TE elasticity by means of high-fidelity numerical simulations. This is highly challenging and interesting from both a technical and physical point of view. To enable such simulations a virtual boundary method was extended to compressible flows and implemented into an in-house DNS code. In the following sections the summaries from the individual chapters are repeated and concluding remarks about the effect of elasticity are presented in section 8.1.5.

8.1.1 Virtual Boundary Condition for Moving Bodies in High-Fidelity Simulations with Application to Aeroacoustics

The current state of the art of immersed boundary methods to simulate non-grid conforming and moving bodies has been outlined. To the author's knowledge no method for direct noise computations involving moving bodies has previously been reported in literature. From the methods for incompressible flows the boundary data immersion method (BDIM) was chosen to be extended for compressible flows. The compressible formulation uses the BDIM meta equation to map the velocity and temperature fields between a solid body and a fluid subdomain. For certain applications, such as the simulation of bluff bodies, the proposed mapping of the continuity equation as an interface

condition between fluid and solid can enhance robustness of the simulation. In addition, an efficient algorithm to evaluate the signed distance function on curvilinear grids was presented.

A thorough validation of the novel compressible BDIM framework showed that the derivative correction increases the accuracy of the simulations compared to the first order approach. In particular the discontinuity of the velocity gradient at the wall is modelled much more accurately. This is shown for the very challenging case of a fully turbulent boundary layer where the discontinuity of the velocity gradient is relatively high and a broad range of scales in time and space is present in the flow. The case of a transversely oscillating cylinder in a medium at rest showed that the BDIM is able to predict the noise radiation from a moving body with high accuracy. Furthermore, flow induced noise generated by the interaction of a solid body with unsteady fluid flow can be modelled accurately with the BDIM. In all cases considered, except the simulation of Tollmien-Schlichting waves, the second order correction reduced the solution error and improved the convergence rate. It is speculated, that the instability growth is highly sensitive to the exact value of the velocity gradient at the wall in this case. It can be regarded as a limitation of the BDIM in general that the value of a field quantity at the wall location can inherently never be matched exactly, due to the smoothing. With grid refinement close to the surface the approximation of the value of a field quantity at the wall can be improved, though. However, in the majority of the applications considered in the current work the representation of the value at the wall was not found to be a limitation. However, in general the BDIM for compressible flows offers a computationally efficient yet accurate approach to represent stationary or moving bodies in high-fidelity numerical simulations with application to aeroacoustics. There is no penalty in allowable time step compared to body-fitted simulations when using the BDIM. Also, the grid resolution does not need to be higher than in an equivalent body-fitted simulation to accurately reproduce the compressible flow physics. Part of these results have been published in Schlanderer & Sandberg (2015) and in Schlanderer *et al.* (2017).

In order to enable fluid structure interaction simulations a structural solver that can be coupled to the fluid solver was implemented. The Euler-Bernoulli bending beam was chosen as a structural model. It was validated for deflections in the limit of steady state with accurate results against the analytical solution of this problem. In addition the dynamic behaviour was successfully evaluated with the impulse response to an initial force which was compared to the analytical natural frequencies.

The implemented framework has already been employed successfully for fluid-structure interaction problems (Serrano Galliano & Sandberg, 2016) and is an enabler for several other projects.

8.1.2 Self-Noise of Airfoils with Rigid and Elastic TE Extensions

The effect of rigid and elastic TE extensions attached to a NACA0012 airfoil at angle of attack was simulated. The comparison between a simulation with and without a rigid TE extension employing body-fitted boundary conditions only showed a significantly reduced noise level when the rigid extension was attached. This could be attributed to a smaller laminar separation bubble which introduced overall lower wall pressure fluctuations on the suction side and a reduction of the generated lift.

For the elastic TE extensions two different material parameter sets were investigated. It was found that the structural motion was dominated by the vortex shedding frequency which was close to resonance. In the acoustic far-field higher noise levels in comparison to the rigid TE were found at the vortex shedding frequency for both parameter sets. For the case with the highest deflections the vortex shedding frequency was locked in with the second natural frequency. This lead to a global change of the flow with different location and intensity of the separation bubble. As the incident pressure fluctuations were reduced with that parameter set it is argued that the substantial excess noise originates from the structural motion. The elastic extension with smaller deflections was found to amplify the incident pressure fluctuations which lead to an increased noise level as well. In general, a fair comparison between the rigid and elastic TE extensions was found to be challenging as changes in the hydrodynamic near-field were found far upstream of the actual TE location.

8.1.3 Noise from an Elastic TE of a Flat Plate

For the generic setup to study the influence of TE elasticity using a flat plate with a vortex generator, three different parameter sets for the elastic fraction of the TE have been considered. The effectiveness of a parameter set in reducing TE noise highly depended on the response of the motion to the input loading from the flow. In the far field spectra of the elastic TE's excess noise at the structural frequencies was found. The examination of the hydrodynamic near field showed that this noise can originate from the TE as a result of an amplification of the incident field. However, in most cases the data showed no evidence that the excess noise is radiated from the TE and it is suggested that the excess noise is due to motion induced sound from the elastic body. Finally, a reduction of the radiated noise was found in specific frequency ranges and for one parameter set also globally. This noise reduction was associated with two mechanisms: Firstly, the motion of the TE modified the incident pressure fluctuations and therefore the input to the TE noise mechanism. Secondly, the elastic TE was less efficient in transforming energy from hydrodynamic to acoustic pressure fluctuations.

The investigation of the effect of structural damping showed a potential for significant noise reductions compared to the undamped and the rigid cases. The data indicated that this was achieved by reduced fluctuations of the deflections at the structural and the forcing frequencies. The higher amplitude peak of the incident pressure field at the TE for the damped cases suggests that some noise reduction potential of the elastic TE without damping is compromised. However, this minor unfavourable effect is outweighed by the reduction and elimination of the excess noise at the structural frequencies which leads to an overall noise reduction.

It should be mentioned that results obtained with the current framework are qualitatively consistent with the results published in Schlanderer & Sandberg (2013) with a lower order framework, despite uncertainties about the accuracy of the noise generation from moving bodies represented by the feedback loop immersed boundary approach.

8.1.4 Noise from a Turbulent Flow Convecting Over an Elastic TE

The aforementioned flat plate setup was extended to a three dimensional flow. The noise radiation from the fully turbulent flow over the elastic TE was found to be qualitatively similar to the two dimensional case. However, the noise from the structural motion was found to be relatively more important than in the two dimensional study, thereby reducing the advantage of the elastic TE. The analysis of the near field revealed that the motion of the TE increases the energy for long wavelengths in the spanwise direction at the TE location. Further downstream in the wake the distribution of energy in the spanwise direction is qualitatively the same in the rigid and elastic cases with a higher energy level in the elastic case, though. In addition a new metric to measure the orientation of the turbulent structures was introduced and applied to the wake of the rigid and elastic TE. Apart from small differences no evidence of a topological change of the orientation of turbulent structures was found. Part of these results are published in Schlanderer & Sandberg (2016).

8.1.5 Concluding Remarks About the Effect of Elasticity

In general, the potential of elastic TE's to reduce noise that was predicted by the analytical studies of Jaworski & Peake (2013) and Cavalieri *et al.* (2016) as well as Manela (2011) and Manela & Huang (2013) could be confirmed with the numerical studies conducted in this work. On the one hand, the actual noise reduction that can be achieved critically depends on the response of the structure to the fluid loading. Therefore, the contribution from motion induced sound has to be taken into account in analytical models which is not the case in the study of Jaworski & Peake (2013). On the other hand, the strength of this noise source is likely to become less important for very low Mach

number flows as the scaling of the motion induced noise is M^6 compared to M^5 of TE noise.

Structural damping appears to be an important parameter to enhance the benefits of an elastic TE significantly. The conversion of kinetic energy of the moving structure into internal energy reduces the fluctuations of the structural deflections. Consequently, the motion induced noise is reduced or completely eliminated. Furthermore, the energy from the fluid flow is not only redistributed to the natural frequencies of the structure but also dissipated.

8.2 Future Work

The main contribution of the work was the development of a versatile numerical framework for fluid-structures interaction simulations in the context of aeroacoustics. In addition initial studies on the effect of TE elasticity have been carried out. In the following paragraphs avenues for further studies are outlined.

In-depth Data Analysis To date, a rigorous correlation between the noise received in the far-field and the motion of the elastic TE has not been carried out. Such a correlation would give further insight into how the far-field noise is influenced by the near-field motion. Furthermore, it would be interesting to model the motion-induced sound analytically based on the deflection time history and determine the exact contribution to the overall noise radiation and its directivity pattern. With the insight from these studies criteria to achieve a noise attenuation could be developed.

Effect of Elasticity on Broadband Trailing-Edge Noise In the present work the noise sources investigated showed a tonal behaviour with dominant peaks in the spectra in the acoustic far-field but also of the structural motion. An interesting research question is how an elastic TE would respond to a broad band pressure loading from a turbulent boundary layer and in particular how this would affect the potential for a noise reduction and if excess motion induced noise can be observed as well.

Fully Three Dimensional Structural Deflections The structural model that was employed for the three dimensional simulations in this work did not account for variations in the spanwise direction and thus the structural motion was coherent in this direction. However, a structure that was able to also deform in the spanwise direction would be able to react more directly to local pressure disturbances in the flow and thus lead to reduced correlation length of the flow in the spanwise direction. It is anticipated that this could increase the benefits of elastic TE's for noise reduction.

Elastic Serrated Trailing-Edge Since TE serrations have been shown to be an effective measure for TE noise reduction it would be interesting to investigate if the noise reduction potential of elastic TE's can enhance the benefits of serrated TE's. To that end the BDIM would need to be extended to fully three dimensional geometries and coupled to a finite-element solver to calculate the structural deflections.

Bibliography

Ai, Q., Azarpeyvand, M., Lachenal, X. & Weaver, P.M. 2015 Aerodynamic and aeroacoustic performance of airfoils with morphing structures. *Wind Energy* pp. 657–669.

Ali, S.A.S., Szoke, M., Azarpeyvand, M. & da Silva, C.R.I. 2016 Trailing-Edge Bluntness Flow and Noise Control Using Porous Treatments. In *22nd AIAA/CEAS Aeroacoustics Conference*. AIAA Paper 2016-2832.

Amiet, R.K. 1976 Noise due to turbulent flow past a trailing edge. *Journal of Sound and Vibration* **47** (3), 387–393.

Anderson, J.D. 2001 *Fundamentals of Aerodynamics*, 3rd edn. McGraw-Hill.

Arbey, H. & Bataille, J. 1983 Noise generated by airfoil profiles placed in a uniform laminar flow. *Journal of Fluid Mechanics* **134**, 33–47.

Arina, R. 2008 An Immersed Boundary Method for Aeroacoustics Problems. In *14th AIAA/CEAS Aeroacoustics Conference*. AIAA Paper 2008-3003.

Arina, R., Della Ratta Rinaldi, R., Iob, A. & Torzo, D. 2012 Numerical study of self-noise produced by an airfoil with trailing-edge serrations. In *18th AIAA/CEAS Aeroacoustics Conference*. AIAA Paper 2012-2184.

Azarpeyvand, M., Gruber, M. & Joseph, P.F. 2013 An analytical investigation of trailing edge noise reduction using novel serrations. In *19th AIAA/CEAS Aeroacoustics Conference*. AIAA Paper 2013-2009.

Bae, Y., Jang, J.Y. & Moon, Y.J. 2008 Effects of fluid-structure interaction on trailing-edge noise. *Journal of Mechanical Science and Technology* **22** (7), 1426–1435.

Bae, Y. & Moon, Y.J. 2008 Aerodynamic sound generation of flapping wing. *The Journal of the Acoustical Society of America* **124** (1), 72–81.

Bae, Y. & Moon, Y.J. 2011 Effect of passive porous surface on the trailing-edge noise. *Physics of Fluids* **23** (12), 126101.

Baker, W.E., Woolam, W.E. & Young, D. 1967 Air and internal damping of thin cantilever beams. *International Journal of Mechanical Sciences* **9**, 743–766.

Balaras, E. 2004 Modeling complex boundaries using an external force field on fixed Cartesian grids in large-eddy simulations. *Computers & Fluids* **33** (3), 375–404.

Banks, H.T. & Inman, D.J. 1989 On damping mechanisms in beams. *NASA Contractor Report- 383904* .

Bertagnolio, F., Fischer, A. & Jun Zhu, W. 2014 Tuning of turbulent boundary layer anisotropy for improved surface pressure and trailing-edge noise modeling. *Journal of Sound and Vibration* **333** (3), 991–1010.

Blackstock, D.T. 2000 *Fundamentals of Physical Acoustics*. John Wiley & Sons.

Bogey, C., de Cacqueray, N. & Bailly, C. 2009 A shock-capturing methodology based on adaptative spatial filtering for high-order non-linear computations. *Journal of Computational Physics* **228**, 1447–1465.

Breakey, D.E.S., Fitzpatrick, J.A. & Meskell, C. 2013 Aeroacoustic source analysis using time-resolved PIV in a free jet. *Experiments in Fluids* **54** (5), 1531.

Breugem, W.P. 2012 A second-order accurate immersed boundary method for fully resolved simulations of particle-laden flows. *Journal of Computational Physics* **231**, 4469–4498.

Brooks, T.F. & Hodgson, T.H. 1981 Trailing edge noise prediction from measured surface pressures. *Journal of Sound and Vibration* **78** (1), 69–117.

Brooks, T.F., Pope, D.S. & Marcolini, M.A. 1989 Airfoil self-noise and prediction. *NASA Reference Publiction 1218* .

Cand, M., Sayma, A.I. & Imregun, M. 2004 10th AIAA/CEAS Aeroacoustics Conference. In *10th AIAA/CEAS Aeroacoustics Conference*. AIAA Paper 2004-2816.

Cannell, P.A. 1975 Edge scattering of aerodynamic sound by a lightly loaded elastic half-plane. *Proceedings of the Royal Society A: Mathematical and Physical Sciences* **347**, 213–238.

Cannell, P.A. 1976 Acoustic edge scattering by a heavily loaded elastic half-plane. *Proceedinge of the Royal Society of London Series A: Mathematical and Physical Sciences* **350**, 71–89.

Carpenter, M.H., Norstrom, J. & Gottlieb, D. 1999 A stable and conservative interface treatment of arbitrary spatial accuracy. *Journal of Computational Physics* **148**, 341–365.

Casalino, D., di Francescantonio, P. & Druon, Y. 2004 GFD Predictions of Fan Noise Propagation. In *10th AIAA/CEAS Aeroacoustics Conference*. AIAA Paper 2004-2989.

Cavalieri, A.V.G., Wolf, W.R. & Jaworski, J.W. 2016 Numerical solution of acoustic scattering by finite perforated elastic plates. *Proceedings of the Royal Society A* **472** (2188).

Chase, D.M. 1972 Sound radiated by turbulent flow off a rigid half-plane as obtained from a wavevector spectrum of hydrodynamic pressure. *Journal of the Acoustical Society of America* **52**, 1011–1023.

Chaudhuri, A., Hadjadj, A. & Chinnayya, A. 2011 On the use of immersed boundary methods for shock/obstacle interactions. *Journal of Computational Physics* **230**, 1731–1748.

Chiu, P.H., Lin, R.K. & Sheu, T.W.H. 2010 A differentially interpolated direct forcing immersed boundary method for predicting incompressible NavierStokes equations in time-varying complex geometries. *Journal of Computational Physics* **229**, 4476–4500.

Choi, J.-I., Oberoi, R.C. C, Edwards, J.R. R & Rosati, J.A. A 2007 An immersed boundary method for complex incompressible flows. *Journal of Computational Physics* **224**, 757–784.

Chong, T.P. & Joseph, P.F. 2013 An experimental study of airfoil instability tonal noise with trailing edge serrations. *Journal of Sound and Vibration* **332** (24), 6335–6358.

Chong, T.P., Joseph, P.F. & Gruber, M. 2010 An experimental study of airfoil instability noise with trailing edge serrations. In *16th AIAA/CEAS Aeroacoustics Conference*. AIAA Paper 2010-3723.

Chong, T.P., Joseph, P.F. & Gruber, M. 2012 On the airfoil self-noise reduction by trailing edge serrations of non-insertion type. In *18th AIAA/CEAS Aeroacoustics Conference*. AIAA Paper 2012-2185.

Chong, T.P., Joseph, P.F. & Gruber, M. 2013*a* Airfoil self noise reduction by non-flat plate type trailing edge serrations. *Applied Acoustics* **74** (4), 607–613.

Chong, T.P. & Vathylakis, A. 2015 On the aeroacoustic and flow structures developed on a flat plate with a serrated sawtooth trailing edge. *Journal of Sound and Vibration* **354**, 65–90.

Chong, T.P., Vathylakis, A., Joseph, P.F. & Gruber, M. 2011 On the noise and wake flow of an airfoil with broken and serrated trailing edges. In *17th AIAA/CEAS Aeroacoustics Conference*. AIAA Paper 2011-2860.

Chong, T.P., Vathylakis, A., Joseph, P.F. & Gruber, M. 2013*b* Self-Noise Produced by an Airfoil with Nonflat Plate Trailing-Edge Serrations. *AIAA Journal* **51** (11), 2665 – 2677.

Chordá, R., Blasco, J.A. & Fueyo, N. 2002 An efficient particle-locating algorithm for application in arbitrary 2D and 3D grids. *International Journal of Multiphase Flow* **28**, 1565–1580.

Cozza, I.F., Iob, A. & Arina, R. 2012 Broadband trailing-edge noise prediction with a stochastic source model. *Computers & Fluids* **57**, 98–109.

Crighton, D.G. 1972 Radiation from vortex filament motion near a half plane. *Journal of Fluid Mechanics* **51**, 357–362.

Crighton, D.G. & Leppington, F.G. 1970 Scattering of aerodynamic noise by a semiinfinite compliant plate. *Journal of Fluid Mechanics* **43** (4), 721–736.

Crighton, D.G. & Leppington, F.G. 1971 On the scattering of aerodynamic noise. *Journal of Fluid Mechanics* **46**, 577–597.

Crighton, D.G. & Leppington, F.G. 1974 Radiation properties of the semi-infinite vortex sheet: the initial-value problem. *Journal of Fluid Mechanics* **64**, 393–414.

Criminale, W.O., Jackson, T.L. & Joslin, R.D. 2003 *Theory and Computation in Hydrodynamic Stability*. Cambridge University Press.

Curle, N. 1955 The influence of solid boundaries upon aerodynamic sound. *Proceedinge of the Royal Society of London Series A: Mathematical and Physical Sciences* **231** (1187), 505–514.

Das, C., Mimani, A., Porteous, R. & Doolan, C. 2015 An experimental investigation of flow-induced noise mechanism of a flexible flat-plate trailing-edge. In *Annual Conference of the Australian Acoustical Society*.

Dassen, T., Parchen, R., Bruggeman, J. & Hagg, F. 1996 Results of a wind tunnel study on the reduction of airfoil self-noise by the application of serrated blade trailing edges. *Proceeding of the European Union Wind Energy Conference and Exhibition* pp. 800–803.

De Palma, P., de Tullio, M.D., Pascazio, G. & Napolitano, M. 2006 An immersed-boundary method for compressible viscous flows. *Computers & Fluids* **35**, 693–702.

Desquesnes, G., Terracol, M. & Sagaut, P. 2007 Numerical investigation of the tone noise mechanism over laminar airfoils. *Journal of Fluid Mechanics* **591**, 155–182.

Fadlun, E.A., Verzicco, R., Orlandi, P. & Mohd-Yusof, J. 2000 Combined immersed-boundary finite-difference methods for three-dimensional complex flow simulations. *Journal of Computational Physics* **161** (1), 35–60.

Fasel, H. & Konzelmann, U. 1990 Non-parallel stability of a flat-plate boundary layer using the complete Navier-Stokes equations. *Journal of Fluid Mechanics* **221**, 311–347.

Fertis, D.G. 2006 *Nonlinear Structural Engineering*, pp. 1–61. Springer.

Ffowcs Williams, J.E. & Hall, L.H. 1970 Aerodynamic sound generation by turbulent flow in the vicinity of a scattering half plane. *Journal of Fluid Mechanics* **40**, 657–670.

Finez, A., Jondeau, E. & Roger, M. 2010 Broadband Noise Reduction With Trailing Edge Brushes. In *16th AIAA/CEAS Aeroacoustics Conference*. AIAA Paper 2010-3980.

Froehlich, J., Rodi, W., Kessler, Ph., Parpais, S., Bertoglio, J.P. & Laurence, D. 1998 Large Eddy Simulation of Flow around Circular Cylinders on Structured and Unstructured Grids. *Notes on Numerical Fluid Mechanics* **66**, 319–338.

Garcia-Sagrado, A. & Hynes, T. 2012 Wall pressure sources near an airfoil trailing edge under turbulent boundary layers. *Journal of Fluids and Structures* **30**, 3–34.

Geyer, T., Sarradj, E. & Fritzsche, C. 2010 Measurement of the noise generation at the trailing edge of porous airfoils. *Experiments in Fluids* **48**, 291–308.

Ghias, R., Mittal, R. & Dong, H. 2007 A sharp interface immersed boundary method for compressible viscous flows. *Journal of Computational Physics* **225**, 528–553.

Goldstein, D., Handler, G. & Sirovich, L. 1993 Modeling a no-slip flow boundary with an external force field. *Journal of Computational Physics* **105**, 354–366.

Griffith, B.E. & Peskin, C.S. 2005 On the order of accuracy of the immersed boundary method: Higher order convergence rates for sufficiently smooth problems. *Journal of Computational Physics* **208** (1), 75–105.

Gruber, M., Azarpeyvand, M. & Joseph, P.F. 2010*a* Airfoil trailing edge noise reduction by the introduction of sawtooth and slitted trailing edge geometries. In *20th International Congress on Acoustics, ICA*.

Gruber, M. & Joseph, P.F. 2013 An experimental investigation of novel trailing edge geometries on airfoil trailing edge noise reduction. In *19th AIAA/CEAS Aeroacoustics Conference*. AIAA Paper 2013-2011.

Gruber, M., Joseph, P.F. & Chong, T.P. 2010*b* Experimental investigation of airfoil self noise and turbulent wake reduction by the use of trailing edge serrations. In *16th AIAA/CEAS Aeroacoustics Conference*. AIAA Paper 2010-3803.

Gruber, M., Joseph, P.F. & Chong, T.P. 2011 On the mechanisms of serrated airfoil trailing edge noise reduction. In *17th AIAA/CEAS Aeroacoustics Conference*. AIAA Paper 2011-2781.

Harris, R.E. 2013 Adaptive cartesian immersed boundary method for simulation of flow over flexible geometries. *AIAA Journal* **51** (1), 53–69.

Hayden, R.E., Fox, H.L. & Chanaud, R.C. 1976 Some factors influencing radiation of sound from flow interaction with edges of finite surfaces. *NASA CR* **145073**.

Henderson, R.D. 1995 Details of the drag curve near the onset of vortex shedding. *Physics of Fluids* **7**, 2102–2104.

Herr, M. 2007 Design criteria for low-noise trailing-edges. In *13th AIAA/CEAS Aeroacoustics Conference*. AIAA Paper 2007-3470.

Herr, M. & Dobrzynski, W. 2005 Experimental investigations in Low-noise trailing-edge design. *AIAA Journal* **43** (6), 1167–1175.

Hou, G., Wang, J. & Layton, A. 2012 Numerical Methods for Fluid-Structure Interaction - A Review. *Communications in Computational Physics* **12** (2), 337–377.

Howe, M.S. 1991*a* Aerodynamic noise of a serrated trailing edge. *Journal of Fluids and Structures* **5**, 33–45.

Howe, M.S. 1991*b* Noise produced by a sawtooth trailing edge. *The Journal of the Acoustical Society of America* **90**, 482–487.

Howe, M.S. 1992 Sound produced by an aerodynamic source adjacent to a partly coated, finite elastic plate. *Proceedings of the Royal Society A: Mathematical and Physical Sciences* **436** (1897), 351–372.

Howe, M.S. 1993 Structural and acoustic noise produced by turbulent flow over an elastic trailing edge. *Proceedings of the Royal Society A: Mathematical, Physical and Engineering Sciences* **442**, 533–554.

Howe, M.S. 1999 Trailing edge noise at low Mach mumbers. *Journal of Sound and Vibration* **225** (2), 211–238.

Howe, M. S. 1976 The influence of vortex shedding on the generation of sound by convected turbulence. *Journal of Fluid Mechanics* **76**, 711–740.

Howe, M. S. 1978 A Review of the Theory of Trailing Edge Noise. *Journal of Sound and Vibration* **61** (3), 437–465.

Hu, O., Zhao, N. & Liu, J.M. 2013 A Ghost Cell Method for Turbulent Compressible Viscous Flows on Adaptive Cartesian Grids. *Procedia Engineering* **67**, 241–249.

Hubbard, H.H. & Shepherd, K.P. 1991 Aeroacoustics of large wind turbines. *The Journal of the Acoustical Society of America* **89** (6), 2495–2508.

Husmeier, F., Mayer, C.S.J. & Fasel, H.F. 2005 Investigation of Transition of Supersonic Boundary Layers at Mach 3 Using DNS. In *43th AIAA Aerospace Sciences Meeting and Exhibit*.

Hutcheson, F. & Brooks, T. F. 2004 Effects of angle of attack and velocity on trailing edge noise. In *42nd AIAA Aerospace Sciences Meeting and Exhibit*. AIAA Paper 2004-1031.

Ikeda, T., Atobe, T., Fujimoto, D., Inasawa, A. & Asai, M. 2015 Self-Noise Effects on Aerodynamics of Cambered Airfoils at Low Reynolds Number. *AIAA Journal* **53** (8), 2256–2269.

Ikeda, T., Atobe, T. & Takagi, S. 2012 Direct simulations of trailing-edge noise generation from two-dimensional airfoils at low Reynolds numbers. *Journal of Sound and Vibration* **331** (3), 556–574.

Inasawa, A., Ninomiya, C. & Asai, M. 2013 Suppression of Tonal Trailing-Edge Noise From an Airfoil Using a Plasma Actuator. *AIAA Journal* **51** (7), 1695–1702.

Jaworski, J.W. & Peake, N. 2012 Aerodynamic noise from a poroelastic trailing edge with implications for the silent flight of owls. In *18th AIAA/CEAS Aeroacoustics Conference*. AIAA Paper 2012-2138.

Jaworski, J.W. & Peake, N. 2013 Aerodynamic noise from a poroelastic edge with implications for the silent flight of owls. *Journal of Fluid Mechanics* **723**, 456–479.

Johnson, S.J., Baker, J.P., van Dam, C.P. & D., Berg 2009 An overview of active load control techniques for wind turbines with an emphasis on microtabs. *Wind Energy* **13**, 239–253.

Jones, L.E. 2008 Numerical studies of the flow around an airfoil at low Reynolds number. PhD thesis, School of Engineering Sciences University of Southampton.

Jones, L.E. & Sandberg, R.D. 2012 Acoustic and hydrodynamic analysis of the flow around an aerofoil with trailing-edge serrations. *Journal of Fluid Mechanics* **706**, 295–322.

Jones, L.E., Sandberg, R.D. & Sandham, N.D. 2008 Direct numerical simulations of forced and unforced separation bubbles on an airfoil at incidence. *Journal of Fluid Mechanics* **602**, 175–207.

Kamruzzaman, M., Bekiropoulos, D., Lutz, T., Würz, W. & Krämer, E. 2015 A semi-empirical surface pressure spectrum model for airfoil trailing-edge noise prediction. *International Journal of Aeroacoustics* **14** (5-6), 833–882.

Kennedy, C.A., Carpenter, M.H. & Lewis, R.M. 2000 Low-storage, explicit RungeKutta schemes for the compressible NavierStokes equations. *Applied Numerical Mathematics* **35**, 177–219.

Kennedy, C.A. & Gruber, A. 2008 Reduced aliasing formulations of the convective terms within the Navier-Stokes equations for a compressible fluid. *Journal of Computational Physics* **227**, 1676–1700.

Khadra, K., Angot, P., Parneix, S. & Caltagirone, J.P. 2000 Fictitious domain approach for numerical modelling of NavierStokes equations. *International Journal for Numerical Methods in Fluids* **34** (8), 651–684.

Kim, J.W. 2010 High-order compact filters with variable cut-off wavenumber and stable boundary treatment. *Computers & Fluids* **39** (7), 1168–1182.

Kim, J.W. & Lee, D.J. 2003 Characteristic Interface Conditions for Multiblock High-Order Computation on Singular Structured Grid. *AIAA Journal* **41** (12), 2341–2348.

Kim, J.W. & Sandberg, R.D. 2012 Efficient parallel computing with a compact finite difference scheme. *Computers & Fluids* **58**, 70–87.

Klein, M., Sadiki, A. & Janicka, J. 2003 A digital filter based generation of inflow data for spatially developing direct numerical or large eddy simulations. *Journal of Computational Physics* **186**, 652–665.

Koh, S.R., Meinke, M. & Schröder, W. 2013 Impact of multi-species gas injection on trailing-edge noise. *Computers & Fluids* **75** (20), 72–85.

Kornecki, A., Dowell, E. H. & O'Brien, J. 1976 On the aeroelastic instability of two-dimensional panels in uniform incompressible flow. *Journal of Sound and Vibration* **47** (2), 163–178.

Lai, M.C. & Peskin, C.S. 2000 An immersed boundary method with formal second-order accuracy and reduced numerical viscosity. *Journal of Computational Physics* **160**, 705–719.

Lee, G.S. & Cheong, C. 2013 Frequency-domain prediction of broadband trailing edge noise from a blunt flat plate. *Journal of Sound and Vibration* **332** (21), 5322–5344.

Lee, S. 2013 Numerical modeling of wind turbine aerodynamic noise in the time domain. *The Journal of the Acoustical Society of America* **133** (2), EL94–EL100.

León, C.A., Ragni, D., Pröbsting, S. & Scarano, F. 2016 Flow topology and acoustic emissions of trailing edge serrations at incidence. *Experiments in Fluids* **57** (5), 91.

Lighthill, M.J. 1952 On sound generated aerodynamically: I. General theory. *Proceedinge of the Royal Society of London Series A: Mathematical and Physical Sciences* **211** (1107), 564–587.

Lighthill, M.J. 1954 On sound generated aerodynamically: II. Turbulence as a source of sound. *Proceedinge of the Royal Society of London Series A: Mathematical and Physical Sciences* **222** (1148), 1–32.

Liu, C. & Hu, C. 2014 An efficient immersed boundary treatment for complex moving object. *Journal of Computational Physics* **274**, 654–680.

Liu, M. & Wu, K. 2008 Aerodynamic noise propagation simulation using immersed boundary method and finite volume optimized prefactored compact scheme. *Journal of Thermal Science* **17** (4), 361–367.

Liu, Q. & Vasilyev, O.V. 2007 A Brinkman penalization method for compressible flows in complex geometries. *Journal of Computational Physics* **227**, 946–966.

Liu, X., Jawahar, H.K. & Azarpeyvand, M. 2016 Wake Development of Airfoils with Serrated Trailing Edges. In *22nd AIAA/CEAS Aeroacoustics Conference*. AIAA Paper 2016-2817.

Liu, X., Jawahar, H.K., Azarpeyvand, M. & Theunissen, R. 2015 Aerodynamic and Aeroacoustic Performance of Serrated Airfoils. In *21st AIAA/CEAS Aeroacoustics Conference*. AIAA Paper 2015-2201.

Luo, H., Dai, H., Ferreira de Sousa, P.J.S.A. & Yin, B. 2012 On the numerical oscillation of the direct-forcing immersed-boundary method for moving boundaries. *Computers & Fluids* **56**, 61–76.

Lutz, T., Herrig, A., Würz, W., Kamruzzaman, M. & Krämer, E. 2007 Design and wind-tunnel verification of low-noise airfoils for wind turbines. *AIAA Journal* **45** (4), 779–785.

Lyu, B., Azarpeyvand, M. & Sinayoko, S. 2016 Prediction of noise from serrated trailing-edges. *Journal of Fluid Mechanics* **793**, 556–588.

Maertens, A.P. & Weymouth, G.D. 2015 Accurate Cartesian-grid simulations of near-body flows at intermediate Reynolds numbers. *Computer Methods in Applied Mechanics and Engineering* **283**, 106–129.

Manela, A. 2011 Sound generated by a vortex convected past an elastic sheet. *Journal of Sound and Vibration* **330**, 416–430.

Manela, A. 2012 Vibration and sound of an elastic wing actuated at its leading edge. *Journal of Sound and Vibration* **331**, 638–650.

Manela, A. 2013 On the acoustic radiation of a pitching airfoil. *Physics of Fluids* **25** (7), 071906.

Manela, A. & Huang, L. 2013 Point vortex model for prediction of sound generated by a wing with flap interacting with a passing vortex. *The Journal of the Acoustical Society of America* **133** (4), 1934–1944.

Mankbadi, R.R., Golubev, V.V., Sansone, M., Sewell, C. & Nguyen, L. 2015 Effect of a synthetic jet actuator on airfoil trailing edge noise. *Aeroacoustics* **14** (3&4), 553–568.

Margnat, F. 2015 Hybrid prediction of the aerodynamic noise radiated by a rectangular cylinder at incidence. *Computers & Fluids* **109**, 13–26.

Margnat, F. & Morinière, V. 2009 Behaviour of an immersed boundary method in unsteady flows over sharp-edged bodies. *Computers & Fluids* **38** (6), 1065–1079.

Marsden, A. L., Wang, M., Dennis, J. E. & Moin, P. 2007 Trailing-edge noise reduction using derivative-free optimization and large-eddy simulation. *Journal of Fluid Mechanics* **572**, 13–35.

Martínez-Lera, P., Schram, C., Bériot, H. & Hallez, R. 2014 An approach to aerodynamic sound prediction based on incompressible-flow pressure. *Journal of Sound and Vibration* **333** (1), 132–143.

Mayer, C.S.J., von Terzi, D.A. & Fasel, H.F. 2011 Direct numerical simulation of complete transition to turbulence via oblique breakdown at Mach 3. *Journal of Fluid Mechanics* **674**, 5–42.

Mittal, R., Dong, H., Bozkurttas, M., Najjar, F.M., Vargas, A. & von Loebbecke, A. 2008 A versatile sharp interface immersed boundary method for incompressible flows with complex boundaries. *Journal of Computational Physics* **227**, 4825–4852.

Mittal, R. & Iaccarino, G. 2005 Immersed boundary methods. *Annual Review of Fluid Mechanics* **37**, 239–261.

Mohd-Yusof, J. 1997 Combined immersed-boundary/B-spline methods for simulations of flow in complex geometries. *CTR Annual Research Briefs* .

Moreau, D.J., Brooks, L.A. & Doolan, C.J. 2011 Broadband trailing edge noise from a sharp-edged strut. *Journal of the Acoustical Society of America* **129**, 2820–2829.

Moreau, D.J., Brooks, L.A. & Doolan, C.J. 2012*a* On the noise reduction mechanism of a flat plate serrated trailing edge at low-to-moderate Reynolds number. In *18th AIAA/CEAS Aeroacoustics Conference*. AIAA Paper 2012-2186.

Moreau, D.J., Brooks, L.A. & Doolan, C.J. 2012*b* The effect of boundary layer type on trailing edge noise from sharp-edged flat plates at low-to-moderate Reynolds number. *Journal of Sound and Vibration* **331** (17), 3976—-3988.

Moreau, D.J. & Doolan, C.J. 2013*a* Noise-Reduction Mechanism of a Flat-Plate Serrated Trailing Edge. *AIAA Journal* **51** (10), 2513–2522.

Moreau, D.J., Prime, Z., Porteous, R., Doolan, C.J. & Valeau, V. 2014 Flow-induced noise of a wall-mounted finite airfoil at low-to-moderate Reynolds number. *Journal of Sound and Vibration* **333** (25), 6924–6941.

Moreau, D J & Doolan, C J 2013*b* Tonal Noise from Trailing Edge Serrations at Low Reynolds Numbers. In *19th AIAA/CEAS Aeroacoustics Conference*. AIAA Paper 2013-2010.

Moreau, S. & Roger, M. 2009 Back-scattering correction and further extensions of Amiet's trailing-edge noise model. Part II: Application. *Journal of sound and vibration* **323**, 397–425.

Morse, P.M. 1948 *Vibration and Sound*. McGraw-Hill.

Muldoon, F. & Acharya, S. 2008 A divergence-free interpolation scheme for the immersed boundary method. *International Journal for Numerical Methods in Fluids* **56**, 1845–1884.

Nash, E.C., Lowson, M.V. & McAlpine, A. 1999 Boundary-layer instability noise on aerofoils. *Journal of Fluid Mechanics* **382**, 27–61.

Norberg, C. 1994 An experimental investigation of the flow around a circular cylinder: influence of aspect ratio. *Journal of Fluid Mechanics* **258**, 287–316.

Oberai, A.A., Roknaldin, F. & Hughes, T.J.R. 2002 Computation of trailing-edge noise due to turbulent flow over an airfoil. *AIAA Journal* **40** (11), 2206–2216.

Oerlemans, S., Fisher, M., Maeder, T. & Kögler, K. 2009 Reduction of wind turbine noise using optimized airfoils and trailing-edge serrations. *AIAA Journal* **47** (6), 1470–1481.

Oerlemans, S., Sijtsma, P. & Méndez López, B. 2007 Location and quantification of noise sources on a wind turbine. *Journal of Sound and Vibration* **299** (4-5), 869–883.

Oguma, Y., Yamagata, T. & Fujisawa, N. 2014 Measurement of Aerodynamic Sound Source around a Circular Cylinder by Particle Image. *Journal of Flow Control, Measurement and Visualization* **2**, 105–109.

de Pando, M.A.F. 2012 Tonal noise generation in flows around aerofoils : a global stability analysis. PhD thesis, Ecole Polytechnique Laboratoire d'Hydrodynamique.

Park, J., Kwon, K. & Choi, H. 1998 Numerical solutions of flow past a circular cylinder at Reynolds numbers up to 160. *KSME International Journal* **12** (6), 1200–1205.

Pedersen, E. & Persson Waye, K. 2004 Perception and annoyance due to wind turbine noisea doseresponse relationship. *Journal of the Acoustical Society of America* **116**, 3460–3470.

Peskin, C.S. 1972 Flow patterns around heart valves: A numerical method. *Journal of Computational Physics* **10** (2), 252–271.

Peskin, C.S. 2003 The immersed boundary method. *Acta Numerica* **11**, 479–517.

Pinelli, A., Naqavi, I. Z., Piomelli, U. & Favier, J. 2010 Immersed-boundary methods for general finite-difference and finite-volume Navier-Stokes solvers. *Journal of Computational Physics* **229**, 9073–9091.

Poinsot, T.J. & Lele, S.K. 1992 Boundary conditions for direct simulations of compressible viscous flows. *Journal of Computational Physics* **101** (1), 104–129.

Pope, S.B. 2000 *Turbulent flows*. Cambridge University Press.

Pourquie, M. 2009 Accuracy close to the wall of immersed boundary methods. In *4th European Conference of the International Federation for Medical and Biological Engineering*, pp. 1939–1942.

Pröbsting, S., Scarano, F. & Morris, S. C. 2015 Regimes of tonal noise on an airfoil at moderate Reynolds number. *Journal of Fluid Mechanics* **780**, 407–438.

Pröbsting, S., Serpieri, J. & Scarano, F. 2014 Experimental investigation of aerofoil tonal noise generation. *Journal of Fluid Mechanics* **747**, 656–687.

Pröbsting, S. & Yarusevych, S. 2015 Laminar separation bubble development on an airfoil emitting tonal noise. *Journal of Fluid Mechanics* **780**, 167–191.

Roger, M. & Moreau, S. 2004 Broadband self noise from loaded fan blades. *AIAA Journal* **42** (3), 536–544.

Roger, M. & Moreau, S. 2005 Back-scattering correction and further extensions of Amiet's trailing-edge noise model. Part 1: Theory. *Journal of Sound and Vibration* **286** (3), 477–506.

Russell, D. & Wang, Z.J. 2003 A Cartesian grid method for modeling multiple moving objects in 2D incompressible viscous flow. *Journal of Computational Physics* **191**, 177–205.

Sader, J.E., Coss, J., Kim, D., Fan, B. & Gharib, M. 2015 Large-amplitude flapping of an inverted-flag in a uniform steady flow a vortex-induced vibration. *Journal of Fluid Mechanics* **793**, 524–555.

Saiki, E.M. & Biringen, S. 1996 Numerical simulation of a cylinder in uniform flow: application of a virtual boundary method. *Journal of Computational Physics* **123**, 450–465.

Sandberg, R.D. 2007 A modification of Amiets classical trailing edge noise theory for strictly two dimensional flows. *University of Southampton School of Engineering Sciences – Aerodynamics & Flight Mechanics Group* **Report No.**

Sandberg, R.D. 2009 Generalized cylindrical coordinates for characteristic boundary conditions and characteristic interface conditions. *University of Southampton School of Engineering Sciences – Aerodynamics & Flight Mechanics Group* **Report No. AFM-09/02**.

Sandberg, R.D. 2015 Compressible-Flow DNS with Application to Airfoil Noise. *Flow, Turbulence and Combustion* **95** (2), 211–229.

Sandberg, R.D. & Jones, L.E. 2011 Direct numerical simulations of low Reynolds number flow over airfoils with trailing-edge serrations. *Journal of Sound and Vibration* **330**, 3818–3831.

Sandberg, R.D., Jones, L. & Sandham, N. 2008 Direct numerical simulations of noise generated by turbulent flow over airfoils. In *14th AIAA/CEAS Aeroacoustics Conference*. AIAA Paper 2008-2861.

Sandberg, R.D., Jones, L.E., Sandham, N.D. & Joseph, P.F. 2009 Direct numerical simulations of tonal noise generated by laminar flow past airfoils. *Journal of Sound and Vibration* **320**, 838–858.

Sandberg, R.D. & Sandham, N.D. 2006 Nonreflecting zonal characteristic boundary condition for direct numerical simulation of aerodynamic sound. *AIAA Journal* **44** (2), 402–405.

Sandberg, R.D., Sandham, N.D. & Joseph, P.F. 2007 Direct numerical simulations of trailing-edge noise generated by boundary-layer instabilities. *Journal of Sound and Vibration* **304**, 677–690.

Sandberg, R D & Sandham, N D 2008 Direct numerical simulation of turbulent flow past a trailing edge and the associated noise generation. *Journal of Fluid Mechanics* **596**, 353–385.

Sarradj, E. & Geyer, T. 2013 Airfoil noise analysis using symbolic regression. In *19th AIAA/CEAS Aeroacoustics Conference*. AIAA Paper 2013-2012.

Sarradj, E. & Geyer, T. 2014 Symbolic regression modeling of noise generation at porous airfoils. *Journal of Sound and Vibration* **333** (14), 3189–3202.

Schepers, J.G., Curvers, A.P.W.M., Oerlemans, S., Braun, K., Lutz, T., Herrig, A., Wuerz, W., Mendez Lopez, B., Matesanz, A., Ahrelt, R. & Maeder, T. 2007 SIROCCO : silent rotors by acoustic optimisation. In *Second International Meeting on Wind Turbine Noise, Inst. of Noise Control Engineering*.

Schlanderer, S.C. & Sandberg, R.D. 2013 DNS of a Compliant Trailing Edge Flow. In *19th AIAA/CEAS Aeroacoustics Conference*. AIAA Paper 2013-2013.

Schlanderer, S.C. & Sandberg, R.D. 2015 Boundary Data Immersion Method for DNS of aero-vibro-acoustic systems. In *ERCOFTAC Workshop Direct and Large-Eddy Simulations 10*.

Schlanderer, S.C. & Sandberg, R.D. 2016 DNS of Noise Radiation from a Turbulent Flow Convecting over an Elastic Trailing-Edge. In *22nd AIAA/CEAS Aeroacoustics Conference*.

Schlanderer, S.C., Weymouth, G.D. & Sandberg, R.D. 2017 The boundary data immersion method for compressible flows with application to aeroacoustics. *Journal of Computational Physics* **333** (15), 440–461.

Schlatter, P & Örlü, R 2010 Assessment of direct numerical simulation data of turbulent boundary layers. *Journal of Fluid Mechanics* **659**, 116–126.

Schlatter, P. & Örlü, R. 2012 Turbulent boundary layers at moderate Reynolds numbers: inflow length and tripping effects. *Journal of Fluid Mechanics* **710**, 5–34.

Schlatter, P., Örlü, R., Li, Q., Brethouwer, G., Fransson, J.H.M., Johansson, A.V., Alfredsson, P.H. & Henningson, D.S. 2009 Turbulent boundary layers upt to R_θ = 2500 studied through simulation and experiment. *Physics of Fluids* **21**, 051702.

Schroeder, A, Dierksheide, U, Wolf, J, Herr, M & Kompenhans, J 2004 Investigation on trailing-edge noise sources by means of high-speed PIV. In *12th International Symposium on Applications of Laser Techniques to Fluid Mechanics*.

Schumacher, K.L., Doolan, C.J. & Kelso, R.M. 2014*a* The effect of a cavity on airfoil tones. *Journal of Sound and Vibration* **333** (7), 1913–1931.

Schumacher, K.L., Doolan, C.J. & Kelso, R.M. 2014*b* The effect of acoustic forcing on an airfoil tonal noise mechanism. *The Journal of the Acoustical Society of America* **136** (2), EL78–EL83.

Seo, J.H. & Mittal, R. 2011*a* A Sharp-Interface Immersed Boundary Method with Improved Mass Conservation and Reduced Spurious Pressure Oscillations. *Journal of Computational Physics* **230**, 7347–7363.

Seo, J. H. & Mittal, R. 2011*b* A High-Order Immersed Boundary Method for Acoustic Wave Scattering and Low-Mach Number Flow-Induced Sound in Complex Geometries. *Journal of Computational Physics* **230** (4), 1000–1019.

Serrano Galliano, S. & Sandberg, R.D. 2016 Effect of the leading and trailing edge geometry on the fluid-structural coupling of membrane aerofoils. In *2016 AIAA SciTech*. AIAA Paper 2016-0853.

Singer, B.A., Brentner, K.S., Lockard, D.P. & Lilley, G.M. 2000 Simulation of Acoustic Scattering From a Trailing Edge. *Journal of Sound and Vibration* **230** (3), 541–560.

Stalnov, O., Chaitanya, P. & Joseph, P.F. 2016 Towards a non-empirical trailing edge noise prediction model. *Journal of Sound and Vibration* **372**, 50–68.

Straub, F.K., Ngo, H.T., Anand, V. & Domzalski, D.B. 2001 Development of a piezoelectric actuator for trailing edge flap control of full scale rotor blade. *Smart Materials and Structures* **10**, 25–34.

Su, S.W., Lai, M.C. & Lin, C.A. 2007 An immersed boundary technique for simulating complex flows with rigid boundary. *Computers & Fluids* **36** (2), 313–324.

Taira, K. & Colonius, T. 2007 The immersed boundary method: A projection approach. *Journal of Computational Physics* **225** (2), 2118–2137.

Tam, C.K.W. & Ju, H. 2006 Numerical simulation of the generation of airfoil tones at a moderate Reynolds number. In *12th AIAA/CEAS Aeroacoustics Conference*. AIAA Paper 2006-2502.

Tam, C.K.W. & Reddy, N.N 1977 Sound generated in the vicinity of the trailing-edge of an upper surface blown flap. *Journal of Sound and Vibration* **52**, 211–232.

Tam, C.K.W. & Yu, J.C. 1975 Trailing-Edge noise. *AIAA Journal* **489**.

Taylor, J., Eastwick, C., Lawrence, C. & Wilson, R. 2013 Noise levels and noise perception from small and micro wind turbines. *Renewable Energy* **55**, 120–127.

von Terzi, D.A., Linnick, M.N., Seidel, J. & Fasel, H.F. 2001 Immersed boundary techniques for high-order finite-difference methods. *AIAA Paper 2001-2918* .

Thomsen, J.J. 2004 *Vibrations and Stability*, 2nd edn. Springer.

Timoshenko, S., Young, D.H. & Weaver, W. 1974 *Vibration Problems in Engineering*, 4th edn. John Wiley & Sons.

Toja-Silva, F., Favier, J. & Pinelli, A. 2014 Radial basis function (RBF)-based interpolation and spreading for the immersed boundary method. *Computers & Fluids* **105**, 66–75.

Touber, E. & Sandham, N.D. 2009 Large-eddy simulation of low-frequency unsteadiness in a turbulent shock-induced separation bubble. *Theoretical and Computational Fluid Dynamics* **23**, 79–107.

Tran, P.H. & Plourde, F. 2014 Computing compressible internal flows by means of an Immersed Boundary Method. *Computers & Fluids* **97**, 21–30.

Tritton, D. J. 1959 Experiments on the flow past a circular cylinder at low Reynolds numbers. *Journal of Fluid Mechanics* **6**, 547–567.

Tseng, Y.-H. & Ferziger, J.H. 2003 A ghost-cell immersed boundary method for flow in complex geometry. *Journal of Computational Physics* **192** (2), 593–623.

de Tullio, M.D., De Palma, P., Iaccarino, G., Pascazio, G. & Napolitano, M. 2007 An immersed boundary method for compressible flows using local grid refinement. *Journal of Computational Physics* **225**, 2098–2117.

Udaykumar, H.S., Mittal, R., Rampunggoon, P. & Khanna, A. 2001 A Sharp Interface Cartesian Grid Method for Simulating Flows with Complex Moving Boundaries. *Journal of Computational Physics* **174**, 345–380.

Uddin, H., Kramer, R.M.J. & Pantano, C. 2014 A Cartesian-based embedded geometry technique with adaptive high-order finite differences for compressible flow around complex geometries. *Journal of Computational Physics* **262**, 379–407.

Uhlmann, M. 2005 An immersed boundary method with direct forcing for the simulation of particulate flows. *Journal of Computational Physics* **209**, 448–476.

Vanella, M. & Balaras, E. 2009 A moving-least-squares reconstruction for embedded-boundary formulations. *Journal of Computational Physics* **228**, 6617–6628.

Vathylakis, A., Chong, T.P. & Joseph, P.F. 2015 Poro-Serrated Trailing-Edge Devices for Airfoil Self-Noise Reduction. *AIAA Journal* **53** (11), 1–16.

Wang, S. & Zhang, X. 2011 An immersed boundary method based on discrete stream function formulation for two- and three-dimensional incompressible flows. *Journal of Computational Physics* **230** (9), 3479–3499.

Weidenfeld, M. & Manela, A. 2016 On the attenuating effect of permeability on the low frequency sound of an airfoil. *Journal of Sound and Vibration* pp. 1–14.

Weymouth, G.D. 2008 Physics and Learning Based Computational Models for Breaking Bow Waves Based on New Boundary Immersion Approaches. Phd-thesis, Massachusetts Institute of Technology.

Weymouth, G.D. & Yue, D.K.P. 2011 Boundary data immersion method for Cartesian-grid simulations of fluid-body interaction problems. *Journal of Computational Physics* **230**, 6233–6247.

White, F. 1991 *Viscous Fluid Flow*. McGraw-Hill.

Wilcox, D.C. 1998 *Turbulence Modeling for CFD*, 2nd edn.

Winkler, J., Moreau, S. & Carolus, T. 2010 Airfoil trailing edge noise prediction from large-eddy simulation: influence of grid resolution and noise model formulation. In *16th AIAA/CEAS Aeroacoustics Conference*. AIAA Paper 2010-3704.

Winkler, J., Moreau, S. & Carolus, T. 2012*a* Airfoil trailing-edge blowing: broadband noise prediction from large-eddy simulation. *AIAA Journal* **50** (2), 294–303.

Winkler, J., Sandberg, R.D. & Moreau, S. 2012*b* Direct numerical simulation of the self-noise radiated by an airfoil in a narrow stream. In *18th AIAA/CEAS Aeroacoustics Conference*. AIAA Paper 2012-2059.

Wolf, W.R., Azevedo, J.L.F. & Lele, S.K. 2012*a* Convective effects and the role of quadrupole sources for aerofoil aeroacoustics. *Journal of Fluid Mechanics* **708**, 502–538.

Wolf, W.R., Azevedo, J.L.F. & Lele, S.K. 2012*b* Effects of Mean Flow Convection and Quadrupole Sources on Airfoil Trailing Edge Noise. In *18th AIAA/CEAS Aeroacoustics Conference*. AIAA Paper 2012-2056.

Wolf, W.R., Azevedo, J.L.F. & Lele, S.K. 2013 Effects of mean flow convection, quadrupole sources and vortex shedding on airfoil overall sound pressure level. *Journal of Sound and Vibration* **332** (26), 6905–6912.

Wolf, W.R. & Lele, S.K. 2012 Trailing-Edge Noise Predictions Using Compressible Large-Eddy Simulation and Acoustic Analogy. *AIAA Journal* **50** (11), 2423–2434.

Wolf, W.R., Lele, S.K., Jothiprasad, G. & Cheung, L. 2012*c* Investigation of Noise Generated by a DU96 Airfoil. In *18th AIAA/CEAS Aeroacoustics Conference*. AIAA Paper 2012-2055.

Xu, K., Qiao, W., Ji, L. & Chen, W. 2013 An Experimental Investigation on the near-field turbulence for an airfoil with trailing-edge serrations by using 3-D hot-wire. *Meetings on Acoustics* **19**.

Xu, S. & Wang, Z.J. 2006 Systematic derivation of jump conditions for the immersed interface method in three-dimensional flow simulation. *SIAM Journal on Scientific Computing* **27** (6), 1948–1980.

Yaglom, A.M. 2012 *Hydrodynamic Instability and Transition to Turbulence*. Springer.

Yang, J. & Balaras, E. 2006 An embedded-boundary formulation for large-eddy simulation of turbulent flows interacting with moving boundaries. *Journal of Computational Physics* **215**, 12–40.

Yang, J. & Stern, F. 2012 A simple and efficient direct forcing immersed boundary framework for fluidstructure interactions. *Journal of Computational Physics* **231** (15), 5029–5061.

Yang, X., Zhang, X., Li, Z. & He, G.W. 2009 A smoothing technique for discrete delta functions with application to immersed boundary method in moving boundary simulations. *Journal of Computational Physics* **228** (20), 7821–7836.

Zhang, H.Q., Fey, U., Noack, B.R., Konig, M. & Eckelmann, H. 1995 On the transition of the cylinder wake. *Physics of Fluids* **7** (4), 779.

Zhang, N. & Zheng, Z.C. 2007 An improved direct-forcing immersed-boundary method for finite difference applications. *Journal of Computational Physics* **221**, 250–268.